

**Cellulose Nanocrystals: Plant Design for Up-scaled Production and  
Applications in Green Construction Materials**

**by**

**RISHEN ROOPCHUND**

**Submitted in fulfilment of the academic requirements of**

**Doctor of Philosophy**

in Engineering

Discipline of Chemical Engineering

College of Agriculture, Engineering and Science

University of KwaZulu-Natal

Durban

South Africa

14 October 2021

## **PREFACE**

The research contained in this dissertation was completed by the candidate while based at the Council for Scientific and Industrial Research's (CSIR) Biorefinery Industry Development Facility (BIDF) based in Durban, South Africa. The research was financially supported by the CSIR and South African Department of Science and Innovation (DSI) under the Biorefinery Research Consortium.

The contents of this work have not been submitted in any form to another university, and, except where the work of others is acknowledged in the text, the results reported are due to investigations by the candidate.

---

Signed: Professor B. B. Sithole

Date: 14 October 2021

---

Signed: Dr. J. E. Andrew

Date: 14 October 2021

## DECLARATION 1: PLAGIARISM

*Note that two declaration sections are required if there are papers emanating from the dissertation/thesis. The first (obligatory) declaration concerns plagiarism, and the second declaration specifies your role in the published papers.*

I, Rishen Roopchund, declare that:

- (i) the research reported in this dissertation, except where otherwise indicated or acknowledged, is my original work;
- (ii) this dissertation has not been submitted in full or in part for any degree or examination to any other university;
- (iii) this dissertation does not contain other persons' data, pictures, graphs or other information, unless specifically acknowledged as being sourced from other persons;
- (iv) this dissertation does not contain other persons' writing, unless specifically acknowledged as being sourced from other researchers. Where other written sources have been quoted, then:
  - a) their words have been re-written but the general information attributed to them has been referenced;
  - b) where their exact words have been used, their writing has been placed inside quotation marks, and referenced;
- (v) where I have used material for which publications followed, I have indicated in detail my role in the work;
- (vi) this dissertation is primarily a collection of material, prepared by myself, published as journal articles or presented as a poster and oral presentations at conferences. In some cases, additional material has been included;
- (vii) this dissertation does not contain text, graphics or tables copied and pasted from the Internet, unless specifically acknowledged, and the source being detailed in the dissertation and in the References sections.

Signed: R. Roopchund

Date: 14 October 2021

## DECLARATION 2: PUBLICATIONS

My role in each paper is indicated. The \* indicates the corresponding author.

### Chapter 2

Roopchund, R.\*, Andrew, J. and Sithole, B. 2021. A Review of Global Trends in Cellulose Nanocrystals Production. Status: planned for submission.

### Chapter 7

Roopchund, R.\*, Andrew, J. and Sithole, B. 2021. Novel curing procedures and biomaterial additives to improve green construction materials- critical review and meta-analyses. Status: submitted to *Applied Materials Today* (under consideration).

### Chapter 8

Roopchund, R.\*, Andrew, J. and Sithole, B. 2021. Using cellulose nanocrystals to improve the mechanical properties of fly ash-based geopolymer construction materials. Status: published in *Engineering Science and Technology, an International Journal*.

### Chapter 9

Roopchund, R.\*, Andrew, J. and Sithole, B. 2021. Using cellulose nanocrystals to improve the thermal properties of fly ash-based geopolymer construction materials. Status: planned for submission.

### Chapter 10

Roopchund, R.\*, Andrew, J. and Sithole, B. 2021. Using cellulose nanocrystals to improve the microstructure of fly ash-based geopolymer construction materials. Status: planned for submission.

### Appendix D

Roopchund, R.\*, Andrew, J. and Sithole, B. 2020. Design of a Water Treatment Plant for a novel South African Biorefinery Process using WAVE software. Status: submitted to *Alexandria Engineering Journal* (under review).

Signed: R. Roopchund

Date: 14 October 2021

## ABSTRACT

Two main problems were addressed in this project. Firstly, upscaling technologies from the laboratory scale to industrial scale is difficult in the absence of pilot scale facilities. This research entailed the development of upscaling protocols for large scale production of cellulose nanocrystals (CNC) from sawdust waste biomass to meet increasing end-user demands at the Biorefinery Industry Development Facility (BIDF). Secondly, despite CNC having excellent properties for potential applications in high performance products and materials, CNC applications are still in their infancy, thus needing the demonstration of high impact applications.

To propose potential solutions to these problems, the purpose of this research was to firstly design up-scaled CNC production plants with production capacities ranging from 1 kg/day to 1000 kg/day. These upscaling protocols will ease the difficulty of upscaling the CNC production from the laboratory scale to industrial scale without pilot scale facilities. The second research purpose was to demonstrate the application of CNC in novel green construction materials. The widespread use of ordinary Portland cement (OPC) in the construction industry, and the current landfilling of fly ash are environmentally-degrading. Hence, the CNC-enhanced novel green construction materials used fly ash as a precursor to potentially replace OPC in the construction industry. Furthermore, a database of the mechanical, electrical, thermal, and microstructural properties of the novel green construction material was produced to guide further research and optimizations. Additionally, a universal iterative empirical framework was produced to develop novel green construction materials, whose properties can be customized per the requirements of the target application.

Based on the two main research purposes, the dissertation was divided into two parts: Part A dealt with the up-scaled CNC production process design, and Part B dealt with the application of CNC in the development of novel green construction materials.

Regarding the research design and methodology, the Project Life Cycle Management framework commonly applied in Industry, in conjunction with literary design standards and guidelines, were used in the process design. Software simulations were also used for certain aspects of the process design. The CNC production process design included a de-mineralization

(process) water plant and an acid recovery plant. The equipment sizing and degree of automation were different for each production scale.

For the development of the novel green construction material, meta-analyses coupled with statistical experimental design were used to optimize the experimental trials. The mechanical and electrical test results were used to generate three-dimensional response plots of the CNC effects, thus forming the property database. CNC was found to improve the strength, density, and corrosion resistance (dictated by the electrical resistivity) of the fly ash-based geopolymer construction materials produced at small quantities (optimally 1.7% by volume) when cured for 48 hours with sample rotation. The geopolymer exhibited endothermic properties based on the heat flow analysis, implying its suitability in thermal resistance applications. Furthermore, higher CNC concentrations were found to induce thermal stability during thermal variations in the curing and elevated temperature exposure. Overall, the application of CNC in green construction materials and the empirical framework for the custom development of green construction materials showed substantial potential, thus holding the ability to improve the commercial viability of novel green construction materials to improve their competition against OPC.

The study concluded that the up-scaling protocols developed for CNC production from sawdust waste biomass can be applied in the absence of pilot scale facilities. Furthermore, this study demonstrated that CNC can be applied to develop high performance green construction materials. Only small quantities of CNC (less than 0.5% concentration) were required to improve the thermal and mechanical properties of the novel green construction materials. These small CNC concentrations yielded compressive strengths of up to 8000 kPa and generally reduced the mass loss of samples when exposed to elevated temperatures up to 7%. The broader implication of this project is that the implementation of the desired up-scaled CNC production plant can create employment and boost the economy while providing a steady supply of CNC to meet the growing end-user requirements. Furthermore, the two environmental issues of unsustainable industrial waste disposal and unsustainable OPC building materials can be solved by applying suitable industrial waste materials to produce novel green construction materials as alternatives to OPC using the empirical framework provided in this work.

## ACKNOWLEDGMENTS

Firstly, I would like to express my heartfelt gratitude to my dear Lord for making so many things possible in this project and giving me the ability to do things that were not within my capacity.

After that, I would like to take this opportunity to express sincere gratitude to the following individuals for their invaluable contributions to this project:

- My supervisors, Prof. B. B. Sithole and Dr. J. E Andrew for their guidance, support, and expertise offered in this project.
- Dr. P. Lekha and Ms. L. Musimanyana, of the CSIR Biorefinery Industry Development Facility, for their expertise regarding the SEM-EDX and SEM fracture analyses.
- Ms. L. Maubane, of the CSIR Nanotechnology Innovation Centre, for her expertise in the thermal analyses (TGA-DSC).
- Ms. K. Krishna of the CSIR Information Services for her constant assistance with literary information required for this dissertation.
- Mr. I. Ramlakhan of the Department of Civil Engineering (University of KwaZulu-Natal) for his assistance in the compressive strength tests.
- Dr. A. Swanson of the Department of Electrical, Electronic and Computer Engineering (University of KwaZulu-Natal) for his assistance with the electrical testing.
- Dr. A. du Plessis and Ms. M. Tshibalanganda of the Central Analytical Facilities, CT Scanner Facility (Stellenbosch University) for their assistance with the CT scanning analyses.
- Mr. B. Eslick for his process design expertise and advice based on his many years of experience.

The financial assistance of the CSIR and South African Department of Science and Innovation (DSI) towards this research is acknowledged.

Finally, a special thank you to my family (Reena, Shami, Renata and Kaylen), my friends, and loved ones for their support, and encouragement.

## TABLE OF CONTENTS

	<u>Page</u>
PREFACE .....	ii
DECLARATION 1: PLAGIARISM .....	iii
DECLARATION 2: PUBLICATIONS .....	iv
ABSTRACT .....	v
ACKNOWLEDGMENTS .....	vii
TABLE OF CONTENTS.....	viii
LIST OF TABLES .....	xvii
LIST OF FIGURES .....	xxi
ABBREVIATIONS .....	xxv
CHAPTER 1: INTRODUCTION .....	1
1.1 Background .....	1
1.2 Problem Statements .....	2
1.3 Motivation and Research Aims .....	2
1.4 Thesis Statements .....	3
1.5 Delineations and Limitations.....	3
1.6 Research Contributions .....	3
1.7 Outline of Dissertation Structure.....	4
PART A: CNC PROCESS DESIGN.....	5
CHAPTER 2: A REVIEW OF GLOBAL TRENDS IN CNC PRODUCTION.....	6
2.1 Introduction .....	6
2.2 Part 1: Review of Pilot Plant Production Processes/Facilities .....	6
2.2.1 American Process Inc. ....	6
2.2.2 Blue Goose Biorefineries Inc. ....	9
2.2.3 Forest Products Laboratory .....	10
2.2.4 ICAR-CIRCOT .....	13
2.2.5 InnoTech Alberta.....	14
2.3 Part 2: Review of Pilot Plant Patents .....	16
2.3.1 Domtar Corporation (Patent number: US P,297,111 B1).....	16
2.3.2 FPInnovations (Patent number: US 2010/0286387 A1) .....	18



2.3.3 Hebrew University of Jerusalem (International Publication Number: WO 2012/U14213 A1).....	20
2.3.4 RISE Innventia AB (Patent number: US 8,911,591 B2) .....	21
2.3.6 Nano Green Biorefineries Inc. (International Publication Number: WO 2013/000074 A1).....	22
2.4. Summary and Conclusions .....	25
CHAPTER 3: OPTIMIZATION OF LABORATORY-SCALE CNC PRODUCTION.....	31
3.1 Introduction .....	31
3.2 Results and Discussion .....	32
3.2.1 Proposed Optimization Strategies .....	32
3.2.1.1 Sawdust Delignification.....	32
3.2.1.2 Neutralization, Homogenization, and Purification of CNC Product .....	33
3.2.2 Identification of Alternate Technologies .....	38
3.2.3 Identification of Process Reagents and Disposal Methods .....	39
3.3 Conclusions .....	40
CHAPTER 4: CONCEPT DESIGN.....	41
4.1 Introduction .....	41
4.2 Concept Design Information .....	41
4.3 Preamble to Concept Designs.....	43
4.3.1 Introduction .....	43
4.3.2 Technology Review .....	43
4.3.2.1 Vortex Device for Cavitation (VoDCa).....	43
4.3.2.2 Transmembrane Filtration (TFF).....	45
4.4 Concept Design Options .....	46
4.4.1 Option 1: Advanced (APS + AH) Process .....	46
4.4.2 Option 2: Cavitation-induced Oxidation Process .....	49
4.5 Selection of Preferred Concept Design.....	51
4.6 Capacity-specific Process Concept Designs .....	52
4.6.1 1 kg/day CNC Suspension .....	52
4.6.2 10 kg/day CNC Suspension .....	55
4.6.3 1000 kg/day CNC Suspension.....	57
4.7 Automation Strategy .....	61
4.7.1 Phase 1: Sawdust de-lignification .....	61
4.7.2 Phase 2: Hydrolysis of Sawdust Pulp .....	61

4.7.2 Phase 3: Final Treatment of CNC Suspension Product .....	62
4.8 Block Flow Diagrams .....	63
4.9 Mass Balances .....	64
4.10 Safety Concept.....	68
4.11 Siting Information.....	69
4.11.1 Site Selection.....	69
4.11.2 Site Layout .....	69
4.12 Conclusions and Recommendations .....	70
CHAPTER 5: BASIC DESIGN .....	71
5.1 Introduction .....	71
5.2 Conceptual Process Sequence .....	71
5.2.1 Phase 1: Sawdust de-lignification .....	72
5.2.2 Phase 2: Acid Hydrolysis of Sawdust Pulp.....	72
5.2.3 Phase 3: Final Treatment of the CNC Product.....	73
5.3 List of Plant Operations .....	74
5.4 Mass Balance Calculations.....	77
5.5 Control and Instrumentation (C&I) Design .....	84
5.5.1 C&I Introduction .....	84
5.5.2 C&I Description .....	84
5.5.2.1 Part 1 (De-lignification of Sawdust).....	84
5.5.2.2 Part 2.A (Hydrolysis of Sawdust Pulp).....	88
5.5.2.3 Part 2.B (Spent Acid Recovery) .....	92
5.5.2.4 Part 3 (CNC Purification) .....	97
5.6 Electrical Design.....	100
5.7 Plant Layout .....	102
5.8 Conclusions .....	104
CHAPTER 6: DETAILED DESIGN .....	105
6.1 Introduction .....	105
6.2 Methodology .....	105
6.3 Results.....	109
6.3.1 Piping Design .....	109
6.3.2 Equipment Selection.....	110
6.3.3 Civil and Structural Requirements .....	118
6.3.4 Piping and Instrumentation Diagrams (P&IDs) .....	119

6.4 Discussion .....	125
6.4.1 Primary Design Factors.....	125
6.4.2 Utilities.....	127
6.4.2.1 Electricity .....	127
6.4.2.2 Process Water .....	128
6.5 Conclusion.....	129
6.6 Addendum to Detailed Design .....	129
PART B: APPLICATION OF CNC TO DEVELOP NOVEL GREEN CONSTRUCTION MATERIALS .....	131
CHAPTER 7: NOVEL CURING PROCEDURES, BIO-ADDITIVES, AND CNC TO IMPROVE GREEN CONSTRUCTION MATERIALS: CRITICAL REVIEW AND META-ANALYSES .....	132
7.1 Introduction .....	132
7.2 Literature Review .....	133
7.2.1 Current State of the Construction Industry- An Overview .....	133
7.2.2 Fly ash-based Geopolymers as Green Construction Materials .....	135
7.2.3 Novel Curing Procedures for Fly Ash-based Geopolymers.....	135
7.2.4 Biomaterials to Fortify Construction Materials.....	138
7.2.5 CNC to Fortify Construction Materials .....	143
7.2.6 Meta-analysis as a Literature Tool .....	146
7.3 Materials and Methods.....	147
7.3.1 Literature Review Methodology .....	147
7.3.2 Inclusion Criteria for the Meta-analysis .....	148
7.3.3 Meta-analysis .....	149
7.3.4 Data analysis .....	150
7.4 Results.....	152
7.4.1 Included Studies .....	152
7.4.1.1 Novel Curing Procedures .....	152
7.4.1.2 Reinforcing Biomaterials .....	152
7.4.1.3 CNC .....	153
7.4.2 Meta-analysis .....	155
7.4.2.1 Novel Curing Procedures .....	156
7.4.2.2 Reinforcing Biomaterials .....	157
7.4.2.3 CNC .....	158

7.5 Discussions .....	163
7.5.1 Meta-analyses .....	163
7.5.2 Application of Meta-analysis in Engineering Research .....	165
7.5.3 Framework for Conducting Meta-analyses .....	165
7.6 Conclusions .....	166
CHAPTER 8: USING CNC TO IMPROVE THE MECHANICAL PROPERTIES OF FLY ASH-BASED GEOPOLYMER CONSTRUCTION MATERIALS .....	169
8.1 Introduction .....	169
8.2 Literature Review .....	170
8.2.1 Overview of the Current State of the Construction Industry .....	170
8.2.2 Overview of Green Construction Materials .....	171
8.2.3 Fly ash-based geopolymers as Green Construction Materials .....	172
8.2.4 CNC to Enhance Geopolymer Construction Materials .....	172
8.2.5 The Effect of Alkaline Activators in Geopolymerization .....	175
8.2.6 Corrosion Resistance in Construction Materials .....	175
8.3 Materials and Methods .....	177
8.3.1 Materials .....	177
8.3.1.1 Fly Ash .....	177
8.3.1.2 Sawdust-based CNC .....	177
8.3.2 Geopolymer Mixture Design .....	177
8.3.3 Statistical Experimental Design .....	178
8.3.4 Geopolymer Synthesis .....	179
8.3.4.1 Preparation of Solutions .....	179
8.3.4.2 Geopolymer Moulding .....	179
8.3.4.3 Geopolymer Oven Curing .....	179
8.3.5 Geopolymer Testing .....	181
8.3.5.1 Compressive Strength .....	181
8.3.5.2 Density .....	181
8.3.5.3 Electrical Resistivity .....	182
8.4 Results and Discussion .....	183
8.4.1 Geopolymer Synthesis .....	183
8.4.2 Compressive Strength .....	183
8.4.2.1 Statistical Model .....	183
8.4.2.2 Two-dimensional Interactions .....	184

8.4.2.3 Three-dimensional Response Surface Model.....	186
8.4.3 Density .....	187
8.4.3.1 Statistical Model.....	187
8.4.3.2 Two-dimensional Interactions .....	188
8.4.3.3 Three-dimensional Response Surface Model (24-hour curing) .....	190
8.4.4 Electrical Resistivity .....	191
8.4.4.1 Statistical Model (24-hour curing) .....	191
8.4.4.2 Two-dimensional Interactions (24-hour curing) .....	192
8.4.4.3 Three-dimensional Response Surface Model (24-hour curing) .....	194
8.4.4.4 Statistical Model (48-hour curing) .....	195
8.4.4.5 Two-dimensional Interactions (48-hour curing) .....	196
8.4.4.6 Three-dimensional Response Surface Model (48-hour curing) .....	198
8.4.5 Overall Correlation between the Mechanical Properties .....	199
8.4.6 Geopolymer Development Framework .....	200
8.5 Conclusions .....	201
CHAPTER 9: THE EFFECT OF CNC ON THE THERMAL BEHAVIOUR OF NOVEL GREEN CONSTRUCTION MATERIALS .....	203
9.1 Introduction .....	203
9.2 Literature Review .....	203
9.2.1 Thermal Analysis of Metakaolin Based Geopolymers .....	204
9.2.2 Thermal Properties of Geopolymers Exposed to High Temperature .....	205
9.2.3 Thermal Stability of One-part Metakaolin Geopolymer Reinforced with Spodumene Tailings and Glass Wool.....	206
9.2.4 Experimental Study of TGA Techniques in Geopolymeric Materials .....	208
9.2.5 Thermal Character of Geopolymers Synthesized from Class F Fly Ash.....	209
9.2.6 Summary .....	210
9.3 Materials and Methods.....	213
9.4 Results and Discussions .....	214
9.4.1 Thermo-gravimetric Analysis .....	214
9.4.1.1 General Trends .....	214
9.4.1.2 Comparative Thermo-gravimetric Analyses .....	218
9.4.1.3 Derivative Mass Plots .....	218
9.4.2 Differential Scanning Calorimetry .....	221
9.4.2.1 General Trends .....	221

9.5 Conclusions .....	224
CHAPTER 10: THE EFFECT OF CNC ON THE MICROSTRUCTURE OF NOVEL GREEN CONSTRUCTION MATERIALS .....	226
10.1 Introduction .....	226
10.2 Literature Review .....	227
10.2.1 SEM Analyses .....	227
10.2.2 Elemental Analyses .....	229
10.2.3 X-ray CT Scanning Analyses .....	232
10.2.4 Geopolymer Microstructure .....	233
10.2.4.1 Effect of Geopolymerization on the Microstructure.....	233
10.2.4.2 Geopolymer Matrix Heterogeneity.....	235
10.2.4.3 Mullite Formation.....	235
10.2.4.4 Cracks in the Microstructure .....	236
10.2.4.5 Effect of Chemical Composition on Micro-cracking .....	236
10.2.4.6 Unreacted Fly Ash Particles .....	236
10.3 Materials and Methods.....	237
10.4 Results and Discussion.....	237
10.4 Results and Discussion.....	255
10.4.1 Overall Geopolymer Microstructure.....	255
10.4.1.1 Geopolymer Matrix Heterogeneity.....	255
10.4.1.2 Mullite Formation.....	255
10.4.1.3 Cracks in the Microstructure .....	256
10.4.1.4 Effect of Chemical Composition on Micro-cracking .....	256
10.4.1.5 Unreacted Fly Ash Particles .....	256
10.4.2 Effects of Curing Time and CNC Concentration on Geopolymer Micrographs under 24 and 48-hour Curing Conditions.....	257
10.4.2.1 Sample 1 (0% CNC) .....	257
10.4.2.2 Sample 2 (0.71% CNC) .....	258
10.4.2.3 Sample 3 (0.86% CNC) .....	258
10.4.2.4 Sample 4 (1.28% CNC) .....	258
10.4.2.5 Sample 5 (1.56% CNC) .....	258
10.4.2.6 Sample 6 (1.7% CNC) .....	259
10.4.2.7 Sample 7 (2% CNC) .....	259
10.4.3 Elemental Composition and Si/Al Ratio.....	260

10.4.3.1 General Elemental Composition Trends .....	260
10.4.3.2 Silicon to Aluminium Ratio .....	260
10.4.4 Fracture Analyses .....	261
10.4.5 X-ray CT Slice Imaging .....	262
10.4.6 Internal Porosity .....	264
10.5 Conclusions .....	265
CHAPTER 11: CONCLUSIONS.....	267
11.1 Summary of Findings.....	267
11.1.1 Part A .....	267
11.1.2 Part B .....	268
11.2 Conclusions .....	269
11.2.1 Part A .....	269
11.2.2 Part B .....	270
11.3 Summary of Contributions .....	271
11.3.1 Part A .....	271
11.3.2 Part B .....	272
11.3.3 Implications for Existing Theory.....	274
11.4 Recommendations for Further Work .....	275
11.5 Final Comments and Summary Conclusions .....	275
REFERENCES.....	276
APPENDIX A: PROCESS FLOW DIAGRAMS .....	294
APPENDIX B: PIPING AND INSTRUMENTATION DIAGRAMS .....	295
APPENDIX C: ORIGINAL EQUIPMENT MANUFACTURER CATALOGUES .....	296
APPENDIX D: DESIGN OF A WATER TREATMENT PLANT USING WAVE SOFTWARE .....	297
D.1 Introduction .....	297
D.2 Materials and Methods.....	298
D.2.1 Preliminary Step .....	298
D.2.2 Water Treatment Plant Simulations .....	299
D.2.2.1 UF Design .....	300
D.2.2.2 RO Design .....	302
D.3 Literature Review .....	303
D.4 Results .....	310
D.4.1 UF Results .....	310

D.4.2 RO Results.....	312
D.5 Discussions .....	314
D.5.1 UF Design.....	314
D.5.2 RO Design .....	315
D.6 Conclusions .....	317



## LIST OF TABLES

<b><u>Table</u></b>	<b><u>Page</u></b>
Table 2.1. Transition steps to commercial scale CNC production used by American Process Inc. (Retsina, 2016) .....	8
Table 2.2. Summary of production CNC production parameters at FPL (Reiner and Rudie, 2013) .....	12
Table 2.3. Assessment criteria for CNC production at Nano Green Biorefineries Inc. (McAlpine and Koneshny, 2017) .....	25
Table 2.4. Summary of CNC production technologies .....	26
Table 2.5. Comparisons between the typical treatments .....	28
Table 3.1. Baseline Risk Assessment for laboratory-scale CNC production .....	35
Table 3.2. Identification of alternate technologies for up-scaled CNC production .....	38
Table 3.3. Process reagents and disposal methods .....	39
Table 4.1. Key to Figure 1 .....	42
Table 4.2. Design Pathways .....	43
Table 4.3. Comparison of technology between the existing and proposed processes.....	49
Table 4.4. Comparison of Proposed Concept Designs .....	51
Table 4.5. Potential Anomalies and Mitigation Measures.....	58
Table 4.6. Sawdust Composition.....	64
Table 4.7. Cellulose Morphology .....	65
Table 4.8. CNC Product Suspension Properties.....	65
Table 4.9. Overall Mass Balance .....	65
Table 4.10. De-lignification Stoichiometry .....	66
Table 4.11. Hydrolysis Stoichiometry .....	67

Table 4.12. CNC Datasheet .....	67
Table 5.1. Basic Design- List of Plant Operations .....	74
Table 5.2. Basic Design- Mass and volume production capacities .....	77
Table 5.3. Basic design- Mass balance .....	78
Table 5.4. Basic design- de-lignification stoichiometry .....	79
Table 5.5. Basic design- relation between mass production rate and de-lignification reactor size .....	80
Table 5.6. Basic design- Hydrolysis stoichiometry .....	81
Table 5.7. Basic design- Relation between mass production rate and hydrolysis reactor size .....	82
Table 5.8. Basic design- Recirculation tank sizing .....	82
Table 5.9. Recirculation tank sizes .....	83
Table 5.10. Basic Design- Tank size summary .....	83
Table 5.11. Basic design- Process part 1 C&I .....	84
Table 5.12. Basic design- Process part 2 A C&I .....	88
Table 5.13. Basic design- Process part 2B C&I .....	92
Table 5.14. Basic design- Process part 3 C&I .....	97
Table 5.15. Basic design- Electrical design considerations .....	100
Table 6.1. Key to Darcy-Weisbach equation .....	108
Table 6.2. Piping Design Results .....	109
Table 6.3. Equipment Selection Results .....	111
Table 6.4. Recommended piping clearances .....	119
Table 6.5. Line Keys .....	120
Table 6.6. Equipment Keys .....	122

Table 6.7. C&I Equipment Codes .....	123
Table 6.8. Detailed Engineering Design Categories (International Atomic Energy Agency, 1990).....	126
Table 6.9. OEM Catalogue Index.....	129
Table 7.1. Inclusion Criteria .....	148
Table 7.2. Included studies for novel curing procedures.....	152
Table 7.3. Inclusion criteria for reinforcing biomaterials.....	153
Table 7.4 Qualifying studies included in the meta-analysis.....	154
Table 8.1. Literary correlations between the electrical resistivity and corrosion resistance of construction materials.....	176
Table 9.1. Literature thermal analyses.....	211
Table 10.1 Recommended applications of geopolymeric materials based on silicon to aluminium ratios (Davidovits, 1999).....	231
Table 10.2. SEM micrographs of geopolymer samples under two different curing conditions .....	238
Table 10.3. Fracture analysis micrographs at varying resolutions.....	249
Table 10.4. CT slice images of experimental geopolymer samples.....	251
Table 10.5. Internal Porosity Imaging (not presented to scale).....	252
Table 10.6. Adjusted extended curing procedure to minimize sample cracking.....	263
Table D.1 Gauteng Municipal Water Quality Data.....	299
Table D.2. UF Feed and Permeate Streams Comparison .....	311
Table D.3. UF Module Details.....	311
Table D.4. RO Stream Information .....	312
Table D.5. RO Ion Removal .....	312

Table D.6. UF and RO Cost Comparison .....	313
--	-----

## LIST OF FIGURES

<b><u>Figure</u></b>	<b><u>Page</u></b>
Figure 2.1. Schematic of CNC production used by American Process Inc. (Retsina, 2016) .....	8
Figure 2.2. Schematic of ICAR-CIRCOT CNC production process (“ICAR- Central Institute for Research on Cotton Technology”, n.d.) .....	14
Figure 2.3. Domtar Corporation CNC production schematic (Marcoccia et al., 2016) .....	17
Figure 2.4. CNC production schematic at FPInnovations (Hashaikh et al, 2010) .....	19
Figure 2.5. Catalytic biomass conversion at Nano Green Biorefineries Inc. (McAlpine and Koneshny, 2017) .....	23
Figure 2.6. CNC production schematic at Nano Green Biorefineries Inc. (McAlpine and Koneshny, 2017) .....	24
Figure 4.1. Typical Project Life Cycle Model .....	42
Figure 4.2. TFF Schematic (Dalwadi et al., 2005). (1) Sample reservoir (2) Peristaltic pump (3) Feed pressure gauge (4) Minimate 300 K (5) Transmembrane pressure gauge (6) Screw clamp valve (7) Filtrate collector.....	45
Figure 4.3. Proposed TFF .....	46
Figure 4.4. BFD (Phase 1 CNC Production).....	63
Figure 4.5. BFD (Phase 2 CNC Production).....	63
Figure 4.6. BFD (Phase 3 CNC Production).....	64
Figure 5.1. Basic design- Plant layout.....	103
Figure 6.1. Grundfos Online Pump Selection Tool (Grundfos Product Center, n.d.).....	107
Figure 7.1. Venn diagram of literature review target parameters .....	148
Figure 7.2. Forest plot for novel curing procedures .....	156
Figure 7.3. Funnel plot for novel curing procedures .....	157

Figure 7.4. Forest plot for reinforcing biomaterials. ....	158
Figure 7.5. Funnel plot for reinforcing biomaterials. ....	158
Figure 7.6. Overall Meta-analysis and Forest Plot.....	159
Figure 7.7. Overall Funnel Plot.....	160
Figure 7.8. Meta-analysis and Forest Plot for Sensitivity Analysis 1 .....	161
Figure 7.9. Funnel Plot for Sensitivity Analysis 1 .....	161
Figure 7.10. Meta-analysis and Forest Plot for Sensitivity Analysis 2 .....	162
Figure 7.11. Funnel Plot for Sensitivity Analysis 2 .....	162
Figure 7.12. Empirical framework for conducting meta-analyses. ....	166
Figure 7.13. Relationship between the critical stakeholder contributions.....	168
Figure 8.1. Summary of the statistical experimental design.....	178
Figure 8.2. (a) Alkaline activator solutions (b) CNC solutions (c) Fly ash (d) Moulded geopolymer pastes prior to curing (e) Oven used for curing (f) De-moulded geopolymers post- curing .....	180
Figure 8.3. Compressive strength equipment; A- Tensile testing machine, B- Load indicator, C- base plate, D- Load exertion controls .....	181
Figure 8.4. Electrical resistivity experimental setup; A- Fluke 1577 insulation multimeter, B- Conductive plates, C- Geopolymer sample, D- Current-measuring electrodes.....	182
Figure 8.5. Compressive strength predicted versus actual.....	184
Figure 8.6. Panel plot of compressive strength interactions .....	186
Figure 8.7. Compressive strength surface response model.....	187
Figure 8.8. Density actual versus predicted values .....	188
Figure 8.9. Panel plot of density interactions .....	190
Figure 8.10. Three-dimensional density response curve .....	191

Figure 8.11. Electrical resistivity actual versus predicted model (24-hour curing condition)	192
Figure 8.12. Electrical resistivity interaction panel plots (24-hour curing condition) .....	194
Figure 8.13. Electrical resistivity three-dimensional surface response curve (24-hour curing condition) .....	195
Figure 8.14. Electrical resistivity actual versus predicted model (48-hour curing condition)	196
Figure 8.15. Electrical resistivity interaction panel plots (48-hour curing condition) .....	198
Figure 8.16. Electrical resistivity three-dimensional surface response curve (48-hour curing condition) .....	199
Figure 8.17. Empirical geopolymer construction material development framework.....	201
Figure 9.1. TGA curves for metakaolin-based geopolymers, G1 and G2 (Caballero et al., 2019) .....	205
Figure 9.2. DTA curves for metakaolin-based geopolymers, G1 and G2 (Caballero et al., 2019) .....	205
Figure 9.3. TGA curves of metakaolin geopolymer composites (Lemougna et al., 2020) ....	207
Figure 9.4. TGA curve for fly ash-based geopolymer (Rosas-Casarez et al., 2014) .....	208
Figure 9.5. TGA/ DTA plot for fly ash-based geopolymer (Rickard and van Riessen, 2010) .....	210
Figure 9.6. TGA of 24 hour-cured samples .....	215
Figure 9.7. TGA of 48 hour-cured samples .....	216
Figure 9.8. Overall mass loss at each dosage of CNC.....	217
Figure 9.9. Mass loss comparison between the baseline and optimal CNC dosage with curing condition influence .....	217
Figure 9.10. Derivative mass change for 24 hour-cured samples .....	220
Figure 9.11. Derivative mass change for 48 hour-cured samples .....	221
Figure 9.12. Heat flow analysis for 24 hour-cured samples .....	222

Figure 9.13. Heat flow analysis for 48 hour-cured samples .....	223
Figure 9.14. Heat flow comparison between the baseline and optimal CNC dosage with curing condition influence. ....	224
Figure 10.1 Descriptive model of the alkali activation of fly ash (Pacheco-Torgal et al., 2008) .....	234
Figure 10.2. Micrograph of the binder-aggregate interface (Kupwade-Patil and Allouche, 2016) .....	235
Figure 10.3. Chemical composition of fly ash precursor material .....	245
Figure 10.4. Elemental composition of 24-hour cured geopolymer samples. ....	245
Figure 10.5. Elemental composition of 48-hour cured geopolymer samples. ....	246
Figure 10.6. Average elemental composition comparison. ....	246
Figure 10.7. Elemental composition comparison of 24-hour cured samples with the fly ash precursor. ....	247
Figure 10.8. Elemental composition comparison of 48-hour cured samples with the fly ash precursor. ....	247
Figure 10.9. Effect of curing condition on the Si/Al ratios of the geopolymer samples. ....	248
Figure 11.1. Conceptual framework for green construction Materials .....	273
Figure D.1. Stage 1 of the WAVE design simulation .....	300
Figure D.2 Stage 2 of the WAVE design simulation .....	301
Figure D.3. Specification of the Ultrafiltration stage .....	302
Figure D.4. Reverse Osmosis (RO) Design Stage .....	303
Figure D.5. Summary of the UF Design.....	311
Figure D.6. RO Flow Diagram.....	312



## ABBREVIATIONS

AH	Acid Hydrolysis
API	American Process Inc.
APS	Ammonium Persulfate
AVAP	American Value-added Pulping
BFD	Block Flow Diagram
BIDF	Biorefinery Industry Development Facility
C&I	Control and Instrumentation
CIP	Clean-In-Place
CNC	Cellulose Nanocrystals
CSIR	Council for Scientific and Industrial Research
DP	Differential Pressure
DSC	Differential Scanning Calorimetry
DTA	Differential Thermal Analysis
EDX	Energy-dispersive X-ray Analysis
FTPP	Forestry, Timber, Pulp and Paper
HMI	Human Machine Interface
OEM	Original Equipment Manufacturer
OPC	Ordinary Portland Cement
P&ID	Piping and Instrumentation Diagram
PFD	Process Flow Diagram
PLC	Programmable Logic Controller
PO	Plant Operator
RO	Reverse Osmosis
SEM	Scanning Electron Microscopy
TFF	Tangential Flow Filtration
TGA	Thermo-gravimetric Analysis
UF	Ultra-filtration
VoDCa	Vortex Device for Cavitation
WAVE	Water Application Value Engine

## CHAPTER 1: INTRODUCTION

### 1.1 Background

*“Let every individual and institution now think and act as a responsible trustee of Earth, seeking choices in ecology, economics and ethics that will provide a sustainable future, eliminate pollution, poverty and violence, awaken the wonder of life and foster peaceful progress in the human adventure.” – John McConnell*

Due to the rapid emergence of the fourth industrial revolution, the South African Forestry, Timber, Pulp and Paper (FTPP) Industry has been experiencing a decline. The biorefinery concept was formed to solve this problem by improving the profitability of the FFTP Industry by converting its waste products into high-value materials. In line with the biorefinery concept, this study focuses on converting sawdust waste into cellulose nanocrystals (CNC). Besides providing an environmentally friendly disposal pathway for sawdust waste, CNC is a high-value material with many applications.

The CSIR’s Biorefinery Industry Development Facility (BIDF) has developed a laboratory-scale CNC production process, known as the “(APS + AH)” process. This process uses ammonium persulfate to de-lignify the sawdust, after which the sawdust pulp is acid hydrolyzed to yield the raw CNC that undergoes further purification to reach the final CNC product. Due to the growing demand for sawdust-based CNC, larger production scales are required. As such, this project sought to design up-scaled CNC production processes.

Furthermore, the global construction market is primarily using ordinary Portland cement (OPC) for commercial construction. The production of OPC is a significant contributor to greenhouse gas emissions due to the energy intensity of the process. Aligned to the theme of environmental degradation, the production of fly ash as a by-product waste material from coal-fired power stations is a challenge, as the fly ash is typically disposed of in ash dumps and landfill sites. Combined with the fact that South Africa is currently experiencing a backlog in housing, much interest has been placed on producing fly ash-based construction materials as alternatives to OPC. In a bid to improve the overall properties of fly ash-based construction materials, this project sought to investigate the application of CNC in fly ash-based construction materials.

## **1.2 Problem Statements**

- a) It is difficult to up-scale technologies from a laboratory scale to industrial scale without an intermediate pilot scale. The current CNC production from sawdust waste biomass at the CSIR's BIDF requires upscaling from laboratory scale to industrial scale in the absence of pilot scale facilities.
- b) Despite the excellent potential of CNC for applications in high performance products and materials, CNC applications are still in their infancy. Hence, the demonstration of high impact CNC applications are needed. Specifically, the application of CNC is needed in developing novel green construction materials to potentially replace OPC. The use of industrial waste precursors in the novel green construction materials is also required.

## **1.3 Motivation and Research Aims**

Various studies in the literature have outlined the production of CNC from various types of raw materials: raw eucalyptus biomass (Retsina, 2016; Marcoccia et al., 2016), commercial viscose-grade dissolving pulp (Reiner and Rudie, 2013), dissolving pulp, bleached softwood kraft pulp, bleached hardwood kraft pulp (Ngo et al., 2018), cotton, bacterial cellulose and agricultural waste (ICAR-CIRCOT, n.d.) and paper mill waste sludge (Shoseyov et al., 2012). However, none of the studies demonstrated the production of CNC from sawdust as a precursor. Furthermore, the literature studies have failed to report step-by-step up-scaling and optimizations by following a project life cycle model approach in which a successive and iterative design and optimization cycle is used to arrive at the up-scaled plant designs. Therefore, this research aimed to design up-scaled CNC production plants from sawdust biomass wastes to serve as blueprints to increase the CNC production from laboratory scale to industrial scale in the absence of pilot plant facilities.

Furthermore, various literature studies focused on the application of CNC in OPC materials, but none considered the application of CNC in fly ash-based geopolymer construction materials or other green construction materials (Barnat-Hunek et al., 2019; Dousti et al., 2019; Cao et al., 2016a, b; Mazlan et al., 2015; Liu et al., 2019a). In addition, various studies were limited in the investigative parameters affecting the properties of the green construction materials. Therefore, this research aimed to broaden the understanding of the mentioned limitations in the literature by studying the effect of various influencing parameters on the mechanical, thermal, and microstructural properties of the synthesized CNC-based fly ash geopolymer construction

materials. Consequently, this research aim demonstrated the application of CNC in the development of novel green construction materials that could potentially replace traditional OPC materials.

#### **1.4 Thesis Statements**

The laboratory-scale (APS + AH) process was used as a basis to design an up-scaled CNC production process. The up-scaled designs can be used as blueprints to improve the CNC production capacity in the absence of pilot scale facilities.

The application of CNC in fly ash-based geopolymer construction materials will improve the material's overall mechanical, electrical, and thermal properties. Hence, CNC can be successfully applied in the development of green construction materials.

#### **1.5 Delineations and Limitations**

As a delineation, this project exclusively considered the technical and safety, health, and environmental aspects of the CNC process design. The costing and economic evaluation of the process design were excluded due to the design being aligned to the current global trends and developments in CNC production, which have already exhibited commercial viability.

#### **1.6 Research Contributions**

This research forms the knowledge base of CNC production process technology up-scale and optimization through the combined application of traditional design techniques and industrial iterative design procedures (Project Life Cycle Model). The design method applied in this work can be replicated and applied to other similar studies. Furthermore, this research contributes to the current knowledge base of CNC production trends.

In addition, this research contributes to the current knowledge of fly ash-based green construction material synthesis and optimization by developing an iterative application framework that can be applied to the development of any waste-based green construction material. This research also contributes to the knowledge base of the effect of multiple influencing parameters on the properties of the synthesized green construction materials. This work could contribute to economic growth, sustainability, and affordable construction materials, thereby potentially minimizing the dependence on traditional OPC materials.

### **1.7 Outline of Dissertation Structure**

This dissertation was divided into two main parts: Part A entailed the up-scaled CNC production process design, and Part B dealt with the application of CNC in the development of novel green construction materials. Part A is comprised of Chapters 2 to 6, while Part B is comprised of Chapters 7 to 10.

In Chapter 2, the global trends in CNC production were reviewed and summarized to serve as a baseline for the type and functionality of the technology required in the up-scaled CNC production process designs. Commercial processes and research patents were reviewed.

In Chapter 3, the results of an optimization study undertaken on the laboratory (APS + AH) CNC production process were presented and discussed to guide the design of the up-scaled production processes. Pertinent matters, such as the challenges and shortcomings of the laboratory process, identification of alternate process technologies, environmental and quality considerations, were presented.

Finally, Chapters 4, 5, and 6 presented the Concept, Basic, and Detailed up-scaled CNC production process design phases, respectively, by combining the traditional design strategies with the industrial Project Life Cycle Model. As an addendum to the detailed design reported in Chapter 6, Appendix D presents the design and simulation of a process water plant required for the up-scaled CNC production process.

Chapter 7 presented three systematic reviews and corresponding meta-analyses on the quantified effects of novel curing procedures, fiber reinforcement, and CNC on the mechanical properties of construction materials to streamline the subsequent chapters' experimental work.

Chapter 8 reported the effect of CNC on the mechanical properties (compressive strength, density, and electrical resistivity) of the novel green construction material. Based on the experimental study, an empirical framework for developing novel green construction materials was reported.

Chapter 9 investigated the effect of CNC on the thermal properties (mass loss and heat flow) of the novel green construction materials developed in Chapter 8, while Chapter 10 investigated the effect of CNC on the elemental composition and microstructure of the novel green construction materials.

## **PART A: CNC PROCESS DESIGN**

## **CHAPTER 2: A REVIEW OF GLOBAL TRENDS IN CNC PRODUCTION**

### **2.1 Introduction**

This chapter aims to review and critique the current global production trends of cellulose nanocrystals (CNC) in two parts: commercial production processes and research patents, thereby providing a narrative overview on the subject matter. Various articles and patents were reviewed, analyzed, and critiqued to provide details of CNC manufacture and the steady transition from laboratory-scale to pilot plant-scale and finally towards commercialization. In instances where review papers or patents were not available, company websites were consulted.

The Forestry Industry has experienced a decline in profitability over recent years. There are two major reasons for this. Firstly, only 40% of the harvested raw material is processed into paper products, while the rest is discarded as waste (Sithole, 2017). Secondly, the Paper Industry is losing the battle against digital technology (Forestry South Africa, 2016). The Biorefinery concept was conceptualized to recover the profitability of the failing Industry (Xuan et al., 2012). The biorefinery concept directly addresses the first reason for the declining Forestry Industry by creating new high-value product streams from multiple waste streams.

One such novel product that can be created from lignocellulosic forestry wastes is cellulose nanocrystals (CNC). CNC is the highly structured building block of all plants and has a tremendous range of applications. CNC can be directly extracted from the pulp or (through chemical processing) from forestry wastes such as waste wood and sludge. As the CNC market continues its steady growth trajectory (Nanocellulose market, n.d.), it is vital to understand the development of CNC production processes. This understanding can help compare and analyze the processes to streamlining them into efficient and cost-effective production strategies. This review paper is presented with this motivation. This review is divided into two parts. The first part focuses on current and emerging developments in pilot-scale CNC production, while the second part focuses on the technologies that have been recently patented for the same purpose.

### **2.2 Part 1: Review of Pilot Plant Production Processes/Facilities**

#### **2.2.1 *American Process Inc.***

American Process Inc. (API) is an American company formed in 1995 as an Engineering Consulting company in the Forest Products Industry. Today it is regarded as a global leader in

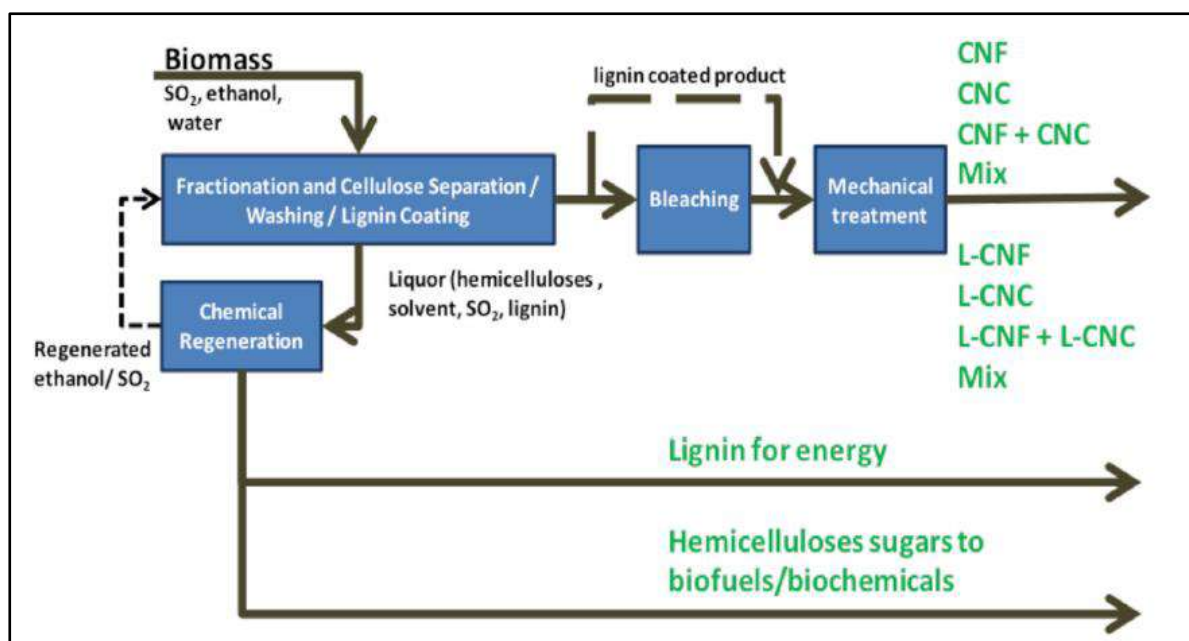
developing technologies for the commercial production of sugar, ethanol, and other high-value chemicals from non-food-based biomass. It is noteworthy that their American Value Added Pulping (AVAP) process can be applied to any lignocellulosic biomass to produce CNC (Nelson and Restina, 2014).

Kim and Retsina (2014) at the AVAP Biorefinery Facility located in Thomaston, USA, developed and commercialized a novel CNC production process for large-scale CNC manufacture. Their review paper described the patented AVAP technology for the commercial production of nanocellulose products (CNC and CNF). The AVAP technology is novel in that it enables flexibility in the morphology and surface properties of the final products. In addition, it is anticipated that the process will be cost-competitive with petroleum-based products, which is uncommon, as most bio-products have not been able to achieve this degree of cost-effectiveness thus far. Hence, the AVAP process is vastly different from the others outlined in this review paper.

The AVAP pre-treatment process was designed such that the eucalyptus biomass is mixed with the sulfur dioxide de-lignifying agent (to aid in the release of cellulose and hemicellulose from lignin), ethanol solvent (to aid the penetration of sulfur dioxide into the biomass material), and water. During this stage, strong lignosulfonic acids are created to facilitate the hydrolysis phase, leading to CNC and cellulose nanofibers (CNF). This is unique from the other processes reviewed that require concentrated sulphuric acid for the hydrolysis phase. The dissolved sugars in the residual liquor are used to produce biofuels and biochemical products. The CNF and CNC products are washed to remove the dissolved lignin and sugars. Every output stream from the process can be refined to obtain valuable products as opposed to disposal. Such recycling is remarkable from an economic and environmental perspective. According to Miller (2016), API has a CNC production capacity of 0.5 tons per day and is therefore considered a leading CNC production company, alongside CelluForce. The reported process is advantageous as it outputs low-cost and clean CNC while having the ability to produce CNC at a large scale (Glassner, 2013).

Regarding the process units involved, the design is simplistic as no mechanical separation units are required, other than a fractionation column used to separate the cellulose from the hemicellulose and lignin fractions. The other process equipment is regarded as standard, thus holding positive implications for process implementation. A simplified schematic is shown in **Figure 2.1** below.





**Figure 2.1. Schematic of CNC production used by American Process Inc. (Retsina, 2016)**

Retsina (2016) presented a Biorefinery optimization workshop in partnership with the US Department of Energy, which outlined the phases, actions, and pitfalls that this project endured before commercialization. The laboratory and pilot-scale technology were developed from 2006 to 2010, followed by production demonstration from 2011 to 2014 until commercialization took place in 2015. Table 2.1 below defines the main phases undertaken by API to develop their CNC production potential: laboratory-scale, pilot-scale, pre-commercialization, and commercial. These phases are noteworthy, as knowledge thereof can streamline the commercialization process. In addition, it is worth considering the pitfalls experienced by American Process Inc. during their trajectory to commercialization to ensure that they are not repeated.

**Table 2.1. Transition steps to commercial scale CNC production used by American Process Inc. (Retsina, 2016)**

Phase	Defining Action	Challenges
Prefeasibility	Development of a viable plan.	The market is not considered. Timelines are overly optimistic.

Laboratory-scale	Conducting bench-scale experiments.	Unrealistic conditions and failing to realize this.
Process design	Design of the process for commercialization and conducting of a techno-economic analysis.	Process design may be performed by an inexperienced team, yielding an unrealistic design with a large number of steps.
Pilot-scale	Performing more extensive batch experiments.	Often ignores the importance of recycling streams, concentration, and energy integration.
Pre-commercial demonstration	Continuous fully integrated operation.	Non-industrial equipment is used, and simulation tools are often not used for validation. There is a need to iterate from the end of this phase to the process design phase.
Commercial plant-scale	Building on scale and start-up.	Inadequate completion of the steps above and the possibility of “reinventing the wheel.”
Continued Operations	Continuous improvement.	Failure to allow for startup curve.

---

### **2.2.2 Blue Goose Biorefineries Inc.**

Blue Goose Biorefineries Inc. is a private Canadian company founded in 2007 to derive biodiesel and cellulosic ethanol from agricultural residues. Over time it was realized that the technology was better suited to producing crystalline forms of cellulose from both technical and economic standpoints (“Blue Goose Biorefineries Inc.,” n.d.). In 2012, the company received funding to scale up this technology, resulting in implementing a pilot plant facility in Saskatoon, which began production in 2014. According to Millner (2016), Blue Goose holds a CNC production capacity of 100 kg per day. The pilot plant produces CNC for sale while generating process data for commercial-scale plant design. Although acetate-grade dissolving pulp is used for CNC production, other biomass types have been successfully converted (“Blue Goose Biorefineries Inc.,” n.d.).

The production method employed at Blue Goose Biorefineries is based on the transition metal-catalyzed oxidation of lignocellulosic biomass. The chemistry employed is similar to the

Fenton-Haber reaction cycle, characterized by the spontaneous reactivity of the biomass with the input reagents. The process is driven by radical generation. Considering that radicals are highly reactive due to having an unpaired electron, they react very quickly with the biomass (“Blue Goose Biorefineries Inc.,” n.d.). The process comprises two oxidation stages (which occur in two separate reactors) with an intermediate alkaline extraction phase. The first oxidation reaction is performed on fibrous biomass, which significantly reduces the biomass fiber length. The reaction is deemed complete by visual observation of the suspension colour change from greyish to white (“Blue Goose Biorefineries Inc.,” n.d.). The oxidation reaction generates carboxylic acids, which are made soluble by the subsequent alkaline extraction step. These weak acids exhibit relatively low solubility under acidic or neutral conditions. The extraction reaction mechanism entails the addition of sodium hydroxide into the suspension to increase the solubility of the acids, thus enabling separation from the (now partly disintegrated) biomass. This separation results in the ability to have them washed from the CNC product (“Blue Goose Biorefineries Inc.,” n.d.).

The second oxidation reaction step enables the separation of the non-CNC biomass portion. The CNC product can then be washed, de-watered, and packaged (“Blue Goose Biorefineries Inc.,” n.d.). Although no detailed design information was available at the time of review, it was reported that the pre-requisites for effective operation are proper mixing, temperature control, and maintaining the correct ratio of oxidant to biomass. Although, the Blue Goose process seems straightforward, more information outlining the process yield, techno-economics, and optimization techniques is required to gain a holistic understanding of the process.

### ***2.2.3 Forest Products Laboratory***

The Forest Products Laboratory (FPL) of the U.S. Department of Agriculture (USDA) began producing CNC in 2006 in relatively small batches of 20 grams (Reiner and Rudie, 2013). As the CNC demand increased, the FPL increased their batch size to 25 kg with a total weekly capacity of 50 kg by up-scaling their laboratory-scale process to pilot-scale. Pilot-scale operations began in July 2012. The value in reviewing this process is twofold: the technical findings and the opportunity to understand the up-scale trajectory.

The initial laboratory-scale process entailed hydrolyzing 20 g of wood pulp (commercial viscose-grade dissolving pulp) with 64% sulphuric acid for an hour. The hydrolysis step was followed by centrifugation to separate the residual cellulose from the acid, after which dialysis

and ion exchange was used to remove the residual acid and salt. When the demand for the CNC increased, the group scaled up their laboratory process to one kg of CNC. Due to the larger quantities, the hydrolysis reaction is quenched by dilution and the solution neutralized. The CNC is then gravity-settled to the bottom of a 900 L tank. The salt solution is then decanted from the 900 L tank, the CNC is diluted, and the remaining salt is removed using membrane filtration (Reiner and Rudie, 2013). In addition, membrane filtration replaced the dialysis step. During the membrane filtration step, the CNC is circulated through a tubular ultra-filtration (UF) system through which the dilute salt and sugar components get passed, while the CNC is retained. De-mineralized water is then used to dilute the retained CNC to achieve a 1 weight% concentration (Reiner and Rudie, 2013). Despite the energy intensity of membrane filtration, a trade-off must be realized between production capacity and separation time versus alternate technologies such as dialysis. Considering the increasing CNC demand, the trade-off seems to have been met.

The mentioned operation continued until funding was obtained for new pilot plant equipment to produce CNC at the 20 kg scale. The new pilot plant comprises five reactors that are configured to produce CNC and CNF using TEMPO treatment. This review focuses on the CNC aspect of the production process. The CNC reaction uses a 400 L De Dietrich glass-lined reactor for the hydrolysis reaction, a 6000 L reactor for the initial quenching, and a 4000 L reactor to neutralize and settle. The plant also has a 400 L glass-lined reactor to dilute the sulphuric acid and a membrane filtration system to remove the residual sodium sulfate and glucose (Reiner and Rudie, 2013).

The process is initiated by strip-cutting 50 kg machine-dried kraft rayon-grade dissolving wood pulp into 0.6 by 40 cm strips and packing them into a 400 L glass-lined reactor placed under a nitrogen atmosphere enclosed within a water jacket to maintain the temperature at 45 °C. The second 400 L glass-lined reactor is used to heat the 300 L of the 64 weight % sulphuric acid, then sprayed over the top of the dried pulp strips (Reiner and Rudie, 2013). After adding 100 L of sulphuric acid, the dried strips are degraded and rotated as a tangled mass under the spray nozzles. After adding another 100 L of sulphuric acid, the strips are turned over and mixed. The total acid addition step requires 15 minutes, and the resulting slurry is stirred for the next 90 minutes. At this stage, the pulp to acid ratio is 1:10 on a mass basis. The reaction is quenched by transferring the suspension into a 6000 L reactor containing 1200 L of water. The suspension

is further diluted to 3000 L when 2 L of 4 weight % hypochlorite solution is added to de-colour the suspension (Reiner and Rudie, 2013).

After that, the suspension is neutralized by adding 5-8 weight % sodium hydroxide. Subsequently, the suspension is split between the 6000 L and 4000 L reactors and diluted to a volume of 11000 L. Thereafter, the CNC suspension is settled, and the salt/sugar solution decanted from the two reactors. The suspension is diluted a second time to reduce the sodium sulfate concentration to approximately 1 weight %, thus enabling the CNC particles to disperse into the solution. The suspension is then transferred to the ultrafiltration system for further purification (Reiner and Rudie, 2013). The CNC suspension is circulated in a tubular ultrafiltration system (Membrane Specialists, A19 modules) in which the dilute salt/sugar solution passes through the membrane while the CNC is retained. De-ionized water is added in to maintain the CNC concentration at 1 weight % while the filtration is continued until the residual salt concentration corresponds to a conductivity of 40-50  $\mu\text{S}/\text{cm}^2$ . This process requires a total dilution time of 24 hours and 20,000 L of deionized water (Reiner and Rudie, 2013).

Following the purification step, the CNC suspension is filtered using a 20-micron polypropylene cartridge-style filter and concentrated to 5 weight % solids via the ultrafiltration system. The overall yield is 50%. A summary of the production information is outlined in Table 2.2 (Reiner and Rudie, 2013).

**Table 2.2. Summary of production CNC production parameters at FPL (Reiner and Rudie, 2013)**

Production Parameter	Value
Production capacity per batch	25 kg CNC suspension

Maximum number of batches per week	2
Maximum production capacity per week	50 kg CNC suspension
Suspension concentration	5-10 weight % CNC
CNC reaction and neutralization time	8 hours
Settling and initial purification time	24 to 48 hours
Membrane filtration time for final salt removal	24 hours
Freeze-drying capacity per week	3 kg

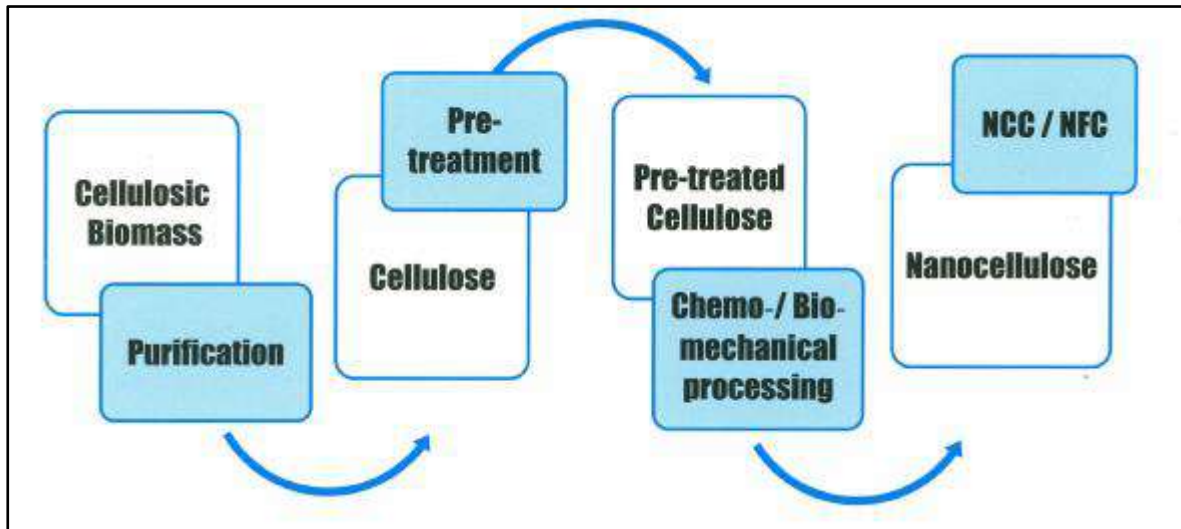
---

#### **2.2.4 ICAR-CIRCOT**

The Indian Council for Agricultural Research (ICAR) has a Central Institute for Research on Cotton Technology (CIRCOT), which primarily uses cotton, bacterial cellulose, and agricultural biomass as the primary raw materials in their nanocellulose production process. Considering the energy intensity of nanocellulose production (either CNC or CNF), ICAR uses chemical, biological and mechanical pretreatments to decrease the energy requirements (“ICAR- Central Institute for Research on Cotton Technology,” n.d.). Concerning technological advancements, the CIRCOT developed and patented three novel processes to produce nanocellulose from cotton fibers and linters. Furthermore, ICAR-CIRCOT established a novel nanocellulose pilot plant that can produce 10 kg of nanocellulose material (CNC and CNF- exact proportions not mentioned) within an eight-hour shift. The patented pretreatment processes can reduce the energy requirement in nanocellulose production by 40% (via enzyme technology) and 35% (via chemical technology) (“ICAR- Central Institute for Research on Cotton Technology,” n.d.). This pilot plant is noteworthy, as it is the first of its kind in India.

Based on the information available on the ICAR website, an established homogenization procedure was found to prepare microcrystalline cellulose through traditional hydrochloric acid hydrolysis processes. The novelty in this approach is that the material is treated with zinc chloride for two hours to initiate swelling of the material. After that, the material is rinsed in water and subjected to homogenization under pressure conditions up to 40 000 psi. The produced nanocellulose (comprised of CNC and CNF) has an average length and thickness of less than 500 and 50 nm, respectively. The zinc chloride pretreatment decreased the number of passes for complete conversion from 10 to 5. This remarkable 50% reduction in energy

requirements corresponds to a yield exceeding 95%. The process sequence can be viewed in **Figure 2.2** below (“ICAR- Central Institute for Research on Cotton Technology,” n.d.).



**Figure 2.2. Schematic of ICAR-CIRCOT CNC production process (“ICAR- Central Institute for Research on Cotton Technology”, n.d.)**

### **2.2.5 InnoTech Alberta**

InnoTech Alberta is owned by Alberta Innovates, a Canadian-funded corporation founded to improve the living quality of Albertans. InnoTech Alberta produces CNC from residual crop and wood fiber to develop new environmentally sustainable products. The novel CNC pilot plant was commissioned in 2013 with a production capacity of 100 kg per week. From the commercialization perspective, this provides a critical platform for developing novel, high-value CNC applications. In addition, InnoTech Alberta undertakes the complete characterization of the CNC being produced to understand the chemical and physical properties, which informs the development of specific applications. Some of these characterization tests include ultra-structure, morphology, chemical composition, and purity (Ngo et al., 2018). From a quality assurance perspective, this integration is valuable. There are four major phases in the InnoTech CNC manufacture cycle, with characterization tests being performed at each stage Ngo et al. (2018):

- Pre-treatment of feedstock (if required).
- Acid hydrolysis.
- Purification by iterative centrifugation and ultrafiltration.
- Drying of the final product.

The process is continuously optimized by re-processing the unreacted cellulosic material, recovering the spent acid, and extracting the sugars from acid recycle. In addition, constant tuning and trouble-shooting of the different plant areas, maintaining tight control on feedstock, reaction conditions, and the final product, development of standard characterization and standardization methods are performed to overcome technical challenges (Ngo et al., 2018).

Various wood pulps are used as the raw material: dissolving pulp, bleached softwood kraft pulp, and bleached hardwood kraft pulp. The CNC yield depends on the feedstock purity and alpha-cellulose content (Ngo et al., 2018). The feedstock is hydrolyzed in a Pfaudler 190 L glass-lined jacketed reactor. Thereafter, 110-115 kg of 63.5-64 weight% sulphuric acid is pumped into the reactor from the acid storage tank. Upon entry, the acid is stirred at 200 rpm and heated to 45 °C by the reactor jacket using low-pressure steam (Ngo et al., 2018). After that, 10 to 13.5 kg feedstock is added and reacted for two hours at a mixing rate of 200 rpm. Proceeding the reaction time, the reaction contents are quenching by pumping 50 kg of water into the reactor at a pulp-to-quench-water ratio of 1:12. The hydrolysate mixture is then transferred from the reactor into a 7500 L storage tank containing 1200 kg of demineralized water to complete the quenching. Immediately after, the reaction contents are neutralized by adding sodium hydroxide (Ngo et al., 2018). The exact quantity of sodium hydroxide was not specified. However, the sodium hydroxide is likely added until neutralization. The CNC purification process is initiated by centrifugation to separate the CNC from the waste stream. A GEA Westfalia SC-35 disk stack centrifuge with a bowl speed of 6500 rpm is used.

The liquid-solid separation is performed at a rate of 90 L/min (Ngo et al., 2018). The centrifugation enables the CNC to be collected as a paste-like cake while the centrate is discarded into sewage. The CNC cake is then pumped to a storage tank and diluted with 1500 L of water. The cake discharge frequency and the hood water spray frequency and duration were optimized to prevent plugging of the transfer pump and lines. Upon contact with 1500 L of water, the CNC cake disperses to form a uniform CNC suspension. This suspension is then pumped back to the centrifuge and processed to remove any traces of large particles, dirt, and unreacted materials that affect the quality of the CNC (Ngo et al., 2018).

This process differs from others, such as the FPL, which does not require the use of the centrifuge and makes use of gravity settling to separate the initial CNC. After centrifugation,



the CNC suspends in the liquid stream, containing large amounts of sodium sulfate salts, glucose, and oligomers. To remove these impurities from the CNC and concentrate the product to 3 weight % consistency, ultrafiltration is used. GEA-Niro produces the UF system with installed membranes produced by PALL Corporation. The membrane size was specified as 800 microns. The UF system is configured with 11-13 modules arranged in parallel, designed to process 1500 L of material over an eight-hour cycle. The CNC suspension is circulated through the parallel series of hollow fiber tube modules allowing the dilute, low-molecular-weight salt or sugar contaminants to pass through the membrane while the CNC particles are trapped within the tubes. The CNC concentration is maintained at 0.5 weight% by adding demineralized water. The primary filtration stage is ended once the suspension conductivity drops below 300  $\mu\text{S}/\text{cm}$  (Ngo et al., 2018).

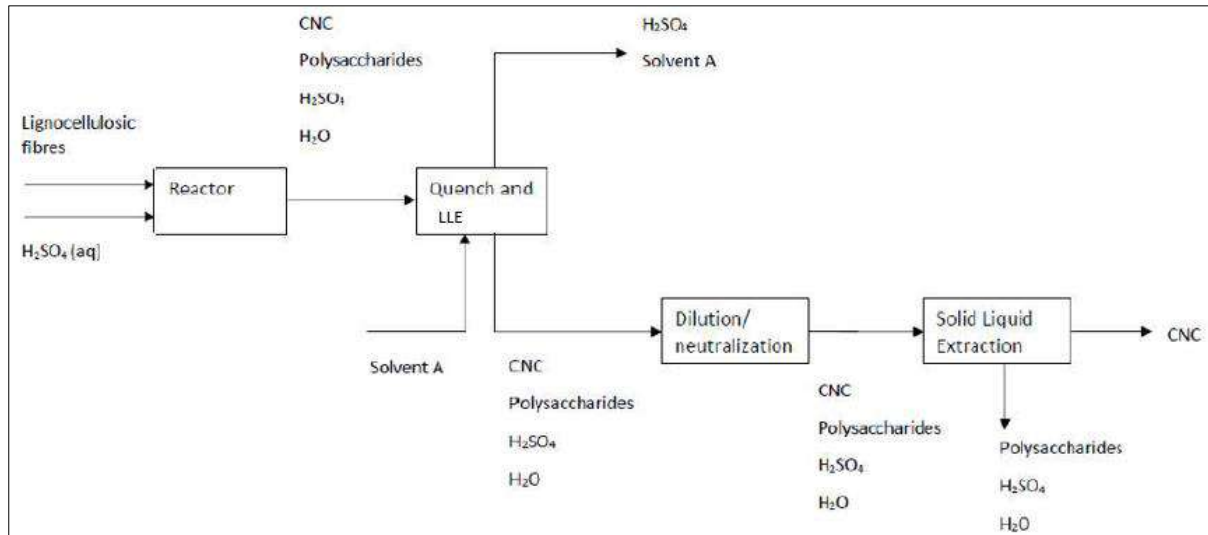
When concentrating the CNC suspension, the UF membranes foul quickly due to the high viscosity of the CNC suspensions. Hence, InnoTech Alberta developed an effective cleaning protocol that allows 80% recovery of the membrane efficiency within two days (Ngo et al., 2018). Additional washing with demineralized water facilitates membrane recovery. Active membrane regeneration ensures effective membrane functioning. The purified CNC suspension is then centrifuged to remove dirt, large particles, and unreacted materials. The colloidal CNC suspension is then filtered using a 20-micron cartridge-style filter to remove dirt and small unreacted cellulosic materials. The clean CNC suspension is then transferred to the UF system for the secondary stage purification. The purified CNC suspension is concentrated to 3 weight% and subsequently pumped to a 300 L transfer vessel (Ngo et al., 2018).

## **2.3 Part 2: Review of Pilot Plant Patents**

### ***2.3.1 Domtar Corporation (Patent number: US P,297,111 B1)***

Domtar Corporation is the largest integrated producer of uncoated free-sheet paper in North America and the second largest in the world, based on production capacity. The company has head offices in Montreal and Fort Mill, South Carolina. The Montreal division developed a novel procedure to manufacture CNC using a water-insoluble solvent to quench the acid hydrolysis reaction and recover the unreacted sulphuric acid, thereby separating it from the stream containing the CNC. The lignocellulosic pulp fibers are hydrolyzed with sulphuric acid. Thereafter, the sulphuric acid-specific water-insoluble solvent is added to terminate the

reaction and enable the separation of the first stream (comprised of 70% unreacted sulphuric acid in the water-insoluble solvent) from the second stream (comprised of CNC and the remaining unreacted sulphuric acid). The procedure can be altered by adjusting the pH of the second stream to above 1 to aid in the separation and recovery of the CNC from the second stream (Marcoccia et al., 2016). These procedures are shown in **Figure 2.3** below.



**Figure 2.3. Domtar Corporation CNC production schematic (Marcoccia et al., 2016)**

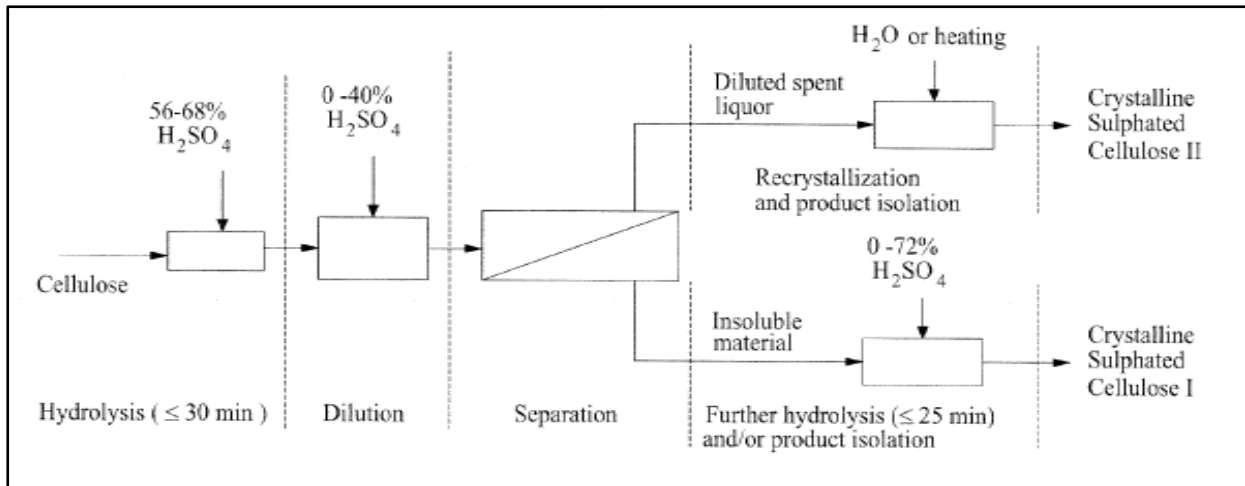
The sulphuric acid is separated from the CNC by liquid-liquid extraction (LLE) techniques, which separate the sulphuric acid trapped within the CNC suspension using the water-insoluble solvent. The second stream is diluted in water or neutralized before solid-liquid separation (Marcoccia et al., 2016). In some embodiments, almost all the unreacted sulphuric acid in the first stream can be recovered using a second water-insoluble solvent. This results in a third stream (comprising all the unreacted sulphuric acid and the second water-insoluble solvent) and a fourth stream (comprised of the first water-insoluble solvent). The unreacted sulphuric acid is then separated from the second water-insoluble solvent using traditional techniques, such as distillation. In some embodiments, the first water-insoluble solvent is different from the second to facilitate separation and collection of the third and fourth streams using LLE (Marcoccia et al., 2016). In some embodiments, pH adjustment of the second stream is performed by water dilution, whereas in others, it is performed by adding some primary material (Marcoccia et al., 2016).

Bleached pulp is used as the feedstock. The concentration of the sulphuric acid used for the hydrolysis reaction varies between 40 to 60%. Instead of terminating the hydrolysis reaction

solely by dilution, the water-insoluble solvent migrates the sulphuric acid from the aqueous phase (containing the CNC and dissolved polysaccharides). Increasing the pH of the streams is desirable, as it reduces downstream equipment capital costs as the stream is less corrosive. Therefore, glass-lined equipment would not be required, eliminating the expense of handling and transporting acidic materials (Marcoccia et al., 2016). The stream containing the polysaccharides and water separated from the CNC is sent to a waste treatment facility to digest the polysaccharides (Marcoccia et al., 2016). The water-insoluble solvents were not specified.

### **2.3.2 FPIInnovations (Patent number: US 2010/0286387 A1)**

The patent registered by FPIInnovations outlined a method for producing crystalline sulfated cellulose II (mercerized) materials with a relatively low degree of polymerization from spent sulphuric acid previously used in the cellulose hydrolysis. According to Hashaikeh et al. (2010), the crystalline sulfated cellulose I materials includes cellulose whiskers, microcrystallites and nanocrystals, crystalline nanocellulose, and stable colloidal cellulose suspension. The crystalline sulfated cellulose II materials are typically soluble in concentrated sulphuric acid solutions. Furthermore, the aqueous diluent includes (but is not limited to) 0 to 40% sulphuric acid. The method entails separating the spent acid from the cellulose I materials (cellulose typically derived from wood pulps) by dilution from 64% to 10-50% by adding up to 40% sulphuric acid. This step is followed by settling and decanting (or centrifuging), after which the diluted spent liquors are added to water or heated at 30-80 °C for a time frame not exceeding 48 hours. After that, the re-crystallized sulfated cellulose II materials are recovered by filtration and washing or by washing and freeze-drying. The method can be used to produce both crystalline sulfated cellulose I and II materials (Hashaikeh et al., 2010). A process schematic is shown in **Figure 2.4** below.



**Figure 2.4. CNC production schematic at FPInnovations (Hashaikeh et al, 2010)**

Sulphuric acid hydrolysis of cellulose to form cellulose whiskers, microcrystallites or nanocrystals is generally performed by mixing the cellulose with concentrated sulphuric acid (approximately 64%) at temperatures between 45-65 °C. The hydrolysis reaction is performed for a minimum duration of 20 minutes at 45 °C and 15 minutes at 65 °C (Hashaikeh et al., 2010). The spent liquor contains residual sulphuric acid and soluble cellulose degradation products. The acid-insoluble, sulfated cellulose (with a typical yield of less than 50%) is separated from the spent liquors by settling and decanting or centrifuging and repeated filtration and washing (Hashaikeh et al., 2010).

Per the patent, the sulfated cellulose II materials are recovered by diluting the spent liquors from concentrated (56-68%) sulphuric acid hydrolysis with an aqueous diluent (preferably 0-40% sulphuric acid solution), separating the diluted spent liquors from the acid-insoluble sulfated cellulose and adding the diluted spent liquors to water. These steps enable the recrystallization and isolation of the sulfated cellulose II material. It is further outlined that the volume of the mentioned diluent is typically 0.2 to 5 times the volume of the spent liquor. In contrast, the volume of water to which the diluent is added is typically 0.5 to 3 times the volume of the diluted spent liquor (Hashaikeh et al., 2010). In addition, the separated acid-insoluble sulfated cellulose materials can be further hydrolyzed without further sulphuric acid to increase the acid concentration to 64-68% to provide highly crystalline, sulfated cellulose I materials (Hashaikeh et al., 2010).

### **2.3.3 Hebrew University of Jerusalem (International Publication Number: WO 2012/U14213 A1)**

This invention by Shoseyov et al. (2012) holds significance, as it can produce CNC from solid waste by-products from Pulp and Paper mills, as opposed to their disposal in landfill sites. Papermill waste is typically discarded due to the high impurity content. The CNC production process is cost and energy effective. However, no costing or techno-economic study was available at the time of review. The invention outlines a process to recover cellulose from sludge. This recovered cellulose is then used for CNC production (Shoseyov et al., 2012). The sludge contains impurities, the type, and concentration of which depends on the source of the sludge. Sludge could contain anything between 5 and 60% cellulose (Shoseyov et al., 2012). Shoseyov et al. (2012) conceded that the recovery process yields a cellulose purity of 90%, sufficient to allow further manipulation of the cellulose material. It is worth noting that from a lean manufacturing perspective, this concept eliminates one of the significant wastes commonly encountered in production processes: overproduction- or the unnecessary over-processing of a product to a higher purity specification that is not required by the end-user or next phase of the process.

Typically, the paper sludge contains high levels (40 to 60%) of dry solids comprised of wood bark, plastics, and metals. Mechanical separation techniques remove these solid contaminants. The process occurs as follows: the sludge is homogenized and exposed to relatively weak acidic treatment under agitation. The acidic treatment is not strong enough to degrade the amorphous regions of the cellulose polymer and may be repeated at least twice. Centrifugation then separates the liquid phase containing the soluble non-cellulosic material from the solid phase containing the cellulose. The separated soluble material is then washed to obtain pure cellulose-containing less than 5 to 10% impurities by mass (Shoseyov et al., 2012). In other embodiments of the patent, the liquid phase is removed after acidic treatment, and a new volume of acid is introduced several times to wash the solid phase containing the cellulose. The cellulose material separated from the acidic liquid phase may be collected, dried and re-suspended before use, or it may be collected and used as an aqueous suspension. After that, the process uses pure cellulose to produce CNC (Shoseyov et al., 2012).

In the CNC production phase, the acid used to degrade the amorphous regions of the pure cellulose is different from the acid used to dissolve the impurities. Alternatively, the same acid can be used at a greater concentration. The acid treatment must allow preferential degradation

of the amorphous regions (hydrolysis) by using an aqueous acid solution at a concentration range between 20 and 60%. The higher acid concentration also dissolves additional impurities in the liquid medium, thus separating the highly pure CNC fibers. According to Shoseyov et al. (2012), sulphuric acid exhibits the optimal degradation required in the process. The time frame for the hydrolysis is adequate to destroy the amorphous domains. In some embodiments, the acid may be recycled. Acid recycle is advantageous as it recovers valuable components found in paper waste. In some embodiments, the mineral acid is recycled. The procedure entails the extraction of the mineral acid by organic acid, converted to mineral acid, and reused in the acidification chamber. As such, the mineral acid may be extracted and recovered by backwashing the extract phase with water concentrations similar to those in the original solutions (Shoseyov et al., 2012).

Once the amorphous cellulose regions have been degraded, the CNC is washed for several cycles in water. The remaining cellulose is separated, dialyzed against water, and mechanically dispersed to produce CNC. The hydrolyzed sugars can be fermented to produce bioethanol. In addition, sulphuric acid causes the formation of gypsum, which can be recovered and used for construction or as a fertilizer and soil conditioner (Shoseyov et al., 2012). This beneficiation is remarkable as alternate by-products provide an opportunity for more significant economic benefit.

#### **2.3.4 RISE Innventia AB (Patent number: US 8,911,591 B2)**

The raw material in the reactor is heated until a suitable pressure is built up. In one embodiment, 1 to 4% of the raw material in water suspension is heated to 180 °C in a closed reactor. The fibers are accelerated through an outlet at reduced pressure causing the raw material to disintegrate. The lower pressure may be ambient or lower, such that a sufficient pressure difference is achieved. The pressure can be lowered in several steps, corresponding to several accelerations. The nano pulp exiting the reactor outlet is collected in a cyclone (Lindstrom et al., 2014). In a third embodiment, there is steam flow. The rapid steam production optimizes the disintegration of the raw material. The steam flow containing the disintegrated raw material passes through a contracting nozzle, the outlet of which causes a sudden expansion. This method varies the nanocellulose homogeneity by adjusting the flow speed, elevated pressure in the reactor, and pressure reduction speed and geometry. The nanocellulose may comprise fibrils and other particles within the size range of 10 to 250 nm (Lindstrom et al., 2014). In the

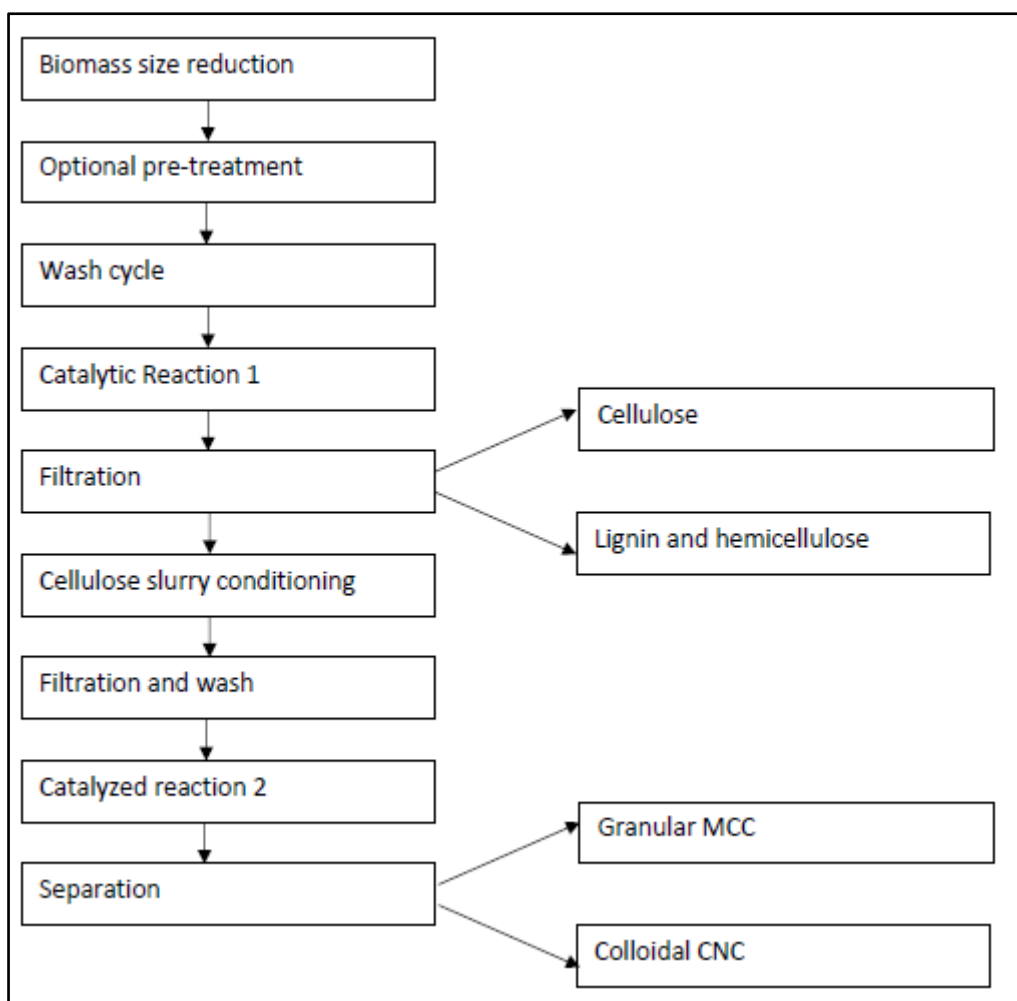
fourth embodiment, the pulp fibers are pre-treated by milling, enzymatic degradation, the introduction of charges, carboxymethylation, acidic hydrolysis, alkaline hydrolysis, or a combination of any of these methods. These procedures weaken the fibers, increasing the nano pulp yield. In the fifth embodiment, the gas or liquid flow steam conforms to flow speed within the range of 50 to 1000 m/s. The reactor pressure is held within the range of 2 to 13 bar (Lindstrom et al., 2014).

### **2.3.6 Nano Green Biorefineries Inc. (International Publication Number: WO 2013/000074 A1)**

Nano Green Biorefineries Inc. is a private technology development company in the United States. The company is developing technology to produce CNC from a wide variety of biomass sources. The development of Nano-Green's intellectual property is done by its subsidiary, Blue Goose Biorefineries Inc. In addition, the company has licensed the use of CNC for strengthening concrete from the Purdue Research Foundation.

The technology patented by Olkowskl and Laarveld (2013) allows a relatively efficient biorefining method of biomass, resulting in cellulose, lignin, hemicellulose, and their respective degradation products. This production is achieved by a catalytic reaction to degrade complex lignocellulosic structures into their constituents by reactive oxygen species generated from hydrogen peroxide using a transition metal catalyst within an acidic medium. In addition, fractionation and de-polymerization techniques are used to yield the end products (cellulose, hemicellulose, and lignin) along with their corresponding degradation products. The invention is reported to exhibit a high yield (Olkowskl and Laarveld, 2013).

The catalytic process is regulated to achieve varying biomass degradation rates to produce platform chemicals. The lignin and cellulose fractions are then treated separately using different catalytic reactions (Olkowskl and Laarveld, 2013). One embodiment allows the treatment of recalcitrant lignin by hydrolysis pretreatment. Another embodiment allows the generation of MCC and CNC in colloidal form through a second catalytic reaction. Notably, the proportions of MCC and CNC and their size and colloidal properties can be controlled by the duration and strength of the catalytic reaction and post-catalytic treatment. A process schematic is shown in **Figure 2.5** below.



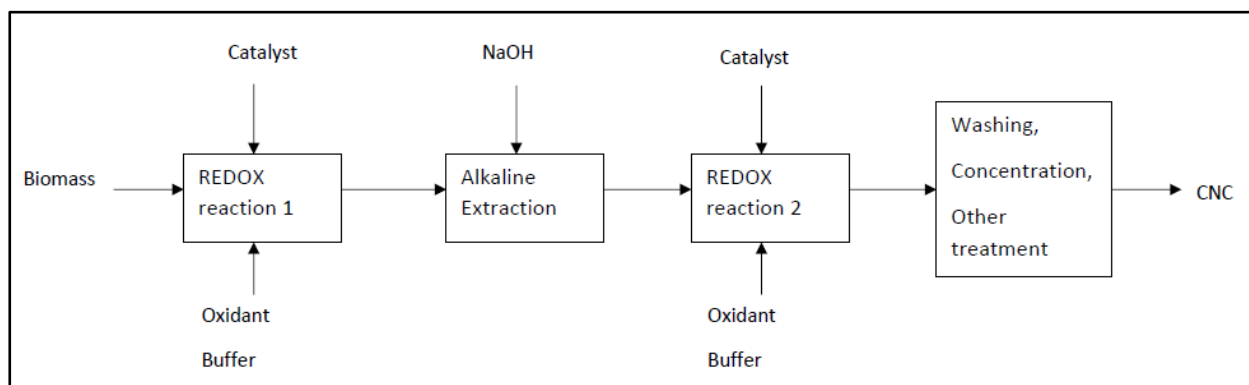
**Figure 2.5. Catalytic biomass conversion at Nano Green Biorefineries Inc. (McAlpine and Koneshny, 2017)**

Nano Green also patented the technology to produce crystalline cellulose (patent number: WO 127938 A1). The production process entails reacting the cellulosic raw material in an aqueous slurry comprising a transition metal catalyst and hypochlorite solution (having an initial pH greater than 6 and final pH less than 9) and subsequently recovering the crystalline cellulose fraction (McAlpine and Koneshny, 2017). The initial pH of the slurry is greater than 7 (preferably between 9 and 12) and has an oxidation-reduction potential exceeding 500 mV. As the hypochlorite is consumed, the pH is gradually reduced to less than 9 (preferably less than 7). A buffer is used to control the pH during or upon reaction completion (McAlpine and Koneshny, 2017).

In some cases, the oxidation reaction proceeds to completion due to a significant decrease in the Oxidation Reduction Potential (ORP). The oxidation reaction is repeated to produce the



crystalline cellulose. The CNC is preferably washed in an alkaline solution before the oxidation step. In another aspect, CNC is produced by reacting the cellulosic material in an aqueous transition metal catalyst and hypochlorite solution slurry and washing the cellulosic material in an alkaline solution. The reaction is then repeated before recovering the CNC fraction (McAlpine and Koneshny, 2017). A schematic of the process is shown in **Figure 2.6**.



**Figure 2.6. CNC production schematic at Nano Green Biorefineries Inc. (McAlpine and Koneshny, 2017)**

Interestingly, the standards for deciphering between good and poor-quality CNC based on several parameters are presented in this patent. No such standards were previously reported in other inventions at the time of review. The assessment criteria are presented in Table 2.3 (McAlpine and Koneshny, 2017).

**Table 2.3. Assessment criteria for CNC production at Nano Green Biorefineries Inc. (McAlpine and Koneshny, 2017)**

Measurement	Good Quality	Poor Quality
Cake on filter paper	Rubbery or greasy texture	Soft or fibrous texture
Microscope image 10 X	Small visible particles with no particles after sonication	Visible fibers several microns in length
Visible appearance of gel or suspension	Relatively clear with evidence of Rayleigh scattering. Sample becomes clear with ultrasound	Opaque gel, white or off-white and remains opaque after ultrasound treatment
Size by Dynamic Light Scattering (DLS)	One size peak at around 100 nm	Two size peaks. One at 800 nm to 1500 nm
Zeta potential	Below -30 mV	Higher than -30 mV in association with settling particles

No evidence was reported to suggest that the process has been conducted on a pilot plant scale. However, it is still significant to explore the CNC production process and recovery. In addition, the CNC quality criteria can be applied to other processes to ensure that the CNC production is taking place optimally.

#### **2.4. Summary and Conclusions**

A summary of the process technologies is shown in Table 2.4 below.

**Table 2.4. Summary of CNC production technologies**

Process	Process Steps			
	Feedstock Pretreatment	Chemical Treatment	Separation	Purification
<b>Part A: Commercial Processes</b>				
American Process Inc.	Fractionation with sulphuric acid, ethanol, and water	Bleaching	Unspecified mechanical separation	Not specified
Blue Goose	Catalytic oxidation (stage 1)	Catalytic oxidation (stage 2)	Not specified	Washing and dewatering
Forestry Products Laboratory	None (raw material is pulp, rather than biomass)	Acid hydrolysis	Gravity settling	Sodium hydroxide neutralization and ultrafiltration
ICAR-CIRCOT	Zinc chloride treatment, rinse, and high-pressure homogenization	Acid hydrolysis	Not specified	Not specified
Innotech Alberta	Not mentioned	Acid hydrolysis	Centrifugation	Ultrafiltration
<b>Part B: Patented Processes</b>				
Domtar Corporation (Patent number: US P,297,111 B1)	Not mentioned	Acid hydrolysis	Liquid-liquid extraction using a water-insoluble solvent	Dilution and neutralization

FPIInnovations (Patent number: US 2010/0286387 A1)	Not mentioned	Acid hydrolysis	Gravity settling and decanting or centrifugation	Further acid hydrolysis
Hebrew University of Jerusalem WO 2012/U14213 A1	Homogenization of sludge	Successive acid hydrolysis	Centrifugation	Washing
RISE Innventia AB (Patent number: US 8,911,591 B2)	Acceleration and disintegration of biomass	Not needed (pulp is the end product)	Not needed (pulp is the end product)	Not needed (pulp is the end product)
Nano Green Biorefineries Inc. (International Publication Number: WO 2017/127938 A1)	Mechanical size-reduction	Catalytic oxidation	Filtration	Washing and concentration

---

Based on the findings presented in Table 2.4, the pretreatments were vast because no single pretreatment was commonly found. This finding is attributed to the fact that specific pretreatments are required for specific biomass feedstocks. The two most common chemical treatments were identified as acid hydrolysis and catalytic oxidation. Both treatments have their own set of advantages and disadvantages, as shown in Table 2.5.

**Table 2.5. Comparisons between the typical treatments**

<b>Chemical treatment</b>	<b>Advantages</b>	<b>Disadvantages</b>
Acid hydrolysis	The acid can be recycled to improve the efficiency and viability of the process.	<ul style="list-style-type: none"> <li>• Acid is regarded as a toxic reagent.</li> <li>• Acid hydrolysis is a lengthy and corrosive procedure.</li> </ul>
Catalytic oxidation	<ul style="list-style-type: none"> <li>• Less toxic process conditions are relative to acid hydrolysis.</li> <li>• The process units are not designed for corrosion resistance (cheaper to implement).</li> </ul>	<ul style="list-style-type: none"> <li>• Catalysts are expensive and prone to fouling.</li> </ul>

The two most common separation methods were identified as gravity settling and decanting and centrifugation. From an economic perspective, gravity settling is preferred. Several purification methods were identified: washing and dewatering, sodium hydroxide neutralization, and ultrafiltration. As with the pretreatments, the product purification depends on the required degree of purity and final product specifications dictated by the end-user applications. Less common technologies across all the major production phases were identified in the patented processes. The less common technologies are notable as they allow the exploration of alternate technologies, thus enabling the development and commercialization of more efficient methods.

Much interest has been placed on the technological advancements in the field of CNC production in recent times. Although some processes can be deemed more straightforward and

economical than others, more effective processes can only be realized by active research and development efforts. This point is clearly illustrated by the varying innovations and methods presented by the reviewed patents. Although patented technology might not have been demonstrated on a pilot-plant or commercial scale at the time of review, optimization is required for commercialization.

The overall findings of this Chapter revealed that the demand for CNC is steadily increasing, thereby giving rise to the development of pilot-scale manufacturing facilities by leading Research Groups and Forestry Departments globally. The American Process Inc. (API) (USA) and CelluForce Inc. (Canada) are considered to be the leading CNC-producing companies in the world (holding respective production capacities of 1 and 0.5 tons per day) (Miller, 2016). Regarding the CNC production process, most companies scale up the biomass acid hydrolysis step traditionally used on a laboratory scale. However, the differences in process steps are conspicuous in the subsequent process phases. Some companies perform iterative centrifugation and homogenization steps of the CNC slurry, whereas others opt for simple dilution using stirred tanks. Some companies engage the use of catalysts, whereas others do not. Hence, the current production technologies are diverse, each with inherent advantages and pitfalls. These findings were used to guide the up-scaled process designs in the subsequent design Chapters (6 to 8).

The production technologies reviewed in this Chapter are diverse. However, each company or patent holder had specific design justifications when selecting and implementing these. A “one size fits all” approach cannot be used when designing a CNC production process. Instead, specific biomass sources and conditions must be considered to select the best configuration. Trial tests on a laboratory scale also provide invaluable insights in this regard.

Although acid hydrolysis is commonly used among various companies and patent holders to remove the amorphous regions of the lignocellulosic raw materials, it was not the only method. Furthermore, the CNC separation (from the hydrolysate) and homogenization stages varied distinctly, offering valuable insights into the currently available technologies. Considering that this Chapter reports an active comparison between the various pilot plants and patents at the time of review, it keeps the reader abreast with the latest developments in CNC production on a global basis.

Before increasing production capacities, many of the reviewed companies had to undergo a swift and well-planned transition from the laboratory scale. This Chapter explored the current technologies employed and considered the critical phases for such a transition. The relatively large number of CNC production patents that have been recently released conceded the growing interest in this novel material.

## CHAPTER 3: OPTIMIZATION OF LABORATORY-SCALE CNC PRODUCTION

### 3.1 Introduction

The optimization study entailed undertaking several production cycles of CNC in the CSIR Biorefinery Industry Development Facility's Analytical laboratory using the in-house ammonium persulfate and acid hydrolysis (APS + AH) process. The production process was split into three main phases for simplicity and the ability to produce CNC within the allocated 8-hour working day:

- Phase 1: Delignification of the sawdust using the APS reagent.
- Phase 2: Acid hydrolysis of the de-lignified sawdust "pulp."
- Phase 3: Neutralization, homogenization, and purification of the resulting CNC via successive centrifugation, ultrasonication, and dialysis.

To acquire the practical information required to design up-scaled CNC production processes from this optimization study, the aims of this Chapter were as follows:

- a) To understand the challenges and shortcomings of the existing laboratory-scale production process of CNC at the BIDE, optimization methods can be proposed regarding efficiency, raw material (reagent) consumption, and health and safety risks.
- b) To understand the steps in the production cycle, the equipment involved, and the existing control mechanisms and identify alternate equipment/technologies to perform similarly (or improved) functions.
- c) To understand the laboratory-scale production cycle from an environmental perspective: identifying the harmful reagents and proposing effective containment, recycle (if possible), and disposal methods.



## 3.2 Results and Discussion

### 3.2.1 Proposed Optimization Strategies

#### 3.2.1.1 Sawdust Delignification

In the delignification step, the preparation of the APS solution presents the following safety, health, environmental, and quality concerns:

- The step involving the preparation of the APS solution requires the boiling of de-ionized water to aid in the dissolution of the APS. The oxidation rates of the APS are greatly enhanced when heated, giving rise to highly reactive species such as sulfate and hydroxyl radicals. These radicals cause a series of chain reactions in which organic materials are reduced. The boiling water may constitute a burn hazard and requires careful handling.
- When the boiling water is added to the solid APS, a rapid effervescence of the solution occurs. When enclosed, the mixture exhibits an explosive hazard due to the pressure build-up. Hence, it is realized that when up-scaling, this step must be performed in a vessel equipped with pressure-release functionality.
- Once the APS solution is cooled, the precipitation of solid APS takes place. Hence, careful thermal control is required.
- Once the de-lignification reaction in the round bottom flask is ready to begin, the sudden motion of the stirrer causes some of the sawdust particles to adhere to the vessel walls. These sawdust particles remain unreacted as the reaction progresses, thereby acting as contaminants in the final product.

Currently, the following controls are in place to mitigate the factors mentioned above:

- Thermal gloves are worn when forming the APS solution.
- The de-lignification vessel is left open to ambient conditions to prevent any pressure build-up.
- The APS solution is prepared over an electric heater under a fume hood to allow manual temperature control and dissolve the APS into the deionized water. Once effervescence is observed, the solution is removed from the heat. Once precipitation is observed, the

solution is placed back into the heat. This iterative strategy continues until the APS solution is formed and transferred into the round bottom flask containing the sawdust.

To prevent the adherence of sawdust remnants on the vessel walls, a variety of methods can be used individually or collectively:

- Roughly 60% of the APS solution is decanted into the sawdust, while the remaining 40% is reserved to wash down any specs of sawdust remaining on the walls of the round bottom flask after stirring has been initiated. This action is performed using a Pasteur pipette.
- Once the stirring has proceeded, there is often a distinct formation of a sawdust “rim” on the side of the vessel wall. To remove this, the stirrer is periodically stopped, and the reaction solution is used to rinse the sides of the vessel.
- The stirrer is placed at the lowest possible speed (RPM) before initiating the stirring action to minimize the number of sawdust particles that adhere to the vessel walls (thereby being excluded from the de-lignification reaction).

In light of the above, the following optimization methods are proposed:

- Instead of making up the APS solution and then adding it to the sawdust, a more effective technique would be to add the appropriate quantity of the APS powder into the sawdust mass before adding the required amount of deionized water just before stirring the resulting slurry. This action eliminates the challenge of effervescence and precipitation, as well as the inherent burn hazards.
- In addition, it is recommended to use a non-stick reagent to eliminate the problem of sawdust particles adhering to the walls of the de-lignification vessel. Alternatively, the round bottom flask currently used can be replaced with a vessel that has been micro-polished on the internal, or coatings such as silicone, polytetrafluoroethylene (PTFE) can be used to reduce the surface roughness significantly.

#### 3.2.1.2 Neutralization, Homogenization, and Purification of CNC Product

- Successive centrifugation-ultrasonication cycles are performed to neutralize and homogenize the CNC product. This process is energy, water, and time intense.

- The gaskets of the ultrasonicator were found to wear out due to heating of the equipment regularly. This finding could be attributed to the inadequate capacity of the equipment to handle the prolonged ultrasonication cycles that were imposed.
- It was realized that the ultrasonication cycle did not deliver a uniform suspension viscosity/consistency. The number of cycles after which the suspension uniformity and thickness are improved was inconsistent with each run. In some instances, the suspension thickness was suddenly lost and could not be regained by performing further ultrasonication cycles.

Currently, the following controls are in place to mitigate the factors mentioned above:

- Spare gaskets are kept at hand to allow efficient replacement when the older gaskets wear out. All students and technicians were trained on the replacement technique for the gasket.
- Discretion is used when performing the ultrasonication cycles by monitoring the viscosity of the CNC suspension. As soon as a suitably uniform suspension was detected, the ultrasonication was stopped.

Instead of performing the current neutralization and ultrasonication techniques, the following methods are proposed:

- The dosing of a caustic reagent can neutralize the acidic CNC slurry after the hydrolysis phase. Liquid dregs could be considered a potential reagent in this regard as it offers a green alternative to traditionally used chemicals. However, there is a need to consider the effect of contaminants on the CNC product present in the liquid dregs. This action depends on the required purity of the CNC as dictated by its envisioned application.
- Instead of ultrasonication, vigorous agitation could achieve homogenization of the CNC suspension.
- In the case of the CNC suspension, adequate mixing can only occur when the fluid is in motion, which can only be achieved using large impellers that sweep through the entire volume of the vessel. It is proposed to use a helical ribbon impeller within a stirred tank reactor to achieve homogenization of the CNC suspension. This impeller blade travels close to the tank wall to drive overall circulation to generate turbulence in

viscous materials. Hence, it is ideally suited to the homogenization of the CNC suspension.

A baseline risk assessment was undertaken based on the health and safety risks identified in the laboratory-scale process (Table 3.1). The baseline risk assessment accounts for the safety considerations in each of the CNC process phases: making up of the APS solution, delignification of the sawdust, making up of the sulphuric acid solution, acid hydrolysis of the sawdust pulp, ultrasonication, and dialysis of the CNC product.

**Table 3.1. Baseline Risk Assessment for laboratory-scale CNC production**

<b>Task</b>	<b>What are the hazards?</b>	<b>What are you already doing?</b>	<b>Do you need to do anything else to control this risk?</b>	<b>Action by who?</b>
Making up of APS solution	<p>Inhalation/ingestion of APS powder (safety and health hazard).</p> <p>Burn with boiling water for making up the solution (safety and health hazard).</p> <p>Burn with heating mantle when heating the solution</p>	<p>Powder mass is measured inside a weighing device-minimizes inhalation.</p> <p>Thermal gloves are worn.</p> <p>Thermal gloves are worn.</p> <p>First aid kit is available in the</p>	No	-

	<p>(safety and health hazard).</p> <p>Slip of glass vessel resulting in cuts (safety and health hazard).</p> <p>Contact with skin and eyes (safety and health hazard).</p>	<p>laboratory for cuts.</p> <p>Goggles and chemical-resistant laboratory coats, and safety boots are worn.</p>		
Delignification of the sawdust	<p>Pressure build-up inside the reaction vessel (safety and health hazard).</p> <p>Splash into eyes (safety and health hazard).</p> <p>Fume inhalation (safety and health hazard).</p>	<p>The reaction vessel is left open to the atmosphere.</p> <p>Goggles are worn.</p> <p>The delignification occurs inside a fume-hood.</p>	No	-
Making up of sulphuric acid solution	<p>Glass slips- resulting in cuts (safety and health hazard).</p> <p>Acid spill (safety, health and</p>	<p>First aid kit is available in the laboratory for cuts.</p> <p>Acid spill kit is available in the laboratory.</p>	Safety respirators are required.	-

	<p>environmental hazard).</p> <p>Acid inhalation (safety and health hazard).</p> <p>Contact with eyes and skin (safety and health hazard).</p>	<p>Safety goggles, chemical-resistant laboratory coats, and safety boots are worn.</p>	<p>2% caustic solution can be kept in a spray bottle to neutralize the acid on the skin.</p>	
<p>Acid hydrolysis of the sawdust “pulp.”</p>	<p>Acid spills/leaks (safety, health and environmental hazard).</p> <p>Contact with eyes and skin (safety and health hazard).</p> <p>Glass slips- resulting in cuts (safety and health hazard).</p>	<p>Acid spill kit is available in the laboratory. Safety goggles, chemical-resistant laboratory coats, and safety boots are worn. An eyewash station is available. First aid kit is available in the laboratory for cuts.</p>	<p>No</p>	<p>-</p>
<p>Ultrasonication</p>	<p>The loud sound caused by the ultrasonication device (health hazard).</p>	<p>The unit is contained in a sound abatement chamber.</p>	<p>Earmuffs are to be worn.</p>	<p>SHEQ Committee.</p>

Dialysis	Glass slips/breakages resulting in cuts (safety and health hazard).	First aid kit is available in the laboratory for cuts.	No	-
----------	---	--	----	---

### 3.2.2 Identification of Alternate Technologies

Table 3.2 below indicates the existing process technology used in the laboratory-scale process and the related technologies used in up-scaled production processes.

**Table 3.2. Identification of alternate technologies for up-scaled CNC production**

Process Phase	Existing Technology	Alternate Technology for up-scaled production.
Preparation of APS solution	Manual make-up by APS dissolution in hot water	The APS solution is made up in the de-lignification reactor before adding the sawdust to the reactor.
Sawdust de-lignification	The reaction occurs for six hours in a stirred round bottom flask in a water bath at 60°C	A jacketed glass-lined stirred tank reactor is proposed.
Separation of sawdust pulp from the spent APS solution	Vacuum filtration	To be confirmed in the design phase (Chapters 4 to 6).
Making-up of sulphuric acid solution	Manual make-up	The acid solution is made up in the hydrolysis reactor before adding the sawdust to the reactor.
Acid hydrolysis of sawdust pulp	The reaction occurs for two hours in a stirred round bottom flask in a water bath at 50°C	A jacketed glass-lined stirred tank reactor is proposed.

Quench of the hydrolysis reaction	The reaction contents are decanted into deionized water	The reactor contents are dumped into a quench vessel. Alternatively, the reactor contents are pumped into the quench vessel containing process water.
Separation of raw CNC from the spent acid solution	Centrifugation	To be confirmed in the design phase (Chapters 4 to 6).
Homogenization and neutralization of CNC	Ultrasonication and successive dilution	Vortex cavitation and sodium hydroxide neutralization.
Purification of CNC (removal of salts)	Dialysis	Ultrafiltration.

### 3.2.3 Identification of Process Reagents and Disposal Methods

The reagents used in the CNC production are shown below (Table 3.3), along with the proposed disposal methods.

**Table 3.3. Process reagents and disposal methods**

Process Phase	Reagent	Disposal Method
Sawdust de-lignification	APS	Alternate uses of spent APS can be investigated (beneficiation).
Acid hydrolysis of sawdust pulp	Sulphuric acid	The spent sulphuric acid can be recycled using adsorption with activated carbon.
Homogenization and neutralization of CNC	Sodium hydroxide proposed for neutralization in up-scaled production	The sodium hydroxide becomes neutralized and therefore does not pose any environmental hazard in the CNC product.



### **3.3 Conclusions**

Considering that the laboratory-scale production process was studied, the process challenges were identified, and optimization strategies were proposed, the first aim was met. As in all production processes, environmental health and safety considerations are pertinent. This matter was clearly outlined in Chapter 1 under the environmental health and safety issues for nanomaterials, indicating that the absence of health and safety considerations could nullify a production process, regardless of its efficiency. As such, the Baseline Risk Assessment can be used as a guideline for the proposed process design phases (Chapters 4 to 6).

Based on the laboratory-scale CNC production process, alternate technologies were identified to apply in larger production systems (pilot and commercial scales). The proposed technologies will be explored in greater detail in the design phases of the project. The disposal methods of the reagents used in the laboratory-scale CNC production process were also considered a means of minimizing their potential impacts on the environment. It was realized that the spent sulphuric acid could be recycled. A recycling process for the spent acid is included in the project's design phases.

Despite the ability to deal with the laboratory-scale CNC production challenges, the challenges pose a challenge in ensuring optimal performance in an up-scaled production process (if a linear up-scaling model is used). Hence, the recommended optimization strategies will be incorporated in the scaled-up CNC production plant designs (Chapters 6 to 8). The scaled-up plant designs will be based on the unit operations identified in the laboratory. They will be designed for the following production capacities: 1 kg, 10 kg, and 1 ton per day CNC. This task entails creating process flow diagrams (PFDs) (Appendix A), piping and instrumentation diagrams (P&IDs) (Appendix B), specifying system components, process modeling, and simulation to ensure proper equipment sizing, systems control.

## **CHAPTER 4: CONCEPT DESIGN**

### **4.1 Introduction**

The aims of the concept design were threefold: to present various conceptual CNC production process options, critically evaluate each process option's advantages and disadvantages, and identify the most feasible concept design to be expanded in the subsequent design phases (Basic and Detailed). In line with International Atomic Energy Agency (1990) recommendations, the Concept design describes the studies and defines the process systems.

Currently, CNC production occurs at the Biorefinery Industry Development Facility (BIDF) on a laboratory-scale, while the demand from various end-users continues to grow. Up-scaled production facilities must be designed to meet these demands. The design phase aims to improve the production capability and capacity of the BIDF. It has been widely established that the primary lignocellulosic input to the CNC production process is sawdust waste emanating from the South African Forestry, Timber Pulp and Paper (FTPP) Industry. The actual processes to convert the sawdust to the desired CNC output material are presented in this concept design.

This concept design is the first phase in the process plant design cycle and outlines all the potential process options to produce CNC on a larger scale. Several conceptual options are presented and evaluated to arrive at the most feasible solution, to be expanded in the subsequent design phases (basic and detailed). This concept design outlines the proposed conceptual processes for the following production capacities: 1 kg per day CNC, 10 kg per day CNC, and 1 ton per day CNC.

### **4.2 Concept Design Information**

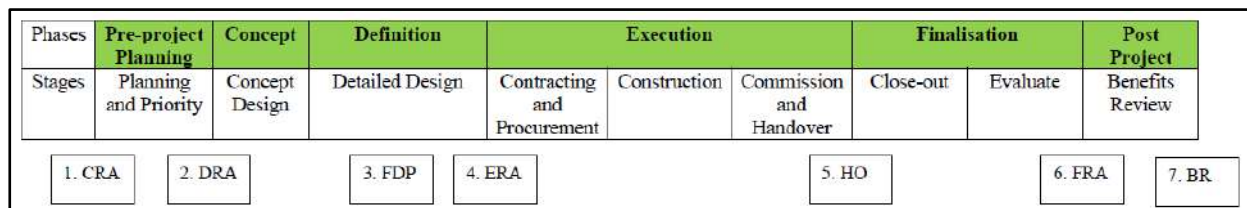
This Chapter outlines the conceptual options available to produce CNC from sawdust waste from various South African Forestry, Timber Pulp and Paper (FTPP) mills on three production scales: pilot-plant scale (1 and 10 kg per day CNC production) and commercial scale (1 ton per day CNC production) to improve the current production capacity of the BIDF.

The overall scope of the plant design phase comprises the following deliverables: process flow diagrams (PFDs), process and instrumentation diagrams (P&IDs), specifying system components, process modeling and simulation to ensure proper equipment sizing, systems control, and identifying the optimal plant design. These deliverables are developed and

optimized as the design cycle progresses from conceptual through to detailed phases. The conceptual solution options, technical risks identified, and outstanding issues for this design phase are indicated in this report.

The purpose of this Chapter is to elaborate as to how the current (laboratory-scale) CNC production capacity at the BIDF can be increased by proposing conceptual solutions for three different production capacities: 1, 10, and 1000 kg/day. The envisioned pilot and commercial-scale production plants are based on the unit operations identified in the laboratory.

The design methodology follows the Project Life Cycle Model (PLCM), an approved industrial governance framework. The PLCM governs the structuring and management of projects. All projects are required to pass through specific decision control gates to allow for investment and implementation of decision-making. Whenever introducing a change to a process, or an entirely new plant/process, the Engineering Change Management (ECM) process is followed under the PLCM. A schematic of the PLCM is outlined in **Figure 4.1**.



**Figure 4.1. Typical Project Life Cycle Model**

**Table 4.1. Key to Figure 1**

Key		
1	CRA	Concept Release Approval
2	DRA	Definition Release Approval
3	FDP	Final Design Package
4	ERA	Execution Release Approval
5	HO	Handover
6	FRA	Finalization Release Approval
7	BR	Benefits Realization

### 4.3 Preamble to Concept Designs

#### 4.3.1 Introduction

Two process designs are presented and compared. The most feasible design is scaled according to the required production capacity (1 kg/day, 10 kg/day, and 1 ton/day CNC suspension). The options differ in the biomass breakdown and required pre-treatment phase. The first design offers a chemical breakdown using APS as the de-lignifying agent, whereas the second design offers a mechanical breakdown using the principle of cavitation. Both processes make use of acid hydrolysis, followed by a final treatment phase. A summary of the design pathways is shown in Table 4.2 below.

**Table 4.2. Design Pathways**

Process Phase	Concept Design Option	
	1. Advanced APS + AH	2. Cavitation-induced Biomass Oxidation coupled with solvent extraction
1. Biomass Breakdown	Sawdust de-lignification using APS chemical.	Sawdust oxidation using Vortex Device for Cavitation (VoDCa).
2. Acid Hydrolysis	Sulphuric acid (64%).	
3. Final Treatment of CNC Product	<ul style="list-style-type: none"><li>• Neutralization by caustic.</li><li>• Homogenization by VoDCa.</li><li>• Desalination by Transmembrane Filtration (TFF) (20-microns).</li></ul>	

#### 4.3.2 Technology Review

##### 4.3.2.1 Vortex Device for Cavitation (VoDCa)

Hydrodynamic cavitation is a process intensification tool to improve the efficiency of biomass delignification (Terán Hilaes et al., 2013). The findings of Baxi and Pandit (2012) endorsed hydrodynamic cavitation due to the delignification rate of hydrodynamic cavitation being up to 5 orders of magnitude greater than those obtained using acoustic cavitation. Typically, hydrodynamic cavitation is coupled with other treatments to intensify the delignification process. The study of Thangavelu et al. (2018) coupled hydrodynamic cavitation with enzymatic pretreatment of wood biomass to attain a 47.4% delignification rate. Decreased

energy requirements of the biomass conversion process were also achieved. Higher delignification rates can be achieved by coupling hydrodynamic cavitation with extraction. The cavitation of wheat straw biomass at 100 W and 20 kHz for 35 minutes at 60°C coupled with extraction with 60% 0.5 M sodium hydroxide methanol solvent yielded up to 78.5% delignification (Sun et al., 2002).

The proposed involvement of VoDCa in sawdust oxidation (Option 2) and CNC suspension homogenization (Options 1 and 2) is noteworthy. VoDCa offers an alternative to ultrasonication, as it can be used as a standalone technology or integrated into a continuous process. Traditionally, rotor-stator mixer types have been used for homogenization and emulsification applications. However, traditional technologies are limited in that they are only adept at levels in the magnitude of 2 microns. High-pressure homogenizers offer better emulsification and dispersion in solutions at the sub-micron level.

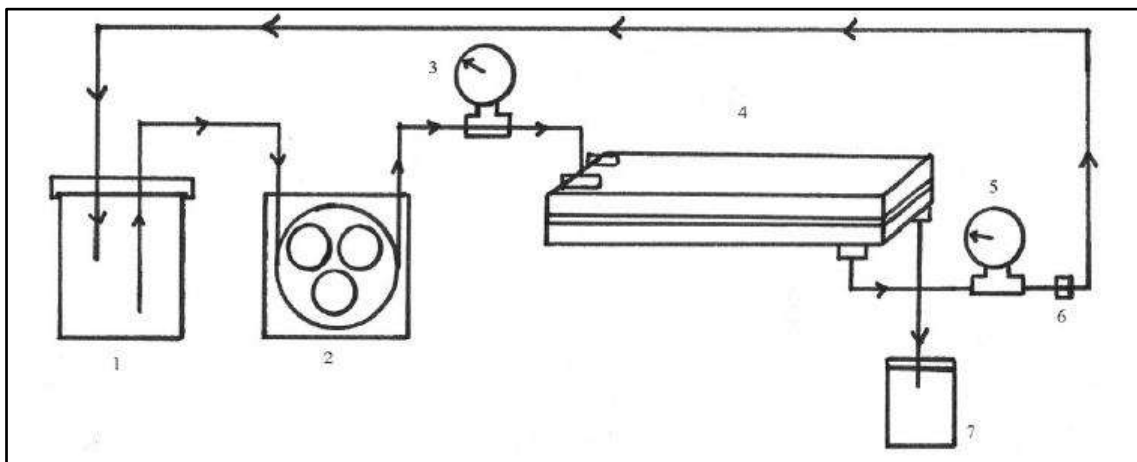
On the other hand, the high operating pressures of these homogenizers are a safety concern. Furthermore, the maintenance, energy consumption, and scale-up pose their challenges. These machines are expensive and require frequent replacement of the worn parts.

Cavitation technology is proposed as a solution to these problems. Hydrodynamic cavitation occurs in venturi or orifice devices to create a substantial pressure drop resulting in the pressure decreasing to a magnitude under which the liquid reaches a boiling point relative to this pressure. This action results in the formation of micro-bubbles or vapour-filled cavities. These cavities then move with the fluid flow to the high-pressure region of the device, where they implode. The implosion causes intense pressure and temperature exertions within the fluid (5000 K and 1000 bar). These high-impact forces cause the disintegration of any medium around the imploding cavitation bubbles. This occurrence results in the degradation of the suspension particles, causing dispersion. This phenomenon can also be classified as emulsification and homogenization of the suspension (Kozyuk, 1999). Despite the apparent advantages of hydrodynamic cavitation, the venturi and orifice devices still choke or constrict due to narrowing the fluid flow. Furthermore, if the bubbles implode near the surface of the device walls, erosion results.

A VoDCa is comprised of a tangential flow inlet and cylindrical axial-flow outlet connected to a disc-shaped chamber. This design imparts and conserves angular momentum resulting in vortex fluid flow. The cavitation bubbles are created in the low-pressure region and collapse in

the vortex core in the high-pressure region, ensuring that the device walls are protected from erosion. The vortex cavitation device is not prone to clogging and offers a lower capital expenditure than traditionally used hydrodynamic cavitation devices such as the venturi and orifice. Hence, this device is recommended as the preferred alternate technology to ultrasonication.

Similarly, TFF is proposed as an alternative to dialysis. As with the potential use of cavitation technology, it can either be applied as a standalone unit or integrated as a unit operation within a continuous process. TFF was applied in the work of Dalwadi and Sunderland (2007) to purify a nanoparticle suspension of surfactant contaminants. The de-contamination rate was deemed efficient. The nanoparticle suspension was purified at transmembrane pressures ranging between 10 to 20 psi using a TFF system comprised of a Minimate™ fabricated with Omega™ 300 K membrane (PALL Scientific). The suspension was circulated through the system using a peristaltic pump. The system setup can be viewed in **Figure 4.2** below.



**Figure 4.2. TFF Schematic (Dalwadi et al., 2005). (1) Sample reservoir (2) Peristaltic pump (3) Feed pressure gauge (4) Minimate 300 K (5) Transmembrane pressure gauge (6) Screw clamp valve (7) Filtrate collector**

#### 4.3.2.2 Transmembrane Filtration (TFF)

A similar setup can be used to remove the salts from the CNC suspension. Further research revealed that a TFF system could be applied to sample volumes ranging from 10 ml to thousands of liters (PALL Corporation). TFF is easier and faster than dialysis and allows higher product concentrations to be achieved in less time without centrifugal devices. TFF requires the CNC suspension to be added to the reservoir with the corresponding connections to pump

and pressure gauges. The system in **Figure 4.3** can be proposed at this stage for the pilot plant processes (1 kg/day and 10 kg/day) (PALL Corporation).



**Figure 4.3. Proposed TFF**

#### **4.4 Concept Design Options**

##### ***4.4.1 Option 1: Advanced (APS + AH) Process***

This process is a modified version of the (APS + AH) process proposed by Andrew (2018) currently used at the BIDE. Although the sawdust de-lignification and acid hydrolysis operations are included, the final treatment phase was modified.

The proposed process entails the following operations:

- De-lignification of sawdust.
- Acid hydrolysis of the de-lignified sawdust “pulp.”
- The final treatment of the CNC product.

The required process units are as follows:

- De-lignification stirred tank jacketed reactor.
- Process water heater.
- Cake filtration module.

- Hydrolysis glass-lined stirred tank jacketed reactor.
- Portable pump.
- Flexible hose.
- CNC recirculation tank.
- Vortex device for cavitation (VoDCa).
- Tangential flow filtration (TFF) module.

The required reagents are as follows:

- APS powder as the de-lignification agent.
- Concentrated sulphuric acid (98%).
- Process water to prepare the APS solution, sulphuric acid solution, quench the hydrolysis reaction, and general rinsing.
- Sodium hydroxide pellets to neutralize the final CNC suspension (pH control).

It was aimed to keep the design minimalistic and technically proficient at producing high-quality CNC. The process runs in semi-batch mode as each process operation occurs in continuous batches.

In Phase 1 (Sawdust de-lignification) of the process, stoichiometric quantities of sawdust, APS solids, and hot process water is added into the de-lignification reactor. Hot process water ensures optimal dissolution of the APS solids. The stirrer is initiated, and the reaction is allowed to run for 6 hours. The temperature of the jacketed reactor must be maintained at 60 °C. Once the reaction is complete, the contents are comprised of de-lignified cellulosic matter termed “sawdust pulp.” The sawdust pulp has a paste or slurry-like texture and is then pumped out of the de-lignification reactor through a cake filter module. This step causes the sawdust pulp to adhere to the filter membrane as retentate, while the filtrate can be collected for beneficiation. The retentate can be washed by passing two passes of water through the cake filter. The retentate can then be collected, labeled, and stored.

In Phase 2 (Acid Hydrolysis of Sawdust Pulp), stoichiometric quantities of process water and concentrated sulphuric acid are added to the glass-lined reactor and stirred for at least ten minutes to ensure the formation of a uniform acidic solution. The acid is added to the water. A



corresponding stoichiometric quantity of the sawdust pulp is then added into the reactor and hydrolyzed for 1 to 2 hours.

The hydrolysis reactor is to be marked with volumetric increments and placed on an elevated platform. The reactor should be fabricated with a vertical observation pane to allow visual observation of the reactor interior. Once the hydrolysis reaction period has lapsed, it must be quenched by pumping a predetermined volume of water into the reactor. This pumping can be done using a portable pump or a conventional hose. The volumetric increments on the reactor wall serve as a guide for the quantity of quench water to be added. After that, the reactor contents are allowed to settle. The vertical observation pane can be used in the initial stages to monitor the settling of the colloidal CNC suspension. Once adequate settling has taken place, there should be two distinct phases visible: the spent sulphuric acid on the top and the denser CNC suspension at the bottom. The drain valve should then be opened to allow the CNC suspension to gravity drain into the CNC recirculation tank using a flexible hose. After that, the remaining spent acid should be drained into the adsorption tank for recovery. The hydrolysis reactor can then be rinsed with a basic solution, washed, and kept in readiness to process the next batch of sawdust pulp.

The final treatment of the CNC suspension (Phase 3) is comprised of three integrated operations contained in one recirculation loop:

- **Neutralization of the CNC suspension** by dosing with a predetermined quantity and concentration of sodium hydroxide. Jar tests are undertaken to ascertain the optimal quantity and concentration. The neutralization step can be done in the tank by adding the caustic and agitating the contents for at least ten minutes using a stirrer. After that, the below operations can be performed by pumping the neutralized suspension through the recirculation loop.
- **Homogenization of the CNC suspension** allows the suspension to disintegrate, thereby yielding a gel-like texture. Various devices have been considered for this purpose, such as rotor-stator-type mixers and high-pressure homogenizers. A vortex device for cavitation (VoDCa) is recommended due to its low energy consumption and high efficacy.
- **Purification of the CNC suspension** by passing it through a 20-micron tangential flow filtration (TFF) module. This operation replaces the previous dialysis operation by

removing the dissolved salts/sugars present in the suspension. The TFF design enables it to be self-cleaning and not readily susceptible to blockages. This functionality provides a practical and rapid method for salt removal from the final CNC product.

The intense temperature and pressure conditions within a collapsing cavitation bubble can cause various chemistry effects on the molecular level, such as bond breakage, free radical formation, molecular and atomic excitation (Suslick, 1990). This phenomenon was exploited by Langenecker (2010) when the effects of cavitation were combined with adsorption to remove the salts from water for desalination applications. Langenecker (2010) conceded that when metallic salts are contained within the liquid combined with surface-active particles, the sodium and chlorine radicals interact with the particles to form new combinations. The particles can then be removed by simple filtration, resulting in desalination. Langenecker (2010) researched the recirculation treatment loop proposed for the final treatment phase in which cavitation assists the breakdown of the dissolved salts and sugars, thereby reducing the load on the TFF. The number of circulations through the VoDCa and TFF must be optimized by monitoring the texture and salt removal per cycle. Table 4.3 below compares the technologies currently used at the BIDF to perform the final treatment steps against the proposed integrated method.

**Table 4.3. Comparison of technology between the existing and proposed processes**

Process Requirement	Technology	
	Existing Process	Proposed Process
Neutralization	Successive centrifugation and dilution	Caustic dosing
Homogenization	Successive ultrasonication	VoDCa
Purification	Dialysis	TFF

#### ***4.4.2 Option 2: Cavitation-induced Oxidation Process***

In this configuration, the biomass feed is oxidized to degrade it into its major constituents: cellulose, hemicellulose, and lignin. The oxidation step replaces the de-lignification step in the previous configuration. The oxidized biomass is then subjected to acid hydrolysis and final treatment as in the previous configuration.

The proposed process entails the following operations:

- Delignification of sawdust using VoDCa coupled with solvent extraction.
- Acid hydrolysis of the oxidized lignocellulosic matter.
- Final treatment of the CNC product.

The process units required are outlined below:

- VoDCa recirculation skid.
- Aeration device.
- Hydrolysis glass-lined stirred tank jacketed reactor.
- Portable pump.
- Flexible hose.
- CNC recirculation tank.
- Vortex device for cavitation (VoDCa).
- Tangential flow filtration (TFF) module.

The reagents required are outlined below:

- Concentrated sulphuric acid (98%).
- Process water to make up the sulphuric acid solution, quench the hydrolysis reaction, and general rinsing.
- Sodium hydroxide pellets to neutralize the final CNC suspension (pH control).

In Phase 1 (Biomass Oxidation using VoDCa) of the process, the VoDCa can produce reactive radicals by homolytic cleavage of the water caused by the extreme temperature and pressure conditions during the collapse or implosion of the micro-bubbles (Jain et al., 2019). This characteristic is exploited in this process step. The sawdust is added to a predetermined quantity of water and recirculated through the cavitation skid for a predetermined period. An aeration device can be inserted into the feed tank of the cavitation skid to increase the oxidation rate. Two mechanisms cause the sawdust to degrade into its constituents (cellulose, hemicellulose, and lignin):

- The free radicals attack the sawdust particles (oxidative action).

- The collapse of microbubbles generates extreme shear forces that rupture the cell walls, thereby enhancing the oxidative action of the free radicals.

In the initial trials, grab samples of the sawdust slurry must be analyzed for cellulose concentration to optimize the recirculation time. Once the optimal time has elapsed, the cavitation pump can be stopped, pipes drained, and the contents of the feed tank pumped into the hydrolysis reactor using the portable pump to initiate Phase 2. A solvent extraction step is required to remove the lignin content (Sun et al., 2002).

In Phase 2 (Acid Hydrolysis of Oxidized Cellulose), the recirculated sawdust slurry degrades into its principle lignocellulosic components. These constituents are contained in aqueous form and require acid hydrolysis to degrade the amorphous regions of the cellulose chain. A similar hydrolysis procedure from the first configuration is recommended. Once the hydrolysis reaction is complete, it must be quenched. After that, the reactor contents are allowed to settle before draining the CNC suspension for final treatment in Phase 3.

Phase 3 (Final Treatment of the CNC Product) is identical to that outlined in the previous configuration.

#### 4.5 Selection of Preferred Concept Design

The advantages and disadvantages of each configuration are outlined in Table 4.4 below.

**Table 4.4. Comparison of Proposed Concept Designs**

Option	Advantages	Disadvantages
1	<ul style="list-style-type: none"> <li>• Laboratory-scale trials have already been performed on this process configuration- reaction stoichiometries, reagent concentrations, and reaction conditions are already known and optimized.</li> <li>• Safety hazards and risks are known, and mitigation measures</li> </ul>	Greater chemical requirement (for de-lignification of the sawdust), implying a greater safety risk associated with the use of APS.

---

are already implemented.

---

2	<ul style="list-style-type: none"><li>• This configuration eliminates the need for APS chemical for de-lignification (massive OPEX savings can be achieved). Instead, it uses the mechanical principle of cavitation to induce oxidation of the raw biomass into its cellulose, hemicellulose, and lignin constituents.</li><li>• Lower power requirement by eliminating the six-hour de-lignification reaction under elevated temperature (60 °C) and agitation.</li></ul>	Laboratory-scale trials are required to determine the optimal oxidation and hydrolysis conditions.
---	---	--

---

Considering that the premise of this work was to expand on the existing (APS + AH) process at the CSIR BIDE, Option 1 was selected as the preferred option. Consequently, the three CNC production capacities: 1 kg/day, 10 kg/day, and 1000 kg/day were based on the (APS + AH) production method. Further details are outlined below.

#### **4.6 Capacity-specific Process Concept Designs**

Based on the mass balance calculations presented in Section 4.9, the capacity-specific process designs are outlined below.

##### ***4.6.1 1 kg/day CNC Suspension***

These designs are based on a 10% CNC suspension concentration. The mass balances used for the equipment sizing can be viewed in Section 9. This capacity is almost on the same scale as laboratory production. Hence, there are some aspects of laboratory equipment and vessels proposed to be used in this design. The process is carried out in batch mode and requires substantial human intervention. Further details are outlined below for each of the phases.

The equipment required are outlined below:

- 20 L Teflon or PTFE plastic bucket for the sawdust de-lignification and acid hydrolysis phases.
- Rotating overhead stirrer (acid resistant) for the above vessel.
- Portable electric heater for the de-lignification vessel.
- Water bath maintained at 60 °C.
- Vacuum filter and filter paper.
- 80 L Teflon or PTFE plastic vessel (bucket or mini Jojo tank can be used) to purge the hydrolysis reaction by quenching.
- 0.5 to 1 m wooden rod for stirring the 80 L plastic vessel at the beginning of the quenching procedure.
- Customized treatment skid comprised of a TFF (20 microns) unit and VodCa unit designed for 1 L circulation of 10% CNC concentration suspension. The skid is a closed-loop and requires a feed tank and recirculation pump. This configuration allows the manual transfer and circulation of CNC suspension into and through skid as a means of final treatment after the hydrolysis phase.

The materials required are outlined below:

- 437 g sawdust.
- 4.4 L APS solution (this requires 2.98 kg APS powder).
- 6.55 L 64% sulphuric acid solution.
- 65.5 L quench water.
- Sodium hydroxide pellets.

Per the mass balance (Section 4.9), in Phase 1 (Sawdust de-lignification), 437 g of sawdust is weighed and placed into the 20 L plastic bucket. 2.98 kg of the APS powder and the corresponding quantity of process water is added into the plastic bucket. The electric heater is placed at the base of the plastic bucket to maintain the temperature at 60 °C. The overhead stirrer is used to stir the contents for six hours. At the end of the six-hour reaction, the electric heating element and stirrer are switched off, and the de-lignified pulp slurry is decanted into the vacuum filter and filtered. There should be approximately 290 g of sawdust pulp forming

the retentate on the filter paper. The retentate is flushed at least twice with clean process water under vacuum before the pulp is removed from the filter paper, heat-sealed, and labelled.

The packaged pulp is then stored in the cold storage, while the vacuum filter, bucket, electric heater, and stirrer must be washed, dried, and stored away. The pulp can be removed from the cold storage and immediately hydrolyzed as and when required

In Phase 2 (Acid Hydrolysis of Sawdust Pulp), the concentrated acid and corresponding make-up process water to reach the 64% concentration are placed into the 20 L plastic bucket. The acid is added to the water. The electric heating element is placed at the base of the bucket and set at 50 °C. After that, the stirrer is switched on, and the hydrolysis reaction is run for an hour. During this time, the 80 L Teflon or PTFE plastic vessel is filled with roughly 65.5 L of quench water by connecting a flexible hose to a tap. Once the reaction time has elapsed, the stirrer and heating element is stopped and removed from the 20 L plastic bucket. The CNC slurry is then dumped into the 80 L plastic vessel and stirred for at least 5 minutes. The contents are settled for at least an hour. After settling, two distinct layers should be present: the bottom layer comprises the untreated CNC suspension, and the top layer comprises the dilute spent acid. The top layer can be manually removed by careful emptying using a small jug or vessel (not to disturb the bottom layer containing the untreated product suspension). 0.9 L of water should then be added to the remaining suspension and briefly stirred with the wooden rod.

In Phase 3 (Final Treatment of CNC Suspension Product), the required quantity of sodium hydroxide pellets is added into the untreated suspension and stirred using the wooden rod for at least 5 minutes or until the pellets are completely dissolved. The quantity required for neutralization is to be determined by trial and error using a pH meter. The target pH is 7. Alternately, a neutralization test can be done on a sample of suspension and scaled up for the entire batch. The neutralized suspension is fed into the VoDCa recirculation tank and circulated until a homogeneous suspension is obtained. This observation occurs visually and requires trial runs to establish the optimal cavitation time. During this time, the salt and sugar impurities are removed by the TFF, resulting in the final purified CNC suspension, which can be isolated into the feed/holding tank of the treatment skid and drained into a glass storage bottle. The storage bottle must be labelled.

The storage bottle is stored in cold storage, while the cavitation skid is washed and stored.

#### **4.6.2 10 kg/day CNC Suspension**

This process occurs on a larger scale relative to the previous and requires specialized equipment for the specific application outlined below.

- 60-70 L de-lignification stirred tank jacketed reactor.
- Water heater to make up APS solution in the above reactor.
- Cake filtration module.
- 80-90 L hydrolysis glass-lined stirred tank reactor with an internal acid-resistant heating element.
- Portable pump.
- 10 m Flexible hose.
- CNC recirculation tank.
- Vortex device for cavitation (VoDCa).
- Tangential flow filtration (TFF) module.

The materials required are outlined below:

- 4.37 kg sawdust.
- 43.7 L APS solution (this requires 29.9 kg APS powder).
- 65.5 L 64% sulphuric acid solution.
- 655 L quench process water.
- Sodium hydroxide pellets.

This configuration is carried out in batch mode with less manual intervention than the previous configuration. The hydrolysis reactor must be placed on an elevated platform. The specific details of the process are outlined below.

In Phase 1 (Sawdust de-lignification), 4.37 kg of sawdust is placed into the de-lignification reactor with 29.9 kg APS powder. The appropriate quantity of process water is filled into the reactor to make up the APS solution to the required 3 M concentration. The make-up process water is heated in a heating vessel and transferred into the reactor using a portable pump. The reactor jacket is set to maintain the temperature of the reactor at 60 °C. The overhead stirrer is switched on, and pressure release mechanisms are activated to ensure that the reactor operation is within safe pressure limits. The de-lignification reaction is run for six hours. After that, the



overhead stirrer and heating jacket are switched off, the outlet valve is opened, and the de-lignified sawdust pulp slurry is pumped through the cake filter. The pulp retentate is then washed by filling the de-lignification reactor with 30-35 L of water and having this volume pumped through the cake filter. The filtrate can be collected for beneficiation, while the 2.9 kg pulp can be removed from the filter, heat-sealed in plastic, and labelled.

The package can be stored in cold storage for the next hydrolysis batch, while the de-lignification reactor and filter can be washed and kept in readiness for the next batch.

In Phase 2 (Acid Hydrolysis of Sawdust Pulp), the hydrolysis reactor must be accessible by stairs. The reactor design must incorporate a vertical watch glass for visibility of the settling stage after the quench. It should also be designed so that the height dominates the diameter and radius for better settling and draining visibility of the CNC suspension. The reactor should be heated using an internal heating element rather than an external heating jacket to enable visibility of the internal settling.

The required quantity of make-up water is pumped into the reactor using a hose or a portable pump. Thereafter, the required quantity of concentrated sulphuric acid is decanted into the reactor. The heating element is set to maintain a reaction temperature of 50 °C. The temperature probe indicates when the acidic mixture is at the required temperature to begin the hydrolysis reaction. As soon as the required reactor temperature is reached, the pulp is inserted, and the stirrer is started. An hour later, the reaction is ready to be quenched. 8.75 L of water is pumped into the reactor. Graduation marks along the side of the reactor and visual observation through the watch pane are used to pump the correct quench volume into the reactor. Subsequently, the contents are briefly stirred using the wooden rod and allowed to settle. Once the settling time has elapsed, the outlet drain valve located at the reactor base is opened until the bottom CNC slurry layer has been completely drained into the final treatment recirculation tank. This action is done by connecting the flexible hose from the reactor base to the inlet of the final treatment recirculation tank. The remaining spent acid within the hydrolysis reactor is then drained into the acid recycle vessel, after which it can be washed and kept in readiness for the next batch.

Phase 3 (Final Treatment of CNC Suspension Product) requires the custom-fabrication of the recirculation unit connected to the final treatment tank. The recirculation unit is comprised of the following process units:

- VoDCa unit designed for 7.7 L of suspension.
- Centrifugal pump to recirculate the slurry.
- TFF located after the VoDCa unit designed for 7.7 L of suspension.

This phase is initiated by pumping 8.75 L dilution water into the final treatment tank. This phase is followed by opening the outlet valve and starting the recirculation pump. The suspension is recirculated until the optimal homogenization, and salt removal efficacy has been achieved. This check requires initial grab sample analyses through the recirculation loop and dictates the optimal recirculation time. A preliminary set of standards has been outlined in Chapter 5, Table 16 (CNC Quality Criteria), to serve as quality benchmarks in this regard. Once the final treatment has reached completion, the 10 kg CNC suspension is drained into several glass bottles and labelled.

The bottles can be stored in cold storage. The recirculation system can then be flushed with a standard industrial CIP solution and washed.

#### ***4.6.3 1000 kg/day CNC Suspension***

This capacity is the largest and requires a similar method of operation as the previous configuration. Considering that this capacity is industrial scale among CelluForce and API, it requires more automation controls. The details are outlined below.

The equipment required are outlined below:

- 6000 L glass-lined stirred tank jacketed reactor for sawdust de-lignification.
- Water heater to heat the water required to make up the APS solution in the above reactor.
- Cake filtration module.
- 73 000 L hydrolysis glass-lined stirred tank reactor with an internal acid-resistant heating element.
- 1000 L final treatment tank.
- Custom fabricated recirculation final treatment skid comprised of:
  - 0.8 m<sup>3</sup> CNC recirculation tank.
  - Vortex device for cavitation (VoDCa).
  - Tangential flow filtration (TFF) module.

- Recirculation pump.
- Flow, level, and temperature indicator.
- Associated pumps, valves, lines, and indicators.

The materials required are outlined below:

- 437 kg sawdust.
- 4.4 m<sup>3</sup> APS solution (this requires 2989 kg APS powder).
- 6.6 m<sup>3</sup> 64% sulphuric acid solution.
- 65.5 m<sup>3</sup> quench process water.
- Sodium hydroxide pellets.

There are no portable pumps or flexible hoses in this configuration due to the greater degree of automation and control.

In Phase 1 (Sawdust de-lignification), a bucket conveyor is used to empty the 437 kg of sawdust into the reactor. Similarly, the APS is transferred into the reactor. The heated make-up process water at 60 °C is then pumped into the reactor from the water heater. Once the reagents enter the reactor, the heating jacket maintains the reactor temperature at 60 °C. The overhead stirrer is switched on, and the reaction is run for the next six hours. The temperature and pressure are monitored, and an alarm is sounded if they transgress the allowable limits. Subsequently, the reaction is stopped to allow the Process Engineer or Technician to make the necessary adjustments outlined in Table 4.5 below.

**Table 4.5. Potential Anomalies and Mitigation Measures**

<b>Reaction Parameter</b>	<b>Condition</b>	<b>Consequence/s</b>	<b>Corrective Action/s</b>
Pressure	High	Explosion risk	Activate pressure release valves to 100% capacity
Temperature	High	Possible de-nature of APS chemical- resulting in reduced de-lignification	Reduce the jacket temperature or switch off jacket heating until the temperature drops within range

	Low	Inadequate de-lignification	Increase the jacket temperature
Impeller Speed	High	Non-uniform de-lignification	Reduce the impeller speed
	Low	Inadequate agitation for uniform de-lignification	Increase the impeller speed

Once the reaction time has elapsed, an alarm is sounded to notify the plant personnel. Immediately after, the reactor outlet valve is opened (these actions are automated by selecting them from the human-machine interface (HMI) in the plant control room), and the slurry is pumped through the filtration module. The retentate forms the sawdust pulp “cake” on the filter while the filtrate enters the APS waste flow bin. Internal nozzles rinse the delignification reactor. The rinse nozzles are activated through the HMI in the control room. The rinse water is pumped through the filter to deposit the remnants of pulp onto the cake and rinse the sawdust pulp. There should be roughly 290 kg of sawdust pulp deposited on the filter. The sawdust pulp is manually removed by the plant Technicians using shovels and placed into a storage container. The storage container is kept in cold storage until the hydrolysis reactor is ready for a new batch of pulp. Once filled, the APS waste flow bin is transported on a forklift to wastewater treatment.

In Phase 2 (Acid Hydrolysis of Sawdust Pulp), the required quantity of make-up process water is pumped into the hydrolysis reactor from the process water storage tank. The process water storage tank contains a heating element that maintains the water temperature at 60 °C. The hydrolysis reactor is equipped with level control. Once the required volume of make-up water is reached, then the pump automatically stops. Subsequently, the required quantity of concentrated sulphuric acid is pumped into the reactor. Again, the level control is used to regulate the influent acid volume, such that 6.6 m<sup>3</sup> of 64% sulphuric acid solution is made up. The reactor jacket is set to maintain the reaction temperature at 50 °C. Once the reactor has reached the required temperature, the conveyor belt automatically starts and empties the 291 kg of sawdust pulp into the reactor.

The overhead stirrer then agitates the reaction contents until the reaction time of one hour has elapsed. Once the reaction time has elapsed, the stirrer and heating jacket are automatically

switched off. Subsequently, 65.5 m<sup>3</sup> of quench water is pumped into the reactor to purge the hydrolysis reaction. The stirrer is switched on for 5 minutes to enhance the purge process. Thereafter, the contents are separated, and the CNC slurry settles to the bottom of the reactor. A turbidity indicator scans through the height of the hydrolysis reactor. It identifies the height of the CNC slurry layer at the bottom (which is denser than the spent acid layer and therefore exhibits greater turbidity). This strategy controls the outlet valve by opening it only for as much time as required to drain the CNC slurry from the base of the reactor into the recirculation tank. Once the CNC slurry is drained, the valve is closed, and the remaining spent acid is pumped into the acid recovery system.

In Phase 3 (Final Treatment of CNC Suspension Product), roughly 97 L of CNC slurry is drained into the recirculation tank. This slurry forms the 10% CNC constituent of the final product. A water make-up volume of 875 L (remaining 90%) is then pumped into the recirculation tank. The pump is controlled by a level indicator and automatically switches off once the required volume of make-up water is added into the tank. The stirrer is switched on for 5 minutes immediately after and subsequently stopped. At this stage, the contents comprise the 10% CNC solution. However, it requires neutralization, desalination, and homogenization. These will all be performed in this final treatment phase.

Subsequently, the neutralization process is initiated. The recirculation tank is equipped with a pH indicator connected to the caustic dosing pump. Based on the pH of the tank contents, the dosing pump automatically doses the required quantity of caustic to achieve neutral pH. The dosing pump is programmed using a pH curve based on laboratory-scale neutralization studies. The CNC slurry is now ready to begin the homogenization and desalination phase. The recirculation tank outlet valve is opened, and the pump is switched on. The slurry is passed through the VoDCA device and TFF before re-entering the recirculation tank. The loop is equipped with a real-time analyzer to determine the concentration of the dissolved salts. While the desalination occurs within the recirculation loop, the VoDCA disintegrates and emulsifies the slurry, yielding a gel-like texture. Once the salt concentration falls within specification, the suspension is returned to the recirculation tank. The tank is equipped with a manual valve at the base to allow manual transfer of the final product into packaging bottles. Once all the product is removed, the entire recirculation skid begins a self-clean operation (CIP).

## **4.7 Automation Strategy**

The control narrative for the commercial scale production process is shown below.

### ***4.7.1 Phase 1: Sawdust de-lignification***

- The level indicator monitors the make-up water inflow and stops the pumps once the desired height (volume) of water is attained to make up the 3M APS solution.
- The de-lignification reactor has a timer that only begins once the reactor temperature has reached 60 °C. The timer is controlled by the thermostat, which sounds alarms to notify the Plant Operator (PO) when the temperature exceeds or drops below the operating range.
- If the reactor pressure exceeds the safe limit, the high-pressure alarm is sounded.
- After the six-hour reaction time has elapsed, a signal is sent to the HMI requesting authorization from the PO to open the reactor outlet valve. This action signals the reactor outlet pump to pump the contents through the filter.
- The outlet valve is closed.
- Once the reactor is empty, the PO initiates reactor rinsing by initiating the rinse nozzles. The rinse nozzles perform the rinsing action for 10 minutes.
- The outlet valve is opened after the rinse time has elapsed.
- This outlet pump pumps rinse water through the filter, constituting the washing phase.

### ***4.7.2 Phase 2: Hydrolysis of Sawdust Pulp***

- The PO initiates the hydrolysis phase from the HMI, signaling the inlet valve to open.
- The hot water pump pumps water into the reactor to make up the acid solution.
- The level indicator monitors the water level and sends a signal to the level controller once the desired water height (volume) has been reached to stop the pump.
- The concentrated acid pump pumps acid into the tank. The height by which the tank volume should increase due to the acid addition is predetermined (as with the hot water). Once the predetermined level has been reached, the level controller stops the acid dosing pump.
- The reactor jacket maintains the temperature at 50 °C.
- Once the 50 °C temperature is reached, the inlet valve is opened, and the PO is notified to initiate the conveyor system.

- The PO then initiates the reaction, which begins the following sequence:
  - The inlet valve is closed.
  - The overhead stirrer begins to stir the solution for the one-hour duration of the reaction.
  - After the one-hour period has elapsed, the stirrer and heating jacket are switched off.
  - The inlet valve is opened.
  - The quench water pump pumps the quench water into the reactor. This pump is level-controlled, i.e., as soon as the required volume of quench water has been added, the pump switches off.
  - The inlet valve is closed.
  - The stirrer is switched on for five minutes.
- A predetermined settling time is allowed for the CNC slurry to settle and form the bottom layer. This layer corresponds to a certain height. The outlet valve is opened to allow the CNC slurry layer to drain into the recirculation tank, after which it closes.
- The outlet pump begins to pump the spent acid to the acid recovery tank.

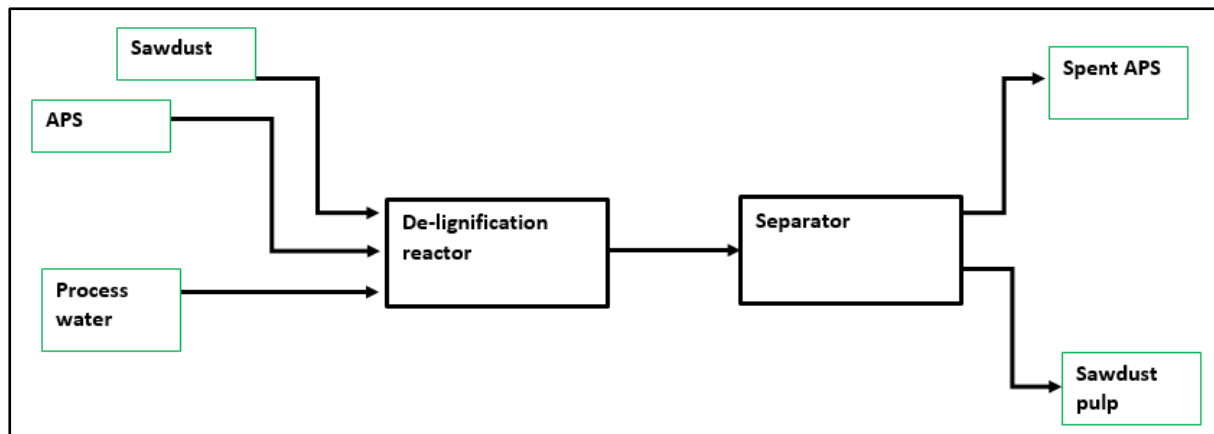
#### ***4.7.2 Phase 3: Final Treatment of CNC Suspension Product***

- The PO initiates the dilution water pump to pump the dilution water into the final treatment/ recirculation tank. The pump is level-controlled and stops once the required height (volume) of water is reached.
- The stirrer starts for five minutes.
- The PO initiates the caustic dosing. The pH indicator and controller control the dosing pump.
- Once the pH is within 6.5 to 8.5, the recirculation tank outlet valve is opened.
- This action signals the recirculation pump.
- The salinity indicator and controller control the recirculation pump. Once the salinity is acceptable, the recirculation tank outlet valve is closed. The pump stops after returning all the contents into the recirculation tank.
- Alternatively, the optimal recirculation time can be determined by trial runs. The recirculation pump is stopped after the time elapses.
- The suspension is manually transferred into bottles.

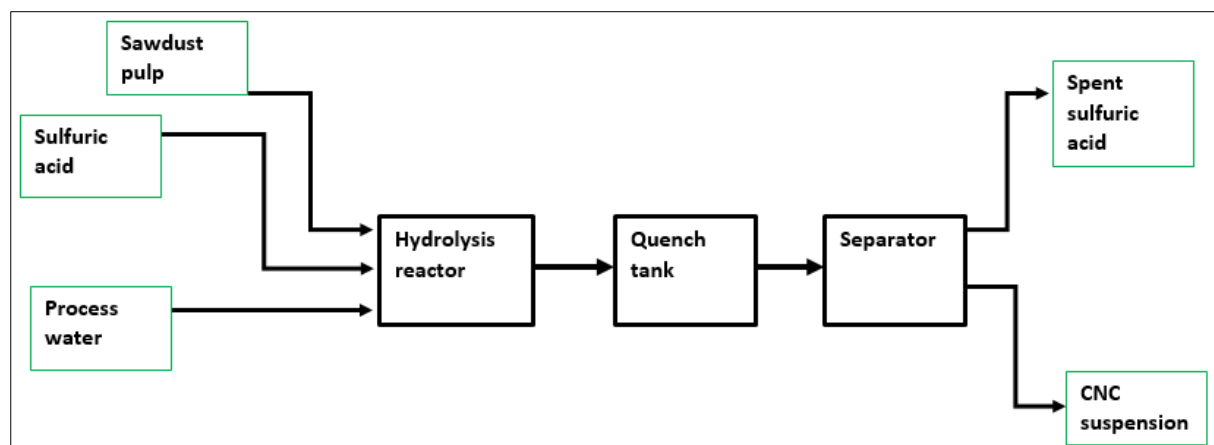
- The system undergoes a CIP.

#### 4.8 Block Flow Diagrams

The Block Flow Diagrams (BFDs) for each process phase are shown in **Figure 4.4** to **Figure 4.6** below.

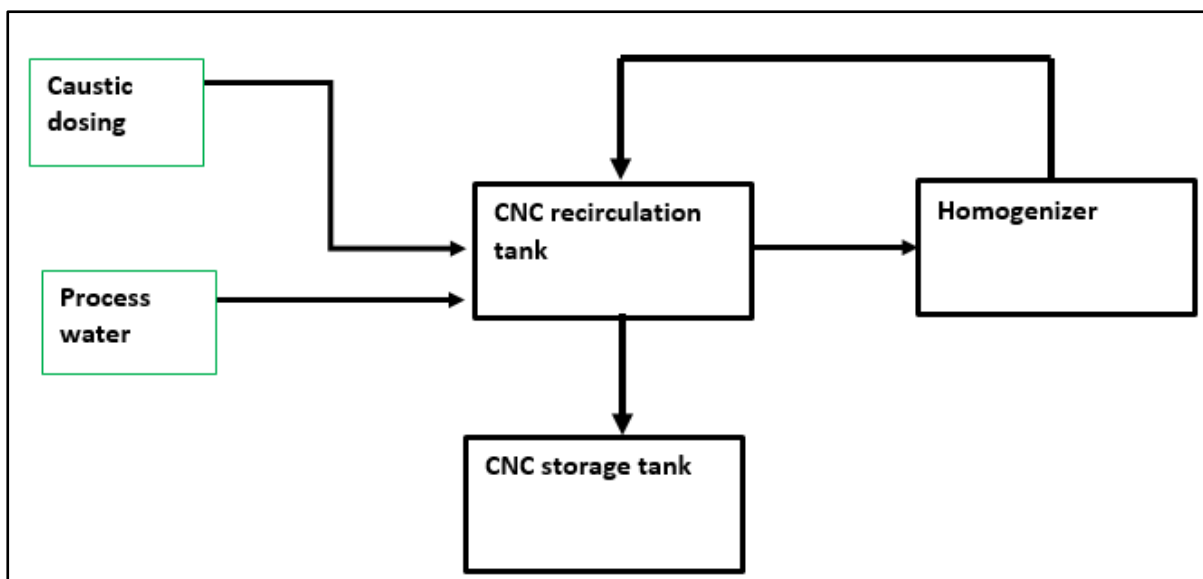


**Figure 4.4. BFD (Phase 1 CNC Production)**



**Figure 4.5. BFD (Phase 2 CNC Production)**





**Figure 4.6. BFD (Phase 3 CNC Production)**

#### 4.9 Mass Balances

After developing the Block flow diagrams, the different streams that enter or leave the blocks and the consumption of reagents could be calculated (International Atomic Energy Agency, 1990). This step required primary laboratory data, such as throughput, reagent dosages, solid to liquid ratios of process streams, retention times, temperatures, and pressures in the different unit operations. The mentioned data was obtained from the laboratory process and was used to size the equipment and piping. The mass balance calculations are outlined in Table 4.6 to Table 4.12 below.

**Table 4.6. Sawdust Composition**

Component	Range (%)	Average (%)	Weighted Average (%)
Cellulose	35-55	45	45.9
Hemicellulose	20-35	27.5	28.1
Lignin	15-36	25.5	26

**Table 4.7. Cellulose Morphology**

Phase	Composition (%)
Crystalline	70
Amorphous	30

**Table 4.8. CNC Product Suspension Properties**

Property	Value	Comment
CNC concentration	10%	A 10% reference value was used based on Blue Goose's 1 to 15% concentration (volume basis) (Blue Goose Biorefineries Inc., n.d.)
Suspension density	1300 kg/m <sup>3</sup>	The density range lies between 1000 and 1600 kg/m <sup>3</sup> based on FPL and Clemson University studies (Reiner and Rudie, 2013)
CNC suspension mass	10 kg/day	The 10 kg/day production capacity was used as the baseline for this calculation
CNC suspension volume	7.69 L	Based on the above CNC suspension mass and density

**Table 4.9. Overall Mass Balance**

Parameter	Quantity	Comment
Starting sawdust	436,681.20 g	
Lignin contained in the above	113,626.20 g	To be removed by de-lignification reaction
Post delignification	323,055.00 g	Sawdust without the lignin (sawdust pulp)
Pulp loss in vessel transfer	10%	Estimate
Pulp remaining after transfer loss	290,749.50 g	
Hemicellulose contained in the raw sawdust	110,284.30 g	Based on Table 4.6 (sawdust composition)

Cellulose contained in the above	180,465.20 g	Based on Table 4.6 (sawdust composition)- contains crystalline and amorphous components
Post hydrolysis crystalline cellulose in the above	126,325.60 g	Based on Table 4.7 (cellulose morphology)- assuming 100% hydrolysis efficiency
Post hydrolysis CNC volume	97.17 L	Constitutes 10% of the CNC suspension- the rest is 90% water
Water volume for suspension dilution	874.56 L	
Water + CNC mass	1000 kg	Provides the required 1000 kg/day CNC production capacity

**Table 4.10. De-lignification Stoichiometry**

Parameter	Quantity	Comment
The ratio of sawdust to APS solution in laboratory-scale production	2 g per 20 mL	Based on (APS + AH) process used by the CSIR
Sawdust required for 1000 kg/day production	436,681.20 g	From Table 4.9
APS solution concentration	3 M	3 moles per liter of solution
APS molar mass	228.20 g/mol	
APS mass/ liter solution	684.60 g/L	
APS solution required	4,366.81 L	Based on ratio
Mass of APS required	2,989.40	Based on the g/L value
Sawdust density	344 kg/m <sup>3</sup>	Anval Valves (Pty) Ltd- Bulk Density Chart (Liu, n.d.)
Sawdust volume	1,269.42 L	Based on required mass and density

Required reactor volume	5,636.23 L	Sum of APS volume and sawdust volume
-------------------------	------------	--------------------------------------

**Table 4.11. Hydrolysis Stoichiometry**

Parameter	Quantity	Comment
Ratio of sawdust to acid in laboratory-scale production	2 g per 30 mL	Based on (APS + AH) process used by the CSIR
Sawdust required for 1000 kg/day production	436,681.20 g	From Table 4.9
Sawdust pulp mass being hydrolyzed	290,749.50 g	From Table 4.9
Sawdust pulp density	2000 kg/m <sup>3</sup>	Estimate
Sawdust pulp volume	145.4 L	Based on pulp density and mass
Sulphuric acid required	6,550.22 L	3 moles per liter of 64% sulphuric acid solution
Quench water required	65,502.18 L	
Required reactor volume	72,197.80 L	Sum of pulp, acid, and quench water volume

The CNC Product Specification Datasheet is shown below (Forestry Product Laboratory).

**Table 4.12. CNC Datasheet**

Parameter	Specification	Unit
Appearance	White, odourless	
Concentration	11-12.5	weight% aqueous gel
Fiber dimensions	5-20	nm wide
	150-200	nm long
Surface property	Hydrophilic	
Density	1	g/cm <sup>3</sup> gel
	1.5	g/cm <sup>3</sup> dry powder
Required storage conditions	Store under refrigeration	

#### **4.10 Safety Concept**

Generally, the following safety considerations are to be followed for all production capacities:

- a) The plant must be located in a vicinity secluded from the public area or minimum traffic to avoid a risk of acid vapour inhalation.
- b) The use of breathers on the bulk storage tanks of the respective chemicals also prevents vapour inhalation.
- c) The chemical storage and handling areas have bunds, and only the delivery lines are to be run outside the proximity of the bund walls.
- d) During construction, the contractors involved in this project adhere to the General Safety Regulations of the OHSA 85 of 1993. This practice ensures that all personnel are well equipped with the required safety equipment and protective clothing. In addition to this, all personnel performing work on this project must be aware of the safety hazards associated with the projected activities. The appropriate signage and notices must be present on-site during the execution stage.

It is recommended to consult a standard construction baseline risk assessment for the substantial safety risks, as listed below:

- Site Establishment
- Fall Protection
- Offloading Material & Equipment Manually and using a Mobile Crane
- Operating a Telescopic Handler
- Assembly, Erection of Steel
- Installation of piping
- Grinding and Cutting with a 9" & 4" Grinder
- Oxy-Acetylene Operations
- Hand-held Drilling Machine
- Arc Welding Operations
- Manual Handling of Material & Equipment
- Rigging of Material & Equipment
- Transporting of Employees to and from site
- Using a Man Cage with a Mobile Crane
- Installation of Cable Racks

- Cable Pulling
- Gland and Termination
- Fabrication and Installation of Support Steel
- Trenching using a TLB
- Environmental
- Occupational Health & Hygiene

## **4.11 Siting Information**

### ***4.11.1 Site Selection***

The designs proposed in this document could be built on any production site. However, specific requirements for site selection should be followed. These are outlined below (Coulson and Richardson, 2005):

- a) Distance and ease of access to the marketing area.
- b) Raw material supply.
- c) Transport facilities.
- d) Availability of labour, utilities, and power.
- e) Environmental impact and waste disposal.
- f) Local community considerations.
- g) Climate.

### ***4.11.2 Site Layout***

The site layout (depending on the production capacity) requires the following facilities (Coulson and Richardson, 2005):

- a) Storage areas for raw materials and products.
- b) Maintenance workshops with stores and operating supplies.
- c) Laboratories for process control.
- d) Emergency service stations, including fire stations.
- e) Utilities.
- f) Effluent disposal plant.
- g) Offices or park homes for general administration.
- h) Amenity buildings, such as canteens and medical centers.

- i) Car parks.

#### ***4.12 Conclusions and Recommendations***

Although the cavitation-induced oxidation method holds tremendous potential, laboratory-scale trials must be undertaken to gain a deeper understanding of the process and optimize the production before it can be considered for up-scaling. This process would be incredibly beneficial in achieving operational expenditure savings by eliminating APS chemical and heating for the six-hour de-lignification period.

There are pronounced differences in the operation modes for the 1, 10, and 1000 kg/day CNC production. The 1 kg/day capacity is very similar to the current laboratory-scale production. However, the transition from 10 kg/day to 1000 kg/day sees extreme automation and tighter control mechanisms using control interlocks and signals to ensure accurate timing, reagent dosing, and reaction conditions.

This Concept design provided the foundation for the subsequent design phases in which detailed equipment specification is undertaken (among other deliverables) to provide a greater degree of detail to the actual requirements for implementing whichever production capacity is desired.

Industrial data was used from Maines University and Forestry Products Laboratory (FPL) to approximate the properties of the CNC suspension for the preliminary equipment sizing. It is recommended that the BIDE develops its CNC property database to allow more accurate designs to be performed. Furthermore, consideration should be given to developing the cavitation-induced oxidation process as an alternate to sawdust de-lignification.

## **CHAPTER 5: BASIC DESIGN**

### **5.1 Introduction**

The Basic Design aimed to expand upon the optimal CNC production process design identified in the Concept Design Chapter. The expansion of the design entailed the following:

- a) Mass balance calculations leading to equipment sizing results for the de-lignification reactor, acid hydrolysis reactor, add the final treatment tank.
- b) Control and Instrumentation design
- c) Electrical design
- d) Plant layout

Considering that two main production processes were proposed, the basic design expands both options. For this purpose, the first documents required are a technical manual and the conceptual project document. The Basic Design phase builds upon the Concept Design phase, focusing on optimizing the design and providing more detail to allow final specifications for the Detailed Design phase. According to International Atomic Energy Agency (1990), the plant layout is performed within the scope of the basic design. In addition, the chemical process, list of plant operations, and piping were considered in this Chapter. Per the recommendations for the basic design phase outlined by the International Atomic Energy Agency (1990), it was anticipated that the project risk would be decreased by the following actions being achieved in the Basic Design phase:

- Tightening the project scope.
- Identifying all major equipment.
- Enacting preliminary safety and operations reviews.

### **5.2 Conceptual Process Sequence**

Based on the optimization study of the laboratory-scale CNC production process conducted and reported in Chapter 3 and the review of CNC production process technologies reported in Chapter 2, the conceptual process sequence was proposed.



### ***5.2.1 Phase 1: Sawdust de-lignification***

- Stoichiometric quantities of sawdust, APS solids, and hot water are added into the de-lignification reactor. In less advanced configurations, this is done manually. In advanced configurations, conveyor mechanisms and pumps are used and interlocked with level/volume/mass control.
- The stirrer is started, and the reaction is run for 6 hours at 60 °C.
- The sawdust pulp is pumped out of the de-lignification reactor into a separation unit. The solids (comprising the de-lignified sawdust pulp) are separated from the spent APS solution.
- The de-lignification reactor is rinsed and kept in readiness for the next batch operation. In more advanced configurations, the rinsing mechanism is controlled with a pH transmitter which stops the rinse procedure once a neutral pH is achieved (signaling that all the APS chemical has been washed out of the vessel).
- The spent APS solution is sent to APS recovery, while the sawdust pulp is temporarily stored to be transferred into the hydrolysis reactor. In more advanced configurations, the sawdust pulp is conveyed directly into the hydrolysis reactor after forming the acidic solution in the reactor.

### ***5.2.2 Phase 2: Acid Hydrolysis of Sawdust Pulp***

- Stoichiometric quantities of water and concentrated sulphuric acid are added into the glass-lined reactor and briefly agitated to form a uniform acidic solution. This action can be manually undertaken in less advanced configurations. However, in more advanced configurations, the transfer mechanisms (pump or conveyor) are done by level/volume/mass control.
- A corresponding stoichiometric quantity of sawdust pulp is then added into the reactor and hydrolyzed for one to two hours. During this time, the reactor is maintained at 45 °C.
- The hydrolysis reaction is quenched by pumping a predetermined volume of water into the reactor. This action is done manually using a portable pump and physical observation of the rising water level using a watch glass/panel integrated into the reactor in less advanced configurations. In more advanced configurations, this action is done by level control.

- In less advanced configurations, the reactor contents are settled. The vertical observation pane is used in the initial stages to monitor the settling of the colloidal CNC suspension. Once adequate settling has occurred, the CNC suspension is gravity-drained into the CNC recirculation tank using a flexible hose. In more advanced configurations, the CNC is separated from the spent acid using a separation unit.
- The hydrolysis reactor is rinsed with a basic solution, washed, and kept in readiness to process the next batch of sawdust pulp.
- The spent acid is transferred into the adsorption tank for recovery, while the CNC is transferred into the recirculation tank for final treatment.

### ***5.2.3 Phase 3: Final Treatment of the CNC Product***

- The CNC suspension is neutralized with sodium hydroxide. In less advanced configurations, jar tests are used to ascertain the optimal quantity and concentration of caustic to be dosed. In more advanced configurations, the dosing is interlocked with pH monitoring and control.
- The CNC suspension is then pumped through a VoDCa device in the recirculation loop to disintegrate the nanoparticles in the suspension, thereby yielding a gel-like texture. It is also pumped through a 20-micron tangential flow filtration (TFF) module to remove the salts from the final CNC product. In advanced configurations, the final treatment step is done using pH, viscosity, and salinity control.

Graphic descriptions of the process phases can be viewed in the process flow diagrams in Appendix A. The list of plant operations is shown in Table 5.1.

### 5.3 List of Plant Operations

**Table 5.1. Basic Design- List of Plant Operations**

<b>Batch Phase</b>	<b>Description</b>	<b>Unit Operations</b>	<b>Purpose</b>	<b>Associated Control Instruments</b>
1	Sawdust De-lignification	APS solids conveyor into the reactor	Reactant insertion into the reactor	Mass controller
		Sawdust pneumatic conveyor into the reactor	Raw material insertion into the reactor	Mass controller
		Water pump into the reactor	Reactant insertion into the reactor	Level/volume controller
		Water heater	Intensification of the de-lignification reaction	Temperature controller
		De-lignification reactor	Facilitation of the de-lignification reaction	Timer
		Reactor stirrer	Agitation of the reactor contents and ensure uniform reaction mechanisms	Timer
		Reactor jacket	Insulation and maintenance of the optimal reactor temperature (60°C)	Temperature controller
		Separator	Separation of the solid and liquid fractions (sawdust pulp and spent APS, respectively) at the end of the reaction	Timer
		Associated piping	Transfer of reactants and products into and out of the reactor	Actuated/solenoid valves linked to PLC
		Reactor rinse ball/nozzles	Post-reaction reactor rinse	pH controller

2.A	Sawdust Pulp Hydrolysis	Hydrolysis glass-lined reactor	Facilitation of the hydrolysis reaction	Timer
		Reactor stirrer	Agitation of the reactor contents and ensure uniform reaction mechanisms	Timer
		Reactor jacket	Insulation and maintenance of the optimal reactor temperature (40°C)	Temperature controller
		Sawdust pulp conveyor into the reactor	Reactant insertion into the reactor	Mass controller
		Concentrated acid pump into the reactor	Reactant insertion into the reactor	Level/volume controller
		Water pump into the reactor	Reactant insertion into the reactor	Level/volume controller
		Associated piping	Transfer of reactants and products into and out of the reactor	Actuated/solenoid valves linked to PLC
		Reactor rinse ball/nozzles	Post-reaction reactor rinse	pH controller
2.B	Spent Acid Recovery	Activated carbon pneumatic conveyors	Transfer of activated carbon between related vessels comprising the acid recovery phase	Load cell/ mass controller
		Adsorption reactor	Contains the adsorption reaction between the spent acid and activated carbon, resulting in recovered acid	<ul style="list-style-type: none"> <li>• Timer</li> <li>• Actuated/solenoid valves</li> </ul>
		Adsorption reactor agitator	Imposes turbulence required for effective adsorption	Timer
		Adsorption reactor rinse balls/ nozzles	Rinse of reactor internal after the reaction takes place	pH transmitter

		Separation unit	Separation of the recovered acid from the spent activated carbon	Timer
		Recovered acid vessel	Contains the recovered acid from the recovery process	
		Activated carbon wash vessel	Regeneration of the spent activated carbon	<ul style="list-style-type: none"> <li>• Timer</li> <li>• Actuated/solenoid valves</li> </ul>
		Activated carbon vessel wash heating elements	Drying of regenerated activated carbon	<ul style="list-style-type: none"> <li>• Timer</li> <li>• Thermostat</li> </ul>
		Activated carbon wash vessel agitator	Imposes turbulence required for the effective washing operation	Timer
		Related pumps and actuated valves	Transfer of acid (spent and recovered) between related vessels comprising the recovery phase	
3	CNC Final Treatment	Recirculation tank	Holding tank for final treatment of CNC product	
		VoDCa device	Homogenization/emulsification of CNC product	
		Ultrafiltration membrane	Salts removal from CNC product	Differential pressure controller
		Recirculation pump	Transport of CNC product through the final treatment loop	Salinity controller Viscosity controller

				pH controller
		Associated piping	Transfer of CNC product through the final treatment loop	Actuated/solenoid valves linked to PLC
		Recirculation tank rinse	Post-treatment rinse of the recirculation loop	pH controller

#### 5.4 Mass Balance Calculations

Based on the sawdust composition, sawdust morphology, and CNC suspension properties calculated in Section 4.9 of the Concept Design Chapter, the CNC mass production scales correspond to the volume production scales outlined in Table 5.2 below.

**Table 5.2. Basic Design- Mass and volume production capacities**

Mass production rate (kg/day)	Volume production rate (L/day)
1	0.77
10	7.69
1000	769

The sample calculation outlined in Table 5.3 below is based on the 1000 kg/day production scale.

**Table 5.3. Basic design- Mass balance**

<b>Parameter</b>	<b>Value</b>	<b>Unit</b>	<b>Comment</b>
Ratio of sawdust to CNC suspension (mass basis)	1:2.29	-	1 kg of sawdust was found to produce 2.29 kg of CNC suspension (10% concentration) in the laboratory trial studies
Sawdust required for 1000 kg/day CNC suspension	436.7	kg	Based on the above ratio and specified product mass (1000 kg/day)
Lignin contained in the above sawdust	113.6	kg	Based on average weighted sawdust composition (Table 30)
Post-delignification sawdust (pulp) mass	323.1	kg	Assuming 100% lignin removal
Sawdust pulp lost in transfer and filtration steps	10	%	Assumed
Sawdust pulp after losses	290.7	kg	
Hemicellulose contained in the above sawdust pulp	110.2	kg	Based on average weighted sawdust composition (Table 30)
Cellulose contained in the above sawdust pulp	180.5	kg	Based on average weighted sawdust composition (Table 30) Contains both amorphous and crystalline domains as per morphological composition (Table 31)
Crystalline cellulose contained in the above sawdust pulp	126.3	kg	Based on cellulose morphological content (Table 31)

Post-hydrolysis CNC volume	97.2	L	Based on CNC mass and density Comprises 10% of the CNC suspension- the rest is 90% water which is added to create the 10% suspension
Water fraction for dilution	90	%	
Water volume for dilution	874.6	L	Based on the above fraction
Water mass for dilution	874.6	kg	
CNC suspension mass	1000.1	kg	Sum of mass of dilution water and crystalline cellulose (post-hydrolysis)

The de-lignification stoichiometry calculations in Table 5.4 below are based on the 1000 kg/day CNC production scale.

**Table 5.4. Basic design- de-lignification stoichiometry**

Parameter	Value	Unit	Comment
Ratio of sawdust to APS (mass to volume basis)	1:10	g: mL	Based on preliminary laboratory trial studies
Sawdust to be used	436.7	kg	Based on Mass Balance (Table 34) above
APS solution required	4366.8	L	Based on the above ratio
APS solution concentration	3	M (mol/L)	Based on preliminary laboratory trial studies
APS molar mass	228.2	g/mol	Reference: <a href="https://pubchem.ncbi.nlm.nih.gov/compound/Ammonium-persulfate">https://pubchem.ncbi.nlm.nih.gov/compound/Ammonium-persulfate</a>
APS mass/liter of solution	684.6	g/L	Quotient of APS mass and volume



APS mass required for 1000 kg/day production	2989.4	kg	Based on the above quotient
Sawdust density (lower limit)	288	kg/m <sup>3</sup>	Reference: <a href="http://www.anval.net/downloads/bulk%20density%20chart.pdf">http://www.anval.net/downloads/bulk%20density%20chart.pdf</a>
Sawdust density (upper limit)	400	kg/m <sup>3</sup>	
Sawdust density (average)	344	kg/m <sup>3</sup>	Average of the lower and upper sawdust density limits
Sawdust volume	1,269.4	L	Based on sawdust mass and density
Total volume (sawdust and APS solution)	5,636.2	L	Dictates the size of the de-lignification reactor

Based on the above calculations, the CNC mass production scales correspond to the de-lignification reactor sizes shown in Table 5.5.

**Table 5.5. Basic design- relation between mass production rate and de-lignification reactor size**

Mass production rate (kg/day)	De-lignification reactor size (L)
1	5.6
10	56.3
1000	5636.2

The hydrolysis stoichiometry calculations in Table 5.6 below are based on the 1000 kg/day CNC production scale.

**Table 5.6. Basic design- Hydrolysis stoichiometry**

Parameter	Value	Unit	Comment
Ratio of sawdust to sulphuric acid (mass to volume basis)	1:15	g: mL	Based on preliminary laboratory trial studies
Sulphuric acid concentration	64	%	Based on preliminary laboratory trial studies
Sawdust to be used	436.7	kg	As per de-lignification stoichiometry (Table 5.4)
Sulphuric acid volume required	6550.2	L	Based on the sawdust: sulphuric acid ratio
Sulphuric acid density (64%)	1542	kg/m <sup>3</sup>	Reference: <a href="https://wissen.science-and-fun.de/chemistry/chemistry/density-tables/density-of-sulfuric-acid-and-sulfur-trioxide/">https://wissen.science-and-fun.de/chemistry/chemistry/density-tables/density-of-sulfuric-acid-and-sulfur-trioxide/</a>
Sulphuric acid mass	10,100.4	kg	Based on sulphuric acid mass and density
Acid to quench water ratio	1: 10		Based on preliminary laboratory trial studies
Quench water required	65,502.2	L	Based on the above ratio
Total volume (acid and quench water)	72,197.8	L	Dictates the size of the hydrolysis reactor

Based on the above calculations, the CNC mass production scales correspond to the hydrolysis reactor sizes shown in Table 5.7 below.

**Table 5.7. Basic design- Relation between mass production rate and hydrolysis reactor size**

Mass production rate (kg/day)	Hydrolysis reactor size (L)
1	7.2
10	72.2
1000	72,197.8

Based on the above, the final treatment tank size calculations are shown in Table 5.8 below.

**Table 5.8. Basic design- Recirculation tank sizing**

Parameter	Value	Unit	Comment
Separation efficiency of spent acid from raw CNC	90	%	Assumed
Remaining raw CNC post-separation	87.5	L	Constitutes the 10% CNC of the final product suspension
Dilution water to be added	787.1	L	Constitutes the 90% water of the final product suspension
Total volume (CNC and water)	874.6	L	Sum of the water and CNC portions in the final product suspension
Safety (overflow) allowance in recirculation/final treatment tank	20	%	Typical safety allowance
Recirculation/ final treatment tank size	1049.5	L	Sum of CNC suspension constituents and specified overflow safety factor

Based on the above calculations, the CNC mass production scales correspond to the recirculation (final) treatment tank sizes shown in Table 5.9 below.

**Table 5.9. Recirculation tank sizes**

<b>Mass production rate (kg/day)</b>	<b>Recirculation/ final treatment tank size (L)</b>
1	1.1
10	10.5
1000	1049.5

A summary of the tank sizes for each production capacity is outlined in Table 5.10 below.

**Table 5.10. Basic Design- Tank size summary**

<b>CNC Production Capacity (kg/day)</b>	<b>Equipment</b>		
	<b>De-lignification Reactor (L)</b>	<b>Hydrolysis Reactor (L)</b>	<b>Final Treatment Tank (L)</b>
1	5.6	7.2	1.1
10	56.3	722	10.5
1000	5636.2	72,197.8	1049.5

## 5.5 Control and Instrumentation (C&I) Design

### 5.5.1 C&I Introduction

The plant is designed to be equipped with sensors that report their respective data to the Programmable Logic Controller (PLC). The PLC uses this information to make decisions to allow optimal functioning of the process. The PLC is the decision-maker and responds to the data inputs by transmitting signals to controllers to effect changes in the process parameters. The Human Machine Interface (HMI) shows the changes in real-time and primarily aids the Plant Operator (PO) in understanding the status of the process (running, paused, complete, and error). The set of instructions outlined below forms a program that is to be coded into the PLC.

### 5.5.2 C&I Description

A detailed description of the C&I design (comprised of the control components and operation sequence for each process phase) is outlined in Table 5.11 to Table 5.14 below.

#### 5.5.2.1 Part 1 (De-lignification of Sawdust)

**Table 5.11. Basic design- Process part 1 C&I**

Process Aspect	Control Components	Sequence of Operation
Transfer of moistened sawdust from the silo into the de-lignification reactor.	<ul style="list-style-type: none"><li>• De-lignification reactor load cell.</li><li>• Actuated valve (sawdust transfer line).</li><li>• Sawdust pneumatic conveyor.</li></ul>	<ul style="list-style-type: none"><li>• The PLC signals the inlet valve on the sawdust transfer line to the reactor to open.</li><li>• The PLC signals the pneumatic conveyor to transfer the moistened sawdust from the silo into the reactor at the start of the program.</li></ul>

		<ul style="list-style-type: none"> <li>• The load cell monitors and transmits the sawdust mass being deposited into the reactor to the PLC.</li> <li>• Once the required mass of sawdust is transferred, the PLC stops the sawdust conveyor.</li> <li>• The PLC signals the inlet valve on the sawdust transfer line to the reactor to close.</li> </ul>
APS transfer into the reactor.	<ul style="list-style-type: none"> <li>• De-lignification reactor load cell.</li> <li>• Actuated valve (APS transfer line).</li> <li>• APS screw/ bucket conveyor.</li> </ul>	<ul style="list-style-type: none"> <li>• The PLC signals the inlet valve on the APS transfer line to the reactor to open.</li> <li>• The PLC signals the APS conveyor to transfer the APS from the silo into the reactor.</li> <li>• The load cell monitors the mass of APS entering the reactor and transmits this information to the PLC (displayed on HMI).</li> <li>• Once the required combined mass of sawdust and APS is detected, the PLC signals the conveyor to stop.</li> <li>• The PLC signals the inlet valve on the APS transfer line to the reactor to close.</li> </ul>
Hot water transfer into the reactor.	<ul style="list-style-type: none"> <li>• De-lignification reactor level transmitter.</li> <li>• VSD pump (centrifugal).</li> <li>• Actuated valve.</li> <li>• Stirrer.</li> </ul>	<ul style="list-style-type: none"> <li>• The level transmitter continuously records the level of the de-lignification reactor as the hot water is filling it and transmits this information to the PLC.</li> <li>• Once the required water level is reached (corresponding to a predetermined volume), the PLC signals the hot water pump to stop.</li> </ul>

		<ul style="list-style-type: none"> <li>• The PLC signals the hot water actuated valve to close.</li> <li>• The PLC signals the reactor stirrer to begin agitating the contents.</li> </ul>
<p>De-lignification reactor</p> <ul style="list-style-type: none"> <li>• Includes vacuum breaker and pressure release valve (PRV).</li> <li>• Jacket comprised of fiberglass material or polyurethane sprayed into the jacket.</li> <li>• Hot water spiral inside the jacket (80 °C).</li> </ul>	<ul style="list-style-type: none"> <li>• Reactor timer.</li> <li>• Reactor agitator (comprised of electric motor and gearbox to drive the paddles. 960-1440 rpm motor with 20:1 gearbox ratio).</li> <li>• Reactor outlet actuated valve.</li> <li>• Level transmitter.</li> <li>• Differential pressure switch.</li> </ul>	<ul style="list-style-type: none"> <li>• The timer monitors the reaction time.</li> <li>• Begins timing once the agitator is activated.</li> <li>• PLC signals the stirrer to stop once the reaction time has elapsed.</li> <li>• PLC signals the reactor outlet valve to open.</li> <li>• PLC signals the outlet pump to start pumping the contents to the centrifuge.</li> <li>• The level transmitter monitors the decreasing reactor level and relays this information to the PLC.</li> <li>• Based on the above, the PLC stops the outlet pump once the reactor level is close to zero to prevent cavitation.</li> <li>• Transmits signal to the agitator to stop once the designated reaction time has elapsed.</li> </ul>
Rinse of de-lignification reactor.	<ul style="list-style-type: none"> <li>• Rinse outlet actuated valve.</li> <li>• Spray nozzles/ ball.</li> <li>• pH transmitter.</li> </ul>	<ul style="list-style-type: none"> <li>• The PLC signals the rinse outlet valve to open.</li> <li>• The PLC signals the nozzles to start rinsing the reactor.</li> <li>• The pH transmitter records and transmits the pH of the outflowing rinse effluent to the PLC (displayed on HMI).</li> <li>• Once the pH is within the acceptable range (close to neutral), the PLC signals the rinse nozzles/ ball to stop.</li> </ul>

		<ul style="list-style-type: none"> <li>• The PLC signals the outlet valve to close.</li> </ul>
<p>Separation unit</p> <ul style="list-style-type: none"> <li>• Rotating filter with scraper (solid-liquid scraper) operated under vacuum.</li> <li>• Equipped with a manual cleaning device (high-pressure hose).</li> </ul>	<ul style="list-style-type: none"> <li>• Separation unit.</li> <li>• Timer.</li> <li>• Separation unit outlet fluid valve (actuated).</li> </ul>	<ul style="list-style-type: none"> <li>• The PLC signals the start of the separation unit.</li> <li>• The timer begins to record and display the separation time to the HMI.</li> <li>• Once the desired time has elapsed, the PLC signals the centrifuge to stop.</li> <li>• The PLC signals the fluid outlet valve to open, through which the spent APS solution is drained into the APS recovery system.</li> <li>• The PLC signals a display on the HMI for PO intervention to remove the sawdust pulp (solid fraction) from the separation unit.</li> <li>• PO signals to the PLC once the pulp has been removed via the HMI.</li> <li>• The PLC then signals the rinse nozzles/ ball to start the rinse process.</li> </ul>
Separation unit rinse	<ul style="list-style-type: none"> <li>• Rinse water outlet valve (actuated).</li> <li>• pH transmitter.</li> <li>• Rinse nozzles.</li> </ul>	<ul style="list-style-type: none"> <li>• The PLC signals the rinse outlet valve to open.</li> <li>• The PLC signals the rinse nozzles/ ball to start rinsing the centrifuge.</li> <li>• The pH transmitter records and transmits the pH of the outflowing rinse effluent to the PLC (displayed on HMI).</li> <li>• Once the pH is within the acceptable range (close to neutral), the PLC signals the rinse nozzles to stop.</li> <li>• The PLC signals the outlet valve to close.</li> </ul>



### 5.5.5.2 Part 2.A (Hydrolysis of Sawdust Pulp)

**Table 5.12. Basic design- Process part 2 A C&I**

Process Aspect	Control Components	Mode of Operation
Sawdust pulp transfer to the hydrolysis reactor.	<ul style="list-style-type: none"> <li>• Bucket conveyor/ Archimedes screw (depending on moisture content).</li> <li>• Reactor load cell.</li> </ul>	<ul style="list-style-type: none"> <li>• The PLC signals the hydrolysis reactor sawdust pulp inlet valve to open.</li> <li>• The PLC signals the sawdust pulp conveyor to start.</li> <li>• The load cell monitors the mass of the sawdust pulp being deposited into the reactor and displays this information on the HMI.</li> <li>• Once the desired stoichiometric quantity of pulp has been reached, the PLC signals the conveyor to stop.</li> </ul>
Hot water transfer to the hydrolysis reactor.	<ul style="list-style-type: none"> <li>• Hot water outlet valve (actuated).</li> <li>• Hot water outlet pump.</li> <li>• Hydrolysis reactor level transmitter.</li> </ul>	<ul style="list-style-type: none"> <li>• The PLC signals the hot water outlet valve (actuated) to open.</li> <li>• The PLC signals the hot water outlet pump to pump the hot water into the hydrolysis reactor.</li> <li>• The hydrolysis reactor level transmitter continuously records the hot water filling it and sends a signal to the PLC. This level is also signalled on the HMI.</li> <li>• Once the predetermined level (hot water volume) has been reached, the PLC stops the hot water outlet pump.</li> <li>• The PLC signals the hot water outlet valve (actuated) to close.</li> </ul>
Sulphuric acid dosing.	<ul style="list-style-type: none"> <li>• Hydrolysis reactor level transmitter.</li> </ul>	<ul style="list-style-type: none"> <li>• The PLC signals the sulphuric acid outlet valve (actuated) to open.</li> </ul>

	<ul style="list-style-type: none"> <li>• Sulphuric acid dosing pump.</li> <li>• Sulphuric acid dosing line valve (actuated).</li> </ul>	<ul style="list-style-type: none"> <li>• The PLC signals the sulphuric acid dosing pump to pump the acid into the hydrolysis reactor.</li> <li>• The hydrolysis reactor level transmitter continuously measures the combined hot water and sulphuric acid level in the reactor and transmits this signal to the PLC. This level is also signalled on the HMI.</li> <li>• Once the predetermined combined level (hot water volume) has been reached, the PLC stops the sulphuric acid dosing pump. The combined volume of acid and water is fixed to achieve a 64 weight % acid concentration.</li> <li>• The PLC signals the hot water outlet valve (actuated) to close.</li> </ul>
Hydrolysis reactor.	<ul style="list-style-type: none"> <li>• Reactor agitator (comprised of electric motor and gearbox to drive the paddles. 960-1440 rpm motor with 20:1 gearbox ratio).</li> <li>• Timer.</li> <li>• Water storage outlet valve (actuated).</li> <li>• Water storage pump (centrifugal).</li> <li>• Rinse nozzles/ ball.</li> </ul>	<p><b>Reaction sequence:</b></p> <ul style="list-style-type: none"> <li>• The PLC signals the agitator to start stirring the tank contents.</li> <li>• The PLC signals the timer to start recording the reaction time and display this information on the HMI.</li> <li>• Once the reaction time has elapsed, the PLC signals the agitator to stop.</li> <li>• The PLC signals the water storage outlet valve to open.</li> <li>• The PLC signals the water storage pump to start pumping the quench water into the reactor.</li> </ul>

	<ul style="list-style-type: none"> <li>• Rinse outlet valve.</li> <li>• pH transmitter.</li> </ul>	<ul style="list-style-type: none"> <li>• The level transmitter monitors the level of the quench water filling up the reactor. It relays this information to the PLC and displays this as % reactor volume on the HMI.</li> <li>• Once the desired quench volume has been attained, the PLC signals the water storage pump to stop.</li> <li>• The PLC signals the water storage outlet valve to close.</li> </ul> <p><b>Reactor emptying sequence:</b></p> <ul style="list-style-type: none"> <li>• The PLC signals the reactor outlet valve (actuated) to open.</li> <li>• The PLC signals the reactor outlet pump to pump out the reactor contents into the centrifuge.</li> <li>• The level transmitter relays the decreasing reactor level to the HMI and the PLC.</li> <li>• Once the reactor level is zero, the PLC signals the outlet pump to stop.</li> <li>• The PLC signals the reactor outlet valve (actuated) to close.</li> </ul> <p><b>Rinse sequence:</b></p> <ul style="list-style-type: none"> <li>• The PLC signals the reactor rinse outlet valve to open.</li> <li>• The PLC signals the nozzles/ ball to start rinsing the reactor internal.</li> </ul>
--	--	--

		<ul style="list-style-type: none"> <li>• The pH transmitter monitors the pH of the outflowing rinse stream and relays this information to the HMI and PLC.</li> <li>• Once the outflowing pH is within the acceptable range considered neutral, the PLC signals the rinse nozzles to stop.</li> <li>• The PLC signals the rinse outlet valve to close.</li> </ul>
<p>Separation unit</p> <ul style="list-style-type: none"> <li>• Rotating filter with scraper (solid-liquid scraper) operated under vacuum.</li> <li>• Nylon/ Rayon/ Polyethylene filter fabric can be used (acid resistant).</li> <li>• Equipped with a manual cleaning device (high-pressure hose).</li> </ul>	<ul style="list-style-type: none"> <li>• Hydrolysis reactor level transmitter.</li> <li>• Actuated open/close valve (inlet = reactor outlet).</li> <li>• VSD pump (positive displacement).</li> <li>• HP pump VSD controller.</li> <li>• Timer.</li> </ul>	<p><b>Separation operation sequence:</b></p> <ul style="list-style-type: none"> <li>• The PLC signals the separation unit to begin the separation operation.</li> <li>• The separation unit sends a signal to the PLC and HMI once the separation has been complete (and operation has been stopped).</li> </ul> <p><b>Fluid removal sequence (to remove the spent acid and transfer it into the acid recovery system):</b></p> <ul style="list-style-type: none"> <li>• The PLC signals the separation unit fluid outlet valve to open.</li> <li>• The PLC signals the separation unit fluid outlet pump to start pumping out the spent acid into the recovery system.</li> <li>• The separation unit fluid detector signals to the PLC when the spent acid has been removed.</li> <li>• The PLC signals the separation unit fluid outlet pump to stop.</li> <li>• The PLC signals the separation unit fluid outlet valve to stop.</li> </ul>

		<p><b>Solids removal sequence (to remove and transfer the raw CNC from the separation unit to the CNC purification system):</b></p> <ul style="list-style-type: none"> <li>• The PLC signals the separation unit solids (sludge) outlet valve to open.</li> <li>• The sludge can either be removed by a mono pump (progressing cavity pump) or discharged through gravity into the CNC recirculation tank (depending on the elevation and position of the centrifuge).</li> <li>• These operations are linked to the PLC.</li> </ul>
--	--	--

#### 5.5.2.3 Part 2.B (Spent Acid Recovery)

**Table 5.13. Basic design- Process part 2B C&I**

<b>Process Aspect</b>	<b>Control Components</b>	<b>Sequence of Operation</b>
Activated carbon (AC) transfer to the adsorption reactor.	<ul style="list-style-type: none"> <li>• Pneumatic conveyor.</li> <li>• Adsorption reactor load cell.</li> </ul>	<ul style="list-style-type: none"> <li>• The PLC signals the pneumatic conveyor to transfer AC into the adsorption reactor.</li> <li>• The load cell monitors the mass of the AC entering the reactor and transmits this information to the HMI.</li> <li>• Once the required mass of AC has been reached, the PLC signals the conveyor to stop.</li> </ul>
Spent acid transfer to the adsorption reactor.	<ul style="list-style-type: none"> <li>• Spent acid transfer line actuated valve.</li> </ul>	<ul style="list-style-type: none"> <li>• The PLC signals the actuated valve on the spent acid transfer line to open position.</li> </ul>

	<ul style="list-style-type: none"> <li>Spent acid transfer line to adsorption reactor.</li> <li>Acid transfer pump.</li> <li>Level indicator.</li> </ul>	<ul style="list-style-type: none"> <li>The PLC signals the acid transfer pump to start pumping the spent acid from the hydrolysis vessel into the adsorption reactor.</li> <li>The level indicator monitors the volume of spent acid entering the adsorption reactor and transmits this information to the HMI.</li> <li>The PLC stops the acid transfer once the required volume of acid has been achieved.</li> <li>The PLC signals the actuated valve on the spent acid transfer line to close position.</li> </ul>
Adsorption reaction.	<ul style="list-style-type: none"> <li>Reactor agitator (comprised of electric motor and gearbox to drive the paddles. 960-1440 rpm motor with 20:1 gearbox ratio).</li> <li>Timer.</li> </ul>	<ul style="list-style-type: none"> <li>The PLC signals the agitator to start stirring the tank contents.</li> <li>The PLC signals the timer to start recording the reaction time and display this information on the HMI.</li> <li>Once the reaction time has elapsed, the PLC signals the agitator to stop.</li> </ul>
Acid-AC slurry transfer to the separation unit.	<ul style="list-style-type: none"> <li>Reactor outlet valve.</li> <li>Reactor outlet pump.</li> <li>Level transmitter.</li> </ul>	<ul style="list-style-type: none"> <li>The PLC signals the reactor outlet valve (actuated) to open.</li> <li>The PLC signals the reactor outlet pump to pump out the reactor contents into the separation vessel.</li> <li>The level transmitter relays the decreasing reactor level to the HMI and the PLC.</li> <li>Once the reactor level is zero, the PLC signals the outlet pump to stop.</li> <li>The PLC signals the reactor outlet valve (actuated) to close.</li> </ul>

Adsorption reactor rinse.	<ul style="list-style-type: none"> <li>• Reactor rinse outlet valve.</li> <li>• Rinse nozzles/ ball.</li> <li>• pH transmitter.</li> </ul>	<ul style="list-style-type: none"> <li>• The PLC signals the reactor rinse outlet valve to open.</li> <li>• The PLC signals the nozzles/ ball to start rinsing the reactor internal.</li> <li>• The pH transmitter monitors the pH of the outflowing rinse stream and relays this information to the HMI and PLC.</li> <li>• Once the outflowing pH is within the acceptable range considered neutral, the PLC signals the rinse nozzles to stop.</li> <li>• The PLC signals the rinse outlet valve to close.</li> </ul>
Separation.	<ul style="list-style-type: none"> <li>• Timer.</li> <li>• Separation vessel.</li> </ul>	<ul style="list-style-type: none"> <li>• The PLC signals the separation unit to begin operation.</li> <li>• The timer monitors the time and transmits this information to the PLC and HMI.</li> <li>• Once the desired time frame has elapsed, the PLC signals the separation operation to stop.</li> </ul>
Recovered acid transfer to the recovered acid vessel.	<ul style="list-style-type: none"> <li>• Recovered acid transfer line actuated valve.</li> <li>• Recovered acid transfer line to the recovered acid vessel.</li> <li>• Acid transfer pump.</li> <li>• Level indicator.</li> </ul>	<ul style="list-style-type: none"> <li>• The PLC signals the actuated valve on the recovered acid transfer line to open position.</li> <li>• The PLC signals the acid transfer pump to start pumping the recovered acid from the separation vessel into the recovered acid vessel.</li> <li>• The level indicator monitors the volume of recovered acid being pumped from the separation vessel to the recovered acid vessel and transmits this information to the HMI.</li> </ul>

		<ul style="list-style-type: none"> <li>• The PLC stops the acid transfer once all the recovered acid has been pumped to the recovered acid vessel.</li> <li>• The PLC signals the actuated valve on the recovered acid transfer line to close position.</li> </ul>
Spent AC transfer to AC washing vessel.	<ul style="list-style-type: none"> <li>• Pneumatic conveyor from separation unit to spent AC washing vessel.</li> <li>• Spent AC washing vessel.</li> <li>• Load cell in separation unit.</li> </ul>	<ul style="list-style-type: none"> <li>• The PLC signals the pneumatic conveyor to transfer spent AC into the spent AC washing vessel.</li> <li>• The load cell monitors the mass of the spent AC being removed from the separation unit and transmits this information to the HMI.</li> <li>• Once the spent AC has been removed from the separation unit, the PLC signals the conveyor to stop.</li> </ul>
Separation vessel rinse.	<ul style="list-style-type: none"> <li>• Separation vessel rinse outlet valve.</li> <li>• Rinse nozzles/ ball.</li> <li>• pH transmitter.</li> </ul>	<ul style="list-style-type: none"> <li>• The PLC signals the separation vessel rinse outlet valve to open.</li> <li>• The PLC signals the nozzles/ ball to start rinsing the separation vessel internal.</li> <li>• The pH transmitter monitors the pH of the outflowing rinse stream and relays this information to the HMI and PLC.</li> <li>• Once the outflowing pH is within the acceptable range considered neutral, the PLC signals the rinse nozzles to stop.</li> <li>• The PLC signals the rinse outlet valve to close.</li> </ul>
AC wash.	<ul style="list-style-type: none"> <li>• AC wash vessel inlet actuated valve.</li> <li>• Wash water inlet pump.</li> </ul>	<ul style="list-style-type: none"> <li>• The PLC signals the wash vessel inlet valve (actuated) to open.</li> <li>• The PLC signals the wash water pump to begin pumping the water into the wash vessel.</li> </ul>



	<ul style="list-style-type: none"> <li>• Level indicator.</li> <li>• Wash agitator (comprised of electric motor and gearbox to drive the paddles. 960-1440 rpm motor with 20:1 gearbox ratio).</li> <li>• Timer.</li> </ul>	<ul style="list-style-type: none"> <li>• The level indicator monitors the volume of wash water into the wash vessel and transmits this information to the HMI and PLC.</li> <li>• Once the required volume of wash water is achieved in the wash vessel, the PLC signals the pump to stop.</li> <li>• The PLC signals the wash water inlet actuated valve to close.</li> <li>• The PLC signals the agitator to begin.</li> <li>• The timer monitors the agitation (wash) time and displays this information on the HMI.</li> <li>• Once the required wash time has elapsed, the PLC signals the agitator to stop.</li> </ul>
Wash vessel drained.	<ul style="list-style-type: none"> <li>• Wash vessel drain valve (actuated).</li> <li>• Level indicator.</li> <li>• Timer.</li> <li>• Drain sieve.</li> </ul>	<ul style="list-style-type: none"> <li>• Once the desired wash time has been reached, the PLC signals the wash drain valve to open.</li> <li>• The level indicator monitors the decreasing wash vessel level (volume).</li> <li>• Once the wash vessel has been completely drained, the PLC signals the drain valve to close.</li> <li>• The drain is fitted with a suitably sized sieve to ensure that no washed AC escapes through the drain valve.</li> </ul>
AC drying operation.	<ul style="list-style-type: none"> <li>• Heating elements in wash vessel.</li> <li>• Thermostat.</li> </ul>	<ul style="list-style-type: none"> <li>• Once the wash vessel has been drained, the PLC signals the heating elements to begin heating the vessel.</li> <li>• The thermostat monitors the internal temperature and displays this information on the HMI.</li> </ul>

	<ul style="list-style-type: none"> <li>• Timer.</li> </ul>	<ul style="list-style-type: none"> <li>• The PLC uses the thermostat readings to adjust the power input to the heating elements to maintain the desired temperature range inside the wash vessel.</li> <li>• The timer monitors the time and displays this on the HMI.</li> <li>• Once the required heating time has elapsed, the PLC signals the heating elements to stop.</li> </ul>
Dried AC transfer to AC storage vessel.	<ul style="list-style-type: none"> <li>• Pneumatic conveyor from wash vessel to recovered AC storage vessel.</li> <li>• Load cell in wash vessel.</li> </ul>	<ul style="list-style-type: none"> <li>• The PLC signals the pneumatic conveyor to transfer the recovered AC into the AC storage vessel.</li> <li>• The load cell monitors the mass of the recovered AC being removed from the wash vessel and transmits this information to the HMI.</li> <li>• Once the recovered AC has been removed from the wash vessel, the PLC signals the conveyor to stop.</li> </ul>

#### 5.5.2.4 Part 3 (CNC Purification)

**Table 5.14. Basic design- Process part 3 C&I**

<b>Process Aspect</b>	<b>Control Components</b>	<b>Mode of Operation</b>
Water transfer into the recirculation tank.	<ul style="list-style-type: none"> <li>• Hydrolysis reactor level transmitter.</li> <li>• Actuated valve on water tank outlet line.</li> <li>• VSD water tank outlet pump.</li> </ul>	<ul style="list-style-type: none"> <li>• The PLC signals the water outlet valve to open.</li> <li>• The PLC signals the water transfer pump to start pumping the water into the CNC recirculation tank.</li> </ul>

		<ul style="list-style-type: none"> <li>• The level transmitter continuously monitors the fluid level in the tank (corresponds to a volume of fluid) and transmits this information to the PLC. This level is also displayed on the HMI as % tank volume.</li> <li>• The PLC stop the water pump once the desired volume of water is transferred into the recirculation tank.</li> <li>• The PLC signals the water tank outlet valve to close.</li> </ul>
NaOH dosing into the recirculation tank (neutralization).	<ul style="list-style-type: none"> <li>• NaOH dosing tank outlet actuated valve.</li> <li>• NaOH dosing tank positive displacement pump.</li> <li>• Recirculation tank pH transmitter.</li> <li>• Overhead Stirrer.</li> </ul>	<ul style="list-style-type: none"> <li>• The PLC signals the NaOH dosing tank outlet valve to open.</li> <li>• The PLC signals the NaOH dosing tank outlet pump to start pumping NaOH into the recirculation tank.</li> <li>• The PLC signals the recirculation tank stirrer/agitator to start agitating the mixture for homogeneity.</li> <li>• The pH transmitter measures and transmits the pH signal to the PLC. This signal is also displayed on the HMI.</li> <li>• The PLC stops the NaOH dosing pump once a neutral pH has been achieved in the recirculation tank.</li> <li>• The PLC signals the NaOH dosing tank outlet valve to close.</li> <li>• The PLC signals the overhead stirrer to stop.</li> </ul>
CNC recirculation.	<ul style="list-style-type: none"> <li>• VoDCa outlet valve (actuated).</li> <li>• UF outlet valve (actuated).</li> <li>• Recirculation tank outlet pump.</li> </ul>	<ul style="list-style-type: none"> <li>• The PLC signals the VoDCa outlet valve to open.</li> <li>• The PLC signals the UF outlet valve to open.</li> </ul>

	<ul style="list-style-type: none"> <li>• Conductivity transmitter.</li> <li>• Viscosity transmitter.</li> <li>• UF Differential Pressure (DP) Transmitter.</li> </ul>	<ul style="list-style-type: none"> <li>• The PLC signals the recirculation tank outlet pump to start pumping the slurry through the recirculation loop.</li> <li>• The conductivity transmitter records the conductivity of the slurry passing through the loop and transmits this signal to the PLC. This conductivity is also displayed on the HMI.</li> <li>• The viscosity transmitter records the viscosity of the slurry passing through the loop and transmits this signal to the PLC. This viscosity is also displayed on the HMI.</li> <li>• Once the conductivity AND viscosity are located within the range of the CNC final product specification, the PLC signals the recirculation pump to stop once all the product is returned to the recirculation tank.</li> <li>• The differential pressure transmitter on the UF monitors the DP and transmits this signal to the PLC during forward operation. If the DP exceeds the allowable limit, the PLC signals the recirculation pump to stop and return the CNC slurry to the recirculation tank.</li> <li>• The PLC then signals the UF membrane backwash procedure.</li> <li>• Once the backwash has been performed, the PLC signals the recirculation pump to start to resume forward operation.</li> <li>• It is expected that the DP would decrease to acceptable limits following a backwash operation. However, if this is not the case, then the PLC re-</li> </ul>
--	---	--

		<p>signals a premature stop to the forward process and subsequent return of the CNC slurry to the recirculation tank.</p> <ul style="list-style-type: none"> <li>• The PLC then signals a Clean-in-Place (CIP) of the UF membrane.</li> <li>• Once the CIP is complete, the PLC signals the recirculation pump to start to resume forward operation.</li> </ul>
--	--	---

## 5.6 Electrical Design

It is recommended that the following considerations outlined in Table 5.15 be implemented within the Electrical Design.

**Table 5.15. Basic design- Electrical design considerations**

Parameter	Specifications
Junction Boxes	<ul style="list-style-type: none"> <li>• Minimum 3 mm marine-grade aluminium, 1.6 mm 316 stainless steel.</li> <li>• Minimum IP rating 56.</li> <li>• Stainless steel fasteners captive to the lid.</li> <li>• Separate junction boxes for each drive/equipment system.</li> <li>• Fix to the building structure at a height between 1.1 and 1.3 m.</li> <li>• Fit all doors with 316 stainless steel pentile hinges- minimum of 3 hinges if greater than 1.2 m height.</li> <li>• Secure doors with 316 stainless steel 8 mm solid square latches.</li> </ul>
Local Push Button Station	<ul style="list-style-type: none"> <li>• Local control stations must be installed to operate specific equipment or process phases.</li> <li>• The local control stations must have a start and stop push button mounted behind a locked door on an escutcheon.</li> </ul>

	<ul style="list-style-type: none"> <li>• Required on static bypass switch to automatically initiate the transfer from the inverter output to bypass supply and vice versa (if applicable).</li> </ul>
Motor Control Centre	<ul style="list-style-type: none"> <li>• Install inside enclosed buildings/switch rooms.</li> <li>• Standard voltage: 400 V AC, 3 phase + neutral + earth.</li> <li>• Earth via main switchboard.</li> </ul>
Power cables	<ul style="list-style-type: none"> <li>• Orange circular 0.6/1,0 kV with stranded copper conductors, X-90 XLPE, insulated and V-90 PVC sheath for multicore LV power cables.</li> <li>• Black circular 0.6/1.0 kV with stranded copper conductors, X-90 XLPE insulation, and V-90 PVC sheath for single-core LV power cables.</li> </ul>
Control cables	<ul style="list-style-type: none"> <li>• Black or orange circular, 0.6/1.0 kV multicore with stranded copper conductors, V-90 PVC insulation, and V-90 PVC sheath.</li> <li>• Multicore control cables must also include an insulated earth continuity conductor (stranded copper conductor with V-90 PVC insulation).</li> <li>• Must have minimum 3 spare control cores.</li> <li>• Digital and analogue signals must be separated into separate cables (wherever possible).</li> <li>• Globe electrical/ Indiana/ Metalemmms/ Kanade Udyo/ Profab/ Equivalent.</li> </ul>
Cable trays and conduits	<ul style="list-style-type: none"> <li>• Accommodate for 30% allowance for future cabling.</li> <li>• Fit with UV resistant cover.</li> <li>• Stainless steel cable ties to be used.</li> </ul>

	<ul style="list-style-type: none"> <li>• Maximum rung spacing of 300 mm, supported on SS or aluminium brackets bolted/clamped to structures with 316 stainless steel bolts.</li> <li>• NEMA 30C rated.</li> <li>• Mount to maintain 300 mm clearance between racks vertically and 150 mm under structural sections.</li> <li>• All expansion joints to be bonded to ensure continuity.</li> </ul>
Above-ground earthing	<ul style="list-style-type: none"> <li>• Per AS 3000:2007.</li> <li>• Each power correction unit to be fitted with a copper earth bar exceeding a 120 mm<sup>2</sup> section.</li> <li>• M10 earthing connection studs required.</li> </ul>

### 5.7 Plant Layout

Per the International Atomic Energy Agency (1990) recommendations, the plant equipment was distributed so that they can be assembled in small areas with sufficient space allowance for equipment operation. Furthermore, the following general considerations were applied: the unit operations were placed in the middle of the site, where production is predominant, and the reagent and raw material storage stations were located near the entrance (at the plant's boundary) for ease of access to suppliers. The plant layout in **Figure 5.1** depicts the floor plan of the proposed way the plant is laid out. The plant layout is colour-coded as explained below:

- The blue circles represent storage vessels.
- The orange transfer lines represent solids pneumatic conveying systems.
- The green lines represent liquid transfer pipes.
- The grey lines represent slurry transfer pipes.
- The rectangle blocks represent process units.

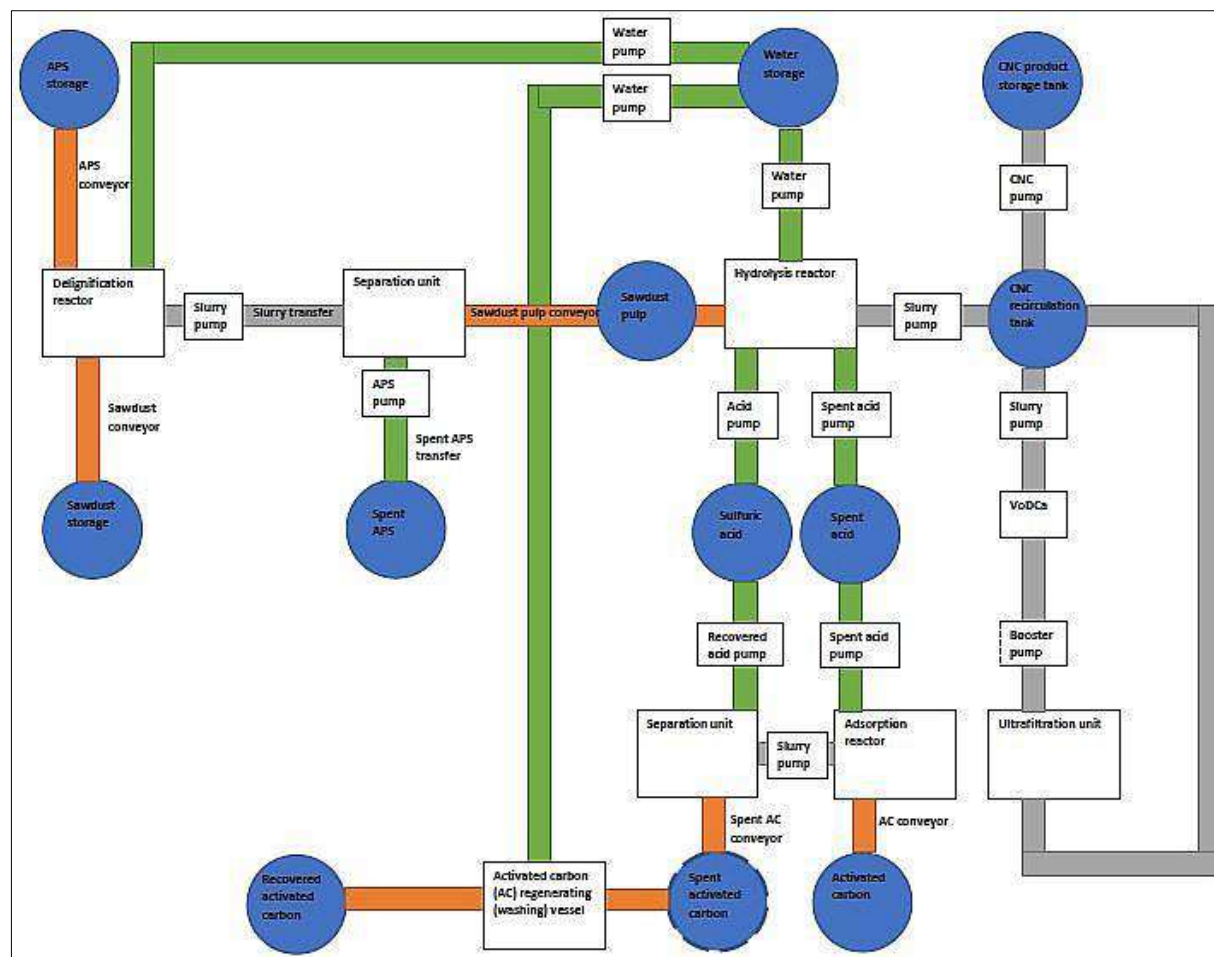


Figure 5.1. Basic design- Plant layout



## **5.8 Conclusions**

Per the recommendations outlined in Chapter 4, the optimal Concept design was expanded in this Chapter. Mass balances consider the physical behaviour of the process concerning inputs, outputs, generation, and accumulation. This process behaviour was used to predict the equipment sizes required in the up-scaled production capacities. In addition, considering that human actions are time-consuming and prone to error, the efficiency of a process is often linked to the lack of human intervention. Hence, the control strategies for each phase of the production process phases were outlined concerning the control components and sequence of operation.

Considering that the electrical design was not a core aim of this Chapter, a brief outline of the electrical design for the CNC production process was presented for the following parameters: junction boxes, local push button stations, motor control centers, power cables, control cables, cable trays and conduits, and above ground earthing. In addition, the considerations for the plant layout outlined in Section 5.7 were used to present the proposed layout. The basic design successfully expanded the optimal concept design, thus enabling the final phase of the process plant design trilogy- the detailed design outlined in the subsequent Chapter.

## **CHAPTER 6: DETAILED DESIGN**

### **6.1 Introduction**

The detailed design is the final stage of the design process, which builds upon the Basic Design and finalizes the pertinent design details. In this detailed design Chapter, the piping and process unit specifications across all three phases of the CNC production process were specified. In addition, according to the outcomes outlined by International Atomic Energy Agency (1990), the product and equipment catalogues from the Original Equipment Manufacturers (OEMs) were sourced and provided as addenda to this Chapter. As such, the scope of this detailed design entailed the following:

- Specifying the interconnecting piping across all process units in the overall CNC production process (from Phase 1 to 3).
- Piping and instrumentation diagrams (P&IDs).
- Selection of industrial process equipment based on specific process conditions. This equipment included:
  - Materials conveying equipment: pumps (liquids and slurries) and conveyors (solids).
  - Process vessels: tanks, storage silos, and reactors.
  - Agitation devices.
  - CIP mechanisms: rinse balls.
  - Solid-liquid separators.
  - Homogenization equipment.

### **6.2 Methodology**

The methodology outlined below was followed for the piping design:

1. The thermophysical properties of the fluids being piped were obtained (density and viscosity). These properties included properties for the process water, delignification slurry, and rinse water.
2. The pressure (head) of each stream was determined based on the Net Positive Suction Head Available (NPSHa).
3. The stream velocity for each stream was set at 1.5 m/s. This velocity is regarded as optimal to prevent water hammering associated with greater fluid velocities.

4. The length of each pipe was specified.
5. Based on the flow and pressure of the streams (Step 2), the process pumps were specified using the Grundfos online pump sizing tool in three steps:
  - Defining the application requirements.
  - Evaluating and comparing compliant pumps.
  - Selecting the optimal pump.

A screenshot depicting the online pump sizing tool is shown in **Figure 6.1** below.

As indicated in the Original Equipment Manufacturer Catalogue for the pumps (Appendix C), the materials of construction were selected to ensure resistance to the media to be pumped.

**Sizing**  
Enter pump sizing

**Catalog**  
Product and services

**Replacement**  
Replace an old pump with a new

**Liquids**  
Find liquid pump

Quick sizing
Advanced sizing by application
Guided selection

Flow (Q)\*
m³/h

Head (H)\*
m

Pump design\*

Circulator pumps  
Endsuction close coupled multistage  
Encapsulated pumps  
Submersible wastewater pumps  
Submersible groundwater pumps  
Immersible pumps  
Inline single stage pumps  
Inline multi stage pumps  
Booster set

Help me select

Expand all
Collapse all

Save sizing parameters
Load sizing parameters

Reset form to defaults

START SIZING

**Figure 6.1. Grundfos Online Pump Selection Tool (Grundfos Product Center, n.d.)**

107

The pump specifications dictated the required pipe diameters on the suction and discharge sides of the pump. For the interconnecting pipes that were not connected to pumps, the inner diameters were calculated as outlined below using the Darcy-Weisbach correlation (6.1) relating the pressure drop and diameter of cylindrical pipes:

$$d = 2f \times \left( \frac{l}{\Delta P} \right) \times \rho \times u^2 \quad (6.1)$$

The symbols of the equation are identified in Table 6.1 below.

**Table 6.1. Key to Darcy-Weisbach equation**

Symbol	Definition
d	Inner diameter
f	Friction factor- specific to pipe material
l	Pipe length
$\Delta P$	Pressure drop across the pipe length
$\rho$	Fluid density flowing through the pipe
u	Fluid velocity flowing through the pipe

The final stage involved matching the calculated inner diameter to the closest standard inner diameter. Standard pipe sizes with corresponding wall thicknesses were used to complete this step.

## 6.3 Results

### 6.3.1 Piping Design

The results of the piping design are shown in Table 6.2 below.

**Table 6.2. Piping Design Results**

Line	Description	Pressure (bar)	Density (kg/m <sup>3</sup> )	Viscosity (Pa.s)	Velocity (m/s)	Length (m)	DN (pumps)	Frictional Factor	Pressure Drop (bar)	ID (mm)	Standard ID (mm)
1	Sawdust	1.01									
2	APS	1.01									
3	Water heater inlet	4.65	1000	8.90E-04	1.5	1					
4	De-lignification water- suction	4.65	1000	8.90E-04	1.5	1	25/32				
5	De-lignification water- discharge	13.27	1000	8.90E-04	1.5	1	25/32				
6	De-lignification slurry- suction	2.23	1200	0.0011	1.5	1	32				
7	De-lignification slurry- discharge	13.27	1200	0.0011	1.5	1	32				

8	Centrifuge outlet-liquid stream	11.27	1000	0.0011	1.6	1.5		0.1	0.4	18.95	DN 20
9	Centrifuge outlet-solid stream	1.01	2000	0.0175		1					
10	Centrifuge rinse water-suction	4.65	1000	8.90E-04	1.5	1	25/32				
11	Centrifuge rinse water-discharge	13.27	1000	8.90E-04	1.5	1	25/32				

### 6.3.2 Equipment Selection

The equipment selection results are shown in Table 6.3 below.

**Table 6.3. Equipment Selection Results**

<b>Description</b>	<b>Qty</b>	<b>Make/Supplier</b>	<b>Model/Dimensions</b>	<b>Service</b>	<b>Materials of Construction/System Components</b>	<b>Process Fluid/Chemical</b>	<b>Design Temperature</b>	<b>Design Flowrate/Volume</b>	<b>Design Pressure</b>
Phase 1	De-lignification of Sawdust								
Sawdust storage silo	1	Jojo	Silo chemical storage tank	Sawdust storage	Virgin LLDPE	Sawdust	65 °C	0.2- 17 m <sup>3</sup> capacity	10 bar (maximum )
Sawdust storage silo stand	1	Jojo	Silo tank stand	Silo support	Steel				
APS storage silo	1	Jojo	Silo chemical storage tank	APS storage	Virgin LLDPE	APS	65 °C	0.2- 17 m <sup>3</sup> capacity	10 bar (maximum )
APS storage silo stand	1	Jojo	Silo tank stand	Silo support	Steel				



Sawdust conveyor	1	Busch	Pneumatic overpressure conveyor	Sawdust transfer	Mink claw and R 5 rotary vane vacuum pumps Samos side channel Tyr rotary lobe blowers	Sawdust		40- 1150 m <sup>3</sup> /h	2 barg overpressure
APS conveyor	1	Busch	Pneumatic overpressure conveyor	APS transfer	Mink claw and R 5 rotary vane vacuum pumps Samos side channel Tyr rotary lobe blowers	APS		40- 1150 m <sup>3</sup> /h	2 barg overpressure
Water storage tank/heater	1	Prestank	4 X 4 X 4 configuration	Water storage	Steel	Process Water		107.1 m <sup>3</sup>	
De-lignification water	2	Grundfos	Product number: 96084250	Water transfer	Cast iron base, stainless steel impeller	Process Water	(-20) to 120 °C	6.9 m <sup>3</sup> /h	13.27 bar discharge head

supply pump									
De-lignification reactor (stirred tank)	1	Buchiglasuster/ TaiJi	Glass-lined stirred tank reactor	De-lignification reaction	Borosilicate glass 3.3 Glass-lined steel PTFE/ PFA/ Tantalum	Sawdust-APS slurry/paste	-60 to 200 °C	0.25 to 10 m3 range 8 to 16 m3 range	-1 full vacuum to 0.5 bar
De-lignification slurry transfer pump	2	Grundfos	Product number: 96084096	De-lignification product transfer	Cast iron base, stainless steel impeller	Sawdust-APS slurry/paste	(-20) to 120 °C	6.9 m <sup>3</sup> /h	13.27 bar discharge head
De-lignification reactor rinse ball	1	Lechler	5B3.539.1Y.D5.20.0	Reactor rinse	316L SS	Water	200 °C (maximum)	49.26 m <sup>3</sup> /h	3 bar
De-lignification slurry separation unit	1	GEA Varipond Biosolids Decanter	Prime 4000	Slurry separation		Sawdust-APS slurry/paste		20 to 35 m3/h dewatering/thickening	

Separation unit rinse ball	1	Lechler	5B3.539.1Y.D5. 20.0	Separator rinse	316L SS	Water	200 °C (maximum)	49.26 m <sup>3</sup> /h	3 bar
Phase 2	Acid Hydrolysis of Sawdust Pulp								
Bulk acid storage tank	1	SG Plastic/ RotoTank	Product volume range: 0.5 to 40 m <sup>3</sup>	Acid storage	PP/HDPE/PVC/P VDF Thermoplastic sheeting Base: flat, sloped, or skirted Top: flat or conical	Sulphuric acid		Rototank: 0.5 to 40 m <sup>3</sup>	
Hydrolysis reactor (stirred, glass-lined)	1	Buchiglasuster/ Taiji	0,25 to 10 m <sup>3</sup> range 8 to 16 m <sup>3</sup> range	Hydrolysis of sawdust pulp	Borosilicate glass 3.3 Glass-lined steel PTFE/ PFA/ Tantalum	Sawdust pulp- sulphuric acid slurry	(-60) to 200 °C	0.25 to 10 m <sup>3</sup> range 8 to 16 m <sup>3</sup> range	(-1) Full Vacuum to 0.5 bar
Hydrolysis water	2	Grundfos	Product number: 96084250	Process water transfer to	Cast iron base, SS impeller	Process water	(-20) to 120 °C	6.9 m <sup>3</sup> /h	13.27 bar discharge head

supply pump				the hydrolysis reactor					
Sulphuric acid supply pump	2	March pumps	TE-5.5C-MD 1&3 Ph Mag Drive Pump	Concentrated acid transfer to the hydrolysis reactor	Propylene front and rear housing impeller Viton o-ring Ceramic shaft and thrust washers	Sulphuric acid		6.81 m <sup>3</sup> /h	12.67 bar discharge head
Hydrolysis slurry product transfer pump	2	Wilfley heavy duty centrifugal pumps	3X2-11 model	Transfer of reaction product to separation unit	Hard iron and stainless steel	Hydrolysis product slurry		600 m <sup>3</sup> /h (maximum)	13.7 bar (maximum)
Spent acid transfer pump	2	March pumps	TE-5.5C-MD 1&3 Ph Mag Drive Pump		Propylene front and rear housing impeller Viton o-ring Ceramic shaft	Sulphuric acid		6,81 m <sup>3</sup> /h	12.67 bar discharge head

					and thrust washers				
Quench water supply pump	2	Grundfos	Product number: 96084250		Cast iron base, SS impeller	Process Water	(-20) to 120 °C	6.9 m <sup>3</sup> /h	13.27 bar discharge head
Hydrolysis slurry separation unit	1	GEA Varipond Biosolids Decanter	Prime 4000			Delignification slurry product		20 to 35 m <sup>3</sup> /h dewatering 20 to 45 m <sup>3</sup> /h thickening	
Phase 3	Neutralization and Homogenization of CNC Product								
Recirculation water supply pump	2	Grundfos	Product number: 96084250		Cast iron base, SS impeller	Process Water	(-20) to 120 °C	6.9 m <sup>3</sup> /h	13.27 bar discharge head
Recirculation tank	1	Prestank	1 X 1 X 1 tank configuration	Water storage	Steel	CNC product		1.52 m <sup>3</sup>	

NaOH dosing tank	1	Grundfos-supplied	2-DDA-FC dosing system		PVC suction hose (2 m) PE de-aeration hose (2 m) PE discharge hose (6 m)	NaOH	25 °C	0.03 m <sup>3</sup> /h	
NaOH dosing pump	2	Grundfos	2-DDA-FC dosing system		PP/PVC dosing head EPDM gaskets Ceramic ball PVC/PE hose	NaOH	25 °C	0.03 m <sup>3</sup> /h	4 bar discharge
VoDCa unit	1	Vivira	Custom design		Steel	CNC product	4726.85 °C (maximum)	Custom-designed	1013.25 bar (maximum)

### ***6.3.3 Civil and Structural Requirements***

The Contractor is required to perform the following activities to complete the civil works:

- a) Review and complete the works' full structural design according to the specifications and standards indicated in the Employer's Works Information.
- b) Suppose an existing site is to be used. In that case, the Contractor must confirm the available space for the plant equipment and perform structural analysis and design on the existing support platform for its reuse to support the proposed plant equipment to be installed.
- c) Design a new support platform or modify the existing support platform or any other existing structures (if required) to accommodate the equipment power supplies.
- d) Conduct tests to determine the material properties of the structural steel used in the construction of the plant equipment to complete the design.
- e) Survey and establish any benchmarks within the Biorefinery sector, which are required to complete the works. Suppose survey information on existing benchmarks within the Biorefinery sector is unavailable. In that case, the Contractor is required to consult the Surveyor-General's office to obtain information on available registered beacons to establish any required benchmarks close to the works.
- f) Equip any new platform with removable hand-railings and access steel ladders.
- g) Ensure the structural integrity of all structural modifications and take full accountability for any modifications made to the structural works.
- h) Submit the detailed design report and finalized drawings for acceptance by the Employer before any construction can occur.
- i) Ensure all designs and modifications are required to be designed for the entire life of the plant.
- j) Ensure all structural designs are per the standards and specifications referenced in the Employer's Works Information.
- k) Ensure all structural steel used is required to be grade S355JR per SANS 50025.

- l) Ensure all areas where items are to be affixed to existing concrete structures must be tested (non-destructive testing methods) to ensure that existing reinforcing steel is not damaged.

#### **6.3.4 Piping and Instrumentation Diagrams (P&IDs)**

International Atomic Energy Agency (1990) recommended that each instrument be assigned a tag number, specified on the instrumentation specification sheet, and listed in the instrument index. Considering that the primary process variables are pressure, temperature, flow, level, density, and mass, these variables were designed to be directly measured, using automatic controls as per the hierarchy of automatic controls outlined in Chapter 4. It is recommended that the piping must be fabricated and tested in the execution (construction) phase according to the appropriately recommended code. Furthermore, the vertical and horizontal clearances for the piping shown in Table 6.4 below (International Atomic Energy Agency, 1990) were applied to the piping design. The P&IDs can be found in Appendix B.

**Table 6.4. Recommended piping clearances.**

<b>A. Minimum Vertical Clearances</b>	
3.7 m	Over access ways within project limits
2.3 m	Within buildings and over stairways
<b>B. Minimum Horizontal Clearances</b>	
0.75 m	Where access ways are required
0.50 m	Where no access ways are required
0.75 m	On platforms

Per the recommendation of assigning tag numbers to each instrument, the Kraftwerk Kennzeichen System (KKS) coding system was used to code the plant lines and equipment as indicated in Table 6.5 to Table 6.7 below.



**Table 6.5. Line Keys**

<b>A. Key for Plant Numbering</b>		
MP	Main process	
WT	Water treatment process	
AR	Acid recovery process	
<b>B. Key for Site Number</b>		
1	Municipal water treatment	
2	Main process phase 1	
3	Main process phase 2	
4	Main process phase 3	
5	Acid recovery	
6	Effluent treatment	
<b>C. Production Line Code</b>		
<b>C.1 Main Process Phase 1</b>		<b>Number</b>
SD	Sawdust transfer line	1
AP	APS transfer line	1
PW	Process water supply line	1
RW	Rinse water supply line	1, 2
RP	Reactor product line	1
RE	Rinse water effluent line	1, 2
SL	Separator liquid product line	1
SS	Separator solid product line	1
<b>C.2 Main Process Phase 2</b>		
PS	Sawdust pulp slurry transfer line	1
SA	Sulphuric acid supply line	1
QP	Quenched product supply line	1
PW	Process water supply line	2
RW	Rinse water supply line	2, 3
RP	Reactor product line	2

RE	Rinse water effluent line	2, 3
SL	Separator liquid product line	2
SS	Separator solid product line	2
<b>C.3 Main Process Phase 3</b>		
CD	Sodium hydroxide dosing line	1
BH	Pre-homogenizer line	1
AH	Post-homogenizer line	1
FP	Final product line	1
PW	Process water supply line	3
<b>C.4 Water Treatment Process</b>		
MW	Municipal water supply line	1
BS	Pre-strained municipal water line	1
AS	Raw water supply to UF membrane	1
UF	UF water supply to UF tank	1
UT	UF water supply to RO membrane	1
RF	RO water supply to RO tank	1
BW	Backwash water supply	1, 2
CW	CIP water supply line	1, 2
CC	CIP chemical supply line	1, 2
CE	BW/ CEB/ CIP effluent line	1, 2
PR	Process water supply to Main Process	1
<b>C.5 Acid Recovery Process</b>		
SP	Spent acid supply line	1
AC	Activated carbon supply line	1
PW	Process water supply line	4
RW	Rinse water supply line	4
RP	Reactor product line	3
RE	Rinse water effluent line	4, 5
SL	Separator liquid product line	3
SS	Separator solid product line	3

**Table 6.6. Equipment Keys**

Equipment	Code		Serial number
	First letter	Second letter	
Main Process Phase 1			
Sawdust storage silo	O	T	1
APS storage silo	A	T	2
Process water storage tank	W	T	3
De-lignification reactor	D	M	1
Separator	S	S	1
Main Process Phase 2			
Sawdust pulp storage vessel	P	T	4
Sulphuric acid storage vessel	F	T	5
Process water storage tank	W	T	3
Hydrolysis reactor	H	M	2
Quench tank	Q	T	6
Separator	S	S	2
Spent acid storage tank	U	T	7
Raw CNC suspension storage tank	N	T	8
Main Process Phase 3			
Process water storage tank	W	T	3
Sodium hydroxide dosing tank	T	T	9
Recirculation tank	R	T	10
Homogenizer	V	K	1
Final product storage tank	F	T	11
Water Treatment Process			
Source water buffer tank	B	T	12

Strainer	I	S	2
UF membrane	U	F	1
UF product buffer tank	E	T	13
RO membrane	M	F	2
RO permeate tank	C	T	14
UF CIP tank	G	T	15
RO CIP tank	J	T	16
<b>Acid Recovery Process</b>			
Spent acid storage tank	U	T	7
Activated carbon silo	I	T	17
Process water storage tank	W	T	3
Adsorption reactor	I	M	3
Separator	S	S	3
Recovered acid storage tank	I	T	18
Washer	I	D	1
Recovered AC silo	I	T	19

**Table 6.7. C&I Equipment Codes**

Equipment	Code	
	First letter	Number 1-16
<b>Main Process Phase 1</b>		
Control valve	CV	7
Level indicator	LI	1
Level transmitter	LT	1
pH indicator	PHI	1
pH transmitter	PHT	1
Centrifuge PLC	SC	1
Delignification reactor PLC	DRC	1
Screw pump	SP	1

Centrifugal pump	CP	4
<b>Main Process Phase 2</b>		
Control valve	CV	10
Level indicator	LI	1
Level transmitter	LT	1
Hydrolysis Reactor PLC	HRC	1
Quench PLC	QC	1
Centrifuge PLC	SC	1
Centrifugal pump	CP	8
<b>Main Process Phase 3</b>		
Control valve	CV	5
Level indicator	LI	1
Level transmitter	LT	1
pH indicator	PHI	1
pH transmitter	PHT	1
DCS: Level indicated control	LIC	1
DCS: pH indicated control	PHIC	1
ISO positive displacement pump	PDP	1
Centrifugal pump	CP	2
Recirculation PLC	RC	1
<b>Water Treatment Process</b>		
DCS: Level indicated controller	LIC	1
DCS: UF Pressure indicated controller	UPIC	1
DCS: RO Pressure indicated controller	RPIC	1
Level indicator	LIC	1
Level transmitter	LT	1
Pressure indicator	PI	4
Pressure transmitter	PT	4
Control valves	CV	10
Centrifugal pumps	CP	5

RO Booster pumps	BP	1
UF Reverse processes PLC	URC	1
RO Reverse processes PLC	RRC	1
<b>Acid Recovery Process</b>		
Control valves	CV	7
Centrifugal pumps	CP	4
Level indicator	LI	2
Level transmitter	LT	2
DCS: level indicated controllers	LIC	2
Adsorption reactor PLC	ARC	1
Centrifuge PLC	SC	1
AC recycle PLC	ACRC	1

## 6.4 Discussion

### 6.4.1 Primary Design Factors

As outlined by International Atomic Energy Agency (1990), the P&IDs were expansions of the PFDs from the Basic Design Chapter. The P&IDs are presented in Appendix B. All process equipment selections were made from standard equipment catalogues to prevent additional costs associated with customizing equipment. In this regard, standard pipe sizes were applied in the detailed design. The OEM catalogues are attached as Appendix C to this Chapter.

According to International Atomic Energy Agency (1990), the detailed engineering design describes the equipment, lines, instrumentation, and structures for unit operations and systems. Table 6.8 below outlines the recommended categories required by completing the Detailed Design phase alongside the reference column indicating how the requirements were fulfilled in this study.

**Table 6.8. Detailed Engineering Design Categories (International Atomic Energy Agency, 1990)**

<b>Category</b>	<b>Sections to be included</b>	<b>Reference</b>
Chemical Process Description	Process diagram	PFDs and P&IDs
	Equipment list	Summary of equipment sizing results (Basic Design, Chapter 5)
	Schematic drawings for tanks, reactors, columns, vessels, heat exchangers, pumps, compressors, and special equipment	As outlined in OEM manuals (Appendix C)
	Design of pipelines	Piping design (Detailed Design, Chapter 6)
	Equipment layout	Plant layout (Basic Design, Chapter 5)
	Engineering flowsheet	P&IDs (Appendix B)
	Instrumentation layout	P&IDs (Appendix B)
	Detailed layout and designs for materials handling	P&IDs (Appendix B) and Plant layout (Basic Design, Chapter 5)
	Operating manual	Process Sequence (Chapter 6)
Mechanical Project Description	Specifications for the purchase/fabrication of vessels and tanks	As outlined in OEM manuals (Appendix C)
	Design and procurement details for stairways, platforms, skid-mounted unit operations, and ventilation systems	As outlined in OEM manuals (Appendix C)
Piping Description	General plan	Piping design (Detailed Design, Chapter 6)

Instrumentation Description	Proposed criteria	Control and instrumentation design (Basic Design, Chapter 5)
	Instrumentation diagrams	P&IDs (Appendix B)
	List of alarms and setpoints	Control and instrumentation design (Basic Design, Chapter 5)
Electrical System Description	Junction boxes	Electrical Design (Basic Design, Chapter 5)
	Local push button stations	
	Lighting and communication plans	
	Motor control centers	
	Power and control cables	
	Cable trays and conduits	
	Above-ground earthing	
Civil Engineering Description	Criteria for civil engineering structures and architecture	Civil and Structural Requirements (Detailed Design, Chapter 6)
	Details for foundations and concrete structures	

### 6.4.2 Utilities

#### 6.4.2.1 Electricity

As per the International Atomic Energy Agency (1990) recommendation, all master controls for plant equipment are to be mounted on C&I panels from which the entire plant is controlled and monitored. These configurations require a designated control room. The electrical contractor must indicate the selected voltage for the plant in the execution phase, depending on the local electricity supply, the size and type of the load, and special equipment requirements (International Atomic Energy Agency, 1990). Furthermore, the contractor must state the voltage, number of phases, power factor, frequency, measurement instrument and location, the maximum power demand, estimated monthly demand, and the power requirement for each plant section.



Electricity to power the plant can either be sourced from a public grid or a diesel generator for smaller production capacities. Due to the corrosive nature of the process reagents, it is recommended that all electrical wires are placed in PVC conduit. The underground duct is typically encased in concrete between the substation and electrical equipment rooms. The electrical substation must be located as close to the plant as possible. Furthermore, the site must be free of corrosive vapours and waste sources to avoid their possible accumulation on electrical insulators. In addition, the substation or power supply must be oriented with the wind to avoid potential problems.

The electrical supply system must have an efficient grounding system to maximize protection to site personnel and minimize damage to equipment. The following equipment must also be considered in the grounding: metallic structures and supports, connectors, conduits, metallic fences, cabinets and equipment housing, and the lighting system. All potential electrical risks must be eliminated in the planning stage of the electrical system. Any exposed parts, equipment, or wiring that can be subjected to mechanical or water damage must be considered potential risk areas.

#### 6.4.2.2 Process Water

Process (de-mineralized) water is needed for the following process activities:

- a) Reagent make-up (APS solution, acid dilution, CNC final treatment).
- b) Washing of vessels after batch operation cycle is complete.
- c) Regeneration of activated carbon.
- d) (Potential) Regeneration of APS.
- e) Utilities.

The complete design of the water treatment plant for de-mineralized water production is reported in Appendix D. As per the suggestion of the International Atomic Energy Agency (1990), the design provided an estimate of the annual water consumption of the process.

## 6.5 Conclusion

This Chapter concluded the commercial plant design procedure per the project life cycle model. The iterative nature of the design process was applied from the Concept Design phase through to this Detailed Design phase. All the necessary information was specified to provide a blueprint to enable the pilot and commercial implementation of the CNC production process. The design objectives were achieved.

Regarding the detailed engineering phase, Dolhert (2008) conceded that the project is ready for detailed engineering upon the conclusion of the project scope and the engineering study. The engineering study comprises the concept and basic design phases as extensively outlined by International Atomic Energy Agency (1990). Dolhert (2008) re-iterated that the detailed engineering phase entails the sizing and specification of equipment, creating detailed process designs, and finalizing equipment layout. These factors concur with those outlined by International Atomic Energy Agency (1990). Hence, the information outlined in the design phases (Concept and Basic, culminating in the Detailed Design) concludes the CNC process plant design.

## 6.6 Addendum to Detailed Design

This addendum comprises the catalogues for the primary process equipment identified in the detailed design phase. The catalogues were obtained directly from the Original Equipment Manufacturers (OEMs). Table 6.9 below provides an index of the catalogues.

**Table 6.9. OEM Catalogue Index**

	<b>Equipment</b>	<b>Manufacturer</b>
	<b>A. Transfer Equipment</b>	
1	Water pumps	Grundfos
2	Acid pumps	March Pumps
3	Slurry pumps	Wilfley Pumps
4	Caustic dosing pumps	Grundfos
5	Pneumatic overpressure conveyors	Busch

<b>B. Cleaning Systems</b>		
6	Rinse balls	Lechler
7	Clean-in Place	SPX Flow Technologies
<b>C. Process Vessels</b>		
8	Process water storage tank	Prestank
9	Stirred tank, glass-lined reactors	Buchiglasuster
10	Chemical storage silos	Jojo
<b>D. Separation Units</b>		
11	Centrifuge	GEA
<b>E. Homogenization Unit</b>		
12	Vortex Device for Cavitation (VoDCa)	Vivira Technologies

**PART B: APPLICATION OF CNC TO DEVELOP NOVEL GREEN  
CONSTRUCTION MATERIALS**

## **CHAPTER 7: NOVEL CURING PROCEDURES, BIO-ADDITIVES, AND CNC TO IMPROVE GREEN CONSTRUCTION MATERIALS: CRITICAL REVIEW AND META-ANALYSES**

### **7.1 Introduction**

Environmental concerns remain one of the main challenges faced by the cement industry (Imbabi et al., 2012). The production of ordinary Portland cement (OPC) is energy-intensive and a significant contributor to industrial greenhouse gas emissions (Komnitsas, 2011). Novel green alternatives to OPC are required to improve the sustainability of the construction industry. Fly ash-based geopolymers are a viable alternative to OPC in the building industry (Imbabi et al., 2012; Komnitsas, 2011). However, more research is required to determine how fly ash-based geopolymers can be enhanced to become commercially viable and reliable to replace OPC completely. This study reviewed three parameters to potentially improve the viability of fly ash-based geopolymer construction materials: novel curing techniques, fiber-reinforcing additives, and CNC as a reinforcing agent.

CNC are nanoparticles derived from cellulose, a renewable resource. Due to their unique optical, rheological, and mechanical properties, CNC are finding widespread applications in the construction, automotive, paper, medical and food sectors. It is a high-strength polymer material whose mechanical properties compare favourably and often exceed traditional reinforcement materials such as stainless steel and Kevlar (Moon et al., 2011). CNC can be produced from forestry and agricultural wastes, thereby decreasing the production costs.

This study systematically reviewed the application of the three potential improvement parameters as strength-enhancing agents for construction materials. Although much research has been undertaken to investigate their application in construction materials, it is challenging to consolidate and quantify the respective overall effects of the three potential improvement factors in construction materials based on multiple literature studies. Such findings would enable researchers to make informed decisions when commercializing novel green construction materials. To close this gap, the aims of this study were threefold. The first aim was to consolidate the relevant literature. The second aim was to statistically determine the overall

effect of CNC on the strength of construction material. Finally, the third aim entailed developing a globally applicable framework to perform systematic reviews and meta-analyses of engineering research using Review Manager (RevMan) software.

It is argued that the three potential improvement factors have positive impacts on the strength of construction materials, implying that they can be applied in the development of novel green geopolymer construction materials to improve the long-term sustainability of the construction industry.

## **7.2 Literature Review**

### ***7.2.1 Current State of the Construction Industry- An Overview***

The cement industry is challenged by depleting fossil fuel reserves, scarce raw materials, increasing demand for construction materials, growing environmental concerns linked to climate change, and a stagnant world economy (Imbabi et al., 2012). The production of OPC contributes to approximately 6% of all industrial carbon emissions (Imbabi et al., 2012) and 5 to 7% of the emissions directly responsible for global warming (Singh and Middendorf, 2020). As such, the cement production industry is the third-largest global carbon dioxide emitting industry (Komnitsas, 2011).

Initiatives such as reducing kiln firing temperatures and using magnesium silicates to eliminate carbon dioxide emissions were taken to decrease the cement industry's environmental footprint. However, they are not entirely practical due to the questionable availability and significant capital investment of the desired magnesium silicates (Imbabi et al., 2012). The calcination phase of the OPC production process results in the most substantial carbon dioxide emissions and entails firing calcium carbonate and silica to produce calcium silicate (Imbabi et al., 2012). Two methods can decrease the carbon dioxide emissions: changing the raw materials in the calcination process and changing the manufacturing process entirely (Imbabi et al., 2012). These recommendations are difficult to implement. Hence, the development of environmentally friendly construction materials is vital. Such alternatives can be classified as "green construction materials."

Green materials are environmentally friendly, durable, bio-based, recycled, and exhibit low toxicity and emissions (Komnitsas, 2011). The market for green construction materials is rapidly expanding (Komnitsas, 2011). Notably, fly ash, blast furnace slag, and silica fumes are typical cement replacement materials validated theoretically and practically (Imbabi et al., 2012), as fly ash-based geopolymers can meet all the outlined criteria for green building material classification.

Geopolymers are cementitious materials formed by chemical activation of aluminosilicate materials at relatively low temperatures (Komnitsas, 2011). Geopolymer cement is produced from secondary raw materials such as fly ash, metakaolin, calcined clays, and zeolite by alkali activation. Geopolymer construction materials can be produced from several waste materials or by-products (including coal combustion ashes, slags, construction, and demolition waste). Geopolymers rely on minimally processed natural minerals and industrial by-products or wastes to provide binding agents (Komnitsas, 2011). Furthermore, geopolymer synthesis uses industrial aluminosilicate by-products (waste) with negligible impact on the environment (Singh and Middendorf, 2020). This feature enables significant energy and carbon dioxide savings in the construction sector, thereby classifying geopolymers as green construction materials.

Despite the advantages of implementing geopolymers as green construction materials, further research is required to improve the technology and strengthen the potential for commercial applications (Komnitsas, 2011). Price stability is mandatory to realize the implementation of green construction materials, (Imbabi et al., 2012). Hence, subsidies should be made available to global green technology manufacturers. Considering that building practitioners often identify the high capital costs as barriers to adopting and investing in green practices (Komnitsas, 2011), the knowledge gap between researchers and practitioners should be closed by enabling the knowledge available to address gaps and limitations, and problems.

The uncertainties in geopolymer production include phase transformation, reaction impurities, and their effect on strength development (Singh and Middendorf, 2020). Hence, further research in these areas is required. Furthermore, the development of ambient temperature-cured geopolymers and the implementation of regulatory standards for uniform geopolymerization processes is recommended.

### ***7.2.2 Fly ash-based Geopolymers as Green Construction Materials***

Substantial quantities of fly ash are generated globally on an annual basis, posing a severe threat to the environment (Gollakota et al., 2019). To avert this threat, fly ash applications must be developed. Hence, the application of fly ash in geopolymer production is a desirable waste beneficiation protocol. Fly ash-based geopolymers were reviewed concerning their clean production, properties, and applications (Zhuang et al., 2016). The geopolymerization process can trap trace toxic metal elements from fly ash. In addition, the silicon to aluminium ratios, the type and amount of the alkali solution, temperature, curing conditions, and additives are critical factors in the geopolymerization process (Zhuang et al., 2016). This finding was consistent with Singh and Middendorf (2020), which reported that the unique properties of the "parent" fly ash transfer to the resulting geopolymers. The mechanical properties of fly ash-based geopolymers can improve by adjusting the silicon to aluminium ratios, alkali solutions, curing conditions, and natural reinforcing agents (Zhuang et al., 2016). Although it was confirmed that fly ash-based geopolymers could be used as novel green construction materials (Zhuang et al., 2016), further studies are recommended to enhance the mechanical performance, scale-up production, and explore new applications.

### ***7.2.3 Novel Curing Procedures for Fly Ash-based Geopolymers***

The previous section of this review presented geopolymers as superior alternatives to OPC in the construction industry. Other than the geopolymer's precursor type and mix design, the curing procedure must be optimized and standardized to yield satisfactory and uniform properties in the final product. A notable recent development is that of microwave curing. Compared to conventional curing mechanisms, such as ovens, microwaves offer quicker heat transfer during geopolymer curing. However, from a practical perspective, the scale-up of microwave curing to pilot and commercial scale requires sophisticated and large-scale microwaves.



In the study of Graytee et al. (2018), a high-strength fly ash-based geopolymer was developed within a relatively short time using microwave curing. The study's main objective was to determine the effect of this novel curing procedure on the strength of the geopolymer. Conventional heat curing methods (such as ambient air, water, and oven) transmit heat externally into the core of the geopolymer being cured (Graytee et al., 2018). In this regard, the study of Graytee et al. (2018) reported faster strength development using microwave curing. In the study of Roopchund (2016), conventional oven curing could not provide spatial uniformity for the heat distribution to the geopolymer samples during curing. Hence, the samples were demoulded at the mid-point of the initial curing procedure and rotated to expose the previously "embedded" parts of the sample to the heat curing procedure (Roopchund, 2016).

The study of Graytee et al. (2018) investigated the effect of short periods (not exceeding 60 minutes) of microwave curing and oven curing at higher temperatures. The results indicated that the compressive strength of microwave-cured geopolymers was more significant than those of the oven-cured samples at 90 and 120 °C. This result is exceptional as it demonstrates that the curing procedure can be used as an additional parameter to strengthen the geopolymer. A remarkable compressive strength of 56 MPa was obtained for the microwave-cured geopolymer within five minutes. This study successfully demonstrated the feasibility of manufacturing fly ash-based geopolymers with sufficient strength in short times through microwave curing. Overall, microwave curing accelerated the early strength development of the geopolymers. In addition, the microwave curing periods were directly proportional to geopolymer strengths. In this regard, the authors identified the control factors as microwave power, batch mass, specimen temperature, and specimen size. Although this study is beneficial in reducing the energy requirements of the curing process on a laboratory scale, it requires the development of pilot-scale and commercial-scale microwave equipment to become practically feasible.

To improve the sustainability of the geopolymerization process, the study of Kastiukas et al. (2020) developed a geopolymer using two curing procedures: microwave curing and oven curing. Additionally, the authors undertook an environmental assessment comparison of the two

curing procedures. The experimental work investigated the effect of the two curing regimes on the compressive strengths of geopolymers. The overall results indicated that microwave curing used less time and produced desired strengths than oven curing. This finding agrees with the study of Graytee et al. (2018). The authors attributed this finding to microwave radiation favouring a greater hydration degree of the precursors in the geopolymer sample. Furthermore, the authors recommended that the temperature, microwave power, and time are optimized to achieve optimum strengths while simultaneously eliminating the cracking within the samples—as indicated by Graytee et al. (2018).

The study of Kastiukas et al. (2020) compared the compressive strength performance of fly ash and granulated blast furnace slag precursors in their respective geopolymers. The fly ash-based geopolymers exhibited more significant compressive strengths than the granulated blast furnace slag-based counterparts. The authors attributed this finding to the lower carbon content in the fly ash, which further indicated the viability of fly ash precursors in geopolymer synthesis as previously indicated in the studies of Zhuang et al. (2016) and Gollakota et al. (2019).

To further increase the curing efficiency in the geopolymerization process, the study of Cai et al. (Cai et al., 2020) developed a self-electrical heating fly ash-based geopolymer. This novel aspect can decrease the energy consumption of traditional curing processes. The authors added carbon black and steel fibers into the fly ash-based geopolymer to improve its electrical conductivity. This action enabled them to investigate the feasibility of curing fly ash-based geopolymers using self-electrical heating by calorimetric quantification. In addition, the authors used three-point bending tests to investigate the influence of electric heating on the flexural behaviour of the synthesized geopolymer samples. The maximum surface temperature of the geopolymers under electric heating reached 67 °C. This finding proved the feasibility of conductive geopolymers with self-electrical behaviors. Furthermore, the three-point bending test results indicated that the flexural strength increased after self-electrical heating.

Based on the calorimetry results, the geopolymerization process occurred slowly under ambient curing conditions, as expected. Hence heat-curing processes are used to enhance the geopolymerization process. To further improve the self-electrical heating behaviour of

geopolymers, the authors recommended adding steel fiber and carbon black into the matrix. In addition, the authors attributed the greater strength and ductility observed in the three-point bending tests to the formation of a denser microstructure due to the addition of carbon black and steel fibers. The overall result indicated that the self-electrical heating method proposed by the authors could significantly increase the eco-efficiency of the geopolymerization process by reducing the energy cost and improving the curing efficiency. Although this work is noteworthy, it cannot apply to the microwave curing process proposed by Graytee et al. (2018) and Kastiukas et al. (2020) for safety reasons. Hence, the advantages and disadvantages of both these novel curing procedures (microwave radiation curing and self-electrical heating curing) must be considered before implementation on a more extensive pilot or industrial scale.

#### ***7.2.4 Biomaterials to Fortify Construction Materials***

There are two documented cases of biomaterials used to fortify construction materials in ancient times (Pacheco-Torgal, 2016). The Romans fortified lime mortars using vegetable fat and used dried blood as an air-entraining agent. In addition, the Chinese used egg white, fish oil, and blood-based mortars due to the imperviousness of these materials to construct the Great Wall of China. These findings implied that using bio-additives in construction materials is not a new practice. Although the science might still be developing, the potential is tremendous. Currently, approximately 15% of OPC contains chemical admixtures to modify their properties. These additives reduce the energy requirements of the production process and maintain the competition against emerging green construction materials (Pacheco-Torgal, 2016). Some examples of biopolymers used in OPC concrete include terminalia chebula and natural sugars (molasses, palm jaggery, and honey) (Sudalaimani, 2017; Sudalaimani et al., 2017; Karthik et al., 2019), short natural fibers (cotton, sisal, raffia, coconut, pineapple leaves, linen, flax, and sweet sorghum) (Korniejenko et al., 2016; Silva et al., 2020) and bio-resins (Gkaidatzis, 2014). Although OPC and dry-mix mortars consume most biopolymers, other building material industries use diverse bio-admixtures (Pacheco-Torgal, 2016). This finding bears testament to the increasing applications of bio-additives in the construction industry. Citing 2014 statistics by the World Health Organization, the construction industry will grow exponentially to accommodate urban population increase from approximately 3.4 billion in 2009 to 6.4 billion

in 2050 (Pacheco-Torgal, 2016). The studies of Komnitsas (2011), Imbabi et al. (2012), and Singh and Middendorf (2020) support this finding, thus indicating the growing demand for biopolymer-based construction materials.

The study of Korniejenko et al. (2016) explored the mechanical properties of geopolymer composites reinforced with natural fibers. The study found that geopolymer composites are a promising ecological alternative to traditional materials due to their cost-effectiveness, environmental benefits, and energy efficiency. Despite these advantages, geopolymers' relatively low tensile and flexural strength must improve to broaden their potential applications (Korniejenko et al., 2016). As such and aligned with the theme of green construction materials (Imbabi et al., 2012; Komnitsas, 2011; Singh and Middendorf, 2020), the study of Korniejenko et al. (2016) investigated the reinforcement potential of short natural fibers such as cotton, sisal, raffia, and coconut on the mechanical properties of fly ash-based geopolymers. The reinforced geopolymers were compared against the baseline (8M alkaline activated geopolymer). The mechanical testing included compressive strength tests, flexural strength tests, and microstructural examinations. According to the scanning electron microscopy analysis, the natural fibers were less coherent within the geopolymer matrix than artificial fibers (such as glass or carbon). Despite this, the compressive and flexural strength tests proved the benefits of the fiber-reinforcement with relatively good mechanical properties, except raffia. This finding was attributed to the fiber size of the raffia, among other characteristics (Korniejenko et al., 2016).

The study of Korniejenko et al. (2016) established a general concern when using fiber-reinforcements: the ability of the fiber to disperse uniformly within the geopolymer matrix. Uniform geopolymer mechanical properties require uniform dispersion. The overall results revealed that the appropriate addition of natural fibers improved the mechanical properties of geopolymer composites. This finding is notable as natural fibers improved the characteristics of the green material, thereby improving its competition against the predominant OPC construction materials.

Resonating with the studies of Korniejenko et al. (2016), Sudalaimani (2017), Sudalaimani and Kumar (2017), and Karthik et al. (2019), the study of Silva et al. (2020) reviewed natural fibers as reinforcing additives for geopolymers. Regarding the use of industrial wastes, Silva et al. (2020) reviewed the use of fly ash, ground granulated blast furnace slag, construction and demolition wastes, and mine tailings to produce high strength geopolymers. In addition, various natural fibers demonstrated successful application in reinforcing geopolymers. These natural fibers included: pineapple leaves, sisal, linen, flax, sweet sorghum, and cotton. The authors found that the fiber type, dimensions, quantity, and pre-treatment of fibers affected the properties of the composites.

Additionally, woven and non-woven layers of natural fibers were more effective than randomly oriented short fibers. The authors asserted that each reported material could produce eco-friendly construction materials due to their favourable aluminosilicate content (Silva et al., 2020). Reinforcement fibers are renewable and readily available since they are mainly plant-based. Notably, the study of Silva et al. (2020) reported that geopolymers produced from raw materials like fly ash, ground granulated blast furnace slag, clay brick powder, concrete demolition waste, and mine tailings showed good mechanical properties comparable to OPC products. This finding agrees with the research of Komnitsas (2011) and Singh and Middendorf (2020).

Resonating with the findings of Roopchund (2016), Silva et al. (2020) asserted that the morphology, size, silica to alumina molar ratio, the alkaline solution to solid ratio, sodium hydroxide concentration, silica to metal oxide molar ratio in the alkaline solution, and curing conditions are key geopolymerization parameters. As expected, the authors reported that the mentioned parameters must adapt to the raw material used. Aligned to the findings of Korniejenko et al. (2016), Sudalaimani (2017), Sudalaimani and Kumar (2017), and Karthik et al. (2019), the study of Silva et al. (2020) found that the fiber type, content (usually between 1 and 5 weight%), dimensions, and strength influence its capacity to reinforce different geopolymer types. In addition, geopolymers reinforced with natural fibers such as sweet sorghum, wool, cotton, sisal, and coir showed increased compressive, flexural, and tensile

strengths (up to 53%, 454%, and 111%, respectively). Despite the significance of this result, the authors failed to investigate the impact of nano-fibers on geopolymer reinforcement.

The study of Sudalaimani (2017) investigated the impact of several bio-additives on the mechanical properties of fly ash-ground granulated blast furnace slag-based geopolymers. In addition, the researchers determined the effect of the bio-additives on the self-curing ability of the geopolymers. Self-curing capabilities in geopolymers are notable, as it reduces the energy requirements of the geopolymerization process. Traditionally, geopolymers are heat-cured to catalyze geopolymerization. However, as indicated in the research of Graytee et al. (2018) and Kastiukas et al. (2020), reducing the geopolymerization energy requirements is critical for geopolymers to classify as green construction materials. The study of Sudalaimani (2017) researched the impact of terminalia chebula and natural sugars: molasses, palm jaggery, and honey as bio-additives on the mechanical properties of the bio-geopolymer concrete and their ability to induce self-curing properties (under ambient conditions). The bio-additives were added at 0.8% (by weight) of aluminosilicate minerals.

Regarding the overall geopolymerization process, other than reducing the energy requirements of the curing process, the alkaline activator concentration can also be optimized (Roopchund, 2016). The study of Sudalaimani (2017) used a 4 M activator concentration. This concentration was notable, considering that the lowest activator concentration used by Roopchund (2016) was 6 M. Overall, the study of Sudalaimani (2017) confirmed that the optimal bio-additives combination of Terminalia chebula and palm jaggery induced self-curing abilities. Furthermore, using this combination yielded a remarkable 31.31% compressive strength increase, 14.70% splitting tensile strength increase, and 27.59% flexural strength increase compared to control specimens cured at ambient conditions.

Aligned with the work of Sudalaimani (2017), the study of Sudalaimani and Kumar (2017) focused on the impact of bio-additives on the durability of fly ash-blast furnace slag-based geopolymers. The geopolymers were chemically attacked to determine the bio-additives impact on the geopolymer resistance. As in the work of Sudalaimani (2017), the bio-additives included

terminalia chebula and natural sugars: molasses, palm jaggery, and honey. The authors immersed the geopolymers in the following chemical solutions: 5% sulphuric acid, 5% sodium sulphate, and 5% sodium chloride for 7, 14, 28, 56, and 90 days to determine the resistance of the geopolymers against chemical attacks. After that, the authors used mercury intrusion porosimetry to determine the effect of the chemical attacks on the porosity and pore size distribution.

After a 90-day immersion period, the geopolymers lost mass and compressive strength in the respective ranges of 2.82–3.91%, 9.67–12.05% under sulphuric acid attack, 0.38–0.68%, 2.15–2.95% under sodium sulphate attack, and 0.28–0.51%, 0.83–1.33% under sodium chloride attack. These findings compared satisfactorily against the respective weight loss and compressive strength loss of the control samples: 13.97%, 33.57% under sulphuric acid attack, 1.64%, 6.45% under sodium sulphate attack, and 0.86%, 2.05% under sodium chloride attack. Hence, the bio-additives led to enhanced durability properties. This finding is notable, especially in geographical areas prone to acid rain. The authors attributed the enhanced geopolymer resistance to stable crosslinked polymer structures, improved homogeneity, more ordered and denser geopolymer binding gel, filling of micro-pores, and refinement of the pore structure in the bio-additives-added geopolymers. The addition of the palm jaggery- Terminalia chebula combination in geopolymers exhibited optimal durability, as previously found in the study of Sudalaimani (2017).

Broadening the work of Sudalaimani (2017), the study of Karthik et al. (2019) investigated the effect of bio-additives on the physicochemical properties of fly ash-ground granulated blast furnace slag-based geopolymers. As previously, the authors implemented ambient curing to reduce the energy requirements. The authors used natural sugars (molasses, palm jaggery, and hone) and terminalia chebula as bio-additives in the fly ash and ground granulated blast furnace slag-based geopolymers. The bio-additives caused stable matrices and orderly geopolymer gels. Overall, the microstructure density increased. The thermal results were notable as they indicated that higher temperatures were required to disintegrate the structure of the geopolymer matrix

with the inclusion of bio-additives. In addition, higher activation rates and more stable networks were observed.

Similar to the result obtained in the study of Sudalaimani (2017), the compressive strength of the geopolymers exhibited an 18.30–35.90% increase. Based on the comprehensive strength results, the authors endorsed the addition of tested bio-additives and recommended their adoption in on-site construction work. This study is an excellent example of bio-based green materials developed for the construction industry, as pointed out in the studies of Komnitsas (2011), Imbabi et al. (2012), and Singh and Middendorf (2020).

#### ***7.2.5 CNC to Fortify Construction Materials***

CNC are an emerging biomaterial known for their high-strength properties. The acid hydrolysis of cellulosic feedstocks typically produces CNC. Notably, waste materials emanating from the Forestry, Timber, Pulp, and Paper Industry can produce CNC. Combining biomaterial applications in construction materials (Pacheco-Torgal, 2016) with the global emergence of geopolymers as novel green construction materials (Imbabi et al., 2012; Komnitsas, 2011; Singh and Middendorf, 2020), CNC can improve the commercial viability of fly ash-based geopolymer construction materials.

Cao et al. (2016a) investigated raw and sonicated CNC on the microstructure of cement. Considering that the dispersion of CNC within the cement matrix is complex, a novel centrifugation method to measure the concentrations of the adsorbed CNC (on the cement surface) and the free CNC (mobile in water) was developed. Most of the CNC (exceeding 94%) were adsorbed, implying uniform dispersion within the cement matrix. In addition, water desorption tests determined the total porosities of cement pastes with raw and sonicated CNC. The 1.2 to 1.6% porosity reduction was attributed to an increased degree of hydration. Despite the relationship of inverse proportionality between the porosity and compressive strength of the construction material (Roopchund, 2016), the relatively small porosity decrease did not justify the energy-intensive sonication dispersion.



The study of Cao et al. (2016b) investigated the effect of CNC dispersion on the cement's strength by investigating the agglomeration potential. Agglomeration inhibits the dispersion of CNC within the cement matrix, leading to the formation of pores, voids, and air entrapment (Cao et al., 2016a). Ultrasonication dispersed the CNC, and rheological measurements quantified the degree of agglomeration. Agglomerates formed when the cellulose nanocrystal concentration exceeded 1.35% by volume. A geometrical percolation model verified this finding by showing that the threshold cellulose nanocrystal concentration resulting in agglomeration was 1.38%. This finding implied that the cellulose nanocrystal concentration must be kept below 1.38% to prevent agglomeration. In addition, the optimal cellulose nanocrystal concentration for maximum strength development was 0.18%. Significantly, a relatively minute concentration of CNC is required to achieve maximum strength development. The ultrasonication dispersion resulted in strength improvements of up to 50%, indicating that the dispersion of CNC is paramount in improving the flexural strength of cement. Although this study used cement paste, the dispersion method can be applied to geopolymers to improve the strength of green construction materials.

Related to the CNC dispersion study of Cao et al. (2016a) and Cao et al. (2016b), the study of Lee et al. (2019a) developed an optimal dispersion method. Two dispersion methods were evaluated: magnetic stirring (ranging from stirring times between 60 to 180 minutes) and high-pressure dispersion at three different pressures (345, 1035, and 1587 bar) and one to three dispersion passes. The study determined the optimal dispersion conditions by analyzing the size and zeta potential of the resulting CNC particles. The average diameter was reduced by approximately 76% at 1587 bar during high-pressure dispersion. Despite the significance of this finding, it may not be practical to implement this high-pressure dispersion technique when commercializing the technology.

Green construction materials such as geopolymers have not been fully commercialized due to two primary uncertainties: financial (Imbabi et al., 2012) and technical (Singh and Middendorf, 2020). The review that follows demonstrates the potential technical benefits of using CNC in construction materials. Although the research focused on adding CNC to OPC, the paradigm

can be applied to geopolymers to fortify green construction materials to achieve more significant commercial potential.

The study of Barnat-Hunek et al. (2019) investigated the effect of CNC on the physical properties of concrete. The study found that CNC improved the freezing-thawing resistance more than 14-fold. This result is exceptional for construction applications required to withstand extreme temperature conditions and was attributed to the efficiency of nanocellulose in concrete hydrophobization. As expected, the addition of CNC altered the morphology and size of cracks and decreased the number of pores in the resulting cement. This result was consistent with the findings of Cao et al. (2016a). Overall, the study reported that the CNC promoted the formation of calcium-silicate-hydrate in the concrete, which improved the density and changed the pore structure and interface characteristics. Consequently, the cellulose nanocrystal addition resulted in improved concrete strength, freezing-thawing resistance, and hydrophobic properties.

Resonating with the study of Cao et al. (2016a), the study of Dousti et al. (2019) investigated the effect of CNC on the porosity and strength development in cement. The strength development was measured over eight weeks under compression and tension. Under the influence of the CNC, the porosity was reduced by 33%, and the surface area was reduced by 66%. These phenomena improved the compressive and tensile strength by 60% within 24 hours. This finding is significant in construction applications that require rapid strength development. The study of Dousti et al. (2019) was novel as it reported the effect of CNC on the hydration of cement paste. The addition of CNC promoted the formation of a network of hydration products, resulting in greater compressive and tensile strengths. This finding was also observed in the study of Mazlan et al. (2016), where the progressive formation of calcium silicate hydrate gel in the cement mortar improved the strength of the cement composites up to 45%. The studies of Barnat-Hunek et al. (2019) and Roopchund et al. (2021) found similar strength improvements.

The study of Liu et al. (2019) investigated the effect of CNC on the compressive strength of cement pastes. The general trend in the reviewed studies (Cao et al., 2016a; Cao et al., 2016b;

Lee et al., 2019a; Barnat-Hunek et al., 2019; Dousti et al., 2019; Mazlan et al., 2016) is that CNC enhanced the mechanical properties of construction materials. A novel aspect of Liu et al. (2019) study is that it used X-ray computed tomography and nitrogen adsorption analyses. The addition of CNC refined the cement pore structure. It was noteworthy that almost no hydration products formed in the cement matrix without CNC.

Lee et al. (2019b) investigated the effect of CNC on the shrinkage rate and mechanical performance. This study was notable as the shrinkage of a refractory material is related to thermal resistance. The aqueous CNC solutions were prepared in the following concentrations by volume: 0.4, 0.8, and 1.2. As recommended in the studies of Cao et al. (2016a), Cao et al. (2016b), and Lee et al. (2019a), ultrasonication dispersed the CNC in aqueous solutions. The optimal CNC solution concentration was 0.8% by volume as it improved the shrinkage rate and mechanical performance. Again, it is notable that only a tiny quantity of CNC was required to achieve the optimal mechanical properties in the construction material (Cao et al., 2016b; Roopchund et al., 2021). Furthermore, this finding implied that only a tiny quantity of CNC would be required for thermal resistance applications, not exceeding the thermal degradation temperature of the CNC within the matrix of the construction material.

#### ***7.2.6 Meta-analysis as a Literature Tool***

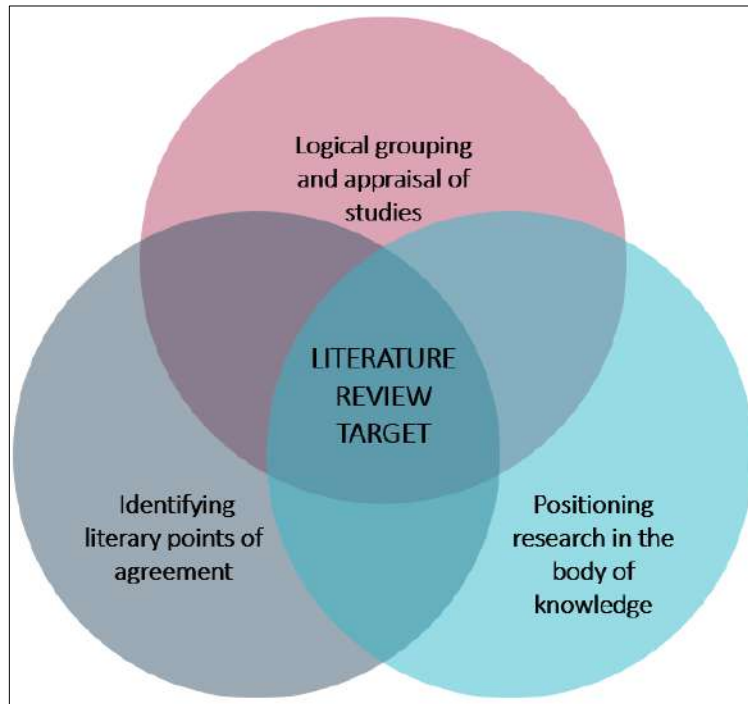
A meta-analysis enables the extraction of knowledge from accumulated studies to validate proof from a vast quantity of literature (Glass, 1976). Considering that the Engineering literature is rich with information, methodical quantitative consolidations of information are required. Unlike clinical research, where systematic reviews and meta-analyses facilitate consolidation efforts, Engineering reviews lack these rigorous quantitative methods (Mikolajewicz and Komarova, 2019). Furthermore, quantitative summaries of research domains are required to generate higher-order conclusions about general trends and patterns (Arnqvist and Wooster, 1995). The meta-analysis quality is justified by the objective quantification of the magnitude of effects, based on a standardized set of statistical procedures (Arnqvist and Wooster, 1995).

### **7.3 Materials and Methods**

Aligned to the recommendations that further studies are needed to enhance the mechanical performance and up-scale the production of green construction materials (Zhuang et al., 2016), the meta-analyses were used to determine the overall effect of novel curing procedures, biomaterial-reinforcements, and CNC on the mechanical properties of construction materials to ascertain the viability of these three parameters in the development of green construction materials. The meta-analyses were conducted per the Preferred Reporting Items for Systematic Reviews and Meta-Analysis (PRISMA) standard (Kamboj, 2016).

#### ***7.3.1 Literature Review Methodology***

The literature search used conjunction and intersection logical operators to maximize the output of relevant studies. The literature was logically grouped and appraised for each of the three potential improvement parameters. The notable points of agreement between the literature sources conceptualized the problem and provided a theoretical framework to the study. Furthermore, the literature review positioned the study in the body of knowledge and showed the underlying principles of the study. Figure 7.1 shows a graphical depiction of the mentioned literature review targets.



**Figure 7.1. Venn diagram of literature review target parameters**

### ***7.3.2 Inclusion Criteria for the Meta-analysis***

Per the recommendation of Kamboj (2016), Table 7.1 outlines the inclusion criteria used in this study.

**Table 7.1. Inclusion Criteria**

<b>Criteria</b>	<b>Preference</b>
Peer-reviewed publications	Peer-reviewed
Experimental study or review	Experimental study
Funding source	Impartial agency
Research motive	Impartial
Relevancy of findings	Relevant to the three potential green construction material improvement factors: novel curing procedures, biomaterial reinforcement additives, and CNC
Clarity of findings	Clear and usable for the meta-analysis

### **7.3.3 Meta-analysis**

Using the Review Manager software (RevMan version 5.4), three separate meta-analyses quantified the effects of the three potential improvement factors on the strength of construction materials: novel curing procedures, reinforcing biomaterials, and CNC. The procedure is outlined below and can be replicated and applied to other Engineering studies (Arnqvist and Wooster, 1995).

- a) A new review wizard simulation page was opened and saved.
- b) The names and publication years of the included literature sources were added under the “Included studies” section.
- c) Once all the literature data were entered into the software, it was visible under the "tree view."
- d) A new comparison was added under the “Data and analyses” section. The comparison was named and saved.
- e) The particular treatment was compared to the control. This step was repeated for all three treatments (novel curing procedures, biomaterial reinforcing agents, and CNC).
- f) An outcome was then added under the comparison by selecting the “add outcome under the new comparison” option.
- g) The data type was specified as "continuous," which enabled the sub-specification of the continuous data variables: mean, standard deviation, and the number of experimental runs for the data sets compared (treatment vs. control). These statistical parameters were calculated using the built-in statistical functions in Microsoft Excel.
- h) A "fixed effect" analysis model was used since the research studies were similar concerning the treatment and control comparisons.
- i) The default confidence interval of 95% was left unchanged.
- j) The new outcome was opened under the “Data and Analysis” section.
- k) The studies of interest were specified by selecting the “add study data” tab above the forest plot section. After the desired studies were selected, the process was completed.
- l) The mean, standard deviation, and the number of experimental runs data were specified for the treatment and control studies undertaken by each of the selected authors or literature sources. The Microsoft Excel calculations were used to ensure accurate

calculation of the statistical parameters (mean and standard deviation) for the control and treatment.

- m) Once the data was added to the simulation, the software automatically calculated the overall statistical parameters. These included the heterogeneity parameters for the overall study group: the I squared value (I<sup>2</sup>) and P-value. The former value indicated the degree to which the studies exhibited heterogeneity to each other. If the I squared value exceeded 50%, it indicated substantial heterogeneity between the studies. The latter value indicated the significance of the heterogeneity.
- n) The forest plot, representing the individual effect of the results of each study, automatically appeared as graphical output. The forest plot indicated whether the respective literature sources favored the treatment or the control. If the treatment was favored, the outcome of interest obtained a better output. The diamond at the bottom of the forest plot represented the overall (combined) effect.
- o) The forest plot, funnel plot, and statistical results were exported from the software.
- p) The overall meta-analysis included studies based on compressive strength and flexural strength responses of the literary construction materials under the influence of the three potential improvement parameters. After that, sensitivity analyses were performed by creating two sub-groups to separate the compressive strength and flexural strength responses (where applicable).

#### **7.3.4 Data analysis**

As outlined in Section 3.3, Step 15, the two main outputs of the meta-analysis are the forest plot and the funnel plot. The forest plot is a graphical representation of the individual literary experimental studies comprising the meta-analysis (Kamboj, 2016). Furthermore, the forest plot is a confidence interval plot and is a standard presentation format for meta-analyses results (Egger et al., 1997a; Lewis and Clarke, 2001). Each study is represented by a square at the point estimate of the treatment effect with horizontal lines extending either side of the block. The block area is proportional to the weight of the study, while the horizontal line provides a confidence interval (Alderson et al., 2004). The overall effect size (displayed as a diamond on the plot) represents the combined effect of the individual studies. The location of the diamond

on the plot indicates whether the treatment or the control will yield the desired effect. Considering the variations in research settings, countries, methodologies, and durations when performing the experimental study, some degree of heterogeneity is present in a systematic review (Alderson et al., 2004). The heterogeneity is quantified by the statistical "I squared" parameter.

The vertical line of no effect separated the treatment and control sides of the forest plot (Kamboj, 2016). The favored side of the plot indicates that the desired results are in that region. This information is helpful as it indicates if the applied treatment would yield the desired results based on literary studies without performing any experimental studies at the outset of an investigation. The confidence interval provides a range of treatment effects compatible with the result of the study. If the confidence interval does not pass through the line of no effect, the result is statistically significant (Alderson et al., 2004). This feature is also helpful as it reveals which literary studies in the meta-analysis are not statistically significant. In addition, forest plots are helpful when comparing smaller sub-groups (sensitivity analyses).

The funnel plot is a graphical representation of the effect size against the study's sample size (Kamboj, 2016). Funnel plots are simple scatter plots of the treatment effects estimated from individual studies (x-axis) against some measure of the corresponding sample size (y-axis) (Alderson et al., 2004). Funnel plots are helpful as they can detect a publication bias in the meta-analysis. Three observations on a funnel plot exhibit a publication bias: negative studies in the lower-left corner of the plot, the filling of the funnel by the plot (Kamboj, 2016), and asymmetry (Alderson et al., 2004). There are various potential causes of asymmetry, such as selection biases (due to factors such as location, language, and citation bias), the poor methodological quality of smaller studies, true heterogeneity (when the effect size depends on the study size), artefactual, and using an inappropriate effect measure (Alderson et al., 2004). A publication bias can cause the effect calculated in a meta-analysis to overestimate the treatment effect (Villar et al., 1997; Egger et al., 1997b). However, improving the quality of the conduct, analysis, and reporting of studies, meta-analyses, and systematic reviews can address a publication bias (Begg et al., 1996, Moher et al., 1995).



## 7.4 Results

### 7.4.1 Included Studies

#### 7.4.1.1 Novel Curing Procedures

Table 7.2 shows the qualifying studies with their corresponding statistical data: mean and standard deviation (SD) for the control and treatment runs as per the inclusion criteria outlined in Table 7.2.

**Table 7.2. Included studies for novel curing procedures.**

Literature Identity		Control			Treatment		
Author	Year	Mean	SD	No.	Mean	SD	No.
Chindaprasirt et al.	2013	20.96	7.59	10	26.38	9.29	36
Graytee et al.	2017	47.33	16.05	18	79	10.15	9
Hong and Kim	2019	44.25	32.88	6	53.9	14.49	51
Kastiukas et al.	2020	22.92	13.94	24	19.29	19.53	12
Narruddin et al.	2018	33	10.68	32	19.85	2.46	18
Onutai	2016	9.25	6.95	8	4.59	3.15	32

#### 7.4.1.2 Reinforcing Biomaterials

Table 7.3 shows the qualifying studies with their corresponding statistical data: mean and standard deviation (SD) for the control and treatment runs, using the inclusion criteria outlined in Section 3.2.

**Table 7.3. Inclusion criteria for reinforcing biomaterials.**

<b>Literature Identity</b>		<b>Control</b>			<b>Treatment</b>		
<b>Author</b>	<b>Year</b>	<b>Mean</b>	<b>SD</b>	<b>No.</b>	<b>Mean</b>	<b>SD</b>	<b>No.</b>
Baykara et al.	2020	3.68	0.59	12	3.57	0.61	6
Karthik et al.	2017a	34.17	1.15	36	26.17	1.35	12
Karthik et al.	2017b	29.76	5.55	18	23.79	4.95	6
Karthik et al.	2019	29.33	5.41	24	22.81	2.63	8
Korniejenko et al.	2016	24.56	7.75	12	24.78	1.89	3
Kumaravel and Sivakumar	2014	28.28	3.82	12	0	0	0
Long et al.	2019	9.5	0.68	8	6.8	0	2
Pham et al.	2019	42.61	9.5	24	32.05	0	8
Sarmin et al.	2019	27.04	7.02	30	59.16	18.33	10
Silva et al.	2020	21.03	13.59	20	24.24	16.27	20

#### 7.4.1.3 CNC

Using the inclusion criteria outlined in Section 3.2, the qualifying studies with their corresponding statistical data: mean and standard deviation (SD) for the control and treatment runs are outlined in Table 7.4. Certain literature studies had multiple experimental runs and were therefore differentiated by a bracketed number corresponding to the respective experimental run.

**Table 7.4 Qualifying studies included in the meta-analysis.**

<b>Literature Identity</b>		<b>Treatment</b>			<b>Control</b>			<b>Description</b>
<b>Author</b>	<b>Year</b>	<b>Mean</b>	<b>SD</b>	<b>No.</b>	<b>Mean</b>	<b>SD</b>	<b>No.</b>	
Barnat-Hunek et al.	2019	49.00	7.52	12	38.80	5.32	6	Concrete reinforcement
Dousti et al.	2019	32.20	20.46	8	25.18	18.03	8	Cement paste reinforcement
Cao et al. (1)	2016	16.24	2.02	32	14.75	3.23	8	Raw CNC
Cao et al. (2)	2016	18.38	2.95	32	14.43	3.40	8	Sonicated CNC (30 minutes)
Cao et al. (3)	2016	17.98	2.69	32	14.78	2.79	8	Sonicated CNC (120 minutes)
Cao et al. (4)	2016	19.96	2.04	32	17.20	0.35	8	28-day strength performance
Cao et al. (5)	2016	18.00	2.71	32	14.88	2.91	8	0.5 ratio of water reducing agent/CNC
Cao et al. (6)	2016	17.14	2.41	32	14.80	3.19	8	Unity ratio of water reducing agent/CNC
Cao et al. (1)	2013	12.78	1.32	10	10.40	0.00	2	3-day strength performance

Cao et al. (2)	2013	16.86	0.34	10	14.80	0.00	2	7-day strength performance
Cao et al. (3)	2013	17.34	0.96	10	16.00	0.00	2	21-day strength performance
Cao et al. (4)	2013	17.50	0.94	12	16.00	0.00	2	28-day strength performance
Mazlan et al. (1)	2015	35.33	5.03	6	28.00	0.00	2	7-day strength performance
Mazlan et al. (2)	2015	40.00	2.00	6	34.00	0.00	2	14-day strength performance
Mazlan et al. (3)	2015	45.67	6.11	6	36.00	0.00	2	28-day strength performance
Mazlan et al. (1)	2020	41.00	4.55	8	33.00	0.00	2	Lime-cured performance
Mazlan et al. (2)	2020	39.88	3.66	8	36.50	0.00	2	Water-cured performance
Mazlan et al. (3)	2020	43.18	5.01	8	31.50	0.00	2	Wrap-cured performance
Liu et al.	2019a	12.17	8.52	6	0.00	0.00	2	Cement paste reinforcement

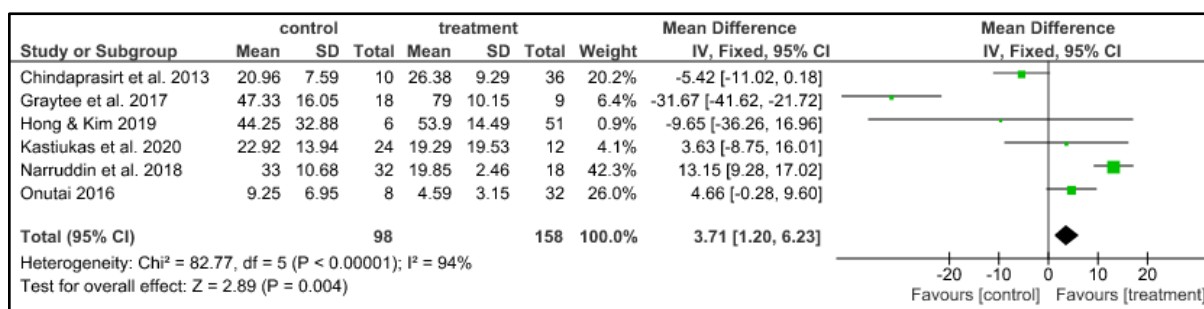
#### 7.4.2 Meta-analysis

The results of the RevMan software comprised the initial inputs (mean, standard deviation, and the number of experimental runs for the control and treatment) and the corresponding outputs (weight, mean difference, and heterogeneity) before undertaking any sensitivity analyses. A few experimental studies had only one control sample (Cao et al., 2016a; Cao et al., 2016b; Liu et

al., 2019; Mazlan et al., 2015; Mazlan et al., 2020), which zeroed the standard deviation and rendered the mean difference "not estimable." Duplicate experimental runs were assumed unless explicitly stated otherwise in the experimental methodologies of the individual studies.

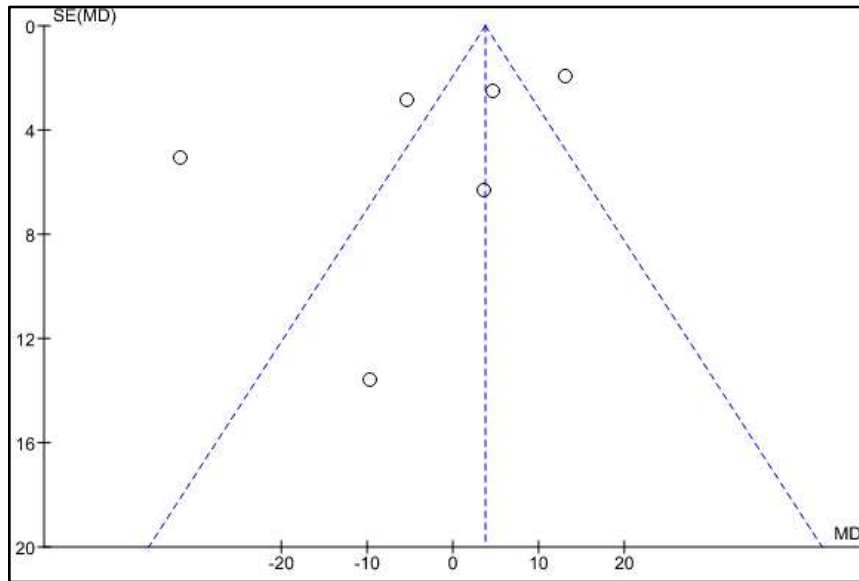
#### 7.4.2.1 Novel Curing Procedures

As shown in the forest plot of novel curing procedures (**Figure 7.2**), all the curing procedures were based on microwave curing techniques. The meta-analysis showed that the overall effect favoured the treatment (microwave curing over traditional curing). Although the treatment was favoured, microwave curing may not currently be practical due to the limited availability of laboratory-scale industrial microwaves.



**Figure 7.2. Forest plot for novel curing procedures**

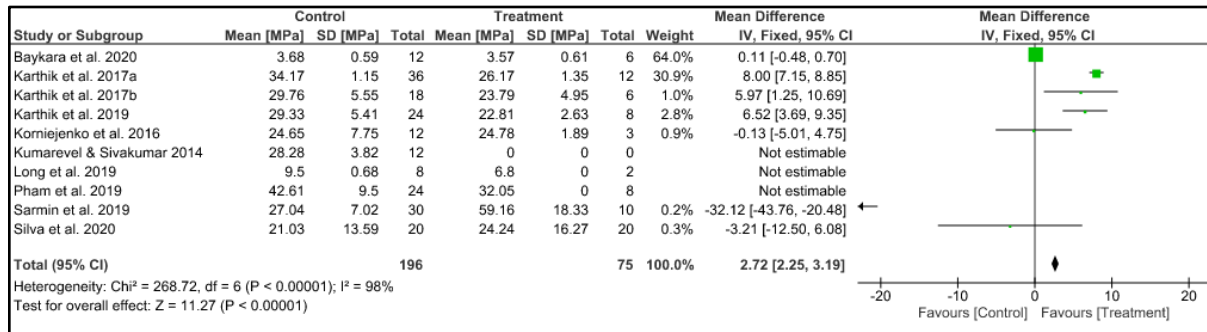
The corresponding funnel plot in **Figure 7.3** was slightly asymmetric and showed one possible indication of a publication bias: distributed studies within the funnel. This finding was attributed to the fact that the novel curing procedures found in the literature were limited to microwave curing. The publication bias indicated that the meta-analysis could not be deemed accurate.



**Figure 7.3. Funnel plot for novel curing procedures**

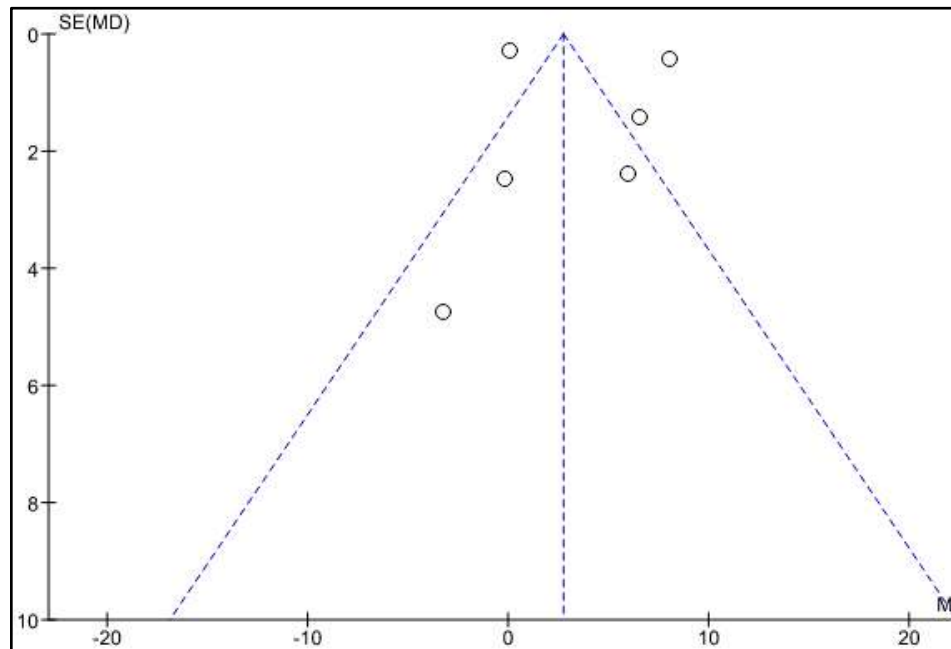
#### 7.4.2.2 Reinforcing Biomaterials

As shown in the Forest plot in **Figure 7.4**, the overall effect of reinforcing bio-additives in construction materials was favourable to the control. This finding implied that using suitable bio-additives to improve the mechanical properties of construction materials is worth consideration. One such biomaterial to be considered is CNC. Therefore, the subsequent meta-analysis study was based on applying CNC to improve the strength of construction materials. Considering that the second aim of this study focused on the influence of CNC on the strength of construction materials, two sensitivity analyses were performed to obtain detailed quantifications on which to base further experimental work which considers the application of CNC.



**Figure 7.4. Forest plot for reinforcing biomaterials.**

The corresponding funnel plot (**Figure 7.5**) showed an almost symmetric distribution of studies. Furthermore, the studies were concentrated towards the apex of the inverted funnel and were not filled with the individual studies. Therefore, the possibility of a publication bias was refuted.

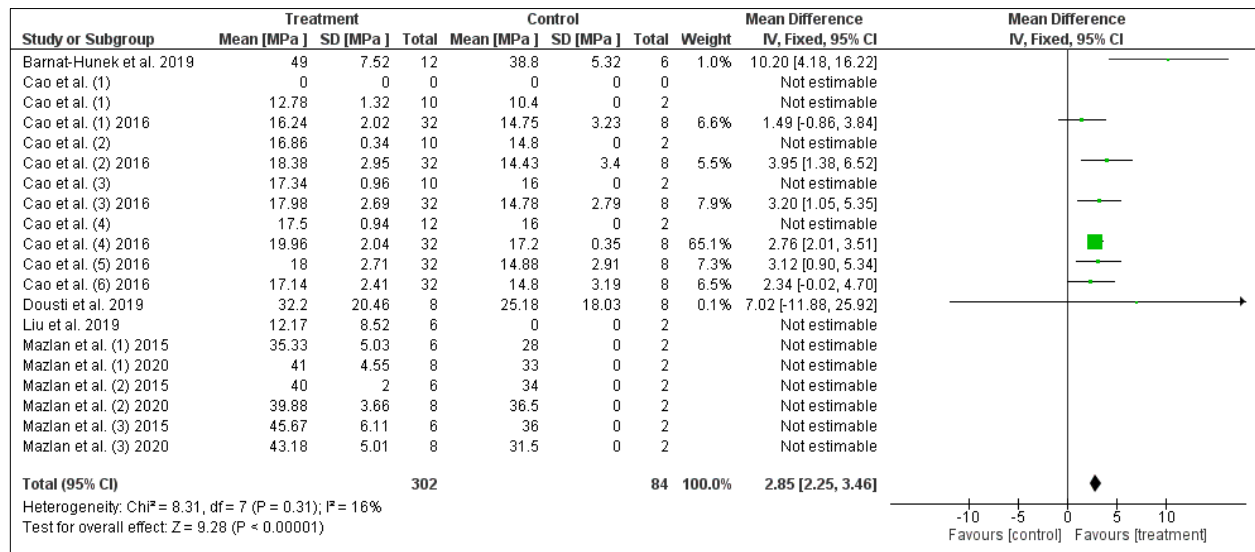


**Figure 7.5. Funnel plot for reinforcing biomaterials.**

#### 7.4.2.3 CNC

**Figure 7.6** (the forest plot for the overall meta-analysis) showed the individual study effects (indicated by square blocks) in the treatment scale. This finding implied that each of the individual studies favoured the treatment. Consequently, the overall effect (indicated by the diamond) was found in the treatment scale. Both phenomena indicated that the desired result of

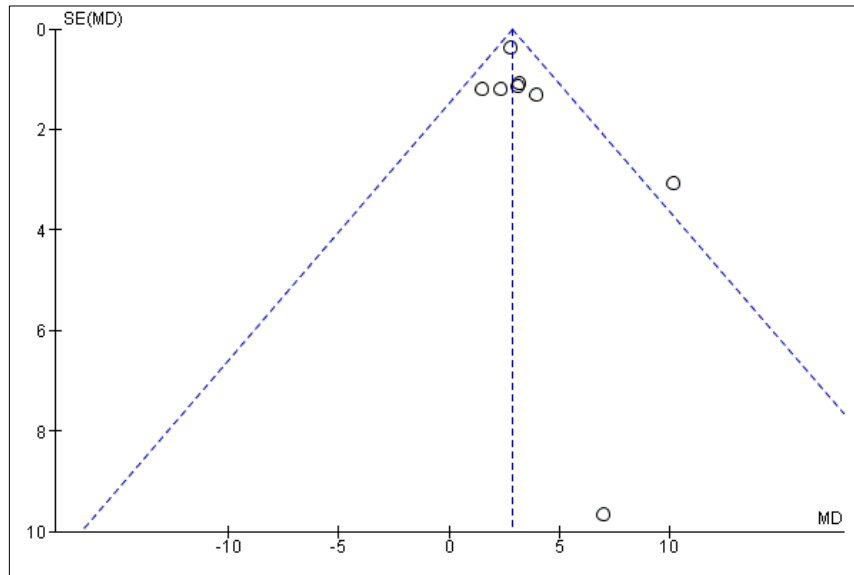
improved strength in construction materials would be obtained under the influence of the treatment (a reinforcement with CNC). This finding indicated that using CNC to reinforce construction materials would yield greater compressive and flexural strengths. These results were statistically significant because the confidence interval of the individual studies did not pass through the line of no effect, except the study of Cao et al. (1) (2016a) (Alderson et al., 2004). The relatively low overall heterogeneity of 16% implied homogeneity among the individual results of the studies included in the overall meta-analysis.



**Figure 7.6. Overall Meta-analysis and Forest Plot**

The overall funnel plot shown in **Figure 7.7** revealed a symmetric distribution of the included studies towards the apex of the inverted funnel. Furthermore, there was a conspicuous absence of the two traits indicating a potential publication bias: negative studies in the left corner of the plot and the filling of the funnel with the plot (Alderson et al., 2004). Both findings positively indicated the absence of a publication bias in the meta-analysis.

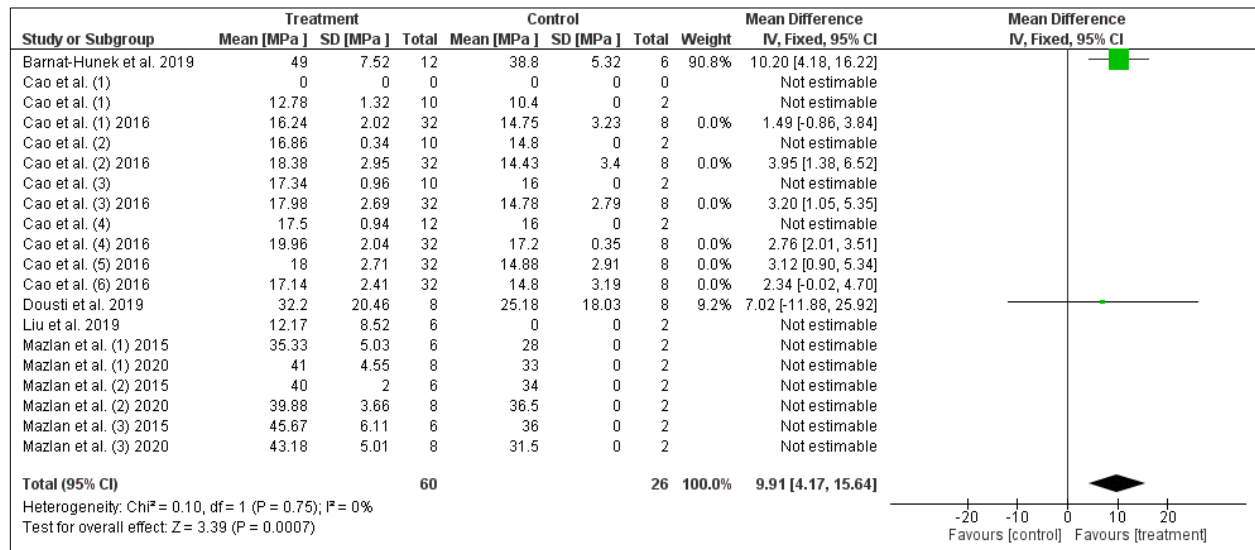




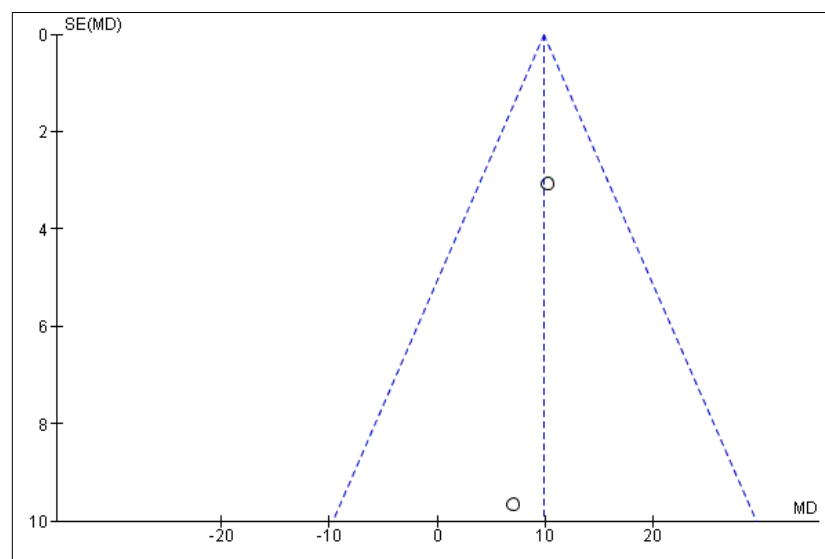
**Figure 7.7. Overall Funnel Plot**

#### 7.4.2.3.1 Sensitivity Analysis 1: Compressive Strength Response

The meta-analysis and corresponding forest plot for the sensitivity analysis comprising the compressive strength responses are shown in **Figure 7.8** and **Figure 7.9**, respectively. The first sensitivity analysis was based on the compressive strength studies from the overall meta-analysis to determine the effect of CNC reinforcement on the resulting compressive strength of the construction materials. The forest plot showed that the treatment (CNC reinforcement) favoured the compressive strength. The forest plot identified the study of Dousti et al. (2019) to be statistically insignificant. However, the study of Barnat-Hunek et al. (2019) exhibited a 98% weight and strongly indicated that the treatment was favoured. Furthermore, a 0% heterogeneity was observed. Additionally, the funnel plot showed no signs of publication bias (Alderson et al., 2004).



**Figure 7.8. Meta-analysis and Forest Plot for Sensitivity Analysis 1**

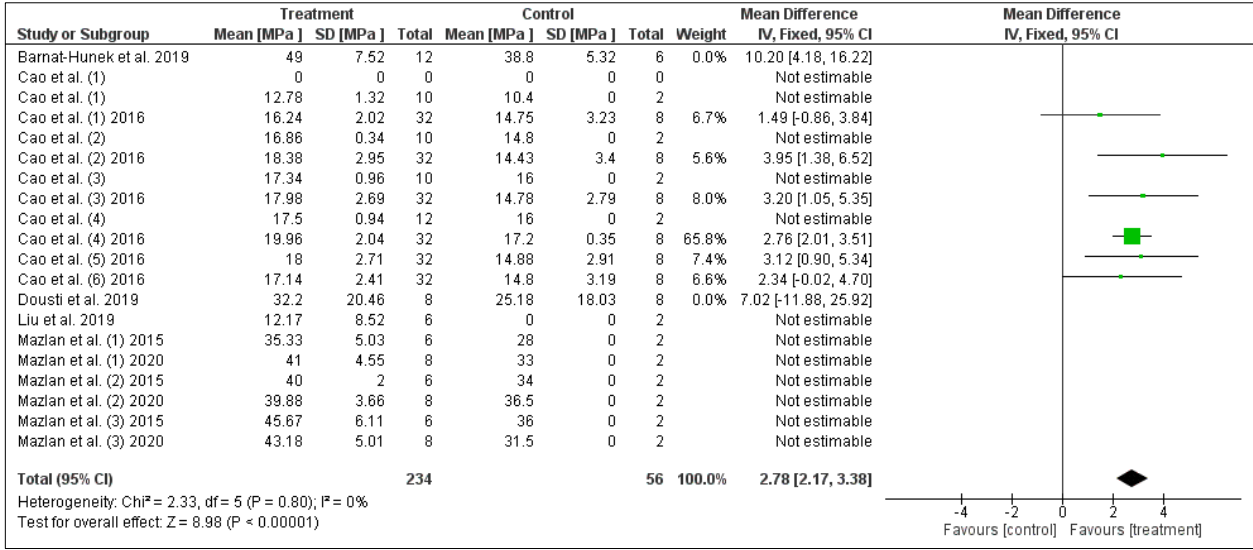


**Figure 7.9. Funnel Plot for Sensitivity Analysis 1**

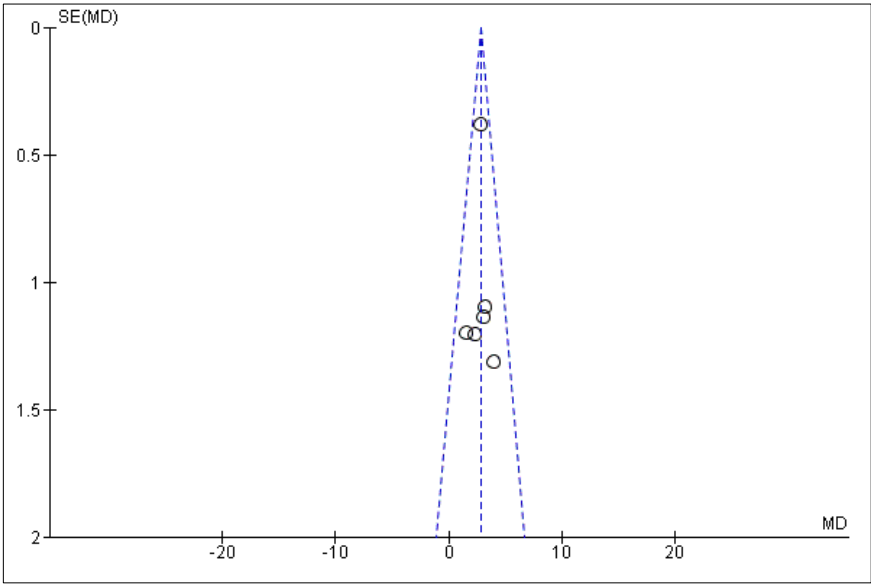
#### 7.4.2.3.2 Sensitivity Analysis 2- Flexural Strength Response

**Figure 7.10** and **Figure 7.11** show the meta-analysis and corresponding forest plot for the sensitivity analysis comprising the flexural strength responses. The second sensitivity analysis demonstrated the effect of CNC reinforcement on the flexural strength of construction materials. All five studies favoured the treatment, as shown by the overall effect on the treatment scale. Of the five studies included in this sensitivity analysis, 80% of the studies were

statistically significant. Furthermore, this sensitivity analysis yielded zero heterogeneity. The funnel plot showed a symmetrical distribution of the individual studies with no signs of publication bias. These findings validated the accuracy of the sensitivity results.



**Figure 7.10. Meta-analysis and Forest Plot for Sensitivity Analysis 2**



**Figure 7.11. Funnel Plot for Sensitivity Analysis 2**

## 7.5 Discussions

### 7.5.1 *Meta-analyses*

Although the meta-analysis for the novel curing procedures indicated an overall positive effect, microwave curing is a relatively new technology with limited availability of suitable microwave ovens. Therefore, microwave curing may not be practical for implementation in the short-term development of novel green construction materials. Further studies on microwave curing and other novel curing procedures are required to prevent potential publication biases in the meta-analyses. The presence of the publication biases further implied that the actual effect of the novel curing procedures might not favour the optimal development of mechanical properties in construction materials.

The overall positive effect of bio-additives in construction materials is beneficial in fortifying construction materials. This finding indicated the potential viability of CNC to improve the mechanical properties of construction materials. No publication biases were observed, thus validating the accuracy of the meta-analysis.

Overall, the inclusion criteria were successful in isolating the relevant experimental research used in the meta-analyses. Regarding the effect of CNC, the overall meta-analysis was based on the effect of CNC on the compressive strength and flexural strength of construction materials. It was notable that the aggregate effect of the overall meta-analysis indicated that the treatment was favored. Hence, the overall effect of CNC reinforcement in construction materials was linked to improved mechanical properties.

Three measures validated the reliability of the meta-analysis results. Firstly, the PRISMA guidelines dictated the study. Secondly, the funnel plot detected the undermining effect of a publication bias. It was noteworthy that no publication bias was present in the study. Thirdly, most of the confidence intervals of the individual studies included in the overall meta-analysis did not pass through the line of no effect. This finding implied that a significant proportion of the contributing studies were statistically significant. These factors were aligned to the meta-

analysis capabilities described by Arnqvist and Wooster (1995) as objective quantitative analysis of the magnitude of effects based on a standardized set of statistical procedures.

When the overall meta-analysis was divided into two response categories (compressive strength and flexural strength) to ensure that a positive effect of CNC reinforcement on the individual strength categories, improved strength performance was observed for both strength responses. The three-fold reliability measures discussed for the overall meta-analysis validated these results. Furthermore, these results were significant as they indicated the potential benefit in experimentally investigating the addition of CNC in green construction materials. These findings are relevant to researchers and industries attempting to make strides in the development of novel green construction materials using CNC as a potential reinforcing agent.

The overall validation of CNC as a potential reinforcing agent in construction materials agreed with the literature (Cao et al., 2016a; Cao et al., 2016b; Barnat-Hunek et al., 2019; Dousti et al., 2019; Liu et al., 2019; Lee et al., 2019a; Lee et al., 2019b; Mazlan et al., 2016). These individual studies proved the benefits of CNC in improving the strength properties of the construction materials investigated in the respective studies.

Considering the increasing number of engineering publications in construction materials, the meta-analysis is a valuable method of quantitative summarising to generate higher-order conclusions (Arnqvist and Wooster, 1995) concerning CNC as a potential reinforcement agent in construction materials to achieve improved strength properties. Considering that the meta-analysis proved that it would be worthwhile to apply CNC in the enhancement and development of green construction materials, it fulfilled the recommendation of Zhuang et al. (2016). Furthermore, the positive result obtained from the meta-analysis implied that further research could be undertaken to develop enhanced green construction materials using CNC. A framework ensuring uniformity in developing and producing CNC-enhanced green construction materials should be developed (Singh and Middendorf, 2020).

### ***7.5.2 Application of Meta-analysis in Engineering Research***

Although meta-analyses are used widely in healthcare studies, it is seldomly applied to engineering studies. Considering the vast quantity of engineering literature, this study demonstrated the applicability and user-efficiency of meta-analyses using RevMan software. Meta-analyses must be undertaken before experimental research for two primary reasons. Firstly, the meta-analysis can predict whether the considered effect would yield a favourable response. This capability has practical implications, as it avoids expensive and time-consuming experimental research if the responses are unfavourable. Secondly, suppose the meta-analysis exhibits a positive response for effect. In that case, it can refine a study through informed estimates of the effect quantity to obtain the desired response range, evidence-based design of experiments, and the development of computational models (Alderson et al., 2004).

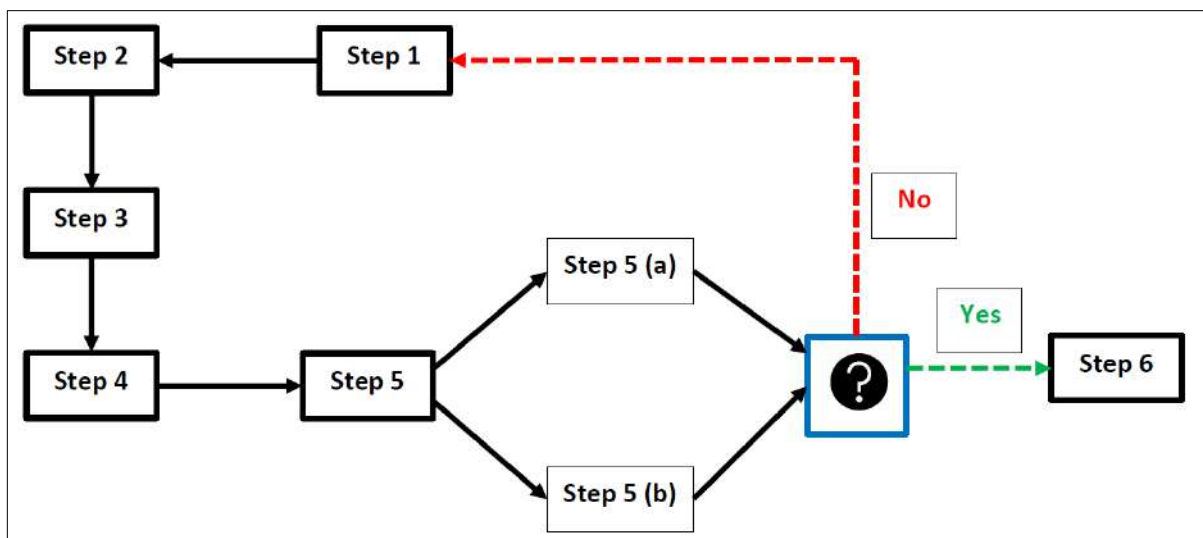
The implication is that academics and industrialists can include meta-analyses in research projects to streamline and optimize their research and development by saving time and money in their experimental or trial studies. The literature (Glass, 1976; Arnqvist and Wooster, 1995; Kamboj, 2016; Alderson et al., 2004; Mikolajewicz and Komarova, 2019) validated the usefulness and applicability of the meta-analysis to this engineering study. This study documented the use of RevMan software in performing meta-analyses and sensitivity analyses to enable the replication and application of these methods in further studies. Considering that the meta-analysis addressed the core argument in this study, the methodology and use of RevMan software were beneficial.

### ***7.5.3 Framework for Conducting Meta-analyses***

Based on the research conducted in this study, the empirical framework was recommended to undertake meta-analyses (**Figure 7.12**). It was notable that although this research aimed to elaborate the functions and usefulness of meta-analyses as an engineering tool, the framework can be applied to multi-disciplinary studies. The steps are outlined below.

- 1) Collection of the relevant literature experimental data.
- 2) Extraction of the relevant data for the treatment and control studies.
- 3) Calculation of the required statistical parameters for each study comprising the meta-analysis: mean and standard deviation.

- 4) Specification of the required statistical parameters from step 3 into the meta-analysis software.
- 5) Analysis of the outputs: (a) Forest plot and (b) Funnel plot.
- 6) The forest plot must be analyzed to determine if the overall effect is located in the treatment or control region. The location of the overall effect indicates if the applied treatment will yield the desired result.
- 7) The funnel plot must be analyzed for publication bias. If undesirable results are found in steps 5 (a) or 5 (b), the process must be restarted at step 1. If not, then step 6 can be attempted.
- 8) Further experimental work can be initiated to optimize the effect of the applied treatment.



**Figure 7.12. Empirical framework for conducting meta-analyses.**

## 7.6 Conclusions

Green construction materials must be considered as an alternative to reduce the use of greenhouse gas producing OPC. However, green construction material alternatives must undergo further development to close the gaps between laboratory-scale production and commercial-scale production and distribution. An empirical model is needed to ensure uniformity in developing and producing the proposed CNC-reinforced green construction

materials. Considering that the meta-analyses can quantify the relevant literature studies on a topic concerning the overall effect of a treatment, it is a valuable tool that can prevent extensive laboratory studies from determining the effect of a treatment. Furthermore, meta-analyses can guide further experimental research by optimizing the experimental ranges and conditions to save money and time, thus expediting experimental research. Such optimization features can benefit dynamic fields that require rapid results, such as green construction materials development.

The meta-analysis proved that CNC as a reinforcing bio-additive (among others) exhibited a positive impact on conventional construction materials' compressive and flexural strength. Hence, further investigations of the impacts of CNC on fly ash-based geopolymer construction materials should be undertaken. In addition, the study recommends that characterization studies on the CNC. Such characterization would help ascertain the effects of different grades of CNC on the resulting reinforced geopolymers.

In the overall development of green construction materials, the key stakeholders are researchers and academics, construction industry leaders, industries producing the waste precursors, and the government. Academics and researchers can use meta-analyses to expedite their research and development activities to produce accurate and reliable results. These results can be shared with construction industry leaders to guide and optimize the scale-up of viable green construction materials from technical and economic viewpoints. The government can provide funding to construction industry leaders to offset the initial start-up costs as an incentive for producing green construction materials with zero or low carbon emissions. Finally, the industries producing the waste precursors used to produce the green construction materials can divert the required quantities of these wastes to the manufacturers of the green construction materials instead of traditional environmental-degrading disposal methods. **Figure 7.13** shows the graphical relationship between the key stakeholders and their corresponding contributions.

The findings addressed the argument as the application of CNC in construction materials was statistically proven to improve the mechanical properties (compressive strength and flexural



strength). Hence, it is worthwhile to undertake further studies to determine the effect of CNC on the mechanical properties of green construction materials.



**Figure 7.13. Relationship between the critical stakeholder contributions**

## **CHAPTER 8: USING CNC TO IMPROVE THE MECHANICAL PROPERTIES OF FLY ASH-BASED GEOPOLYMER CONSTRUCTION MATERIALS**

### **8.1 Introduction**

Environmental concerns remain one of the main challenges faced by the cement industry (Imbabi et al., 2012). The production of ordinary Portland cement is energy-intensive and a significant contributor to industrial greenhouse gas emissions (Komnitsas, 2011). Considering the growing global population, novel green alternatives to ordinary Portland cement are required to improve the sustainability of the construction industry. Fly ash-based geopolymers are a viable alternative to ordinary Portland cement in the building industry (Imbabi et al., 2012, Komnitsas, 2011). However, more research is required to determine how fly ash-based geopolymers can be enhanced to become commercially viable and reliable to replace ordinary Portland cement completely. One option considered in this study was CNC as a reinforcing component in fly-ash-based geopolymers. CNC are nanoparticles derived from cellulose, a renewable resource. Due to their unique optical, rheological, and mechanical properties, CNC are finding widespread applications in the construction, automotive, paper, medical and food sectors. It is a high-strength polymer material whose mechanical properties compare favourably and often exceed traditional reinforcement materials such as stainless steel and Kevlar (Moon et al., 2011).

As part of a more extensive study, a systematic meta-analysis concluded that CNC positively impacted the mechanical properties of construction materials. The aggregate effect of the studies included in the meta-analysis revealed that CNC reinforcement exhibited a positive effect on the compressive strength improvement in ordinary Portland cement construction materials. This effect indicated that it would be beneficial to perform further experimental studies to investigate the reinforcement capabilities of CNC in developing a novel, green construction material using industrial waste streams such as fly ash and sawdust used as a source of cellulose to produce CNC. Both waste streams are disposed of by landfilling or stockpiling, and in the case of sawdust, it is also burned.

The aims of this study were threefold. The first aim was to evaluate the effects of the alkaline activator concentration and CNC concentration on the mechanical properties of fly ash-based geopolymer construction materials. The second aim was to produce a database of the effects of CNC concentration and activator concentration on the mechanical properties of the formed geopolymers in the form of three-dimensional surface response plots. Finally, the third aim entailed developing a globally applicable framework to produce green construction materials based on the work involved to meet the first two aims. Therefore, CNC-enhanced geopolymer construction materials as a green alternative to ordinary Portland cement, upon which the empirical green construction material development framework was based, could contribute to achieving long-term sustainability of the construction industry.

## **8.2 Literature Review**

### ***8.2.1 Overview of the Current State of the Construction Industry***

The construction industry is challenged by depleting fossil fuel reserves, scarce raw materials, increasing demand, growing environmental concerns, and a stagnant world economy (Imbabi et al., 2012). The production of ordinary Portland cement contributes to approximately 6% of all industrial carbon emissions (Imbabi et al., 2012) and 5 to 7% of the emissions directly responsible for global warming (Imbabi et al., 2012). The calcination phase of the ordinary Portland cement production process results in the greatest proportion of carbon dioxide emissions (Imbabi et al., 2012). Two methods were recommended to decrease the carbon dioxide emissions: changing the raw materials in the calcination process or changing the manufacturing process (Imbabi et al., 2012). Considering that these recommendations cannot be easily implemented, greener alternatives are required. Green materials are environmentally friendly, durable, bio-based, recycled, and exhibit low toxicity and emissions (Imbabi et al., 2012). There exists a rapidly expanding market for green building materials (Imbabi et al., 2012). Fly ash, blast furnace slag, and silica fumes are typical cement replacement materials that have been documented and validated (Imbabi et al., 2012).

Geopolymers are cementitious materials with three-dimensional structures formed by activating aluminosilicate materials at low temperatures (Komnitsas, 2011). Geopolymer cement is

produced from secondary raw materials such as fly ash and metakaolin by activating alkali and alkali silicate solutions. It is noteworthy that several waste materials can be utilized to produce geopolymer construction materials. This finding enables energy and carbon dioxide savings in the construction sector, substantiating the classification of geopolymers as green construction materials.

Despite the advantages of geopolymers as green construction materials, further work is required to improve the technology and strengthen the potential for commercial applications (Komnitsas, 2011). To realize the implementation of green construction materials, price stability is mandatory (Imbabi et al., 2012). Considering that building practitioners identified high initial cost premiums as barriers to investing in green practices (Komnitsas, 2011), government subsidies must be made available to green cement manufacturers. Furthermore, the knowledge gap between researchers and practitioners should be closed. Regulatory standards are required to enable optimized and uniform geopolymerization processes (Singh and Middendorf, 2020).

### ***8.2.2 Overview of Green Construction Materials***

Green construction materials are defined as being comprised of at least one waste material, or its production is environmentally friendly, or it has high performance and life cycle sustainability (Suhendro, 2014). Considering that cement manufacture accounts for 8 to 10% of the total global carbon dioxide emissions (Suhendro, 2014), green construction materials are coveted as they reduce the demand for natural resources, the associated energy consumption, and greenhouse gas emissions (Abbas et al., 2006; Shadab et al., 2017). The use of green construction materials prevents the mining of exorbitant quantities of naturally occurring materials for concrete production (Baikerikar, 2014). Green construction materials are advantageous because they reduce environmental pollution, are comparatively economical, and exhibit good thermal and acid resistance (Baikerikar, 2014; Duxson et al., 2007; Mohd Mustafa Al-Bakri, 2012). The use of waste materials results in better compressive and tensile strength, improved sulfate resistance, decreased permeability, and improved workability (Baikerikar, 2014). Green concrete shows more excellent durability, strength development, thermal resistance, and lower shrinkage than Portland cement (Garg and Jain, 2014). The use of fly ash

in green construction materials saves valuable landfill space. It reduces the energy consumption of the production process (Shadab et al., 2017) by eliminating the combustion of fuel and the decomposition of limestone (Mohd Mustafa Al-Bakri et al., 2012).

### ***8.2.3 Fly ash-based geopolymers as Green Construction Materials***

Substantial quantities of fly ash are generated globally, thus posing a severe threat to the environment (Gollakota et al., 2014). Therefore, fly ash as precursor materials in geopolymer production is recommended (Gollakota et al., 2014). The silicone to aluminium ratios, the type and amount of the alkali solution, temperature, curing conditions, and additives are critical factors in the geopolymerization process (Zhuang et al., 2016). The mechanical properties of fly ash-based geopolymers depend on the chemical composition, chemical bonding, and porosity of the geopolymer (Zhuang et al., 2016). The mechanical properties can be improved by adjusting the silicone to aluminium ratios, alkali solutions, curing conditions, and reinforcing agents (Zhuang et al., 2016). Although fly ash-based geopolymers can be used as novel green cement, further studies on fly ash-based geopolymers are recommended to enhance the mechanical performance, scale-up production, and explore new applications (Zhuang et al., 2016).

### ***8.2.4 CNC to Enhance Geopolymer Construction Materials***

Combining the endorsement of biomaterial applications in construction materials (Pacheco-Torgal, 2016) with the global emergence of geopolymers as novel green construction materials (Imbabi et al., 2012; Komnitsas, 2011; Singh and Middendorf, 2020), the application of CNC in the fortification of fly ash-based geopolymers should be considered. CNC are a relatively new class of biomaterials known for their high-strength applications. The production of CNC is environmentally friendly as it can be produced from waste biomass materials.

Cao et al. (2016a) investigated the influence of raw and sonicated CNC on the microstructure of cement paste. Considering that the dispersion of CNC within the geopolymer matrix is a known challenge, a novel method to measure the concentrations of the adsorbed CNC (on the cement surface) and the free CNC (mobile in water) was developed. Most of the CNC (above 94%) actively comprised the cement matrix. Furthermore, the total porosities of cement pastes

with raw and sonicated CNC were determined. The results indicated total porosities of 14.8% and 14.4%, respectively, reducing 16%. It was expected that the decreased sample porosity would yield better strength properties. The sonicated CNC were well dispersed, thereby preventing the formation of agglomerates that can lead to pores, voids, and air entrapment in cement pastes.

Furthering the research of Cao et al. (2016a), the study of Cao et al. (2016b) determined the influence of CNC dispersion within the cement matrix on its strength by investigating the agglomeration of CNC. Agglomeration is undesirable, as it inhibits the dispersion of CNC within the cement matrix. Ultrasonication was used to disperse the CNC, and rheological measurements quantified the agglomeration extent. Agglomerates began to develop when the CNC concentration exceeded 1.35% by volume. A geometrical percolation model verified this experimental finding. According to the model, the threshold CNC concentration resulting in agglomeration was 1.38%. This finding was significant as it indicated that nanocrystals concentration should not be exceeded to prevent agglomeration.

Furthermore, it was found that the optimal CNC concentration for maximum strength development was 0.18%. It is noteworthy that a relatively minute quantity of CNC is required to achieve maximum strength development. A similar result was found in the study of Ghahari et al. (2020), where a 0.2% concentration of CNC improved the compressive strength and fracture properties of the geopolymer. The ultrasonication effectively dispersed the CNC within the cement matrix, resulting in strength improvements of up to 50%, which was greater than the strength improvement of raw CNC alone (20 to 30%). This finding indicated that the dispersion of CNC significantly improves the flexural strength of cement pastes. Although this study was undertaken using cement paste, the novel dispersion method can be applied to geopolymers to enhance green construction materials.

Geopolymers are not fully commercialized due to two uncertainties: financial (Imbabi et al., 2012) and technical (Singh and Middendorf, 2020). The research below demonstrates the technical benefits achieved by the application of CNC in construction materials. Although some

research has focused on CNC addition to ordinary Portland cement, the paradigm can be applied to geopolymers to produce fortified green construction materials.

The study of Barnat-Hunek et al. (2019) determined the effect of CNC on the physical properties of concrete. The study found that CNC improved the freezing-thawing resistance more than 14-fold. This result is exceptional for construction applications required to withstand extreme temperature conditions and was attributed to the efficiency of nanocellulose in concrete hydrophilization. This result was consistent with the study of Cao et al. (2016a). Overall, the CNC promoted the formation of calcium-silicate-hydrate in the concrete, which improved the density and changed the pore structure and interface characteristics. The improved density resulted in improved concrete strength. A similar finding was observed in the study of Dousti et al. (2019). The porosity was reduced by 33%, and the surface area was reduced by 66% by the addition of CNC. The CNC addition increased the compressive and tensile strength by 60% in the first 24 hours. The study of Dousti et al. (2019) was novel as it investigated the effect of CNC on the hydration of cement paste. The CNC promoted the formation of hydration products, resulting in greater compressive and tensile strengths.

The study of Liu et al. (2019a) investigated the effect of CNC on the compressive strength of cement pastes. X-ray computed tomography and nitrogen adsorption analyses revealed that the CNC refined the pore structure in the cement matrix. Almost no hydration products were formed in the cement matrix without CNC addition. Like the research of Liu et al. (2019a), the study of Lee et al. (2016a) investigated the effect of CNC on the mechanical performance of construction materials. The CNC solutions were prepared in the following concentrations by volume: 0.4, 0.8, and 1.2. As recommended in the research of Cao et al. (2016a), Cao et al. (2016b), and Lee et al. (2019b), ultrasonication was used to disperse the CNC in the aqueous solutions. The optimal CNC solution concentration was found to be 0.8% by volume as it improved the shrinkage rate and mechanical performance. This finding reinforced previous research that found that only a small quantity of CNC is required to develop maximum strength development in construction materials (Imbabi et al., 2012).

According to the study of Flores et al. (2017), the addition of CNC to the geopolymer mixture initially delays the hydration but improves the hydration at later stages. It was also revealed that CNC increased the non-evaporable water content to the control mixture. Two CNC concentrations were investigated: 0.4 and 0.8%. At both concentrations, the non-evaporable water content was improved. This finding supported the idea that at higher CNC concentrations, the alkaline activator was slightly diluted due to the additional water content from the solution of CNC. This finding decreased the effectiveness of the alkaline activator. Furthermore, the CNC particles fill the smallest gaps in the mixture paste, thus decreasing the porosity of the sample (Rahmawati et al., 2021).

#### ***8.2.5 The Effect of Alkaline Activators in Geopolymerization***

In the study of Hadi et al. (2018), fly ash with a high aluminosilicate content was activated at lower dosages of sodium silicate and sodium hydroxide. The opposite effect was observed for fly ash with lower aluminosilicate content, which implied that greater activator concentrations are required to activate geopolymers. In the study of Roopchand (2016), the alkaline activator concentration was varied between 6 M to 16 M and was found to be directly proportional to the compressive strength of the resulting geopolymers. The study of Hamidi et al. (2016) investigated the effect of the alkaline activator concentration on the flexural strength of the geopolymer. The activator concentration was directly proportional to the flexural strength until the activator concentration of 12 M was reached. Subsequently, a decline in flexural strength was observed, implying that the 12 M concentration was optimal for flexural strength development.

#### ***8.2.6 Corrosion Resistance in Construction Materials***

The corrosion process in concrete is partially controlled by the transport of ions through the concrete microstructure (Azarsa and Gupta, 2017; Hornbostel et al., 2013). Considering that ions are charged, the ability of a material to resist the transfer of charge depends on its electrical resistivity (Hornbostel et al., 2013). Thus, a relationship is expected between the concrete corrosion and the corresponding electrical resistivity. Although the studies of Alonso et al. (1988), Zainal et al. (2015), and Song and Saraswathy (2007) found clearly defined relationships of inverse proportionality between the electrical resistivity and corrosion



resistance of construction materials, specific experimental requirements are outlined to study the relationship between concrete corrosion and electrical resistivity (Hornbostel et al., 2013):

- a) A working electrode, preferably construction steel embedded in a mortar or concrete sample, reflects practice-related conditions.
- b) A technique to measure corrosion rate, either from the surface or as an embedded device.
- c) A technique to measure concrete resistivity.
- d) A method to initiate corrosion.

The research of Song and Saraswathy (2007) presented an experimental study of the electrical resistivity of geopolymer paste using the Wenner four-probe method. The range of electrical resistivity values obtained varied between 537  $\Omega\cdot\text{m}$  and 61575  $\Omega\cdot\text{m}$ . As with previous studies, a relationship of inverse proportionality between the electrical resistivity and corrosion rate was exhibited (Azarsa and Gupta, 2017; Alonso et al., 1988; Zainal et al., 2015). A guideline to determine the potential corrosion resistance of a construction material based on its electrical resistivity is indicated in Table 8.1.

**Table 8.1. Literary correlations between the electrical resistivity and corrosion resistance of construction materials**

Corrosion Risk	Resistivity Values ( $\Omega\cdot\text{m}$ )	
	Hornbostel et al. (2013)	Song and Saraswathy (2007)
High	< 100	< 50
Moderate	100 to 500	50 to 100
Low	500 to 1000	100 to 200
Negligible	> 1000	> 200

The electrical resistivity of concrete depends on two broad categories: intrinsic factors and factors affecting the resistivity measurements (Azarsa and Gupta, 2017). The intrinsic factors include the water to cement ratio, aging, and pore structure. In contrast, the resistivity measurements' factors include the specimen geometry, moisture content, temperature, electrode

spacing, and presence of rebar. Furthermore, adding reactive supplementary cementitious materials such as blast furnace slag and fly ash leads to higher electrical resistivity due to reduced capillary porosity and hydroxyl ions.

Electrical resistivity measurements can be undertaken using electrodes positioned on a specimen surface or placing an electrode-disc or linear array or a four-probe square array on the concrete's surface (Zainal et al., 2015; Swanson et al., 2020). Four principle device techniques are used to measure resistivity: bulk electrical resistivity test, surface disc test, Wenner four-point line array test, and four-probe square array test.

## **8.3 Materials and Methods**

### **8.3.1 Materials**

#### **8.3.1.1 Fly Ash**

The fly ash was sourced from Matla Power Station (Eskom) in South Africa. It was classified as Class F, with a silicon to aluminium ratio of unity and a low organic content (characterized by a loss on ignition value less than 5%). It was identified as a suitable precursor fly ash material to be used to produce the geopolymers.

#### **8.3.1.2 Sawdust-based CNC**

The sawdust was obtained from Sappi sawmills in South Africa. Considering that the South African Forestry sector's overall yield is only 47% (Sithole, 2017), it is deemed wasteful. To improve the industry's sustainability, sawdust was identified as a viable by-product that could be used to produce CNC, a high-value organic material with a wide variety of applications. The CNC were produced using proprietary technology and were subsequently used as a reinforcing agent for the geopolymer construction materials in this study.

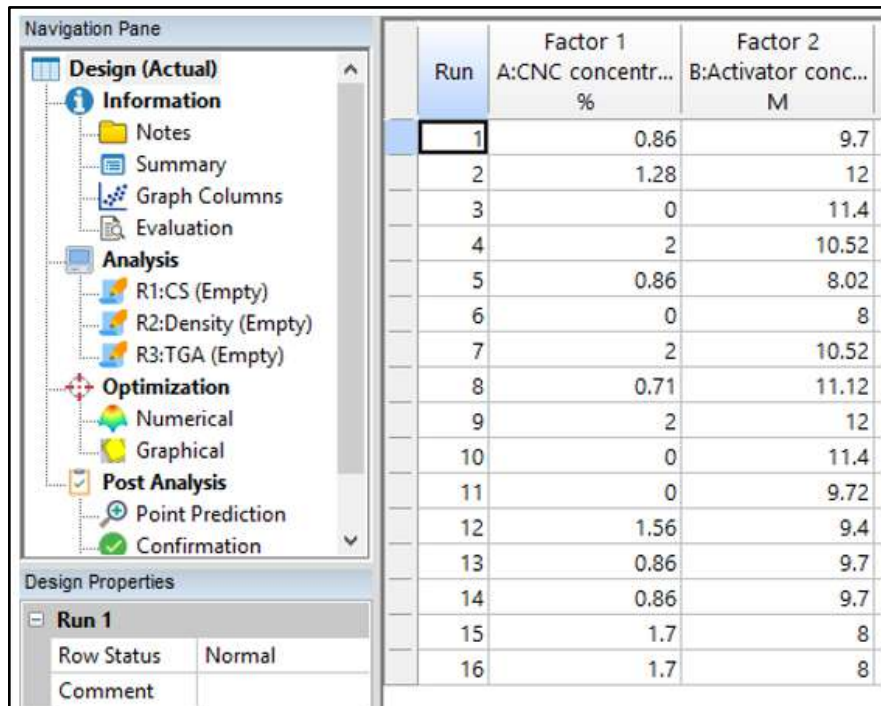
### **8.3.2 Geopolymer Mixture Design**

A trial-and-error procedure was used to design the optimal geopolymer mixture ratios of the comprising components: fly ash, water, alkaline activator, and CNC suspension. The optimal ratio resulted in mixture consistency and workability to allow practical moulding. This optimal

ratio was 60.8 ml of the liquid component (comprising the alkaline activator and CNC solution) to 100 g of the fly ash. The liquid component was comprised of 75% alkaline activator and 25% CNC suspension. For the trials that did not require CNC solution, deionized water was used instead. The geopolymers required multiple tests. Hence it was notable that the mixture design produced four geopolymer cubes per trial.

### 8.3.3 Statistical Experimental Design

The experimental trials entailed variation of the alkaline activator concentration and the CNC concentration. The Design Expert software was used to design the experimental trials to optimize the trial runs statistically. An optimization purpose was selected, and a response surface model was chosen. The response surface model enabled the effects of the parameters (alkaline activator concentration and CNC solution concentration) to be visually observed on a single three-dimensional surface curve. Based on the design requirements, the software's experimental plan was calculated and output as shown in **Figure 8.1**. The combination of the variation factors resulting in the 16 experimental runs can be observed.



The screenshot displays the Design Expert software interface. On the left is the 'Navigation Pane' with a tree view containing 'Design (Actual)', 'Information' (Notes, Summary, Graph Columns, Evaluation), 'Analysis' (R1:CS (Empty), R2:Density (Empty), R3:TGA (Empty)), 'Optimization' (Numerical, Graphical), and 'Post Analysis' (Point Prediction, Confirmation). Below this is the 'Design Properties' section for 'Run 1', showing 'Row Status' as 'Normal' and an empty 'Comment' field. The main area on the right is a table of 16 experimental runs.

Run	Factor 1 A:CNC concentr... %	Factor 2 B:Activator conc... M
1	0.86	9.7
2	1.28	12
3	0	11.4
4	2	10.52
5	0.86	8.02
6	0	8
7	2	10.52
8	0.71	11.12
9	2	12
10	0	11.4
11	0	9.72
12	1.56	9.4
13	0.86	9.7
14	0.86	9.7
15	1.7	8
16	1.7	8

**Figure 8.1. Summary of the statistical experimental design**

### **8.3.4 Geopolymer Synthesis**

#### **8.3.4.1 Preparation of Solutions**

Following the literature recommendation to improve the mechanical properties of the geopolymer construction materials (Zhuang et al., 2016), freeze-dried CNC were mixed into the required quantities of deionized water to produce the required solution concentrations shown in Figure 1. The solutions were left mixing overnight to ensure adequate hydration and dispersion. Novel CNC dispersion techniques were not considered a significant proportion (exceeding 90%) of the CNC were found to be adsorbed into the geopolymer matrix (Cao et al., 2016a). The CNC concentration range was based on the range reported in the literature (Cao et al., 2016a; Cao et al., 2016b; Lee et al., 2019). The required masses of the sodium hydroxide pellets were weighed to prepare the activator solutions, according to the activator concentrations shown in **Figure 8.1**.

#### **8.3.4.2 Geopolymer Moulding**

For each of the experimental runs dictated by the experimental design software (**Figure 8.1**), 100 g of fly ash was weighed, placed into a glass beaker, and contacted with the liquid components (alkaline activator solution and CNC solution). The contents were mixed until a uniform paste was formed. The paste was then decanted into the silicone mould.

#### **8.3.4.3 Geopolymer Oven Curing**

The silicone moulds containing the geopolymer pastes were placed into an oven which was preset at 40 °C. Two different oven curing techniques were investigated: curing at 40 °C for two hours and then at 60 °C for an additional 24 hours. Subsequently, the samples were rotated and cured at 60 °C for 24 hours to ensure spatial uniformity for the curing. Secondly, the samples were cured at 40 °C for two hours and then at 60 °C for another 24 hours. In the second case, the samples were not rotated, and there was no further curing. A pictorial representation of the steps encompassing Section 2.4 can be observed in **Figure 8.2**.



**Figure 8.2. (a) Alkaline activator solutions (b) CNC solutions (c) Fly ash (d) Moulded geopolymer pastes prior to curing (e) Oven used for curing (f) De-moulded geopolymers post-curing**

### 8.3.5 Geopolymer Testing

#### 8.3.5.1 Compressive Strength

Each sample was placed between two flat plates on a Rohloff Universal Tensile Tester. A force was applied, causing the plates to move closer, resulting in the crushing of the sample. The force at which the sample was crushed was recorded and displayed by the machine. This force was the compressive strength of the sample. The compressive strength tests were done in duplicate. The apparatus used to measure the compressive strength of the geopolymer samples is shown in **Figure 8.3**.



**Figure 8.3. Compressive strength equipment; A- Tensile testing machine, B- Load indicator, C- base plate, D- Load exertion controls**

#### 8.3.5.2 Density

The mass of each sample was measured using a Mettler Toledo laboratory scale. The dimensions of each sample were determined using a digital Vernia caliper. The volume of the sample was calculated using the sample dimensions and the density calculated using equation (8.1):

$$\text{Density} = \text{Mass/Volume} \quad (8.1)$$

#### 8.3.5.3 Electrical Resistivity

The following equipment was used for the testing: Fluke 1577 Insulation Multimeter, conductive plates, and measuring electrodes. The geopolymer samples were placed between the top and bottom conductive plates. The Insulation Multimeter included a positive, negative, and a guard terminal. The guard terminal is at the same potential as the negative terminal but not in the measurement path. The guard terminal is used to improve the accuracy of the measurements by eliminating stray measurements. The volume resistivity ( $\rho$ ) relationship to the measured resistance (R), area of the top electrode (A), and height of the construction material sample (h) are mathematically represented by equation (8.2) (Swanson et al., 2020):

$$\rho = \frac{RA}{h} \quad (8.2)$$

The experimental setup used to measure the electrical resistivity of the geopolymer samples is shown in **Figure 8.4**.



**Figure 8.4. Electrical resistivity experimental setup; A- Fluke 1577 insulation multimeter, B- Conductive plates, C- Geopolymer sample, D- Current-measuring electrodes**



## 8.4 Results and Discussion

### 8.4.1 Geopolymer Synthesis

The first curing procedure (48-hour curing with rotation) resulted in cracks in all the geopolymer samples, except for those containing high amounts of CNC (Runs 4, 7, and 9). The cracking was attributed to the rapid exposure of the sample to a higher temperature when rotated and cured for an additional 24 hours. The rapid temperature exposure caused rapid moisture evaporation from the sample's microstructure, culminating in the formation of the cracks (Roopchund, 2016). For the samples containing the high CNC concentrations, the CNC within the geopolymer matrix prevented the rapid moisture evaporation (Flores et al., 2017), thereby preventing cracking. This result was also observed in the research of Lee et al. (2019a). Hence it is recommended that higher CNC concentrations be used for applications that require thermally stable geopolymers instead of high strength geopolymers.

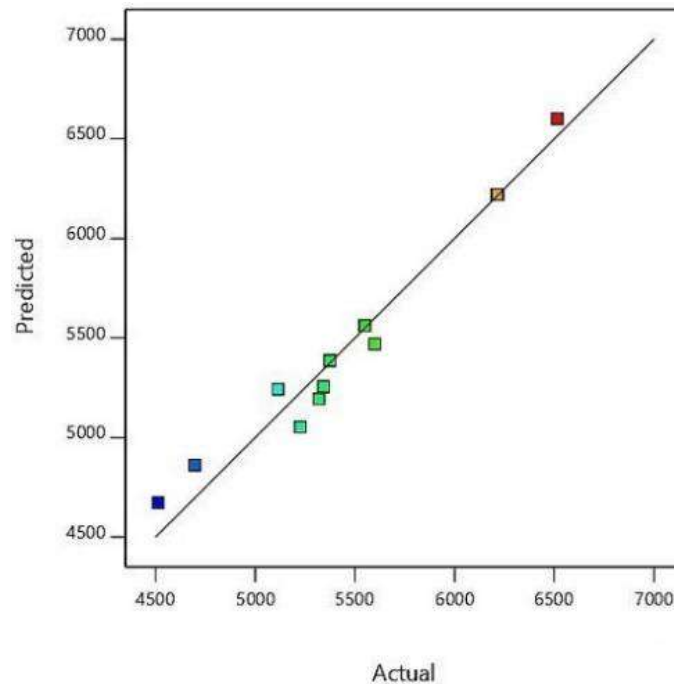
The alternative curing method (without de-moulding and rotating the samples after the initial 24 hours of curing at 60 °C) did not result in any cracks was a good finding as cracking compromises the structural integrity of the geopolymer samples. Hence, de-moulding and sample rotation is not recommended in the curing phase.

### 8.4.2 Compressive Strength

#### 8.4.2.1 Statistical Model

The software recommended the 2FI statistical model to represent the combined effects of the cellulose nanocrystal concentration and alkaline activator concentration on the compressive strength. The adequate precision indicated by the software, combined with the insignificant lack of fit, implied that the model could be deemed accurate. The model accuracy is validated by the graphical representation of the predicted versus actual values in **Figure 8.5**.





**Figure 8.5. Compressive strength predicted versus actual.**

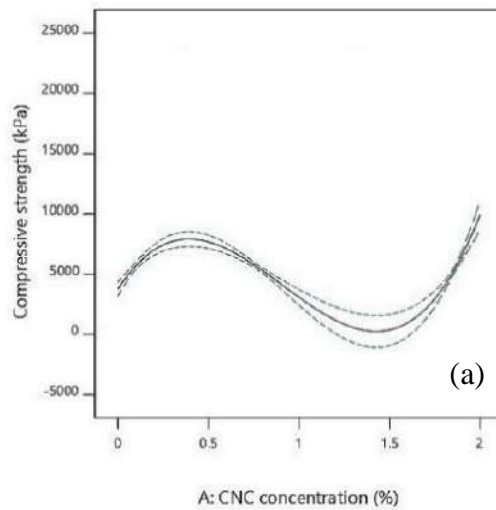
#### 8.4.2.2 Two-dimensional Interactions

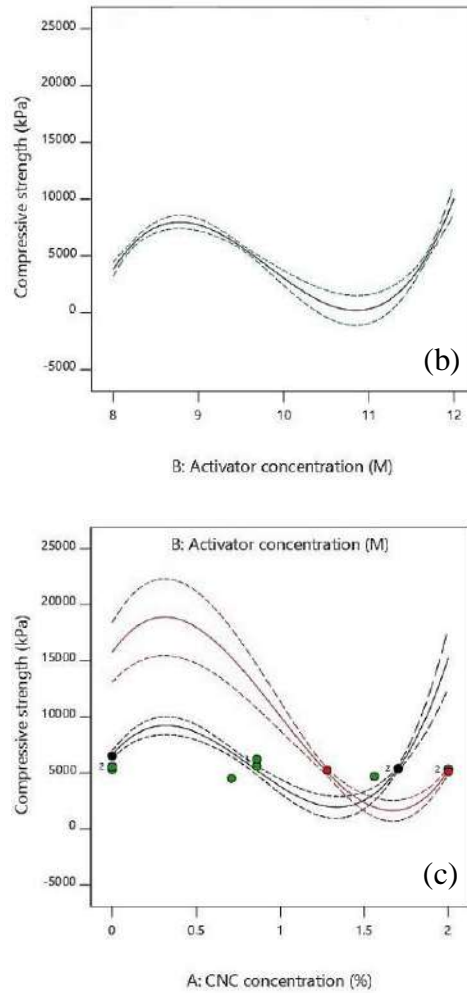
The panel plot in **Figure 8.6** represented the interactions between the individual and combined variation parameters on the compressive strength. It was noteworthy that lower concentrations of CNC favoured the compressive strength in **Figure 8.6** (a), as affirmed by the findings of Cao et al. (2016b), Lee et al. (2019a), Imbabi et al. (2012), and Ghahari et al. (2020). CNC increased the bonding between particles in composite material at smaller concentrations due to their adhesive property (Rahmawati et al., 2021). The increased bonds result in the formation of a network, which improved the strength of the material. Based on the results, the CNC concentration should not exceed 0.5% to avoid reducing the compressive strength. The CNC may likely have agglomerated at concentrations exceeding 0.5% (Cao et al., 2016b), resulting in decreased compressive strength results.

It was evident from **Figure 8.6** (b) that the lower end of the alkaline activator concentration favoured the compressive strength of the geopolymer samples. This finding contradicts the study of Hamidi et al. (2016), in which the best mechanical properties of the geopolymer were obtained at a high alkaline activator concentration of 12 M. However, the result agrees with the

study of Hadi et al. (2018), which indicated that fly ash containing many fine particles and amorphous content would require a low dosage of alkaline activator to achieve good mechanical results. Considering that lower concentrations of CNC solutions and alkaline activators are required for better strength development, the production costs can be reduced. This reduced production cost would effectively aid the long-term sustainability of the green material being proposed and directly addressed the financial concerns when developing green construction materials (Imbabi et al., 2012).

The intersection of the combined interactions shown in **Figure 8.6** (c) was noteworthy as the intersection between the fitted curves would offer a trade-off between the optimal cellulose nanocrystal concentration and alkaline activator concentration on the compressive strength. It can be observed that a combination of “middle point” concentrations offer the best trade-off, which would positively impact the economic sustainability of the production process.

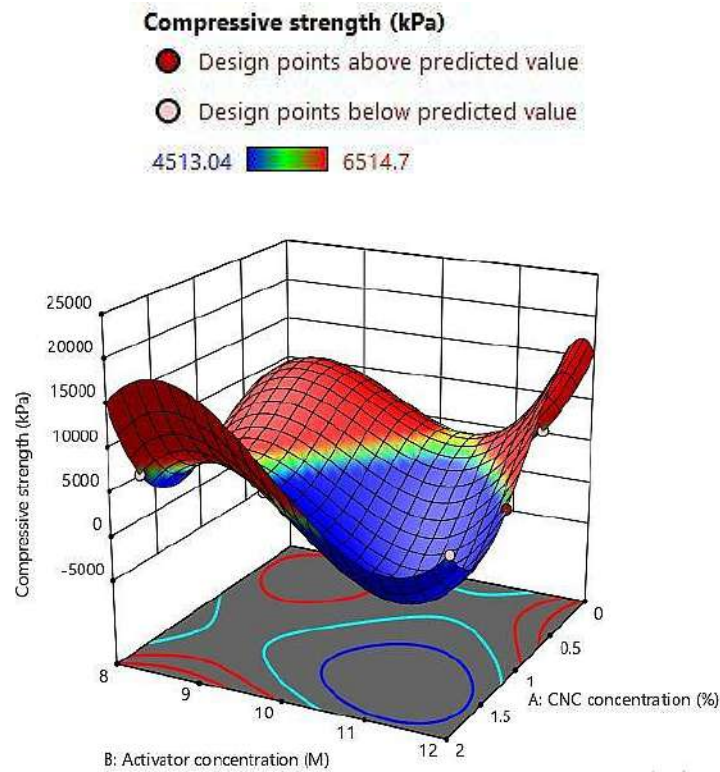




**Figure 8.6. Panel plot of compressive strength interactions**

#### 8.4.2.3 Three-dimensional Response Surface Model

The three-dimensional model depicted in **Figure 8.7** depicted a surface based on the interaction observed in the previous section. It was beneficial that the response curve was colour-coded, highlighting the maximum and minimum compressive strength values. It was noteworthy that the lower to middle compressive strength range was more prominent than the higher end. However, suppose lower concentrations of the CNC (Imbabi et al., 2012, Cao et al., 2016b, Ghahari et al., 2020, Lee et al., 2019) and alkaline activator concentrations (Hadi et al., 2018) were used. In that case, better compressive strengths could have been achieved.

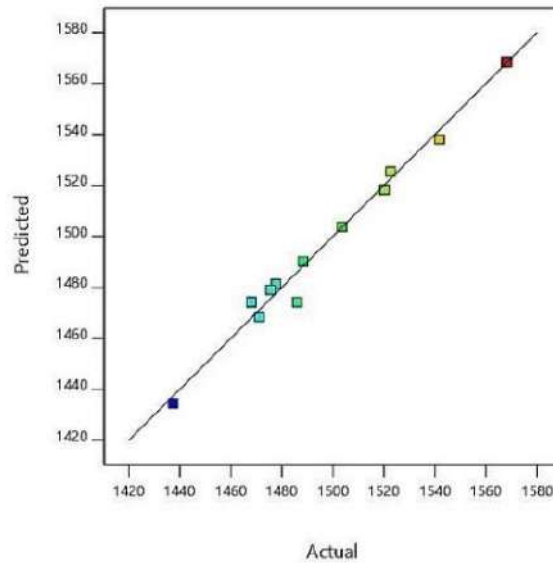


**Figure 8.7. Compressive strength surface response model**

### 8.4.3 Density

#### 8.4.3.1 Statistical Model

The software recommended a cubic statistical model to represent the effects of the alkaline activator and CNC concentrations on the geopolymer density. The statistical F and P values indicated that the model was significant by predicting a maximum 0.01% likelihood of noise data. In addition, the lack of fit was found to be insignificant, implying the validity of the cubic model representation. From the graphical representation of the actual and predicted values shown in **Figure 8.8**, the experimental data points can be observed to follow the linear trend recommended by the software.



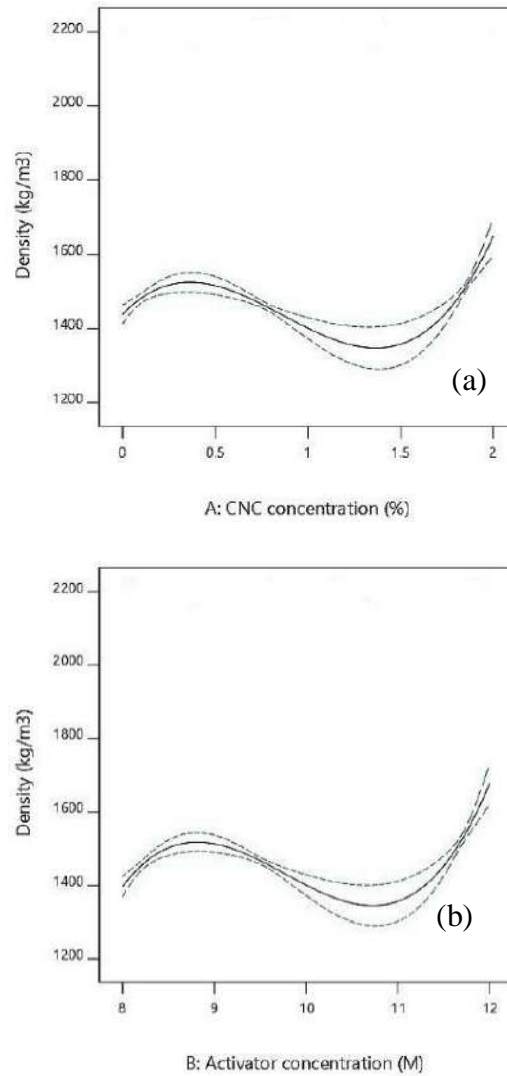
**Figure 8.8. Density actual versus predicted values**

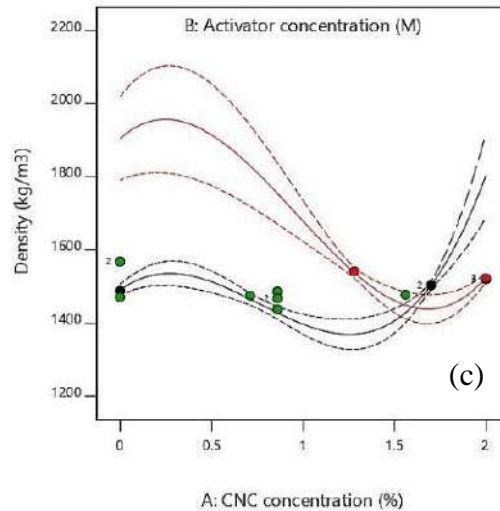
#### 8.4.3.2 Two-dimensional Interactions

**Figure 8.9** (a) clearly showed a cubic relationship between the concentration of CNC and the geopolymer density. To achieve a high-density geopolymer, the concentration of CNC should not exceed 0.5% (the region of the global maximum). Alternatively, a concentration range of CNC within 1.75% and 2% were also found to favoured high geopolymer densities. The higher densities at the higher concentration range were attributed to the fact that as the CNC harden and merge into the geopolymer matrix during the curing process, the additional CNC mass of the higher concentration of CNC became apparent in the density of the formed geopolymer. This finding agreed with those of Cao et al. (2016a) and Barnat-Hunek et al. (2019), where CNC increased the sample density by reducing the porosity and promoting the formation of calcium silicate hydrate, respectively. Furthermore, this finding was supported by the fact that nanosized cellulose-based particles fill the smallest gaps in the mixture paste, thus increasing the overall density (Rahmawati et al., 2021).

It was also notable that the concentration range between 0.5% and 1.75% favoured low geopolymer densities and should be applied for construction applications that required low densities.

The alkaline activator concentration also exhibited a cubic relationship with the geopolymer density, as shown in **Figure 8.9** (b). Again, this mathematical relationship is valuable when attempting to apply geopolymers in low-density construction material applications. The individual interactions are observed in the combined interactions plot of **Figure 8.9** (c). This plot indicated that at concentrations of CNC exceeding approximately 1.5%, the effect of the alkaline activator concentration also influenced the geopolymer density.

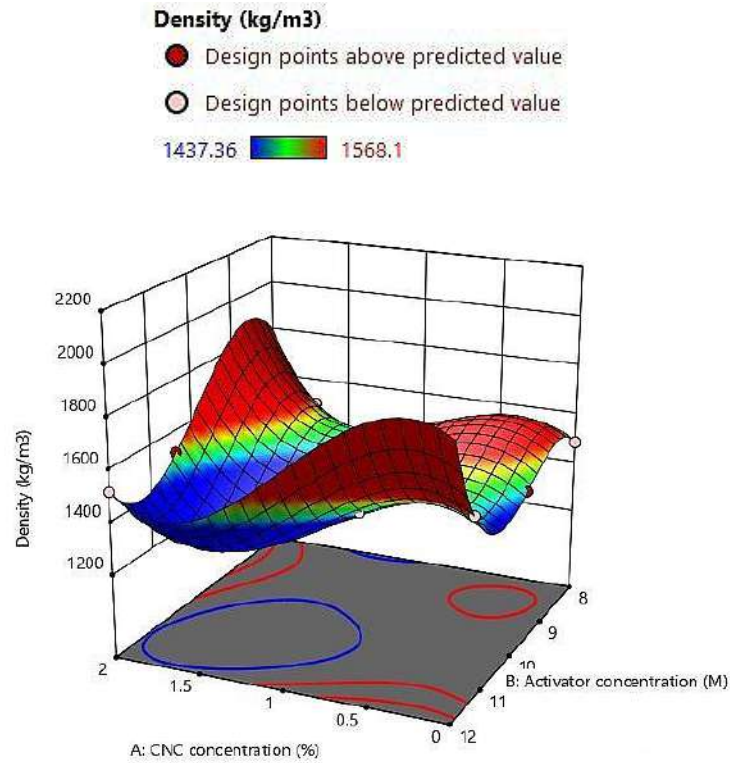




**Figure 8.9. Panel plot of density interactions**

#### 8.4.3.3 Three-dimensional Response Surface Model (24-hour curing)

The cubic functions representing the relationships between the cellulose nanocrystal concentration and alkaline activator concentration on the geopolymer density were exhibited in the three-dimensional response curve in **Figure 8.10**. This finding was favourable as the response model offered a straightforward exhibit of information when customizing a specific density for a specific construction application. This type of analysis can certainly aid the design and development process and support further research to commercialize the application of geopolymers as novel green construction materials.



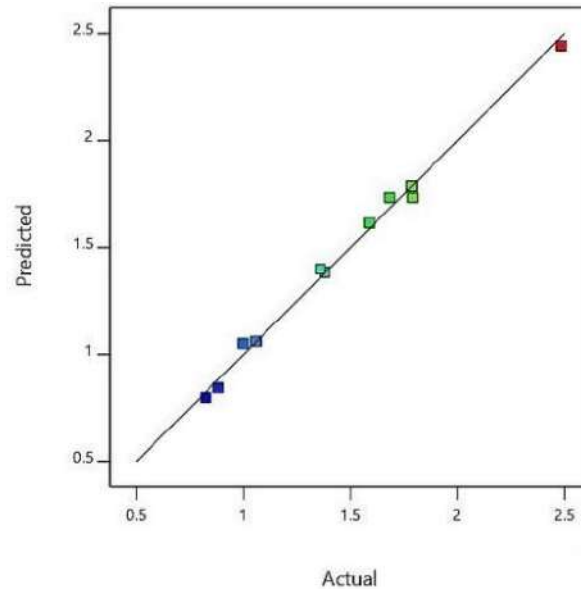
**Figure 8.10. Three-dimensional density response curve**

#### **8.4.4 Electrical Resistivity**

##### **8.4.4.1 Statistical Model (24-hour curing)**

A cubic statistical model was suggested by the software to represent the electrical resistivity data. As with previous statistical models, a linear trend was observed in **Figure 8.11** between the actual and predicted values. The F and P statistical values implied the significance of the model with only a 0.01% likelihood of noise in the data. This high degree of accuracy can be attributed to following the literary recommendations to perform accurate measurements (Azarsa and Gupta, 2017; Hornbostel et al., 2013).





**Figure 8.11. Electrical resistivity actual versus predicted model (24-hour curing condition)**

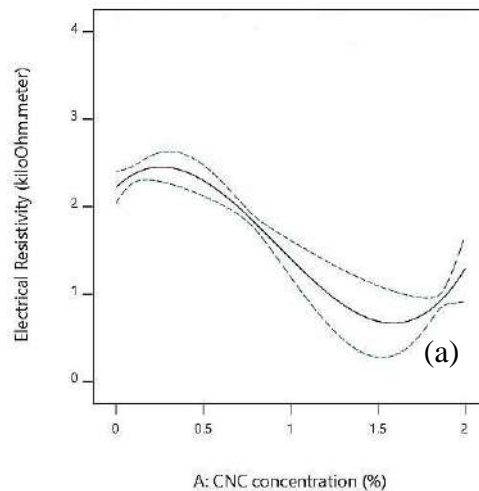
#### 8.4.4.2 Two-dimensional Interactions (24-hour curing)

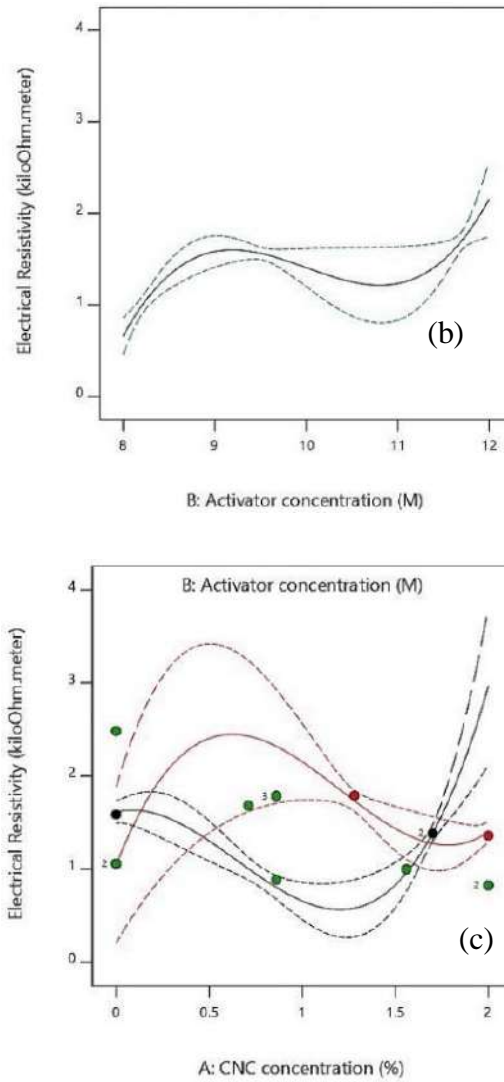
As observed in **Figure 8.12** (a), a decreasing cubic trend was observed between the electrical resistivity and CNC concentration. This finding implied that the lower CNC concentrations favoured the electrical resistivity of the geopolymer construction materials. The electrical resistivity values exhibited a high range (exceeding 800  $\Omega.m$ ). According to the literature, this implied a low to negligible potential for corrosion (Hornbostel et al., 2013; Zainal et al., 2015; Swanson et al., 2020). However, the electrical resistivity range observed for the 24-hour cured samples was substantially lower than that of the 48-hour cured samples. This finding was directly attributed to the relatively higher moisture content present in the geopolymer samples cured for only 24 hours when compared against the samples cured over the 48 hours with rotation. The higher moisture content enabled the effective transfer of ions, thus decreasing the overall electrical resistivity of the construction material. Furthermore, the decrease in electrical resistivity observed with increasing CNC concentrations can be directly attributed to the fact that the CNC solution contains a high moisture content (over 90% by volume).

Considering that a higher CNC concentration yields an inherently higher non-evaporable water content (Flores et al., 2017), the observed decreased electrical resistivity was expected, as

confirmed in **Figure 8.12** (a). Considering that the higher electrical resistivity values are linked to a lower corrosion potential in construction materials (Hornbostel et al., 2013; Zainal et al., 2015; Swanson et al., 2020), it is recommended that lower CNC concentrations be used in the development of the geopolymer construction materials.

As observed in **Figure 8.12** (b), the activator concentration was found to rapidly improve the electrical resistivity as it was increased from 8 to 9 M, after which the electrical resistivity was slightly decreased as the activator concentration was increased from 9 to 11 M. Subsequently, a rapid increase in the electrical resistivity was observed as the activator concentration was increased from 11 to 12 M. It is therefore not feasible to use alkaline activator concentrations within the range of 9 to 11 M. Such feasibility considerations are vital in the development of economic green construction materials (Imbabi et al., 2012). Interactions were observed between the CNC concentration and the alkaline activator concentration at a low CNC concentration of 0.2% and again at a concentration exceeding 1.5%, as confirmed in **Figure 8.12** (c).

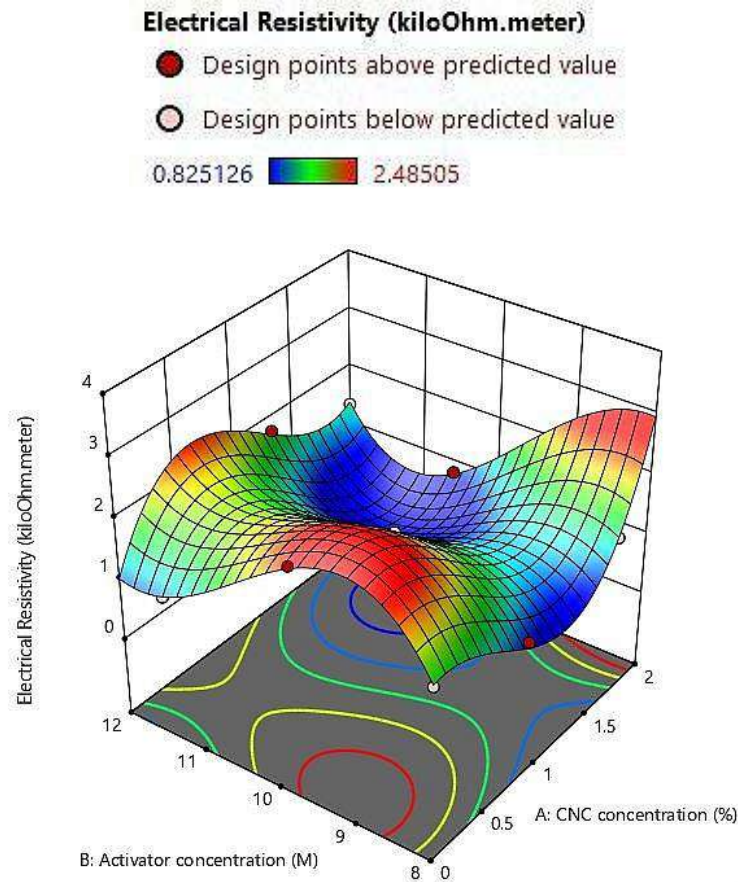




**Figure 8.12. Electrical resistivity interaction panel plots (24-hour curing condition)**

#### 8.4.4.3 Three-dimensional Response Surface Model (24-hour curing)

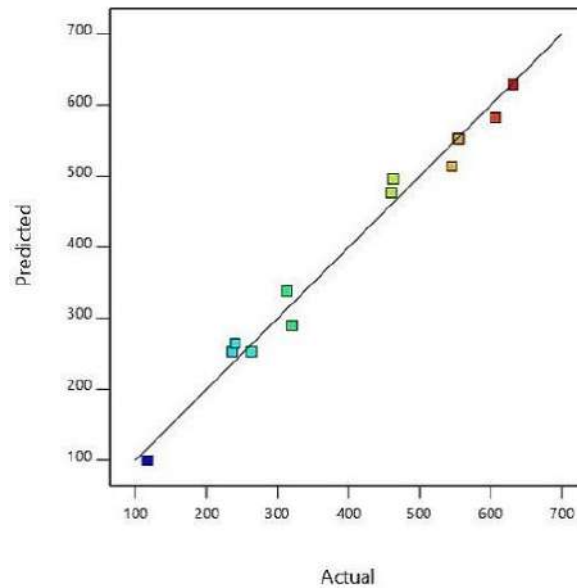
It is apparent from the three-dimensional response plot (**Figure 8.13**) that the most significant electrical resistivity values were achieved at the combined conditions of high CNC concentration and low activator concentration. Depending on the extent to which corrosion resistance is required in the geopolymer construction material being developed, it is recommended that the CNC concentration and activator concentration be adjusted to achieve the desired degree of corrosion resistance. Considering that high CNC concentrations are required, the least alkaline activator concentration must be determined to achieve the desired degree of corrosion resistance to ensure economic feasibility.



**Figure 8.13. Electrical resistivity three-dimensional surface response curve (24-hour curing condition)**

#### 8.4.4.4 Statistical Model (48-hour curing)

The quadratic and cubic statistical models were suggested to represent the electrical resistivity data for the 48-hour cured samples. As with previous statistical models, a linear trend was observed between the actual and predicted values (**Figure 8.14**). The model F value suggested that the recommended model was significant with only a 0.01% chance of noise.



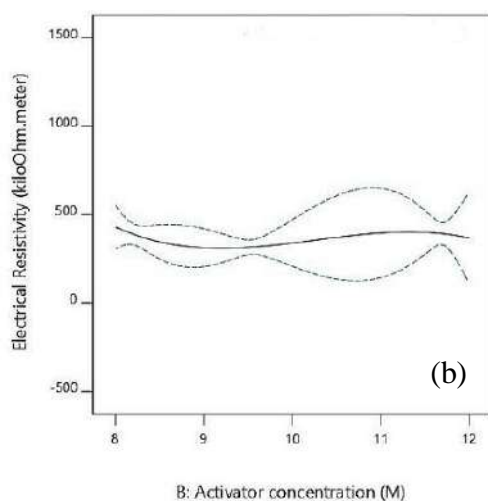
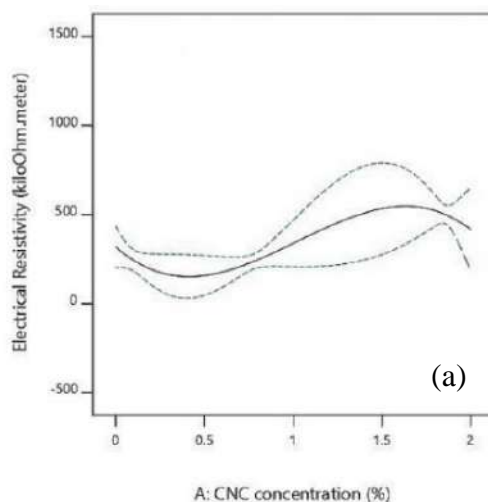
**Figure 8.14. Electrical resistivity actual versus predicted model (48-hour curing condition)**

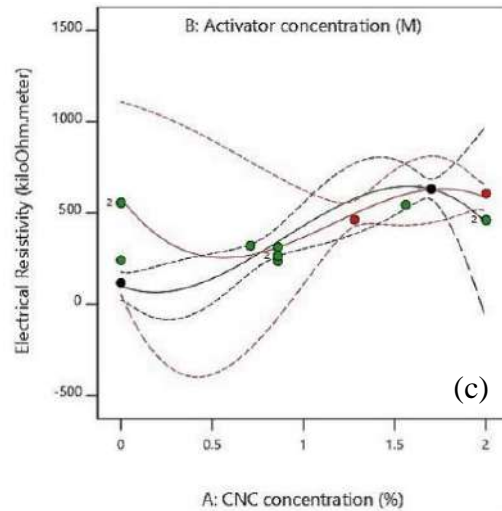
#### 8.4.4.5 Two-dimensional Interactions (48-hour curing)

The results obtained for the 48-hour cured samples differed significantly in two respects when compared against the results of the 24 hour-cured samples. Firstly, the range of electrical resistivity values was substantially greater as compared to the 24-hour cured samples. This finding was directly attributed to the greater degree of moisture removal experienced by the 48-hour samples during the extended curing procedure. Secondly, as observed in **Figure 8.15 (a)**, the electrical resistivity increased as the cellulose nanocrystal dosage was increased. This finding implied that the 48 hour-cured samples enabled greater moisture removal to the extent that the true reinforcing potential of the CNC within the geopolymer matrix could be experienced.

As with the 24-hour cured samples, the effect of the alkaline activator on the electrical resistivity was marginal, as observed in **Figure 8.15 (b)**. This finding implied no need for higher alkaline activator concentrations from the perspective of electrical resistivity. The needless requirement of higher alkaline activator concentrations is a positive finding from the perspective of economic green construction material development (Imbabi et al., 2012).

Based on the intersection of the two independent variables in the combined interaction plot in **Figure 8.15** (c), the presence of an interaction between the two independent variables was confirmed. This interaction implied that the effect of the cellulose nanocrystal concentration depended on the concentration of the alkaline activator. Hence, the alkaline activator concentration would need to be fixed while manipulating the CNC concentration to achieve the desired degree of corrosion resistance.

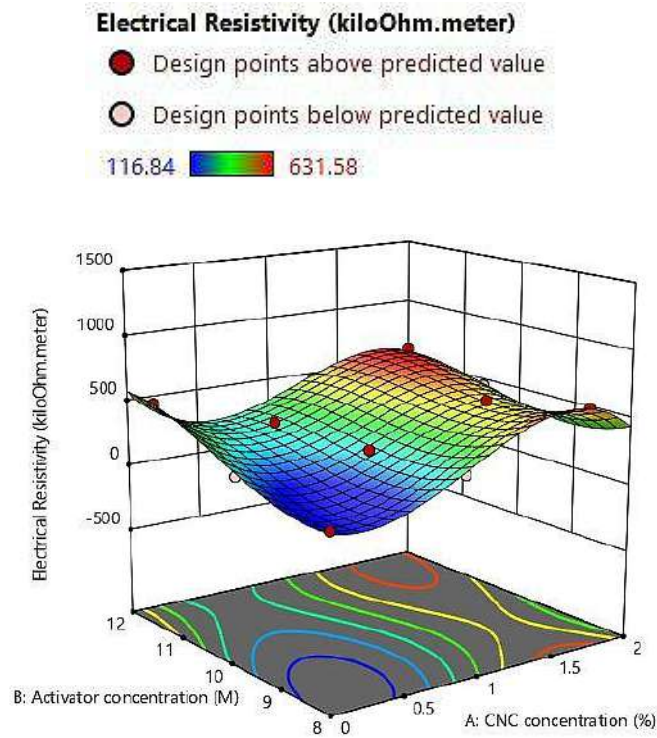




**Figure 8.15. Electrical resistivity interaction panel plots (48-hour curing condition)**

#### 8.4.4.6 Three-dimensional Response Surface Model (48-hour curing)

From the three-dimensional response curves (**Figure 8.16**), it was apparent that the most significant electrical resistivity values were obtained under conditions of high CNC concentration and low alkaline activator concentration. The range of electrical resistivity values obtained under the 48-hour curing conditions implied negligible corrosion resistance (Hornbostel et al., 2013; Zainal et al., 2015; Swanson et al., 2020). From the perspective of corrosion resistance, it is therefore recommended that the 48-hour curing conditions be implemented to develop the geopolymers.



**Figure 8.16. Electrical resistivity three-dimensional surface response curve (48-hour curing condition)**

#### ***8.4.5 Overall Correlation between the Mechanical Properties***

Under certain conditions of CNC and alkaline activator concentrations, the compressive strength of the geopolymer was inversely proportional to the density. In addition, the geopolymer electrical resistivity was inversely proportional to the concentration of CNC and directly proportional to the alkaline activator concentration. However, the relationship between the electrical resistivity and CNC concentration was more pronounced than that of the electrical resistivity and the alkaline activator concentration. Hence, the overall correlation was that the electrical resistivity was directly proportional to the compressive strength, which was inversely proportional to the density.

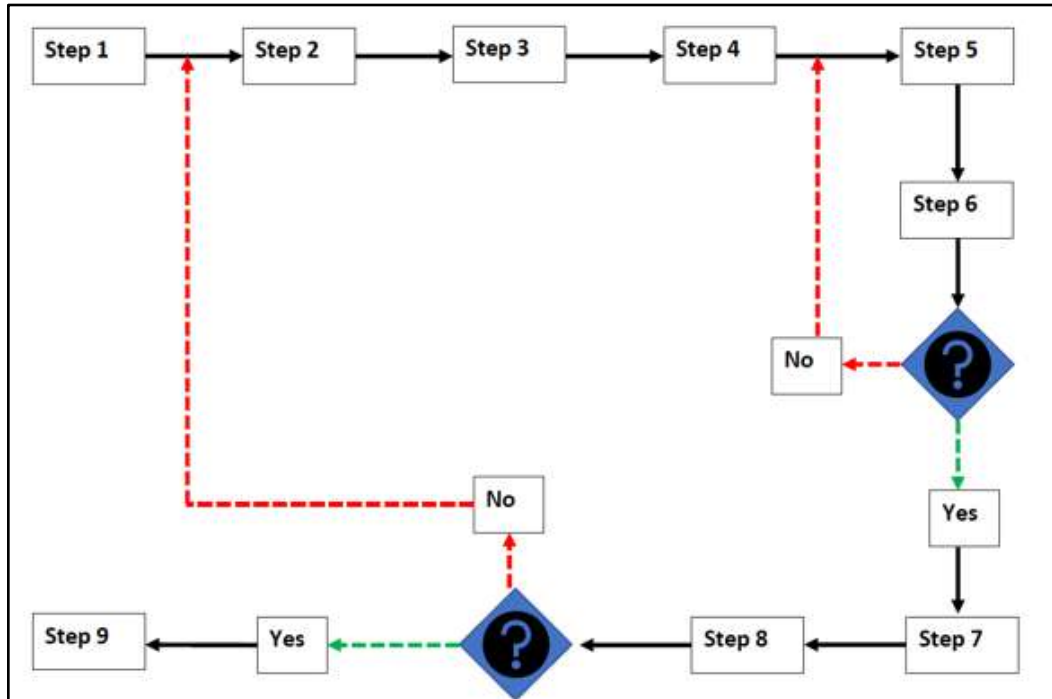


#### **8.4.6 Geopolymer Development Framework**

As per the literary recommendation for uniformity in the geopolymer production process (Singh and Middendorf, 2020; Ghahari et al., 2020), the empirical framework to aid the development of geopolymer construction materials is recommended below:

- 1) Identify and quantify the mechanical properties required in the final product.
- 2) Select the industrial waste aluminosilicate precursor material. Typical cement replacement materials include fly ash, blast furnace slag, and silica fumes (Imbabi et al., 2012, Komnitsas, 2011; Cao et al., 2016b).
- 3) Select the alkaline activator. To improve the production economics, consider waste alkaline materials (such as green liquor dregs from kraft pulp mills).
- 4) Consider using organic or inorganic reinforcement agents, such as fibers (Pacheco-Torgal, 2016; Korniejenko et al., 2016; Karthik et al., 2017a; Karthik et al., 2017b; Karthik et al., 2019, Silva et al., 2020).
- 5) Perform a statistical design of experiment to optimize the experimental runs.
- 6) Select the curing conditions (duration, temperature, and sample rotations). Strive to use ambient temperature curing. However, if this is not possible, try not to exceed 60 °C curing temperature. Observe the effect of the implemented curing temperature on the formed geopolymer samples. If the presence of micro cracks is observed, adjust the temperature and redo step 6.
- 7) Perform the mechanical testing.
- 8) Insert the mechanical testing results in the statistical experimental design model and generate the interaction plots and the three-dimensional response plots. Observe the regions of the three-dimensional response plots corresponding to the desired range of the mechanical properties. If the mechanical results do not meet the required specifications, then revert to step 2.
- 9) If the mechanical results meet the required specifications, the geopolymer development procedure can be accepted.

A graphical flow diagram is shown in **Figure 8.17**.



**Figure 8.17. Empirical geopolymer construction material development framework**

## 8.5 Conclusions

There is a strong need for novel green construction materials. The methodology reported in this study can efficiently develop geopolymers with a significant degree of statistical accuracy. In addition, the effects of varying CNC concentrations on the mechanical properties of the formed geopolymers were realized. It was significant that lower concentrations of CNC (less than 0.5%) yielded higher strength geopolymers and, in some cases, corrosion resistance. Considering that higher CNC concentrations prevented the cracking of geopolymers in unstable curing environments, this presented another application for CNC. Consequently, the first research aim was met.

The statistical methods enabled the custom development of specific mechanical properties as required by the application. The results of the statistical experimental design yielded the detailed experimental database of the mechanical properties of the CNC-reinforced fly ash-based geopolymer construction materials in the form of interaction plots and three-dimensional surface response plots. Hence, the second research aim was met.

Due to the experimental optimizations offered by the statistical experimental design and the iterative nature of the proposed universal empirical model, it was recommended to develop novel green geopolymer construction materials to meet specific mechanical requirements. The results of each iteration can be recorded to guide the inputs of the subsequent iteration until the desired mechanical properties are attained.

The overall conclusion was that the threefold research aims were met, supporting the argument that geopolymers are strong contenders in green construction applications.

## **CHAPTER 9: THE EFFECT OF CNC ON THE THERMAL BEHAVIOUR OF NOVEL GREEN CONSTRUCTION MATERIALS**

### **9.1 Introduction**

Following the application of cellulose nanocrystals (CNC) in the development of reinforced novel green construction materials, this Chapter focused on the effect of CNC on the thermal behaviour of geopolymer construction materials. The thermal behaviour of CNC-reinforced geopolymer construction materials can ascertain their potential in thermal resistance applications. Two types of thermal analyses were undertaken: thermogravimetric analysis (TGA) and differential scanning calorimetry (DSC). The TGA indicated the geopolymer mass loss at high temperatures, while the DSC indicated the heat transfer rate with gradual temperature elevation. As indicated in the Literature Review below (Section 9.2), much research has been undertaken on the thermal behaviour of conventional construction materials and geopolymers. However, the effect of CNC on the thermal behaviour of geopolymers is not known. Understanding the thermal behaviour of CNC-reinforced geopolymers could improve its commercial application in refractory construction applications. Furthermore, the thermal analyses contribute to the property database of the novel fly ash-based CNC-reinforced green construction material developed in the previous Chapter.

Based on the mentioned knowledge gap in the available knowledge, the aims of this Chapter were three-fold. Firstly, to determine the effect of CNC on the thermal behaviour of fly ash-based geopolymer samples. Secondly, to determine the optimal CNC dosage to improve the thermal properties. Thirdly, to determine the best curing procedures to improve the thermal (and mechanical) geopolymer properties.

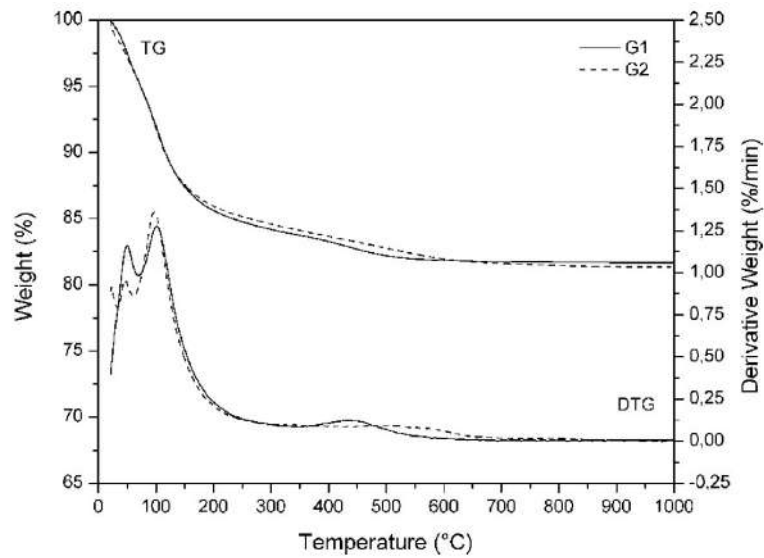
### **9.2 Literature Review**

This review consolidated the information gained from previous studies regarding geopolymer thermal testing and analyses. It was interesting that the reviewed research outlined interpretations of the characteristics observed on TGA and DSC plots. Such analyses are helpful to interpret the mentioned plots to gain a fuller understanding of the thermal behaviour of geopolymer samples under high-temperature exposure.

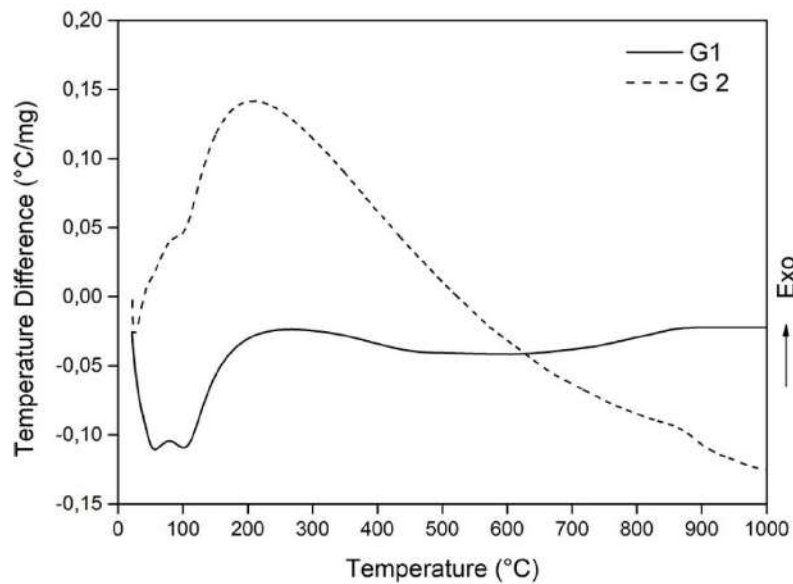
### ***9.2.1 Thermal Analysis of Metakaolin Based Geopolymers***

The research of Caballero et al. (2019) focused on the development of metakaolin-based geopolymer matrices. Two types of metakaolin clays were used as precursor materials to produce two different geopolymers. TGA and DSC analyses were undertaken on metakaolin samples at temperatures between 22°C and 1000°C in a nitrogen atmosphere with a heating rate of 10°C/min. The gradual mass losses between 350-700°C (**Figure 9.1**) were associated with kaolinite dehydroxylation in the metakaolin upon transition into reactive metakaolin. The thermal analyses enabled the identification of mass losses associated with three primary phenomena during geopolymer formation.

Firstly, there was a pronounced mass loss (10-15%) for both geopolymers between 22 and 300°C, associated with the two endothermic peaks visible in the DTA curves. According to Caballero et al. (2019), the 15% mass loss in both geopolymers was due to humidity reincorporation. The samples were not analyzed immediately after the treatment and improperly stored before the analysis. These peaks are associated with the loss of free or slightly bound water in the geopolymer structure. Secondly, a slight mass loss (approximately 2%) from 350 to 700°C was observed. The second phenomenon was associated with the dehydroxylation of the geopolymer matrix and the kaolinite present in metakaolin, removing surface hydroxyl groups and forming new silicon–oxygen–silicon bonds, which produce additional shrinkage in the geopolymer matrix. When the temperature exceeded 600°C, both samples exhibited minimal mass losses (below 0.3%). The corresponding differential thermal analysis plot is shown in **Figure 9.2**.



**Figure 9.1. TGA curves for metakaolin-based geopolymers, G1 and G2 (Caballero et al., 2019)**



**Figure 9.2. DTA curves for metakaolin-based geopolymers, G1 and G2 (Caballero et al., 2019)**

### ***9.2.2 Thermal Properties of Geopolymers Exposed to High Temperature***

The study of He et al. (2020) prepared geopolymers by alkali solution-activated metakaolin clay and fly ash. It was noteworthy that the authors reviewed the thermal and mechanical behaviours

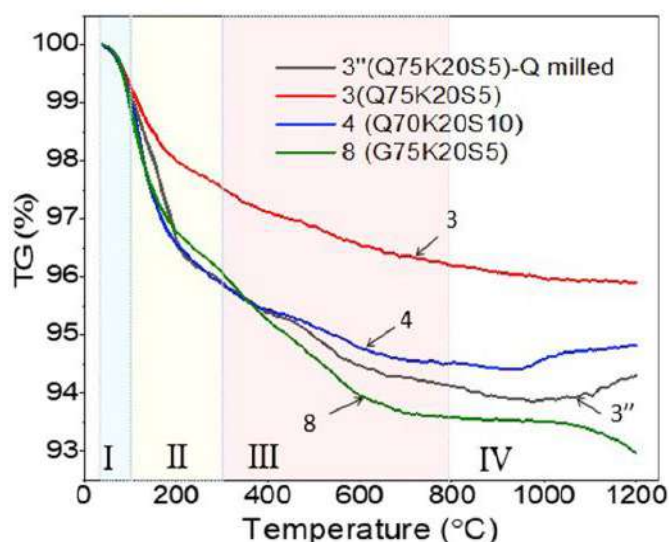
of geopolymers at high temperatures. Usually, these properties are closely related to the raw materials and the constituents of the geopolymers (He et al., 2020). Furthermore, the preparation and testing conditions influence the thermal and mechanical properties of the geopolymers. During geopolymerization, the raw materials, aluminosilicate precursor, and reinforcement materials result in different thermal characteristics upon heating. However, phase transitions can occur during thermal testing regardless of the raw materials (He et al., 2020). The geopolymers exhibited low mass losses, low expansion ratios, and low thermal conductivities at high temperatures. Furthermore, the geopolymer stress-strain curves depended on the geopolymer composition and the temperature. The results of the study indicated that TGA and DSC could determine the thermal stability of materials. The mass loss of the metakaolin-based geopolymer was 13% at 600°C compared to the mass loss exceeding 25% of cement paste. Hence, the geopolymers exhibited advanced thermal resistance compared to conventional construction materials. The incorporation of boiler slag admixture improved the thermal stability. Specifically, the mass loss of the geopolymer made from a mixture of 30% boiler slag and 70% metakaolin was only 9.43% when heated to 1250°C. All curves were exhibited a small endothermic peak between the temperature range of 50 to 150°C, corresponding to the evaporation of free water. Subsequently, a more substantial exothermic peak was observed in the range of 300 to 500°C, attributed to the phase transition of mineral compositions. Generally, the difference between the width and height of the peak reflected the change of chemical constituent and proportion of geopolymer formulation.

### ***9.2.3 Thermal Stability of One-part Metakaolin Geopolymer Reinforced with Spodumene Tailings and Glass Wool***

Lemougna et al. (2020) synthesized metakaolin geopolymer composites reinforced with spodumene tailings (quartz-feldspar sand) and glass wool. Several compositions were prepared with sodium metasilicate anhydrous solutions of concentration range varying between 0.5 and 12.5 mass percentage. The one-part metakaolin geopolymer composites were cured at 60 °C for 24 hours. TGA was used to determine the stability of the geopolymer composites at temperature exposure up to 1200 °C. The metakaolin-glass wool geopolymer composites were stable up to 500 °C, whereas the counterparts containing quartz-feldspar sand were stable up to 1100–1200 °C. Furthermore, the mass loss varied between 4 to 7% at 1200 °C, depending on the mixture

composition. Higher mass losses were observed for the quartz-feldspar geopolymer composites. This finding was attributed to the formation of more geopolymer gel. It was notable that the TGA curves were divided into four regions (Lemougna et al., 2020).

Regarding **Figure 9.3**, the weight loss below 100 °C (region I) corresponded to the evaporation of hygroscopic water, while the weight loss between 100 and 300 °C (region II) corresponded to the evaporation of structural water from the geopolymer gel. The continuous weight loss from 300 °C to 800 °C (region III) was attributed to the condensation of silanol and aluminol groups from the geopolymer gel, thus forming Si–O–Si or Si–O–Al tetrahedral linkages. No significant weight loss was observed above 800 °C (region IV), indicating the absence of further thermal decomposition reactions. Above this temperature, the onset of sintering reactions leading to the formation of a ceramic body became apparent. It was notable that at 1200 °C, the mass retention of the prepared geopolymers varied between 93 and 96%, indicating their relatively good thermal stability.

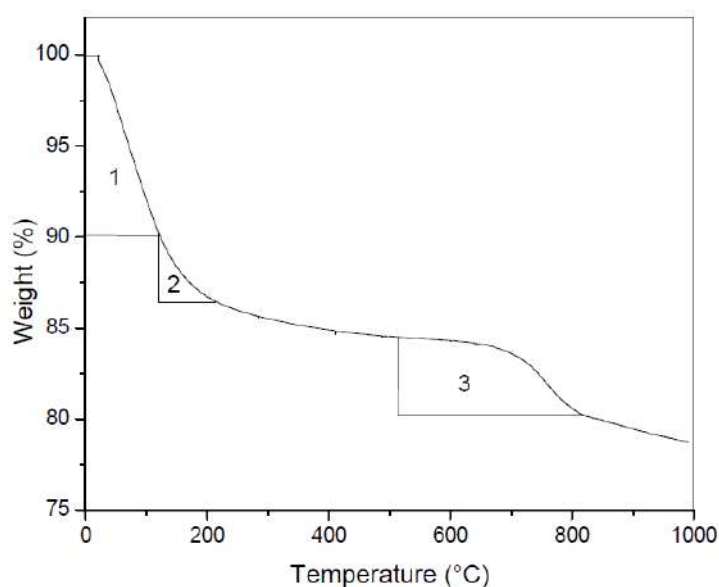


**Figure 9.3.** TGA curves of metakaolin geopolymer composites (Lemougna et al., 2020)



#### 9.2.4 Experimental Study of TGA Techniques in Geopolymeric Materials

The study of Rosas-Casarez et al. (2014) established the TGA procedures for fly ash-based geopolymers by providing a baseline for the analysis of fly ash-based geopolymers. Concerning the thermogram presented by the authors (**Figure 9.4**), the first major decline was attributed to the dewatering of evaporable water present on the surface and porosity of the sample, thus generating a 10% weight loss in the temperature range between 0 to 120 °C (number 1 in **Figure 9.4**). The second notable thermal degradation that occurred between 120 and 200 °C (number 2 in **Figure 9.4**) was attributed to the presence of sodium aluminosilicate hydrate gel. Finally, the weight loss in the temperature range between 450 and 800 °C (number 3 in **Figure 9.4**) was attributed to the formation of carbonates. Overall, the authors deemed the TGA technique useful in differentiating and probing the structural variants and geopolymeric compounds by relating the water binding capacity against the temperature effects. Hence, the TGA technique can be used as a comparative technique between different materials (Rosas-Casarez et al., 2014).

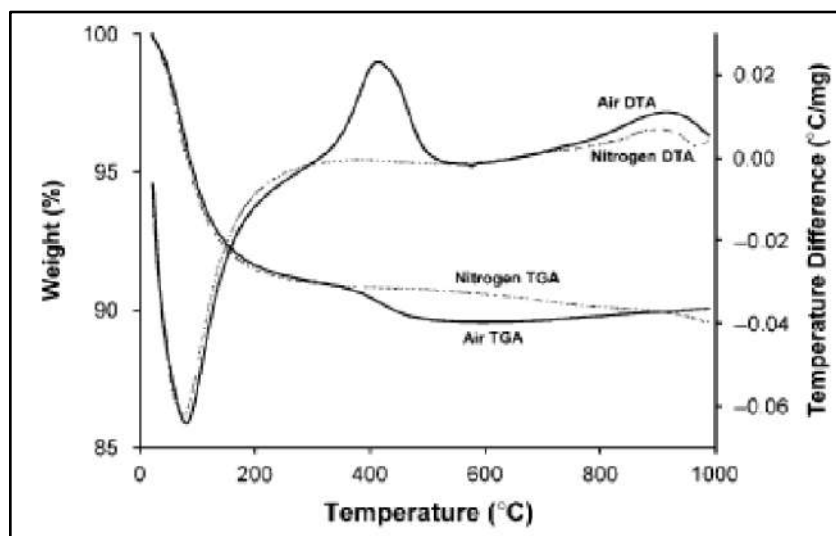


**Figure 9.4.** TGA curve for fly ash-based geopolymer (Rosas-Casarez et al., 2014)

### ***9.2.5 Thermal Character of Geopolymers Synthesized from Class F Fly Ash***

This study by Rickard and van Riessen (2010) investigated the thermal characteristics of fly ash-based geopolymers. The authors used dilatometry, TGA, DTA, XRD, and SEM to characterize the samples. The geopolymers were prepared with nominal ratios of silicon to aluminium of 2.3 and sodium to aluminium of 0.85. The iron oxide in the fly ash was found to substantially influence the thermal expansion and morphology of the geopolymers at temperatures exceeding 500°C. In contrast, volume changes of quartz on either side of the  $\alpha$ - $\beta$  phase transition were found to cause minor variations in thermal expansion.

The thermal study was undertaken on the fly ash precursor material and the resulting geopolymers. The authors found that the mass loss was significantly larger (approximately 10%) in the geopolymers than the fly ash due to the higher initial water content. Referring to the TGA plot in **Figure 9.5** produced by Rickard and van Riessen (2010), an endothermic peak associated with the dehydration of adsorbed and loosely bound water was observed at 80°C for both air and nitrogen atmospheres. In addition, the DTA trace remained endothermic until approximately 250°C due to ongoing dehydration. After that, the broad exotherm peaked at 418°C due to the phase transition of ferrihydrite to hematite. Overall, three major mass change events were observed in the fly ash geopolymers upon heating to 900°C (Rickard and van Riessen, 2010). Firstly, the dehydration of the sample accounted for 80% of the total mass loss and occurred up to 200°C. Subsequently, a mild mass loss was observed between 200°C and 400°C and was attributed to the slow dehydration of the chemically bound residual water. Secondly, the mass loss between 400°C and 600°C was attributed to the dihydroxylation of ferrihydrite as it crystallized to hematite. The mass gain above 600°C was due to the oxidation of the iron species in the geopolymer. The oxidization effect was significant at temperatures exceeding 600°C as more iron species in the fly ash are exposed to the atmosphere due to sample cracking.



**Figure 9.5. TGA/ DTA plot for fly ash-based geopolymers (Rickard and van Riessen, 2010)**

### **9.2.6 Summary**

The analyses from the reviewed research have been consolidated and tabulated (Table 9.1) to guide the analyses and interpretation of the thermal analyses undertaken in the experimental work of this Chapter.

**Table 9.1. Literature thermal analyses**

<b>Temperature (°C)</b>	<b>Reference</b>	<b>Observation</b>	<b>Explanation</b>
< 80	Rickard and van Riessen (2010)	Endothermic peak in the DTA plot.	Dehydration of adsorbed and loosely bound water.
< 100	Lemougna et al. (2020)	Mass loss.	Evaporation of hygroscopic water.
< 120	Rosas-Casarez et al. (2014)	First major decline in the TGA plot.	<ul style="list-style-type: none"> <li>• Evaporation of water from the surface and pores of the sample.</li> <li>• Evaporation of adsorbed free water.</li> </ul>
50 - 150	He et al. (2020)	Endothermic peak in the TGA plot.	Evaporation of free water.
< 200	Rickard and van Riessen (2010)	80% of the total mass loss.	Dehydration of the sample.
120 - 200	Rosas-Casarez et al. (2014)	Second significant thermal degradation in the TGA plot.	Formation of sodium aluminium silicate hydrate.
80 - 250	Rickard and van Riessen (2010)	Endothermic trace.	Ongoing dehydration of the sample.
22 - 300	Caballero et al. (2019)	Two endothermic peaks in the DSC plot corresponding to a 10 to 15% mass loss.	Reincorporation of humidity due to the loss of free or lightly bound water.
100 - 300	Lemougna et al. (2020)	Mass loss.	Evaporation of structural water from geopolymer moisture.
200 - 400	Rickard and van Riessen (2010)	Mild mass loss.	Slow dehydration of chemically bound residual water.

300 - 500	He et al. (2020)	Exothermic peak.	Phase transition of mineral compositions.
350 - 700	Caballero et al. (2019)	2% mass loss.	<ul style="list-style-type: none"> <li>• De-hydroxylation of the geopolymer matrix.</li> <li>• The water release leads to the formation of silicon-oxygen-silicon bonds.</li> </ul>
300 - 800	Lemougna et al. (2020)	1-2% mass loss.	<ul style="list-style-type: none"> <li>• Elimination of structural water and condensation of silanol and aluminol groups from the geopolymer gel.</li> <li>• Formation of silicon-oxygen-silicon and silicon-oxygen-aluminium groups.</li> </ul>
418	Rickard and van Riessen (2010)	Large exotherm.	Phase transition of ferrihydrite to hematite.
400 - 600	Rickard and van Riessen (2010)	Mass loss.	De-hydroxylation of ferrihydrite as it crystallizes to hematite.
450 - 800	Rosas-Casarez et al. (2014)	Third thermal degradation.	Mass loss in the carbonates range.
600	Caballero et al. (2019)	< 0.3% mass loss.	Further water release
	He et al. (2020)	13% mass loss.	
> 600	Rickard and van Riessen (2010)	Mass gain.	<ul style="list-style-type: none"> <li>• Higher temperature exposure causes the viscous flow of aluminosilicates and potential cracking.</li> <li>• Iron species are exposed to the atmosphere and undergo oxidation.</li> </ul>

> 800	Lemougna et al. (2020)	No major mass loss.	<ul style="list-style-type: none"> <li>• Absence of further thermal decomposition reactions.</li> <li>• Onset of sintering reactions.</li> <li>• Formation of the ceramic body.</li> </ul>
1200	Lemougna et al. (2020)	4-7% mass loss.	
1250	He et al. (2020)	9.43% mass loss.	

### 9.3 Materials and Methods

As outlined in Section 3 (Materials and Methods) of Chapter 8, the geopolymers were produced using fly ash from Eskom's Matla power station as the precursor aluminosilicate material. The alkaline activation was undertaken using sodium hydroxide. Various concentrations of aqueous cellulose nanocrystal solutions were prepared using freeze-dried CNC produced from sawdust using a propriety technology developed at the CSIR's Biorefinery Industry Development Facility. The CNC solution concentrations formed included: 0.71, 0.86, 1.28, 1.56, 1.7 and 2%. Subsequently, the fly ash geopolymers were cured under two curing conditions previously investigated in the research of Roopchund (2016): 24-hour curing and 48-hour curing. The latter technique entailed the initial 24-hour curing, followed by removing the samples from the mould, rotation of the samples, and further curing for 24 hours. Considering that crushed samples were required to perform the thermal analyses, the required samples were crushed using a pestle and mortar.

The TGA was undertaken by subjecting the geopolymer to a controlled temperature programme. The TGA/DSC unit (Model TGA Q500/ DSC Q2000, TA Instruments, U.S.A.) was used in the ascending temperature exposure of the samples. The instrument could simultaneously measure the mass change (TGA) and true differential heat flow (DSC) on the same sample from ambient temperature up to 290°C (DSC) and 1,000°C (TGA) at a ramp rate of 2.08 °C per minute. Nitrogen gas was injected at a rate of 25 ml per minute.

The sample's mass change was measured as a function of temperature (Rawlinson, 2006). Furthermore, the DSC analysis was undertaken to identify the endothermic and exothermic peaks indicating specific phenomena relating to the thermal behaviour of the sample that does not involve a change in sample mass.

## **9.4 Results and Discussions**

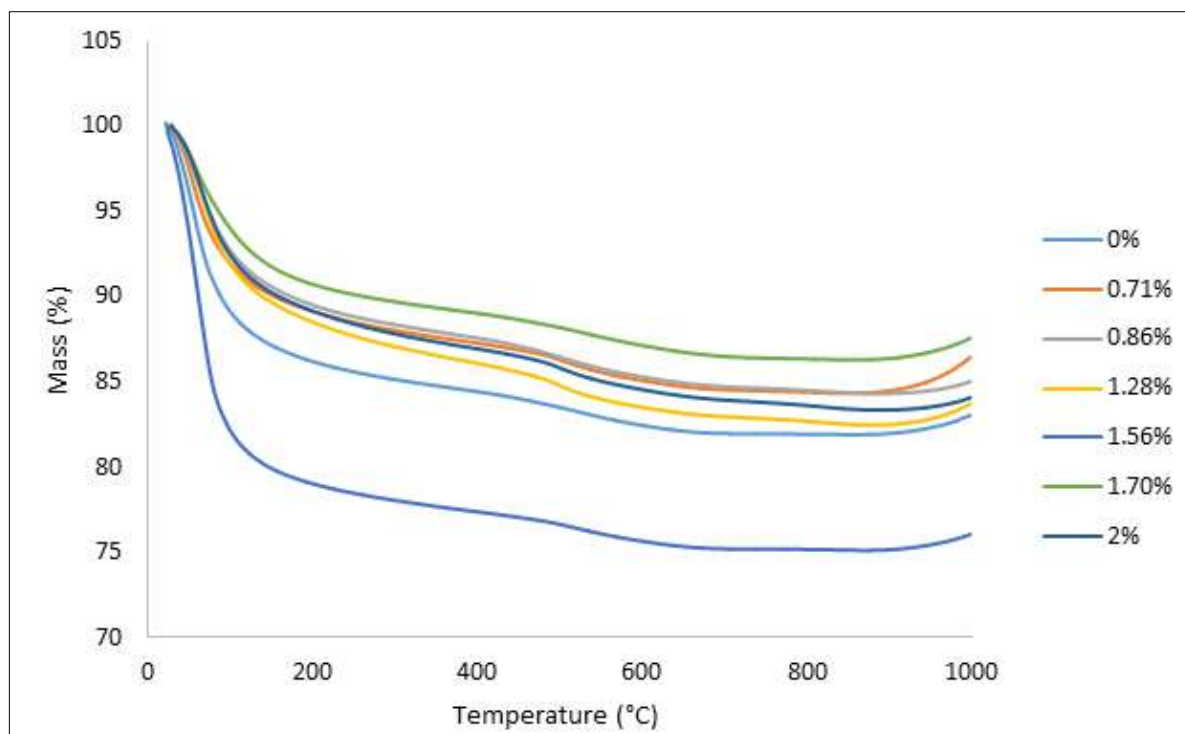
### ***9.4.1 Thermo-gravimetric Analysis***

#### **9.4.1.1 General Trends**

As shown in **Figure 9.6**, the general trend was that all the 24 hour-cured samples, except for the 0.86% CNC dosage, exhibited a steep mass decrease just before reaching 100°C. This observation was confirmed in previous research with various explanations for the rapid mass loss of the geopolymer sample within this temperature range: de-watering as free and adsorbed moisture was evaporated from the sample (Caballero et al., 2019), dehydration of adsorbed and loosely bound water (Rickard and van Riessen, 2010), humidity reincorporation (Caballero et al., 2019) and the evaporation of hygroscopic water (Lemougna et al., 2020). Subsequently, a gradual mass decrease was observed between the temperature range of 100 to 600°C until the mass remained relatively constant between 600 to 950°C. The gradual mass decrease was attributed to the removal of surface hydroxyl groups and the formation of silicon-oxygen-silicon bonds with the elimination of structural water (Caballero et al., 2019; Lemougna et al., 2020) and the de-hydroxylation of ferrihydrite as it crystallizes to hematite (Rickard and van Riessen, 2010).

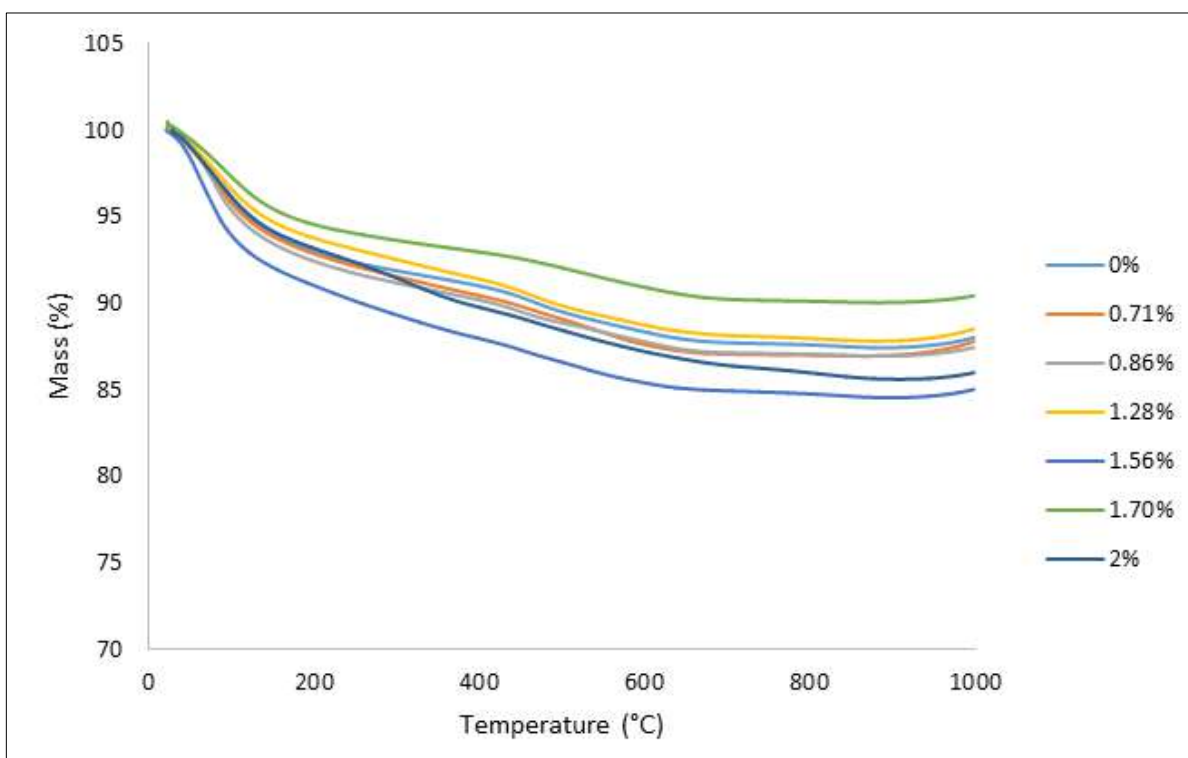
The general trend exhibited by the 48 hour-cured samples (**Figure 9.7**) followed that of the 24 hour-cured samples. The steep mass decrease as the temperature increased to 100°C was attributed to the rapid evaporation of moisture within the samples. At temperatures exceeding 100°C, in addition to the possibilities offered by the literature, it is also possible that the gradual degradation of the CNC within the sample resulted in the gradual decrease in sample mass. The likelihood of this possibility was confirmed by the CNC degradation temperature between 150 to 200 °C (Yildirim and Shaler, 2017). Furthermore, it is notable that the crushing of the samples

for the thermal analysis enabled effective CNC degradation under high-temperature exposure as compared to the CNC degradation contained within solid samples.



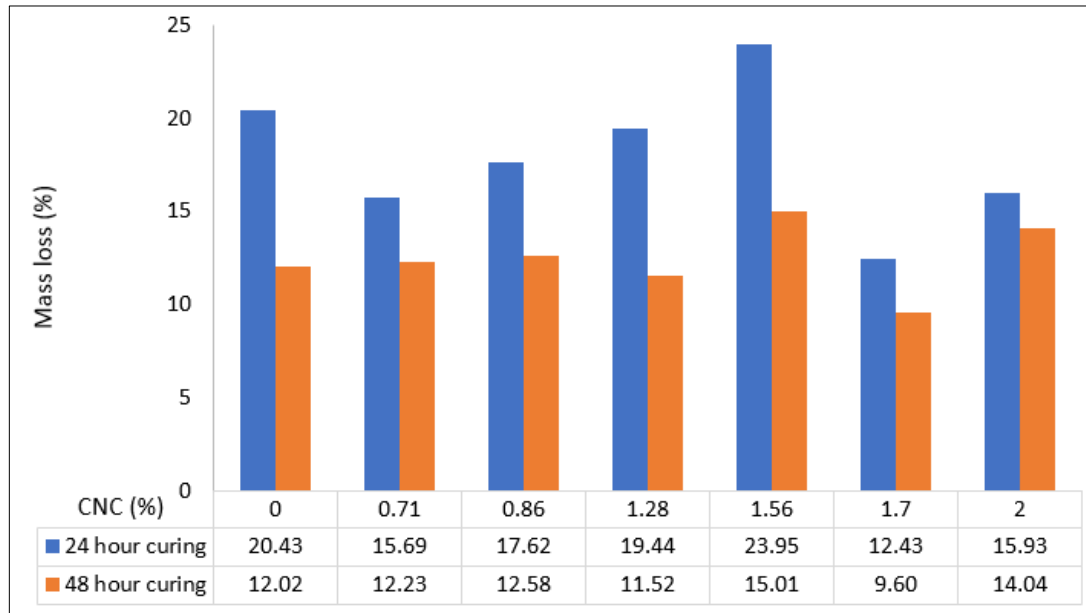
**Figure 9.6. TGA of 24 hour-cured samples**



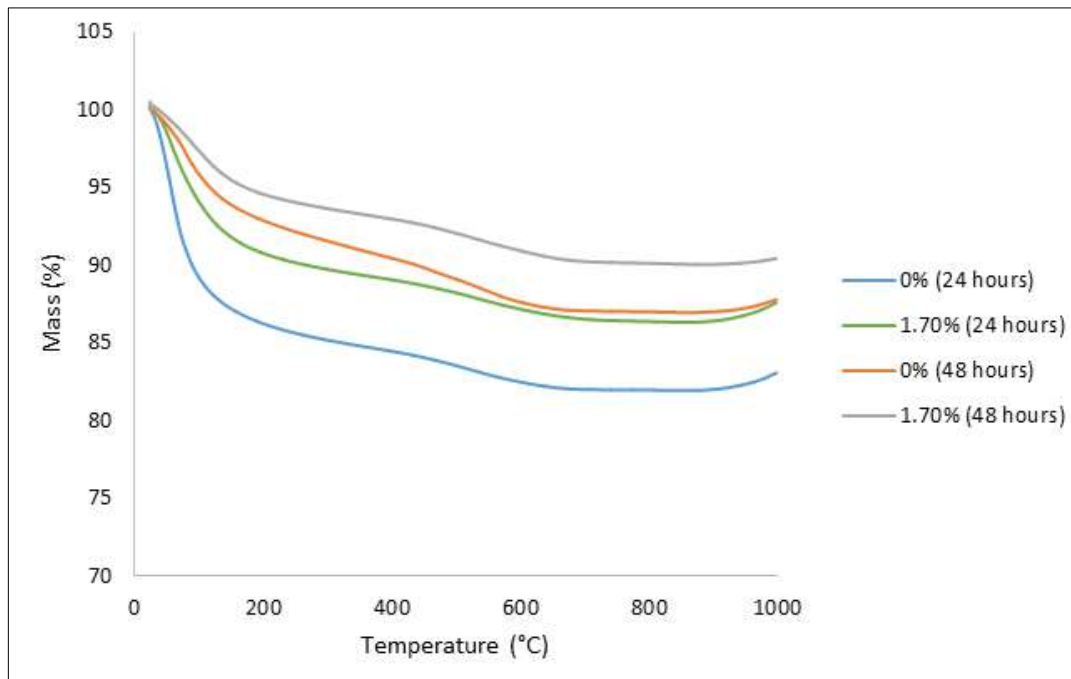


**Figure 9.7. TGA of 48 hour-cured samples**

The overall mass losses for the baseline (0% CNC dosage) and the remaining samples dosed with varying CNC concentrations were calculated and exhibited in **Figure 9.8**. It is noteworthy that the 48 hour curing period resulted in less mass loss at every CNC dosage than the 24 hour curing period. Furthermore, the 1.7% CNC dosage yielded the least mass loss for both curing conditions (24 and 48 hours) compared to the baseline. Hence, the 1.7% CNC dosage was deemed the most suitable concentration for preventing thermal degradation. To minimize the sample mass loss, combining the 1.7% CNC dosage and the 48-hour curing condition is recommended. This finding is shown in **Figure 9.9**, which compared the mass loss of the baseline sample to that of the optimal 1.7% CNC dosage under both curing conditions.



**Figure 9.8. Overall mass loss at each dosage of CNC**



**Figure 9.9. Mass loss comparison between the baseline and optimal CNC dosage with curing condition influence**

#### 9.4.1.2 Comparative Thermo-gravimetric Analyses

As observed in **Figure 9.6** and **Figure 9.7**, the starting masses of the 24-hour and 48-hour cured control samples were identical. However, the 24 hour-cured samples exhibited a steep mass loss within the first 100°C temperature increase. Although both samples exhibited a gradual mass loss as the temperature was increased from 100°C, the 24 hour-cured samples exhibited a mass loss consistently more than that of the 48-hour cured sample. The higher mass loss of the 24-hour cured sample was attributed to two possibilities. Firstly, there could have been incomplete combustion of the organic components within the precursor materials comprising the geopolymers. This finding was confirmed by the loss on ignition not exceeding 5% for the fly ash from which the geopolymers were prepared. Secondly, the shorter curing time may not have been influential in the shrinkage and combustion of the inherent organic components contained within the geopolymer matrix. Hence, upon high-temperature exposure, the organic components would be susceptible to shrinkage and combustion, corresponding to a decrease in the overall mass of the sample.

For the CNC-dosed samples, despite not having the same starting masses, the 24 hour-cured samples exhibited a more significant mass loss compared to the 48 hour-cured samples. Generally, there was no well-defined trend for the effect of the CNC on the mass loss of the samples. However, it was evident that the 1.7% CNC dosage exhibited the least mass loss. Hence the 1.7% CNC dosage was deemed optimal from the perspective of resistance to thermal degradation as previously found in the case of the overall mass loss comparisons. Furthermore, the 1.7% CNC concentration exhibited the most gradual and minimal mass loss with increasing temperature exposure.

#### 9.4.1.3 Derivative Mass Plots

The derivative mass plots represented the rate of change in sample mass. The general trend observed in **Figure 9.10** was that all the 24 hour-cured sample trends showed initial dips immediately, followed by two prominent peaks. The first peaks occurred at approximately five minutes, while the second peaks occurred at approximately 48 minutes. Steep rises and falls characterized the first peaks. Considering that the turning point of the first peaks occurred approximately five minutes into the analysis, it implied that the mass change is most rapid during this time. At the five-minute point, the mass change of all the samples remained

momentarily constant, after which the derivative mass was found to decrease between five to ten minutes drastically. Subsequently, between ten and thirty minutes, the mass change decreased very slightly, after which it remained relatively constant between 30 to 42 minutes. At approximately 48 minutes, all samples showed a pronounced increase and subsequent decrease in mass change, characterized by their respective second peaks. The second peaks corresponded to derivative mass changes less than 0.05 %/°C.

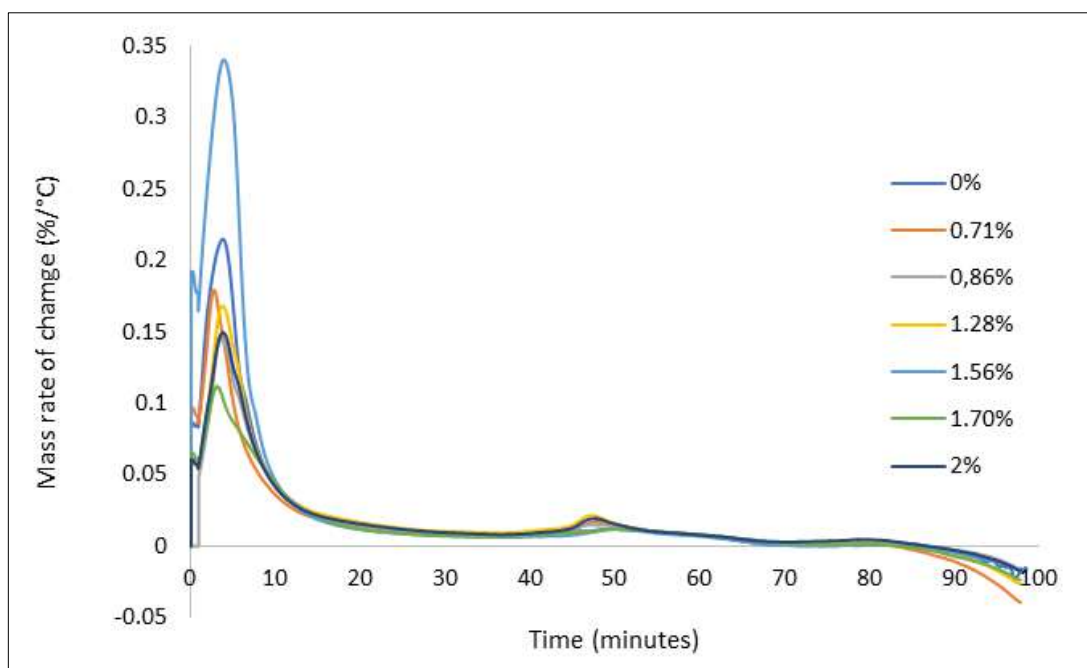
The 1.56% CNC dosage showed the most significant first peak at approximately 0.34 %/°C, followed by the 0% dosage of CNC at approximately 0.22 %/°C. The 0% dosage of CNC was followed by the remaining samples, which exhibited peaks less than 0.2 %/°C. Considering that the 1.56% CNC dosage yielded the greatest mass loss and least thermal stability observed in the TGA plots and overall mass losses, it informed that relatively high peaks indicate undesirable thermal characteristics.

Except for the 1.56% CNC dosage, the 0% CNC dosage exhibited the greatest peak relative to the other CNC dosages. The peak of the 0% CNC dosage corresponded to the sharpest increase and decrease of mass change with temperature change, which implied that the CNC addition improved the thermal stability of the geopolymers. Interestingly, the 1.7% CNC concentration exhibited the smallest peak and was consequently deemed optimal- as confirmed by previous analyses. This finding was confirmed in the mass loss studies in which the 1.7% CNC dosage exhibited the least mass loss. Once the analysis time exceeded an approximate duration of 85 minutes, the mass change became negative. This transition implied that the samples began to gain mass and was attributed to the mass gain associated with the oxidation of iron species as upon temperature exposure exceeding 600 °C (Rickard and van Riessen, 2010). Another possible explanation for the mass gain could be the sintering reactions at temperatures above 800 °C that facilitate the formation of a ceramic structure, inherently leading to a more significant sample mass (Lemougna et al., 2020).

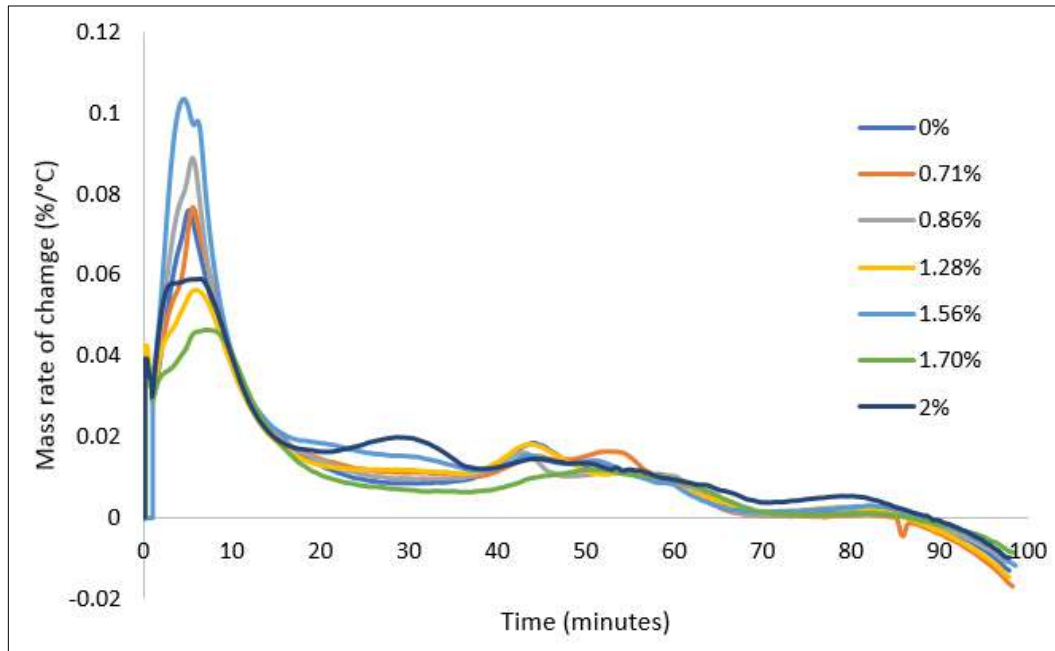
The general trend observed in **Figure 9.11** was that the derivative mass change range of the 48 hour-cured samples was substantially lower than that of the 24 hour-cured samples (maximum of 0.105 %/°C for the 48 hour-cured samples compared to the maximum of 0.304 %/°C for the 24 hour-cured samples). This finding confirmed the previous finding that the 48-hour curing

procedure produced better mechanical and thermal properties than the 24-hour curing procedure. A similar trend was observed in the peaks exhibited by the samples. All the samples showed peaks at approximately five minutes. This finding implied that the maximum increase and decrease in the sample mass change was encountered five minutes from the thermal analysis. The 1.56% CNC dosage exhibited the greatest peak, further implying that this dosage was the least optimal from thermal stability. By contrast, the 1.7% dosage of CNC exhibited the lowest peak, which confirmed the previous findings that the 1.7% CNC concentration is optimal for thermal stability.

Unlike the 24 hour plots, in which there were two dominant peaks, there were multiple broader peaks exhibited by every 48 hour-cured sample throughout the analysis. Interestingly, as with the 24 hour-cured samples, the mass change percentage of all the samples transitioned to the negative scale just before a duration of 90 minutes. This scale transition was due to the mass gain of the samples, as previously discussed. The peaks were substantially lower for each CNC concentration for each 48-hour cured sample than the 24-hour cured samples. This finding implied that less sample mass is lost when the samples are cured for 48 hours compared to 24 hours.



**Figure 9.10. Derivative mass change for 24 hour-cured samples**



**Figure 9.11. Derivative mass change for 48 hour-cured samples**

#### **9.4.2 Differential Scanning Calorimetry**

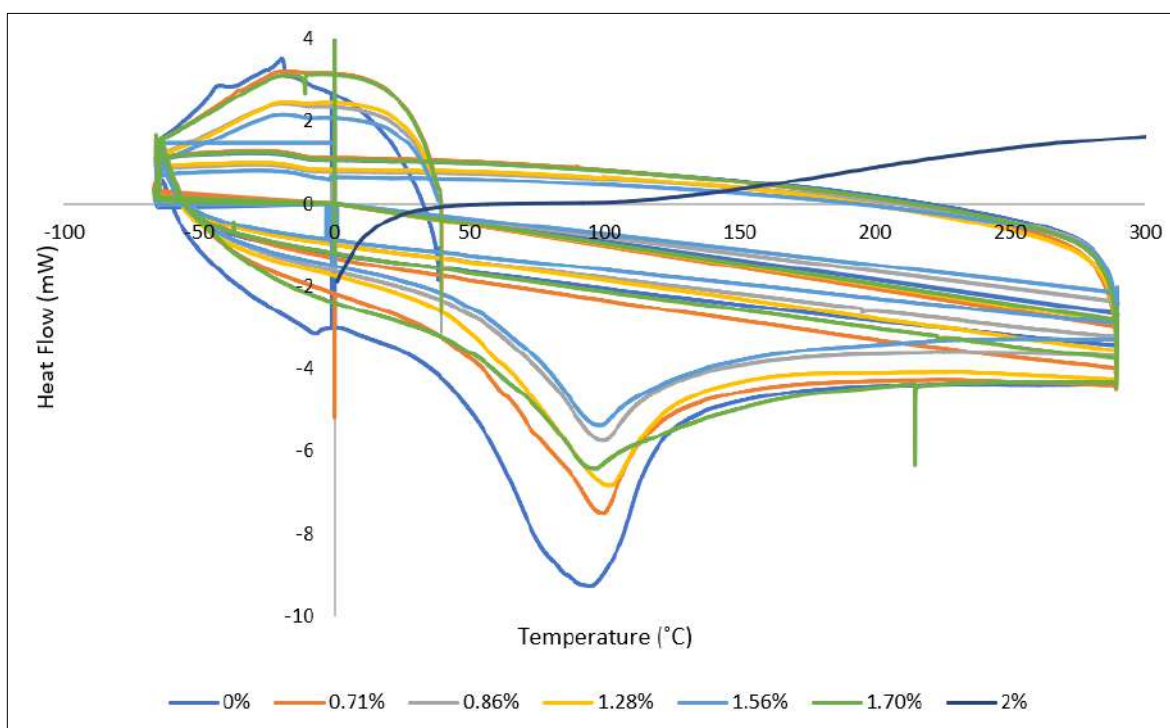
##### **9.4.2.1 General Trends**

The heat flow through a material is an indication of its thermal conductivity. For thermal resistance applications, it is beneficial to develop material with low heat flow capabilities. The opposite holds for applications that require thermal conductivity. Based on heat transfer conventions, positive heat flow implies that heat moves into a material, while negative heat flow implies that heat moves out of the material.

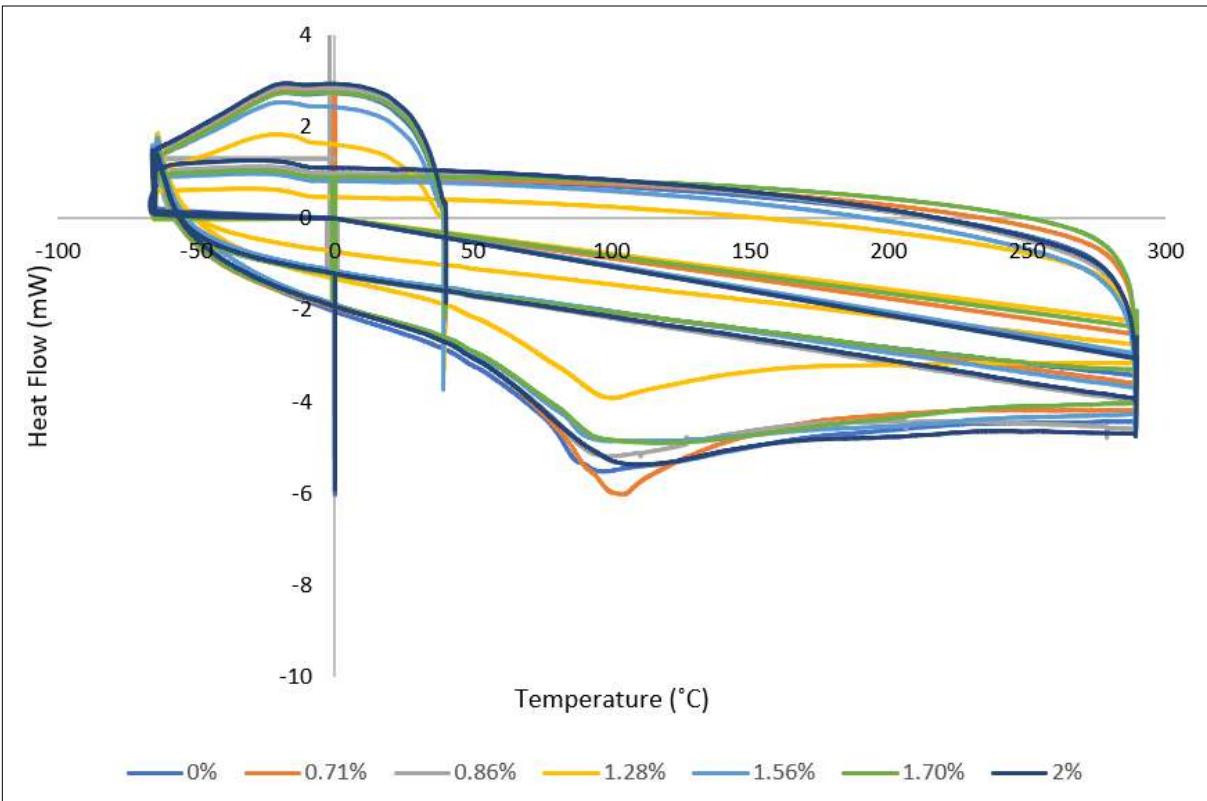
The overall heat flow trends for the 24-hour cured samples (**Figure 9.12**) showed an exothermic peak at approximately 100 °C, attributed to the phase transition of mineral compositions in the sample (He et al., 2020). In contrast, the areas of positive heat flow indicated humidity reincorporation due to the evaporation of free moisture in the sample (Caballero et al., 2019; He et al., 2020). The overall heat flow range was observed between -9.3 mW to 3.5 mW. Visually, it was deduced that there was a greater proportion of endothermic heat flow than exothermic heat flow at lower temperatures (less than 50°C). By extension, this implied a more significant occurrence of phenomena associated with endothermic behaviour, such as melting,

sublimation, solid-solid transitions, and chemical reactions (Rawlinson, 2006). Similar trends were observed for the 48 hour-cured samples (**Figure 9.13**), except that the heat flow range was smaller (-6.02 to 2.9 mW) than that of the 24 hour-cured samples. The smaller heat flow range, especially in the exothermic regions, implied that the 48-hour curing procedure restricted the heat flow from the samples. For each CNC dosage, the 48-hour-cured samples' heat flow trends showed more similarity when compared to the 24-hour trends.

Interestingly, the 1.7% CNC dosage showed lower exothermic peaks (under both curing time conditions) with respect to the baselines and other samples (Figure 9.14). This finding validated the previous findings of the TGA and derivative mass change analyses.

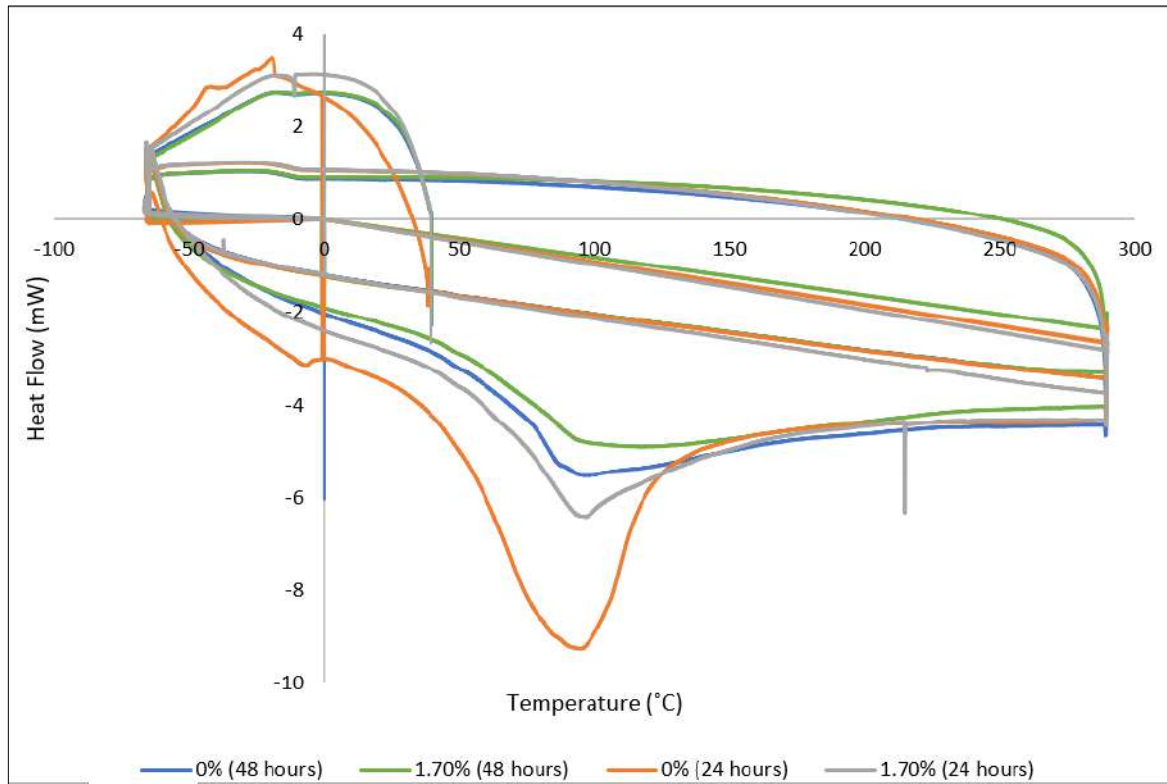


**Figure 9.12. Heat flow analysis for 24 hour-cured samples**



**Figure 9.13. Heat flow analysis for 48 hour-cured samples**





**Figure 9.14. Heat flow comparison between the baseline and optimal CNC dosage with curing condition influence.**

## 9.5 Conclusions

Detailed thermal analyses of the baseline fly ash-based geopolymer and CNC-reinforced geopolymers were undertaken by TGA-DSC. It was noteworthy that the detailed thermal profile firstly contributed to the comprehensive database of properties required to gain a complete understanding of the strengths and limitations of the fly ash-based geopolymer as an alternate green construction material to ordinary Portland cement. Secondly, the thermal profile can be used to optimize the thermal behaviour of the geopolymers for specific applications.

Mass loss is undesirable in construction materials as it leads to shrinkage, which may impede the efficacy of the material in performing the application for which it was designed. In most cases of CNC dosage, the TGA results indicated that the baseline proved more effective in resisting mass loss at elevated temperature exposure. However, the 1.7% CNC dosage was most effective in resisting sample mass loss. Despite being the second-largest CNC dosage, the 1.7%

dosage was still relatively minor to the total volume of the geopolymer sample to which it was dosed. Hence, this finding implied that a relatively small quantity of CNC would be required to improve the thermal stability of the fly ash-based geopolymers under conditions of elevated temperature exposure.

The DSC results indicated that the fly ash-based geopolymer was more endothermic than exothermic at lower temperatures. Endothermic behaviour is associated with heat flow into the sample rather than heat flow from the sample to the surroundings. Hence, the geopolymer can be used in thermal resistance applications.

Other than the CNC dosage, the curing time was identified as an influencing factor in thermal behaviour. The 48-hour curing procedure yielded geopolymers with better thermal properties than the 24-hour curing time and was therefore deemed optimal. The maximum curing time investigated in this study was 48 hours. Although longer curing times may have yielded better geopolymer properties, they would be energy intensive, which is counter-productive to developing green construction materials. Alternatively, a higher curing temperature may be implemented over the 24-hour curing duration with precaution being taken to avoid cracking associated with excessive temperatures in the early stage of the curing procedure. However, in the previous research of Roopchand (2016), the 60°C curing temperature optimally developed geopolymers with satisfactory mechanical and thermal properties and was therefore implemented in this study. Considering the magnitude of these findings, the three-fold aims of this Chapter were met. The recommended further work could include shrinkage and dilatometry tests.

## **CHAPTER 10: THE EFFECT OF CNC ON THE MICROSTRUCTURE OF NOVEL GREEN CONSTRUCTION MATERIALS**

### **10.1 Introduction**

As the internal characteristics of construction materials dictate its external properties, it is important to analyze the internal effects of potential improvement factors. Factors such as compressive strength, density, electrical resistivity, and thermal behaviour of the material are influenced by the sample's internal structure, morphology, and porosity. Typically, scanning electron microscopy (SEM), coupled with energy dispersive X-ray (EDX) analyses, are used to analyze the morphology and elemental composition of the samples, respectively. However, the SEM technique is destructive and requires the crushing of the geopolymer samples for analysis, thus destroying their three-dimensional internal structure. Hence, two additional techniques (fracture imaging and X-ray computed tomography (CT) scanning) were used in this study to analyze the internal sample matrices. The fracture imaging technique involved fracturing the samples, while the X-ray CT scanning technique was non-destructive. Much research was undertaken on the microstructure of reinforced geopolymers. However, little is known about the influence of cellulose nanocrystals (CNC) on the internal geopolymer structure and elemental composition of geopolymers. Furthermore, the effect of increasing CNC concentration on the geopolymer microstructure is not known under different curing conditions. Consequently, the aims of this study were twofold. Firstly, to determine the overall effect of CNC on the geopolymers' microstructure and elemental composition under two curing conditions (24 and 48-hour curing). Secondly, to determine the effect of increasing CNC concentration on the geopolymers' microstructure. It was argued that CNC would positively affect the internal geopolymer matrix, thereby improving its external properties.

## 10.2 Literature Review

### *10.2.1 SEM Analyses*

The study of Schmucker and MacKenzie (2004) focused on the analysis of metakaolin-based-geopolymers. They observed a glass-like matrix containing metakaolinite relicts and impure quartz particles. The quartz impurity was attributed to inefficient mixing of the precursor components. Interestingly, the impurity did not degrade the physical properties of the geopolymer. Heterogeneous areas were found within the glassy aluminosilicate matrix.

The microstructural differences of a variety of materials were investigated in the study of Lecomte et al. (2006). It was notable that the authors investigated ordinary Portland cement (OPC), alkali-activated slag, geopolymers, and a combined slag-based geopolymer. Although the geopolymer micrograph showed a homogeneous binding matrix without aggregate, the others were heterogeneous. The geopolymer and geopolymer-alkali-activated slag samples showed no cracks, unlike the OPC and alkali-activated slag samples. The cracks ran between the slag particles without passing through the slag particles. The authors also found that the matrix in the geopolymer-alkali-activated slag and alkali-activated slag samples were more homogeneous than the OPC sample.

Building on the study of Lecomte et al. (2006), the study of Chindaprasirt et al. (2009) investigated the microstructural differences of fly ash and ground bottom ash-based geopolymers. They found unreacted and partially reacted fly ash and a continuous mass of aluminosilicate in the fly ash geopolymers. Generally, the larger fly ash particles were incompletely reacted. The voids and cracks in the geopolymer matrix were undesirable, as they limited its binding capacity and strength (Chindaprasirt et al., 2009). The microstructure of the bottom ash geopolymer had unreacted and partially reacted irregular coal ash particles. These irregular particles were porous, and negatively influenced the geopolymer strength. Interestingly, such heterogeneous areas were also reported in the studies of Lecomte et al. (2006) and Schmucker and Mackenzie (2004).

Furthering the research of fly ash-based geopolymers, the study of Muzek et al. (2012) identified and monitored their phases. The primary product was sodium silicate gel with unreacted fly ash.

As with previous studies (Schmucker and Mackenzie, 2004; Lecomte et al., 2006; Chindaprasirt et al., 2009), the microstructure was heterogeneous with circular fly ash cavities in the gel. The unreacted porous spheres in the matrix indicated incomplete geopolymerization (Muzek et al., 2012).

The unique study of Nath et al. (2016) focused on the combined effects of the sodium hydroxide alkaline activator concentration and curing temperature on the microstructure of fly ash geopolymers. The gel phases revealed dense gel and tabular structures with hydroxide content. In the final reaction products, the sodium hydroxide concentration affected the reaction temperature. The samples activated with 8 M sodium hydroxide concentration showed higher weight loss than the 10 M samples. Several valuable trends were found in this study. Firstly, the alkali concentration was directly proportional to the sodium oxide/silica molar ratio (de Vargas et al., 2011). Secondly, increasing the alkali concentration increased the pH, which developed the amorphous phase (Nath and Sarker, 2015). Thirdly, the strength increased with increasing silicon to aluminium ratios (Kovalchuk et al., 2007). Finally, with increasing temperatures, the silicon to aluminium ratios decreased as more alumina dissolution, and coordination with the silica chain occurred to form the geopolymer (Nath et al., 2016).

The study of Yazdi et al. (2018) replaced fly ash with ground granulated blast furnace slag to promote early strength development of ambient-cured geopolymers. The fly ash-based geopolymer microstructure was more homogeneous and denser due to the pozzolanic activity of fly ash over an extended period. After 28 days, most fly ash particles were covered with dense amorphous phases, enhancing the interphase bond between the remaining fly ash and the matrix. This phenomenon increased the compressive and flexural strength. This finding was confirmed by the studies of Kim and Lee (2015) and Chindaprasirt et al. (2009).

For geopolymers produced from ground granulated blast furnace slag, the microstructure became more compact and homogeneous when 50% of the fly ash was substituted with slag. Crystalline structures were most prominent for the 100% slag-based geopolymer. The crystalline structures resembled spindle-shaped formations, possibly assigned to calcium carbonate crystals (Yazdi et al., 2018). This finding was noteworthy, as none of the other reviewed studies reported the crystalline structures. The flexural strength increase with

increasing slag content was attributed to the reinforcing effect of these calcium carbonate polymorphs and a satisfactory mechanical bond between the crystals and amorphous phases (Yazdi et al., 2018).

### ***10.2.2 Elemental Analyses***

The geopolymer elemental analysis in the study of Schmucker and MacKenzie (2004) revealed that the crystalline grains comprised alumina and silica in an atomic ratio of 1:1. This finding suggested that the grains were unreacted relicts of dehydroxylated kaolinite. Other grains contained only silicon, corresponding to the quartz impurities. The analysis revealed that the average atomic composition of the geopolymer was 25% aluminium, 55% silicon, and 20% sodium.

Similar to the study of Schmucker and MacKenzie (2004), the geopolymers in the study of Lecomte et al. (2006), contained silicon, aluminium, and potassium due to the dissolution of metakaolin in the presence of potassium hydroxide and sodium metasilicate. The geopolymer matrix also contained magnesium and calcium, due to the partial dissolution of ground granulated blast furnace slag particles (Lecomte et al., 2006). According to the authors, this finding suggested that smaller ground granulated blast furnace slag particles reacted totally. In contrast, the larger ones react partially with alkaline activators to form the binding matrix. A similar result was found in the study of Chindaprasirt et al. (2009). In the alkali-activated slag sample, the ground granulated blast furnace slag dissolved partially and contributed to the binding phase as confirmed by the presence of magnesium, aluminium, and calcium in the matrix. The OPC matrix comprised calcium and silicon with lower quantities of aluminium, magnesium, and potassium.

Based on the elemental analysis in the study of Chindaprasirt et al. (2009), silicon, aluminium, sodium, and calcium were the major elements. The calcium presence was attributed to the large quantity of calcium oxide present in the parent fly ash (Chindaprasirt et al., 2009). The silicon to aluminium ratio for the fly ash geopolymer was 3, compared to 6 for the bottom ash geopolymer. Hence, the alumina leaching the fly ash geopolymer matrix was more effective than that in the bottom ash matrix. According to Fletcher et al. (2005), a greater silicon to

aluminium ratio produces geopolymers with lower strength and higher elasticity. This fact, coupled with the porous nature of the bottom ash particles, caused lower strength in the bottom ash geopolymers.

In the study of Muzek et al. (2012), the gel was comprised of phases containing sodium-silicon-aluminium in the bulk region. This finding implied that in a medium with a high concentration of dissolved silica, the species dissolved from the fly ash surface migrate into the bulk solution (Muzek et al., 2012). Minute quantities of iron, calcium, potassium, and magnesium were also observed in the gel. The latter remnant elements indicated undissolved fly ash phases during the alkali activation.

It was notable that the optimal application of a geopolymeric material can be determined by its silicon to aluminium atomic ratio in the polysialate, as shown in **Table 10.1** (Davidovits, 1999; Abdullah et al., 2011). A low silicon to aluminium ratio (less than 3) results in a very rigid three-dimensional network. A silicon to aluminium ratio higher than 15 results in a polymeric character to the geopolymeric material (Abdullah et al., 2011). For many construction applications, a low silicon to aluminium ratio is desirable (Davidovits, 1999). Furthermore, suppose the geopolymer is targeted at a particular application. In that case, the silicon to aluminium ratio can be adjusted using sodium silicate to alter the material to the specific application (Roopchand, 2016). In the study of He et al. (2016), geopolymers with silicon to aluminium ratios ranging between 2 and 4 were prepared by adding different contents of used silica into the geopolymer matrix.

**Table 10.1 Recommended applications of geopolymeric materials based on silicon to aluminium ratios (Davidovits, 1999)**

Si/Al ratio	Recommended applications
1	Bricks, ceramics, and fire protection.
2	Low carbon cement and concretes.  Radioactive and toxic waste encapsulation.
3	Fire protection fiberglass composite, foundry equipment, heat resistant composites (thermal range between 200 °C and 1000 °C), and tools for aeronautics titanium processes.
> 3	Industrial sealants (thermal range between 200 °C and 600 °C) and tools for aeronautical super-plastically formed aluminium.
20-35	Heat resistant fiber composites.

In the study of He et al. (2016), geopolymers with higher silicon to aluminium ratios (exceeding 4) exhibited greater mechanical properties due to the increased silicon-oxygen-silicon bonds and residual silica as reinforcement. However, these samples also exhibited poor chemical stability in the air, with the occurrence of efflorescence on the surface, which was attributed to their higher residual free potassium ions. For the samples exhibiting silicon to aluminium ratios greater than 3, efflorescence must be avoided using hydrothermal curing procedures at elevated curing temperatures (Roopchund, 2016). The differences in the silicon to aluminium ratios of geopolymer samples were explained in the study of Chindaprasirt et al. (2009). Fly ash and bottom ash were used as precursor materials. The silicon to aluminium ratios of the fly ash and bottom ash geopolymers were 3 and 6, respectively. These ratios indicated that the leaching of alumina in the fly ash geopolymer matrix was better than that in the bottom ash matrix. Although higher silicon to aluminium ratios resulted in geopolymers suitable for sealants and fire-resistant



composite materials (Davidovits, 1999), the study of Fletcher et al. (2005) indicated that they cause lower strength and higher elasticity.

### ***10.2.3 X-ray CT Scanning Analyses***

The study of Gopalakrishnan et al. (2007) focused on X-ray computed tomography in characterizing asphalt concrete. The imaging capabilities of X-ray microcomputed tomography were used to understand pavement internal structures, develop and optimise the parameters describing the internal structure, and relate them to pavement performance. Such findings aid in building durable transportation infrastructures. Hence, the study of Gopalakrishnan et al. (2007) validated the use of CT scanning in optimizing fly ash geopolymers by identifying any undesirable internal phenomena, such that these can be eliminated in subsequent experimental trials. Unlike the study of Gopalakrishnan et al. (2007), the study of Van Steen et al. (2017) used X-ray computed tomography to visualize the formation of corrosion products and micro-cracking in reinforced mortar cylinders. This study demonstrated another valuable application of CT scanning.

The study of Lei et al. (2018) focused on concrete specimens under static and dynamic loadings. The CT images showed the growth, propagation, and penetration of cracks and the failure of concrete samples. The failure followed the areas of structural weakness under the static load. However, in the case of dynamic loading, linear cracks formed rapidly through the aggregate.

Considering that the sample porosity directly influences its density and corresponding compressive strength, the study of Saleh and Livingstone (2004) was noteworthy as it described a method to quantify the internal porosity, air void distribution, cracks initiation, and growth in concrete. Variations in the air void target, potassium level, and type of fine aggregate were introduced into the concrete laboratory specimens. The specimens were stored in water for one year and periodically measured for expansion and scanned by X-ray tomography. The void percentage and distribution were proportional to the quantity of entraining additives. The crack distribution correlated with the potassium quantity. The porosity correlated with the quantity of air-entraining agents.

Based on the advancements in the CT scanning technique and the ability to combine it with other analytical techniques, it provides a robust and effective methodology for non-destructive analyses of cement and concrete samples. Based on the technique's ability to determine the effect of fiber reinforcement on the internal microstructure of the sample, it can effectively analyze the effect of CNC reinforcement on the internal structure of the fly ash-based geopolymer construction materials.

#### ***10.2.4 Geopolymer Microstructure***

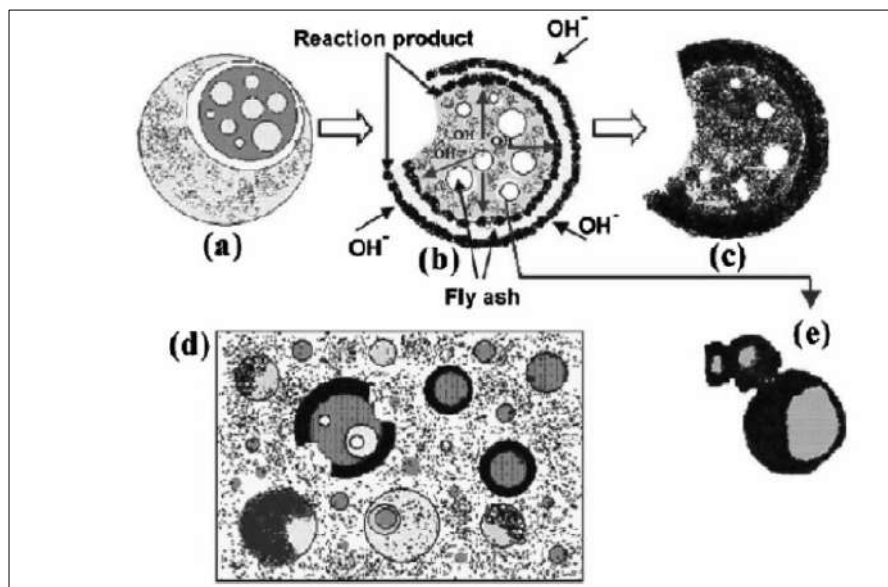
##### **10.2.4.1 Effect of Geopolymerization on the Microstructure**

Geopolymer micrographs show the microscopic effects of the geopolymerization reaction. According to Abdullah et al. (2011), geopolymers are amorphous aluminosilicate cementitious materials synthesized by the polycondensation of geopolymeric precursors and alkali polysilicates. Geopolymerization is a rapid chemical reaction, which occurs in three stages: (1) dissolution of silicon and aluminium atoms from the source material through hydroxide ions, (2) condensation of precursor silicon and aluminium ions into monomers, and (3) polymerization of monomers into polymeric structures. Considering that precursor materials rich in silicon and aluminium are primary geopolymerization requirements, alkali silicate solutions are used to dissolve raw materials to form the reactive precursors required for geopolymerization. A descriptive model of the geopolymerization reaction is shown in Figure 10.1 (Pacheco-Torgal et al., 2008).

For sodium hydroxide-activated fly ash-based geopolymers, there are three main contributors to the geopolymerization (Abdullah et al., 2011): the fly ash, alkali activation, and sodium hydroxide solution. The fly ash reacts with calcium hydroxide during the hydration process to form calcium silicate hydrate and calcium aluminate, reducing the risk of leaching calcium hydroxide. Fly ash improves the matrix permeability by decreasing the water content, thus reducing the remaining capillary pore volume. Furthermore, the spherical shape of fly ash improves the consolidation of the construction material, thus reducing the permeability.

The alkali activation phase entails the dissolution of silicon and aluminium when fly ash is contacted with an alkaline solution. The molecules condense in a gel form, and the alkali

solution attacks the fly ash surface, enters the particle, and then attacks the particle from inside out (Davidovits, 1999). Typically, the gel is observed as a vitreous, glassy layer in SEM micrographs (Lecomte et al., 2006). Consequently, the reaction product is generated inside and outside the shell until the particle is partially or entirely consumed. The type and concentration of alkali solution affect the dissolution of fly ash. The sodium hydroxide concentration is directly proportional to the dissolution of the fly ash. The gel composition analyzed in the sample activated with sodium silicate, and sodium hydroxide is enriched in sodium and aluminium. This aluminosilicate gel is defined as an “alkali-silica reaction” in the research of Kupwade-Patil and Allouche (2016).



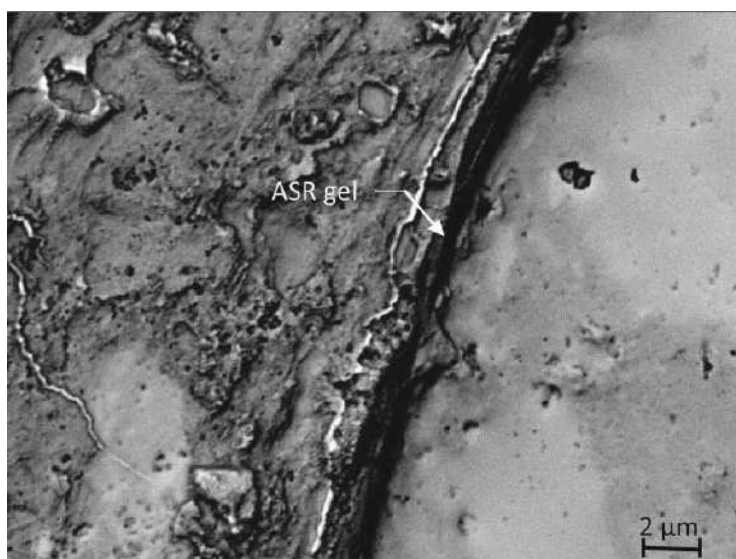
**Figure 10.1 Descriptive model of the alkali activation of fly ash (Pacheco-Torgal et al., 2008)**

According to Abdullah et al. (2006), geopolymers are different from ordinary portland cement as they do not form calcium silicate-hydrates for matrix formation and strength. Instead, geopolymers use the polycondensation of silica and alumina precursors with a high alkali content to attain structural strength. The geopolymer composition is similar to natural zeolitic materials, except that the microstructure is amorphous. However, according to Schmucker and MacKenzie (2005), the morphology of geopolymers is not entirely amorphous.

#### 10.2.4.2 Geopolymer Matrix Heterogeneity

In the study of Schmucker and MacKenzie (2005), the heterogeneous microstructure was evidenced by crystalline fly ash grains within the glassy matrix. Unreacted relicts in the geopolymers were also observed. These unreacted relicts were attributed to the incomplete mixing of the geopolymer paste before curing, which becomes progressively more difficult as the material stiffens before being placed in the mould (Schmucker and MacKenzie, 2005).

Furthermore, the SEM results in the study of Schmucker and MacKenzie (2005) indicated that the sample exposed to higher curing temperatures were identical with those exposed to lower curing temperatures, implying that dehydration failed to alter the geopolymer composition and morphology. Consistent with the study of Schmucker and MacKenzie (2005), the study of Kupwade-Patil and Allouche (2016) found matrix heterogeneity in the form of a clearly defined binder-aggregate interface (**Figure 10.2**).



**Figure 10.2. Micrograph of the binder-aggregate interface (Kupwade-Patil and Allouche, 2016)**

#### 10.2.4.3 Mullite Formation

Mullite formation is indicated by needle-like grains within the geopolymer matrix. The later study of Yazdi et al. (2018) reported these formations as calcium carbonate crystals. However, according to Schmucker and MacKenzie (2005), the EDX analyses of these needle-like crystals' Si/Al ratio confirmed their identification as mullite. In addition to the needle-like crystals, the

micrographs exhibited refined crystals due to the formation of pure alumina from the relicts of the original precursor material (Schmucker and MacKenzie, 2005). The excess silica and alumina in the matrix are converted to mullite by precipitation at higher temperatures. This phenomenon indicated that geopolymers can withstand elevated temperature exposure (Schmucker and MacKenzie, 2005).

#### 10.2.4.4 Cracks in the Microstructure

According to Kupwade-Patil and Allouche (2016), micro-cracks in the geopolymer matrix were linked to the alkali-silica reaction. Furthermore, although the matrix was continuous and relatively dense, voids and cracks were easily observed (Chindaprasirt et al., 2009). The alkali-silica reaction was attributed to reactive aggregates in fly ash-based geopolymer concretes (Kupwade-Patil and Allouche, 2016). Specifically, the alkali-silica reaction gel forms through chemical reactions between hydroxyl ions and silica (Swamy et al., 1988; Diamond, 1975, 1976).

Other studies showed that the alkali-silica reaction was a multistage process at the paste-aggregate interface (Ulm et al., 2000). Firstly, the hydroxyl ions attacked the silanol groups and the siloxane bonds. Secondly, there were expansion products. Depending on the gel formation, internal pressure within the matrix triggered macroscopic expansion and subsequent degradation of the matrix (Kupwade-Patil and Allouche, 2016).

#### 10.2.4.5 Effect of Chemical Composition on Micro-cracking

Diamond (1976) reviewed various reactive aggregates that caused alkali silica reaction expansion. Silica, tridymite, and cristobalite (silicon dioxide) were other reactive silica forms found in volcanic rocks. Low alkali cement used to prevent alkali-silica reaction often contain fly ash and granulated blast furnace slag (Multon et al., 2008; Ostertag et al., 2007).

#### 10.2.4.6 Unreacted Fly Ash Particles

In the study of Kupwade-Patil and Allouche (2016), the unreacted (spherical) fly ash particles co-existed in the amorphous geopolymer matrix. The fly ash was activated by sodium hydroxide and sodium silicate during mixing, resulting in a sodium-silicate gel that gave rise to a cementitious matrix. This reaction led to the formation of sodium aluminosilicate hydrate gel.

According to Chindaprasirt et al. (2009), the geopolymer paste is typically comprised of unreacted and partially reacted fly ash particles and a continuous mass of aluminosilicate.

The geopolymer microstructural considerations outlined in this section will enable the analysis of the geopolymer microstructure using the analytical techniques reported.

### **10.3 Materials and Methods**


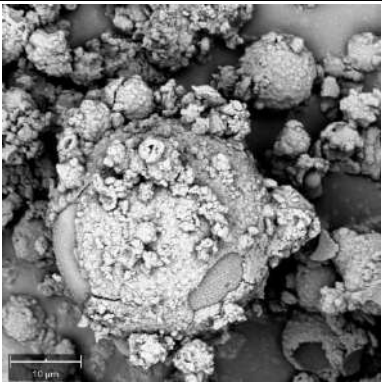
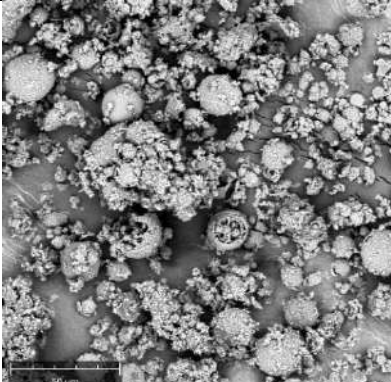
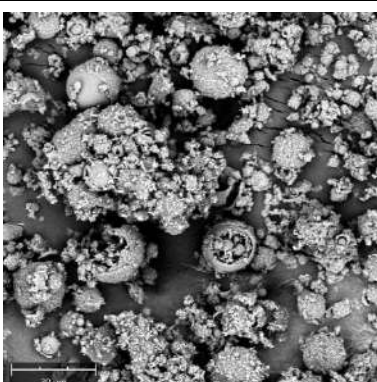
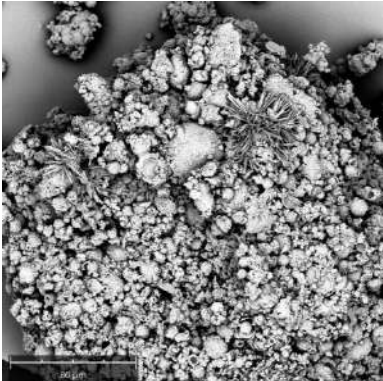

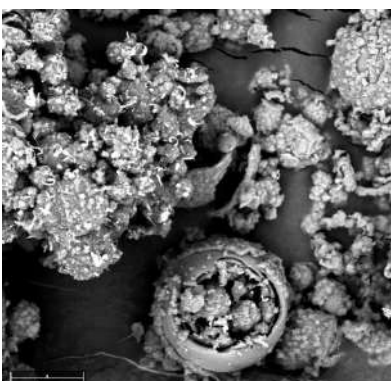
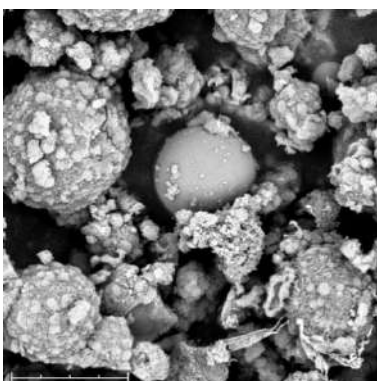
The geopolymers were developed as per the procedure reported in Chapter 8. Subsequently, the geopolymer samples for the SEM-EDX analyses were crushed using a pestle and mortar, prior to analysis. In addition, selected uncrushed samples were analysed using fracture analyses (imaging) and X-ray CT scanning. The selected samples included the following:

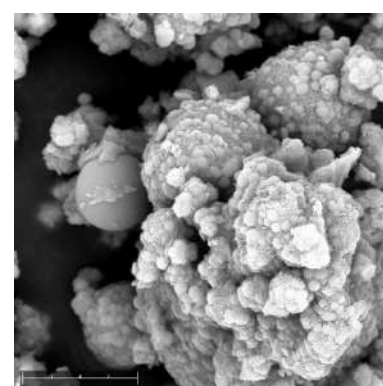
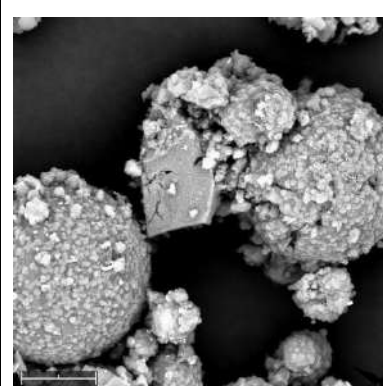
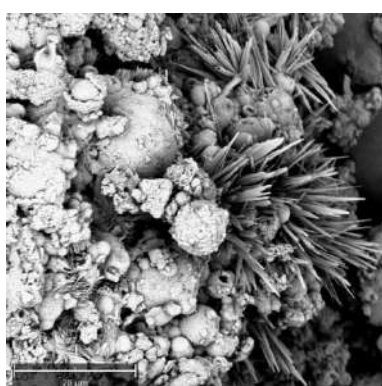
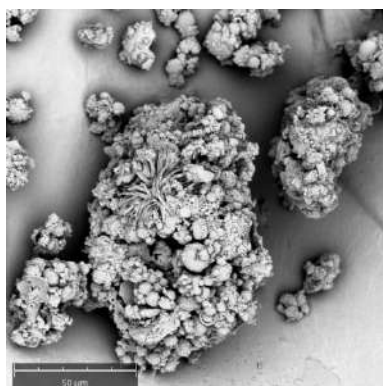
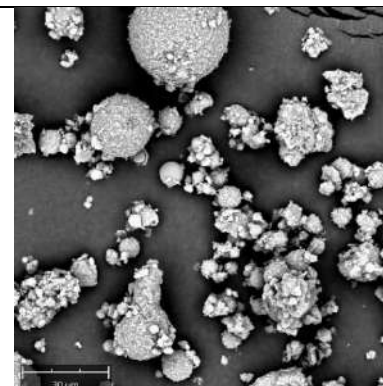
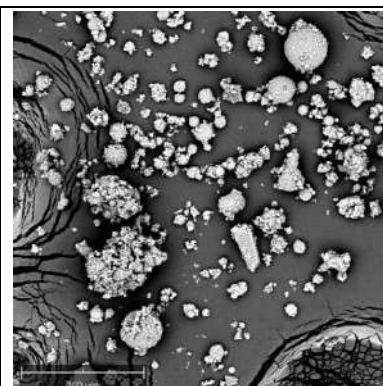
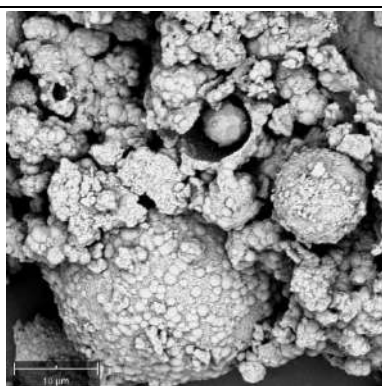
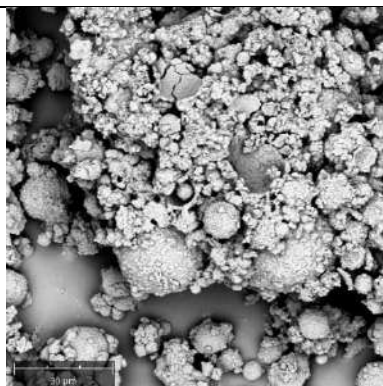
- a) Sample 1: dosed with 0% CNC and cured for 24 hours.
- b) Sample 2: dosed with 2% CNC and cured for 24 hours.
- c) Sample 3: dosed with 0% CNC and cured for 48 hours.
- d) Sample 4: dosed with 2% CNC and cured for 48 hours.

The samples were broken cross-sectionally and micrographed using SEM for the fracture analyses. The X-ray CT scanner (Model Phoenix VTomeX L240, General Electric Industries, United Kingdom) was used. Fast scans were done at 180 kV and involved the recording of 1,000 images during a full rotation of the sample, which lasted approximately five minutes per scan. A background detector calibration was required once before proceeding. The Datos reconstruction software used a modified Feldkamp algorithm to output the data. This methodology was similar that used by Du Plessis and Boshoff (2019).

### **10.4 Results and Discussion**

**Table 10.2. SEM micrographs of geopolymer samples under two different curing conditions**

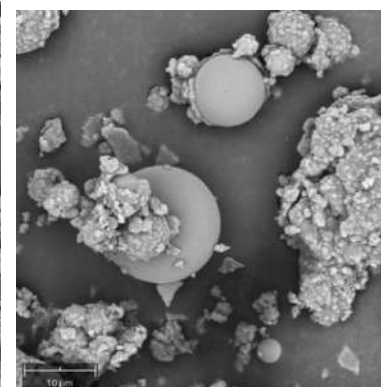
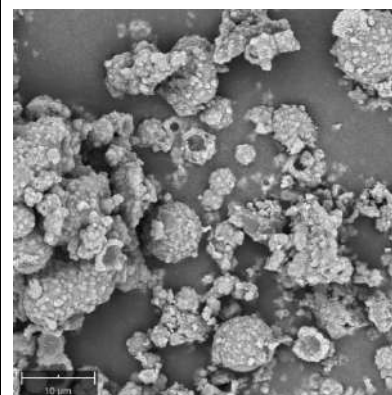
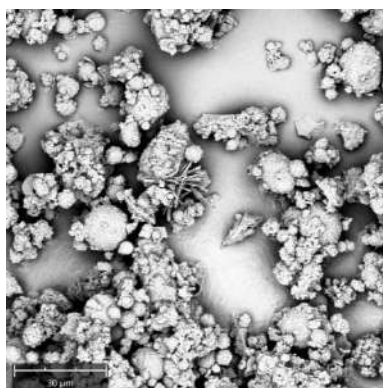
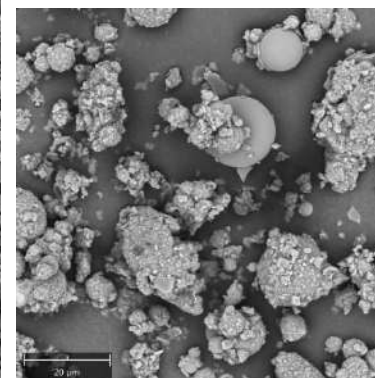
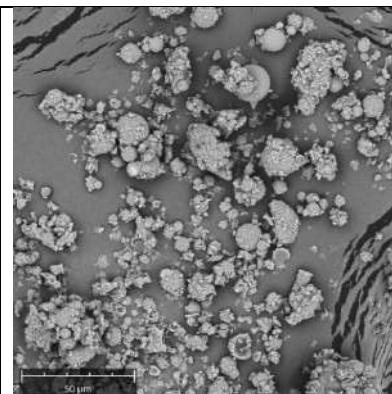
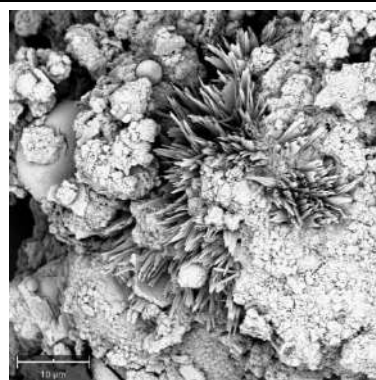
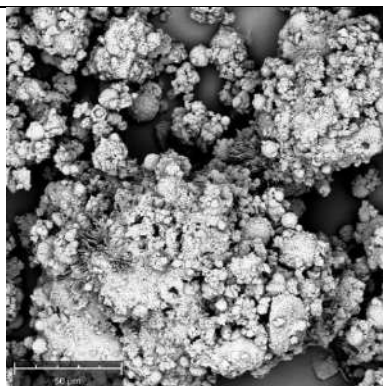
Sample	24-hour curing	48-hour curing
1	Description: 0% CNC, 9.72 M sodium hydroxide alkaline activator	
	 	 
	 	 
2	Description: 0.71% CNC, 11.12 M sodium hydroxide alkaline activator	



3

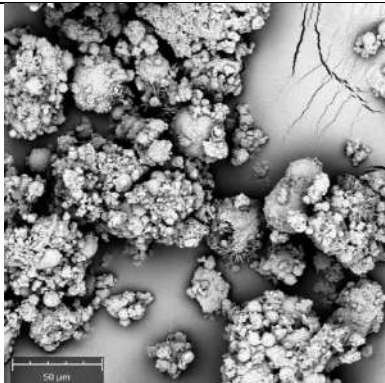
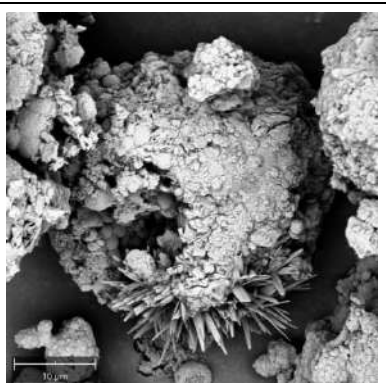
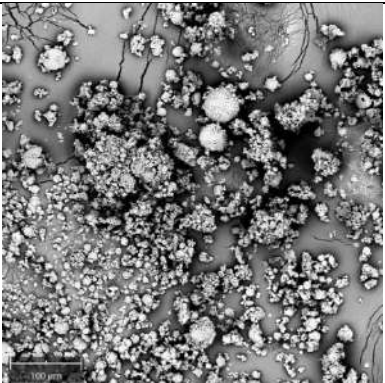
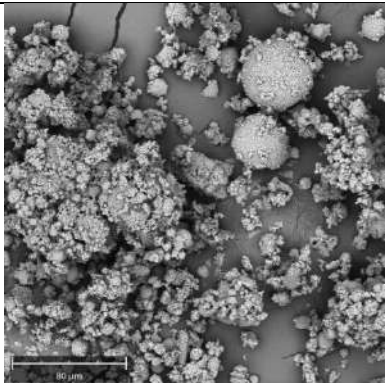
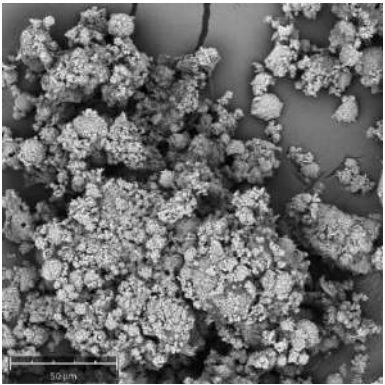
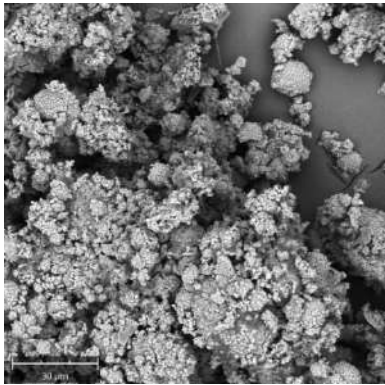
Description: 0.86% CNC, 9.7 M sodium hydroxide alkaline activator

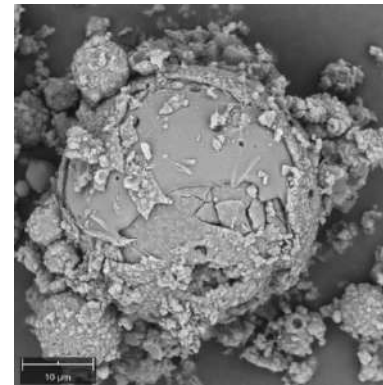
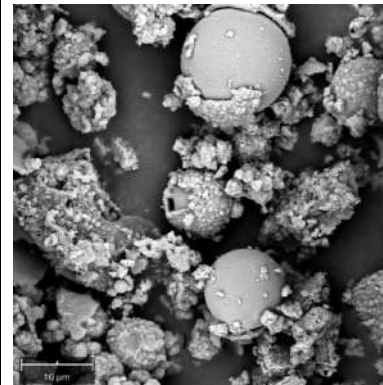
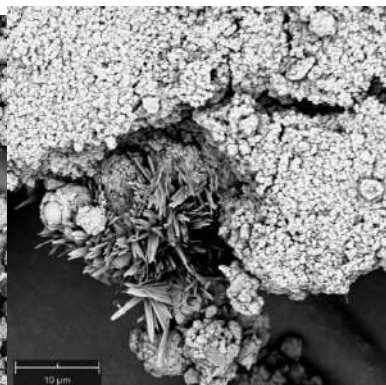
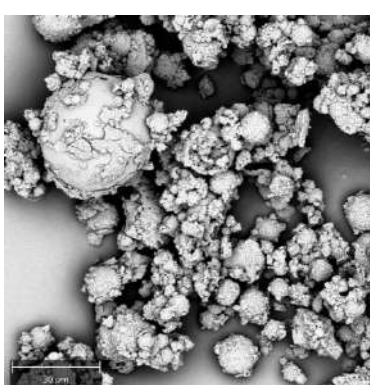
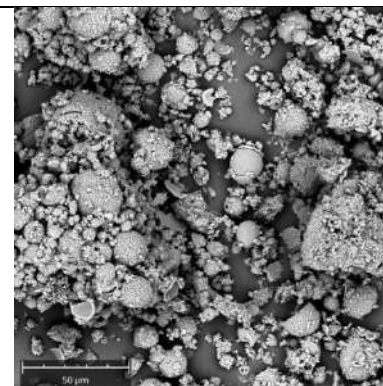
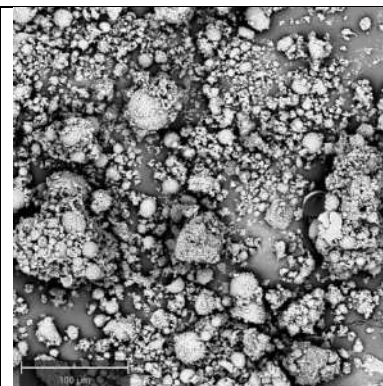
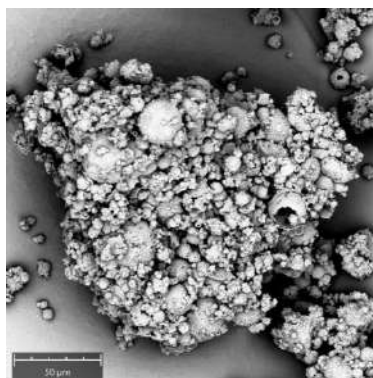
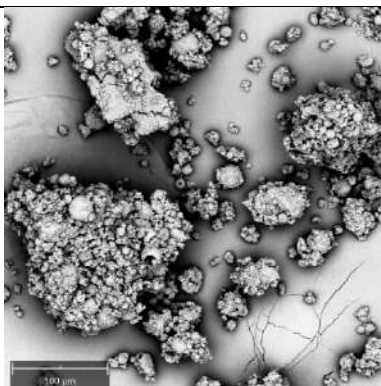




4

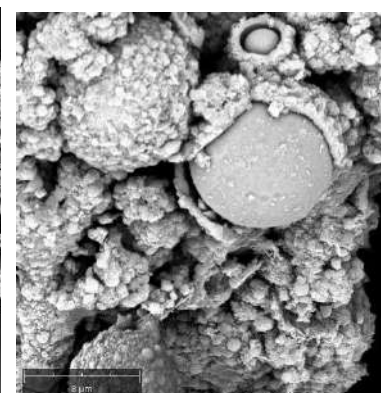
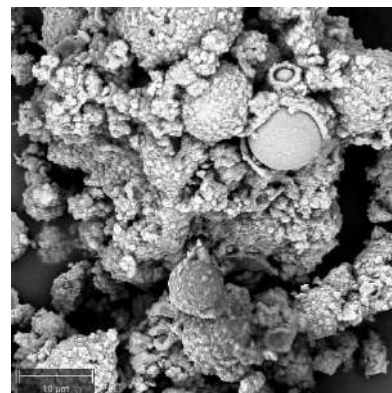
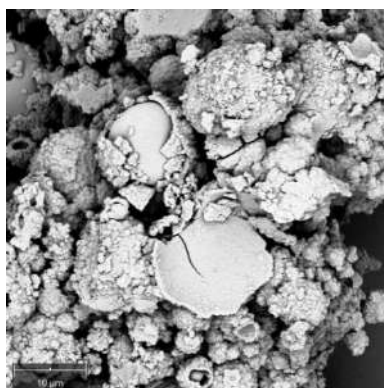
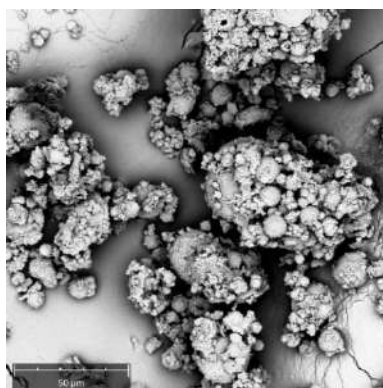
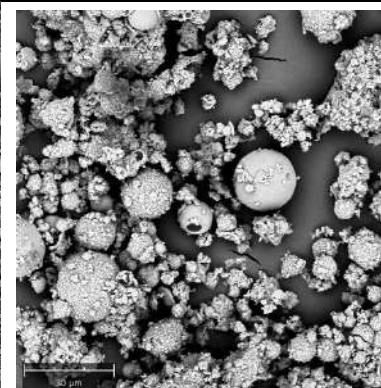
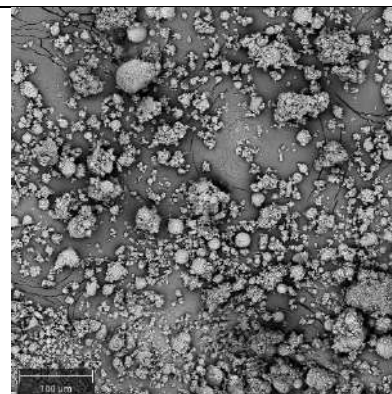
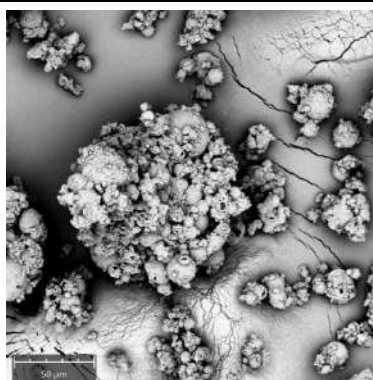
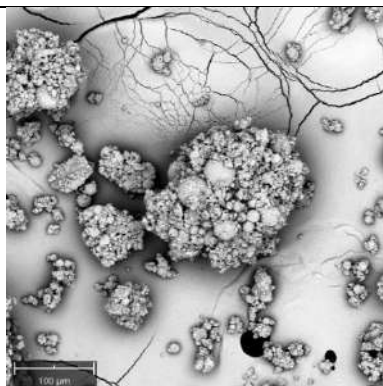
Description: 1.28% CNC, 12 M sodium hydroxide alkaline activator

	 	   
5	Description: 1.56% CNC, 9.4 M sodium hydroxide alkaline activator	



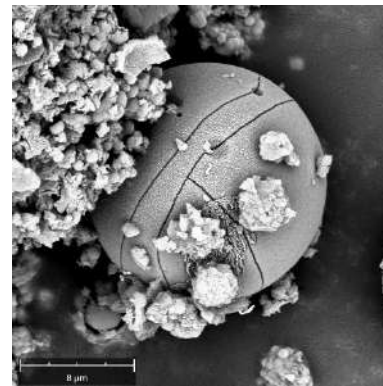
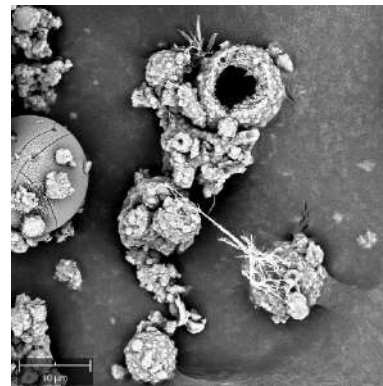
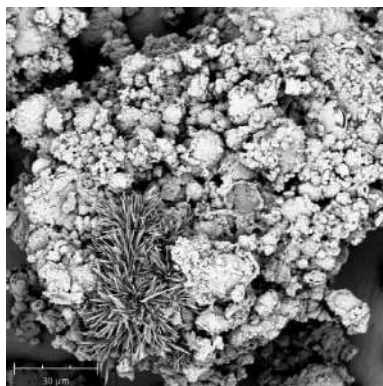
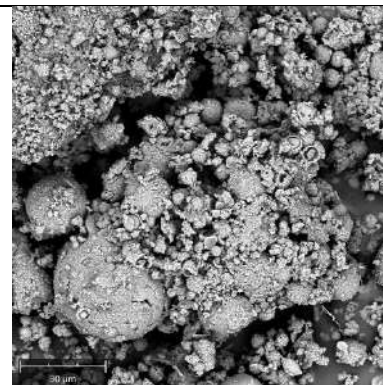
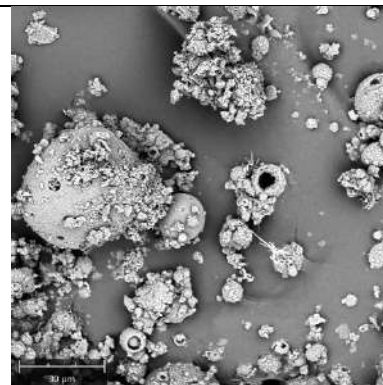
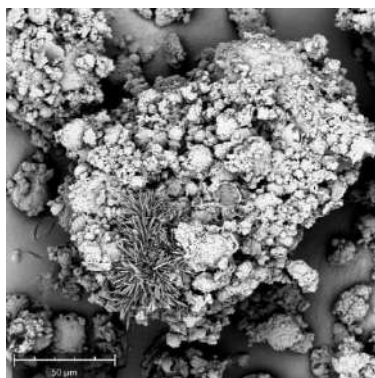
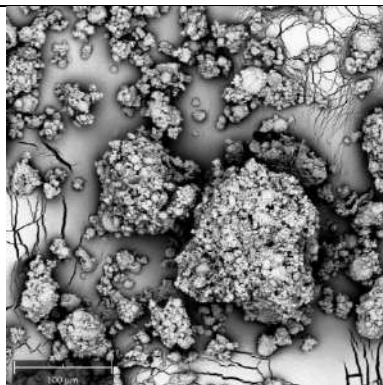
6

Description: 1.7% CNC, 8 M sodium hydroxide alkaline activator

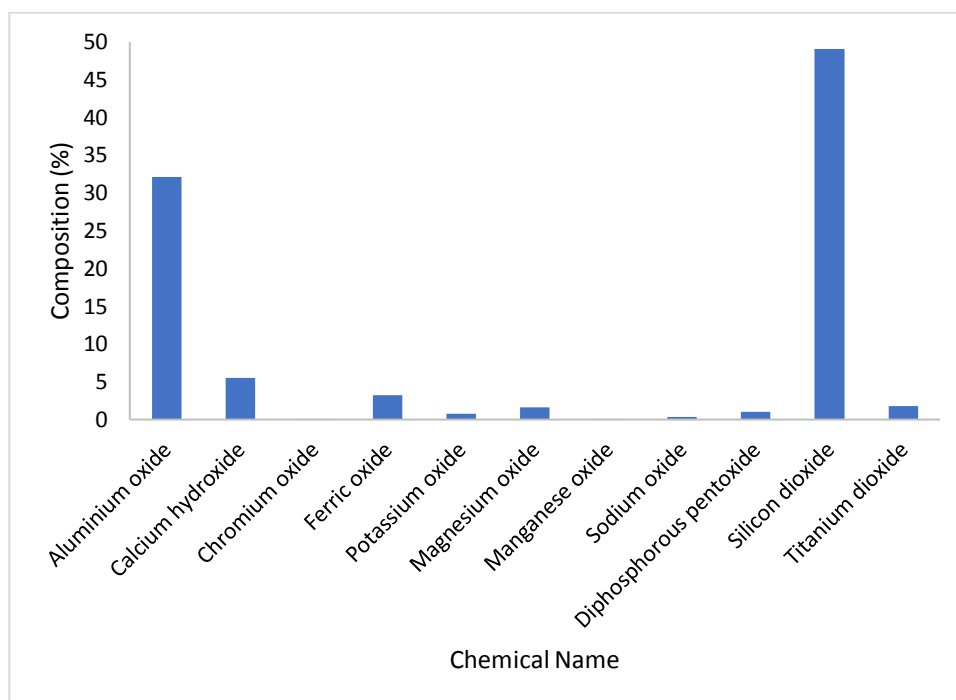


7

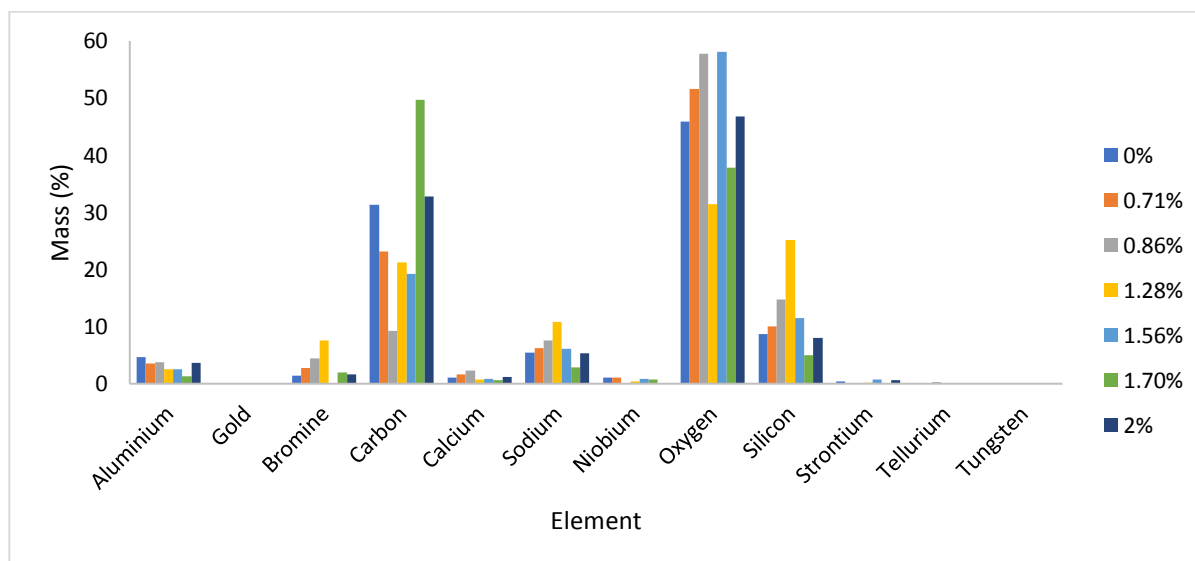
Description: 2% CNC, 12 M sodium hydroxide alkaline activator



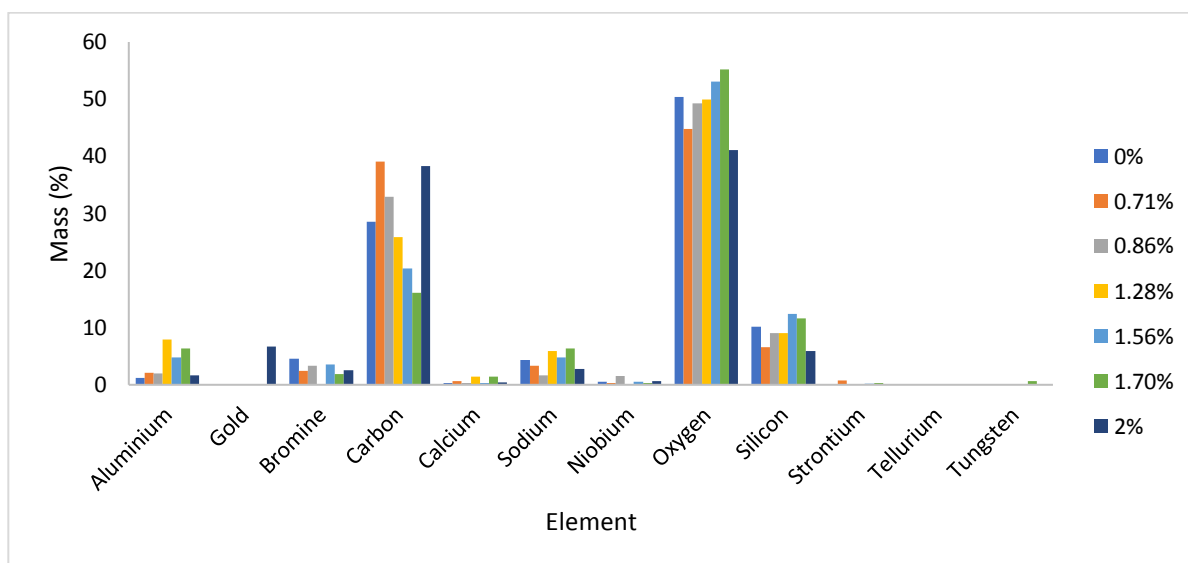




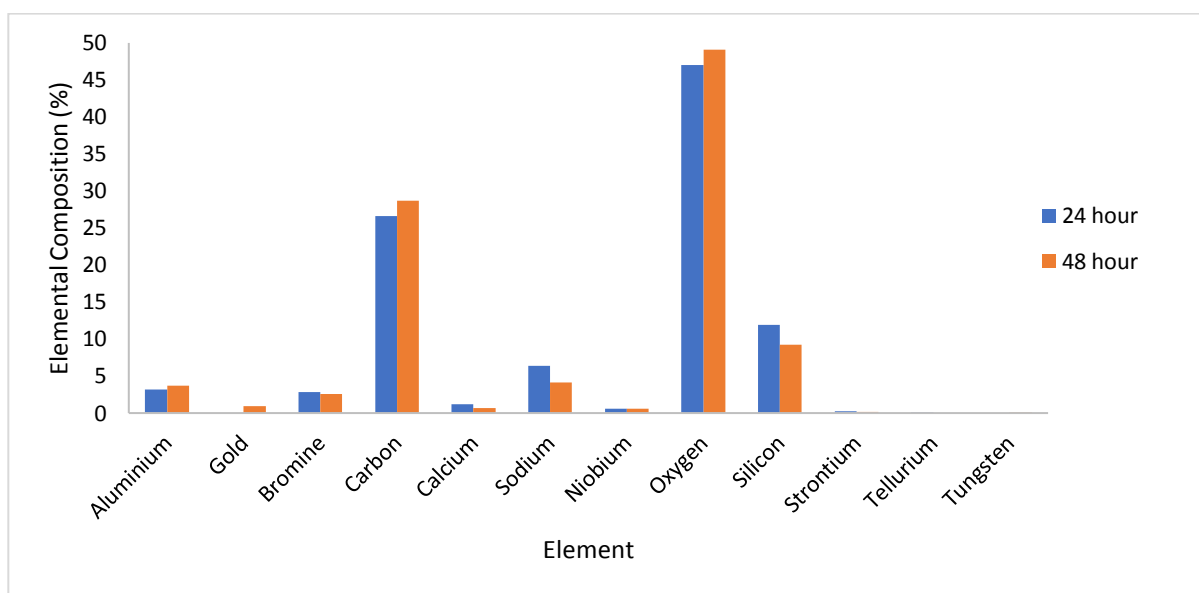
**Figure 10.3. Chemical composition of fly ash precursor material**



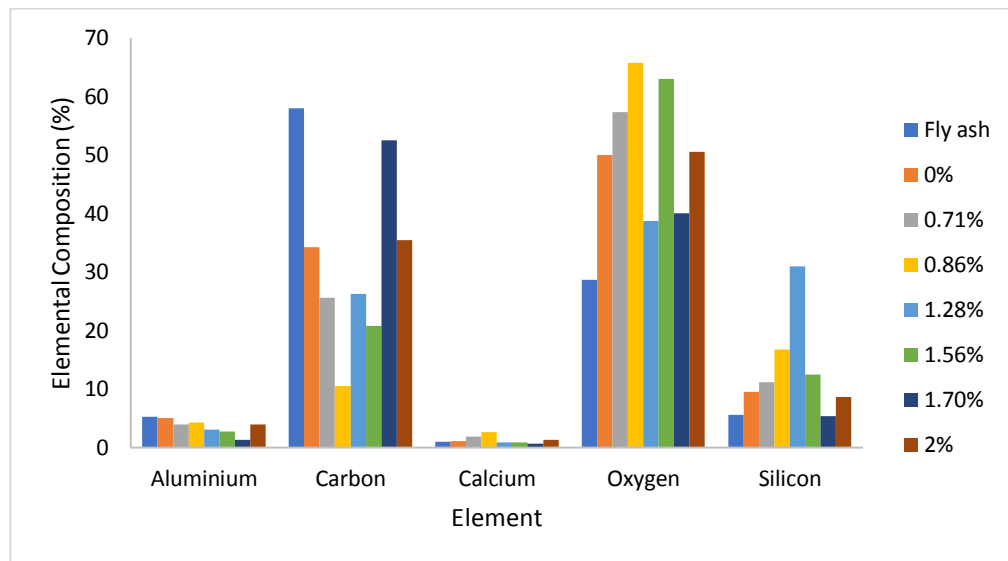
**Figure 10.4. Elemental composition of 24-hour cured geopolymers samples.**



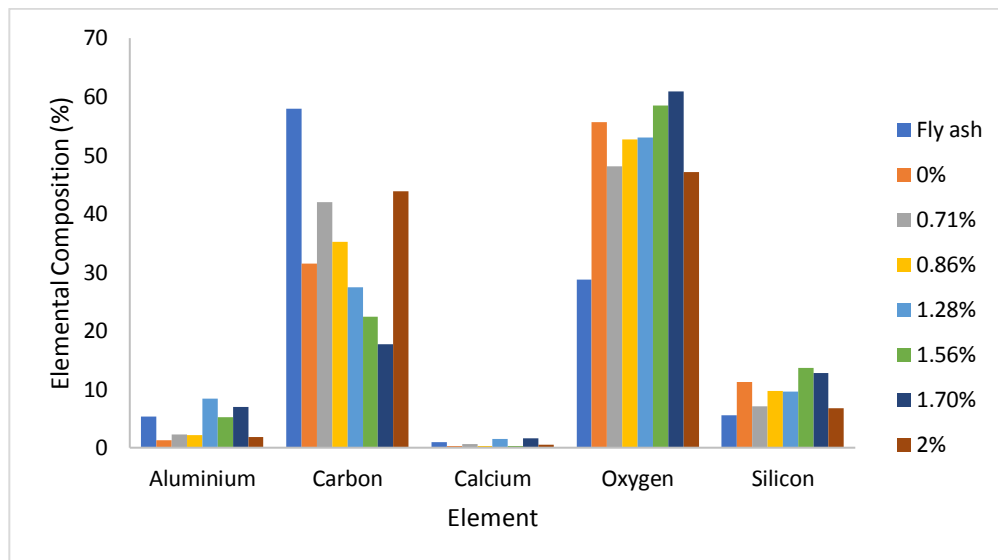
**Figure 10.5. Elemental composition of 48-hour cured geopolymer samples.**



**Figure 10.6. Average elemental composition comparison.**

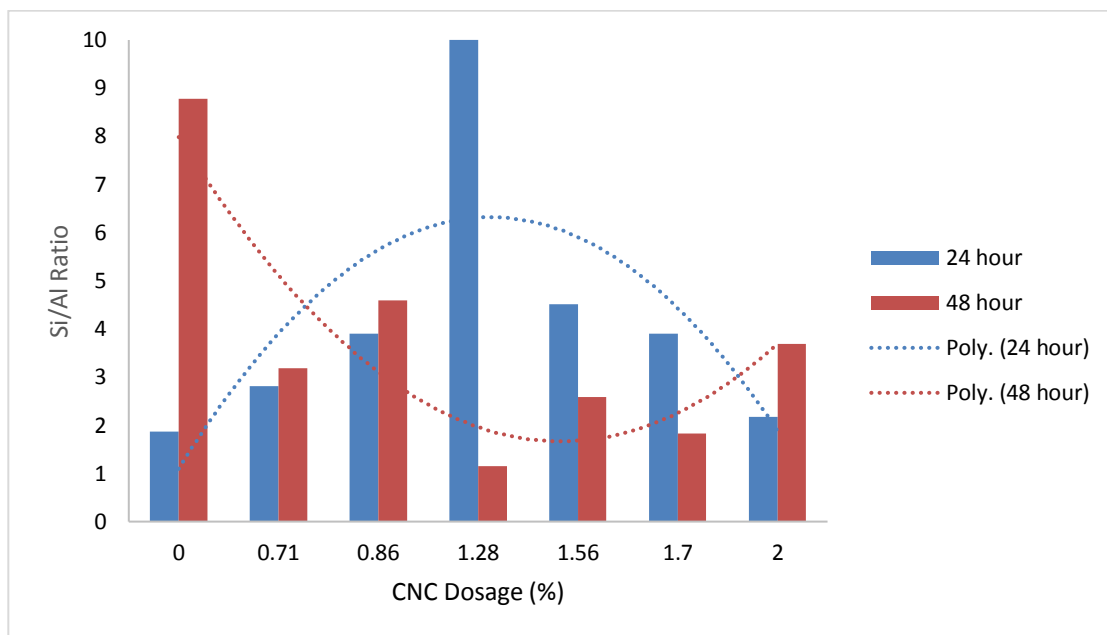


**Figure 10.7. Elemental composition comparison of 24-hour cured samples with the fly ash precursor.**



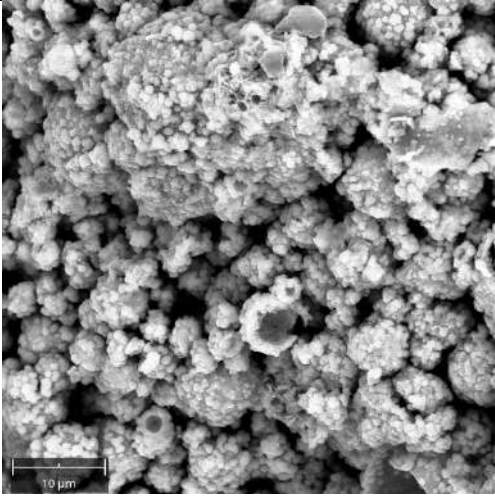
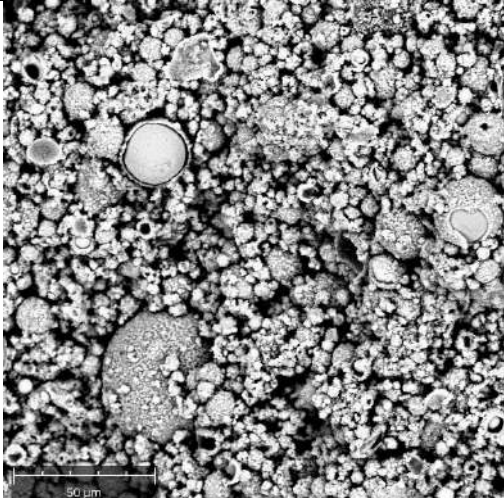
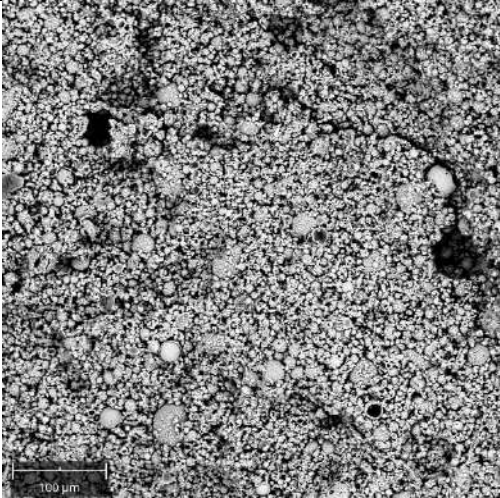
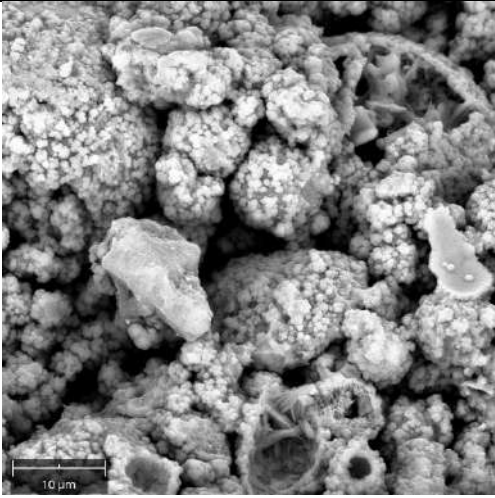

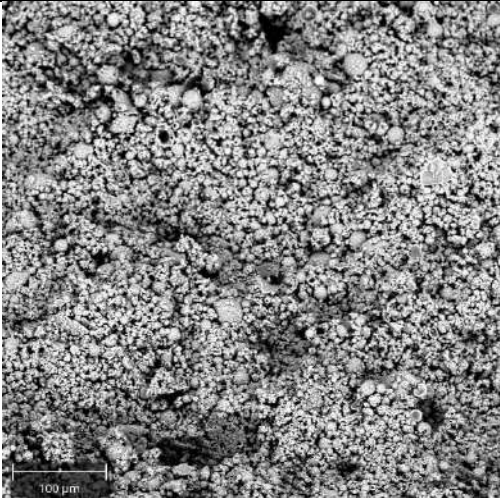
**Figure 10.8. Elemental composition comparison of 48-hour cured samples with the fly ash precursor.**

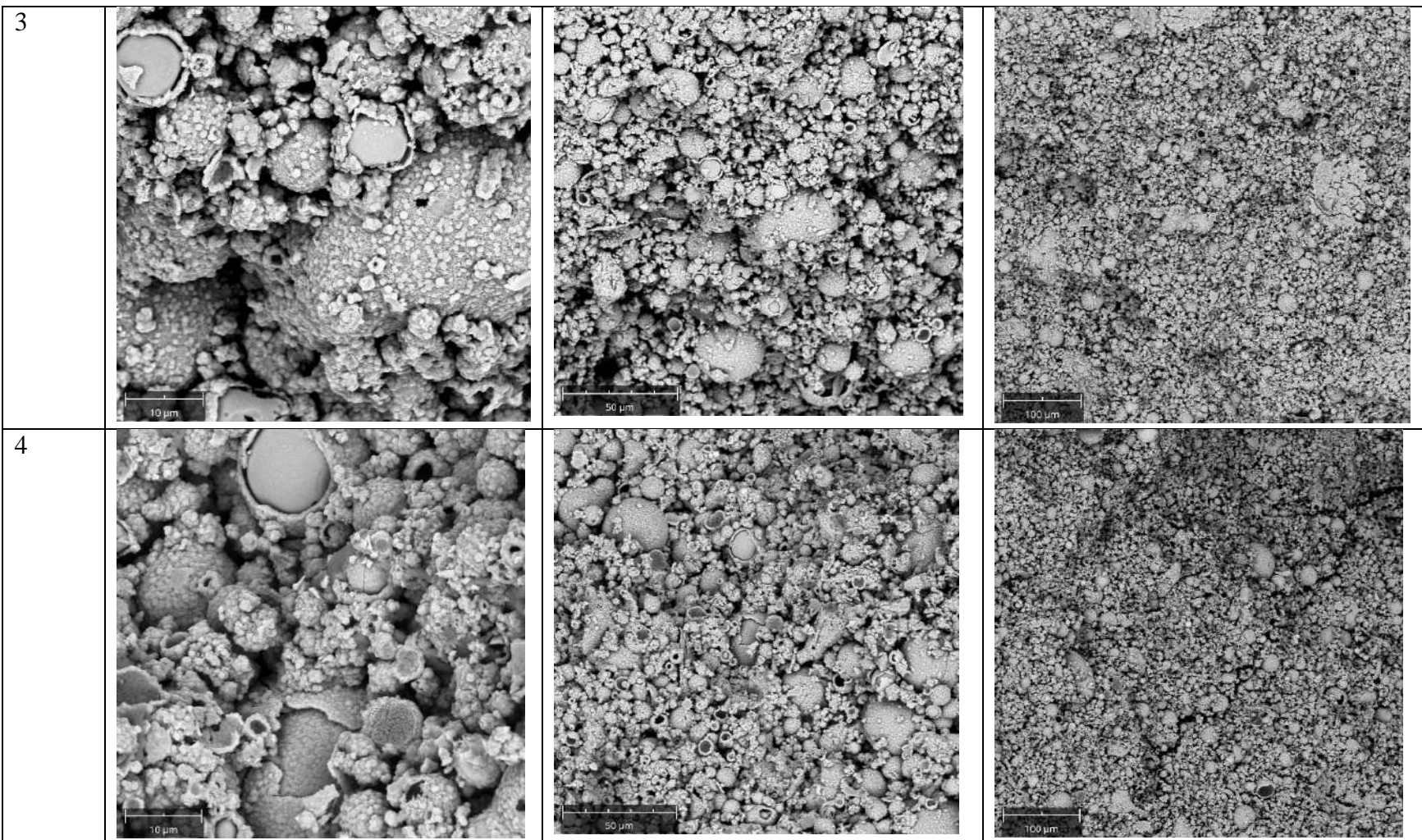




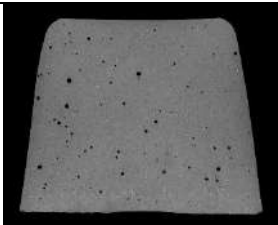
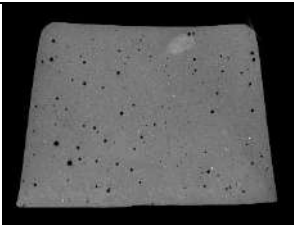
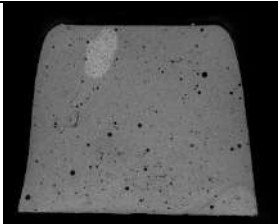
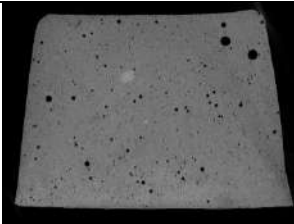
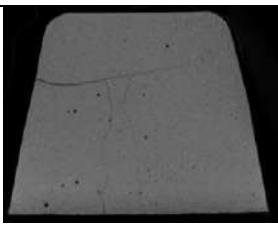
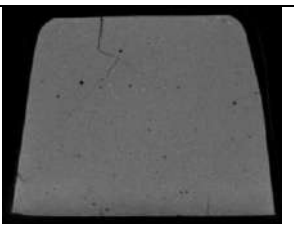
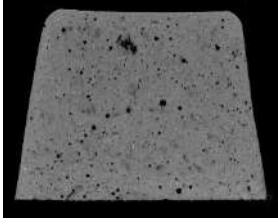
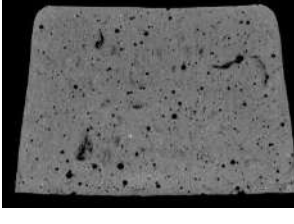
**Figure 10.9.** Effect of curing condition on the Si/Al ratios of the geopolymer samples.

**Table 10.3. Fracture analysis micrographs at varying resolutions.**

Sample	Resolution (microns)		
	10	50	100
1			
2			

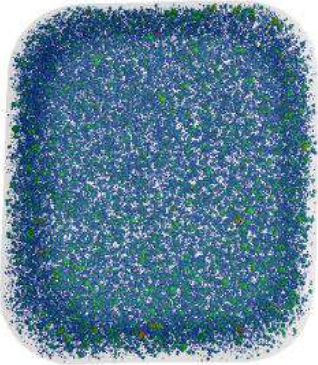
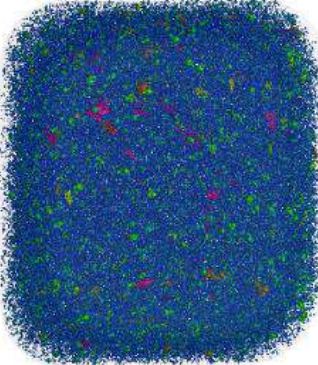
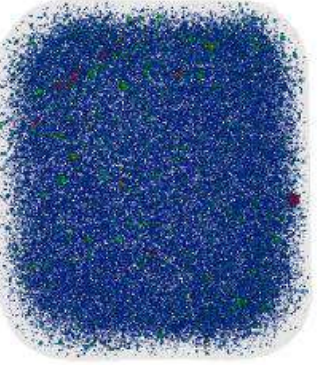
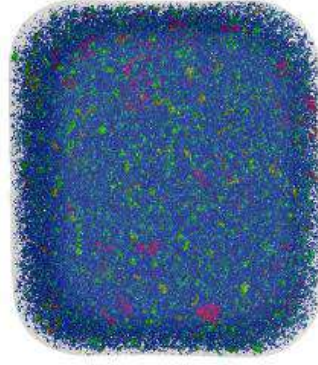
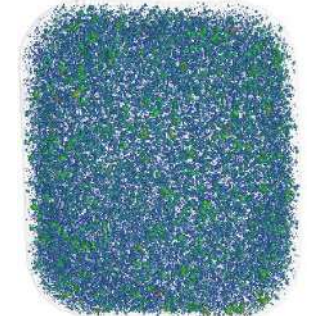
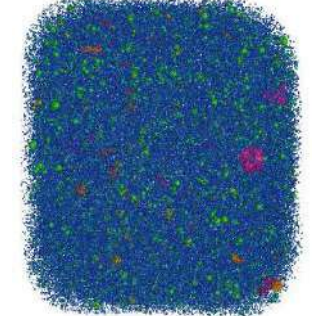
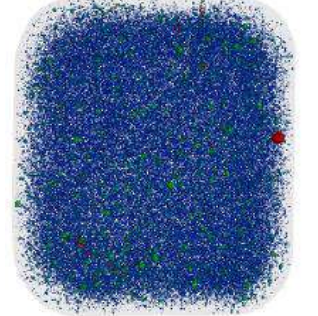
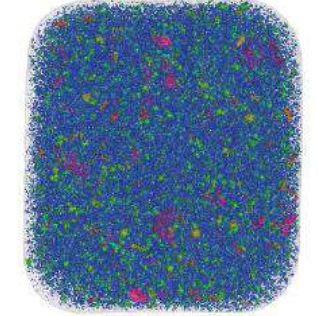
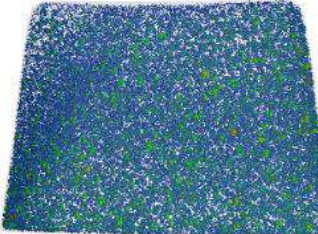
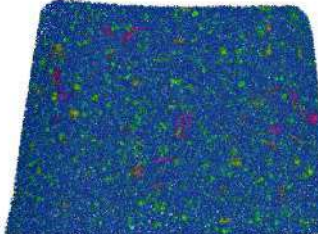
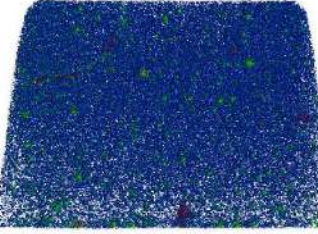
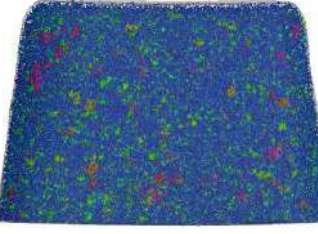


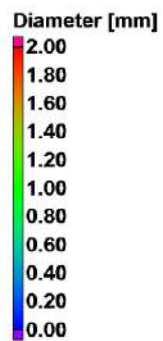
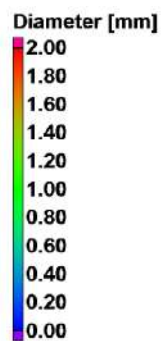
**Table 10.4. CT slice images of experimental geopolymer samples.**

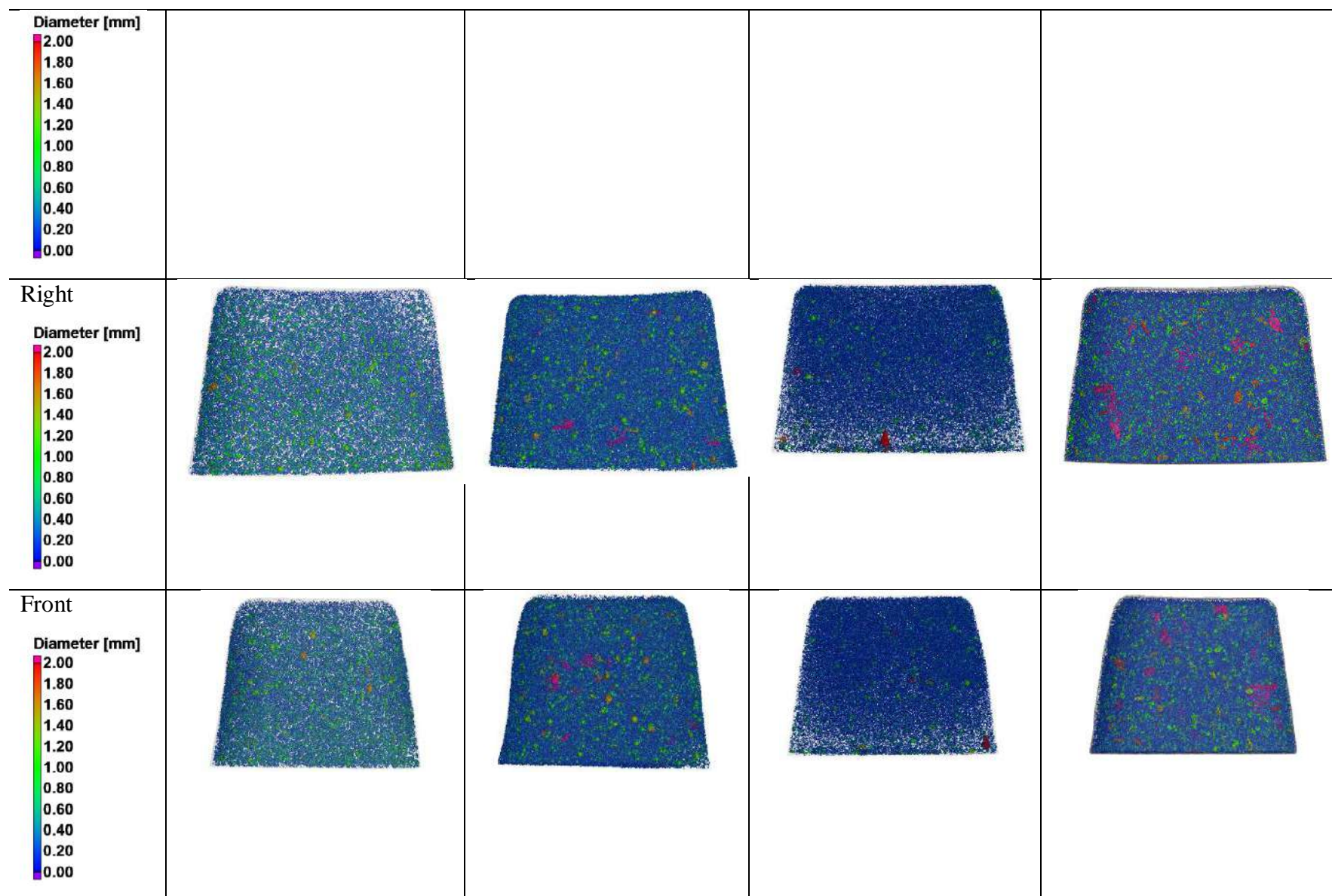
Sample		
1		
2		
3		
4		



**Table 10.5. Internal Porosity Imaging (not presented to scale).**

Position	Sample			
	1	2	3	4
Top				
Bottom				
Left				

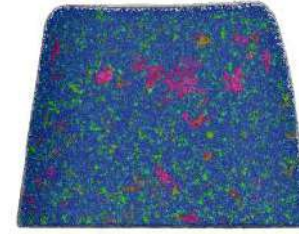
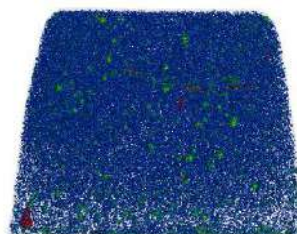
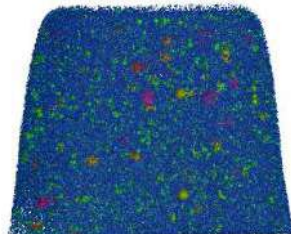
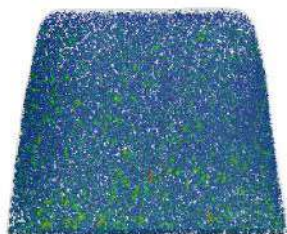
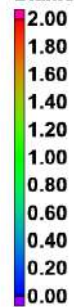






Back

Diameter [mm]



## 10.4 Results and Discussion

### *10.4.1 Overall Geopolymer Microstructure*

#### 10.4.1.1 Geopolymer Matrix Heterogeneity

Various similarities were observed in the SEM micrographs of this study (Table 10.1) and the study of Schmucker and MacKenzie (2005). Firstly, the microstructure showed several heterogeneous areas, evidenced by the crystalline fly ash grains within the glassy matrix. Secondly, the presence of unreacted relicts in the geopolymers was observed. These unreacted relicts were attributed to inadequate mixing of the geopolymer paste before curing (Schmucker and MacKenzie, 2005). The addition of the heterogeneous CNC agglomerates may have accentuated this phenomenon.

Furthermore, the SEM results of Schmucker and MacKenzie (2005) indicated that the sample exposed to higher curing temperatures were identical with those exposed to lower curing temperatures, implying that dehydration failed to alter the geopolymer composition and morphology. This observation was inconsistent with the differences in morphology observed in the samples cured 24 hours compared to the samples cured at 48 hours. According to the study of Kupwade-Patil and Allouche (2016), the prolonged temperature exposure due to the 48-hour curing procedure may have resulted in further alkali-silica reaction, thus changing the microstructure of the 48 hour cured samples compared to that of the 24 hour cured samples.

Another point of similarity of this study to the literature was found in the study of Kupwade-Patil and Allouche (2016). Several micrographs exhibited clearly defined regions of gel and aggregate morphology, resulting in the formation of an interface similar to that shown in **Figure 10.2**.

#### 10.4.1.2 Mullite Formation

As indicated in the study of Schmucker and MacKenzie (2005), the needle-like grains shown in the SEM micrographs of the samples exposed to elevated temperatures were mullite. Furthermore, the more refined crystals were attributed to the formation of pure alumina from the relicts of the original precursor material (Schmucker and MacKenzie, 2005). Similar mullite formations were found in several micrographs (Table 10.1)



#### 10.4.1.3 Cracks in the Microstructure

As indicated in the studies of Kupwade-Patil and Allouche (2016) and Chindaprasirt et al. (2009), the micro-cracks observed in the geopolymer matrix (Table 10.1) were attributed to the alkali-silica reaction. Furthermore, the alkali-silica reaction gel formed during the geopolymerization reaction explained the vitreous phase observed in several micrographs.

Previous studies found that the alkali-silica reaction was a multistage process at the paste-aggregate interface (Ulm et al., 2000) that triggered microscopic cracking of the matrix (Kupwade-Patil and Allouche, 2016). This logic further explained the micro-cracks observed in several samples. Initially, the microcracks were assumed to occur purely due to extended temperature exposure in 48-hour cured samples. However, it was more likely that the extended temperature exposure facilitated the chemical reactions leading to increased gel formation, thus leading to the accumulation in internal pressure, in turn causing the microcracks observed.

The role of calcium in the formation of alkali-silica reaction products is unknown, and it was argued as to whether reaction products with high and low calcium should be classified (Leemann et al. 2011; Wang and Gillot 1991; Hou et al. 2005). However, in this study, the calcium content was low for all samples. Hence, the calcium ions could not have contributed to the formation of alkali-silica reaction gel. It was more likely that the sodium ions contributed to the formation of the alkali-silica reaction gel, as found in the study of Kupwade-Patil and Allouche (2016).

#### 10.4.1.4 Effect of Chemical Composition on Micro-cracking

The chemical composition of the parent fly ash shown in **Figure 10.3** confirmed that silicon dioxide occupied the most significant percentage of the fly ash composition (49%). This finding validated the previous study of Diamond (1976), in which it was found that reactive silica, led to alkali-silica reaction expansion.

#### 10.4.1.5 Unreacted Fly Ash Particles

The micrographs (Table 10.2 and Table 10.3) revealed unreacted fly ash particles in the samples activated with lower concentration activator solutions than those activated with higher concentration solutions. There was inadequate alkaline activator content for the lower alkaline activator concentrations to initiate the dissolution process of the aluminosilicate ions in the fly ash, thus not being able to proceed with the geopolymerization reaction. This finding validated

the study of Chindaprasirt et al. (2009), in which the geopolymer paste was comprised of unreacted and partially reacted fly ash particles and a continuous mass of aluminosilicate.

The reaction extent was directly proportional to the alkaline activator concentration. The reaction extent could be visually observed. There were fewer unreacted fly ash particles observed in the matrix for higher alkaline activator concentrations (between 10 and 12 M). In contrast, for lower alkaline activator concentrations (between 8 and 9 M), more unreacted fly ash particles were observed in the matrix. In most samples, the fly ash particles did not wholly react. This effect was more pronounced in large fly ash particles. This finding was attributed to the fact that the smaller particles exhibit more significant contact areas for the alkali activation process, unlike the larger fly ash particles (Chindaprasirt et al., 2009).

#### ***10.4.2 Effects of Curing Time and CNC Concentration on Geopolymer Micrographs under 24 and 48-hour Curing Conditions.***

The geopolymer micrographs were compared at each variation in CNC concentration and alkaline activator concentration for both curing conditions (Table 10.2). The findings are discussed below.

##### **10.4.2.1 Sample 1 (0% CNC)**

When the baseline samples were compared at the different curing conditions, the fly ash grains were partially reacted and embedded in a smooth alkali-silica gel background under the 24-hour curing condition. There were three primary differences observed between the two baseline samples under the different curing conditions. Firstly, the alkali-silica gel in the 48-hour cured sample exhibited visible micro-cracks that became more apparent as the resolution was increased from 50 microns to 10 microns. Secondly, the fly ash grains of the 48-hour cured sample exhibited a greater reactivity than the 24-hour cured sample. Thirdly, the 24-hour cured sample exhibited mullite formations indicated by needle-like structures (Schmucker and MacKenzie, 2005) absent in the 48 hour cured samples.

These three observations implied that the 48-hour curing resulted in micro-cracks in the geopolymer matrix. It was recommended that the curing process be adjusted to avoid cracking, which weakens the structural integrity of the geopolymer. Furthermore, the 48-hour curing condition facilitated the geopolymerization reaction to a greater extent than the 24-hour curing

condition. This finding was logical as the reaction time was longer, and the fly ash grains were therefore reacted to a greater extent.

#### 10.4.2.2 Sample 2 (0.71% CNC)

The vitreous alkali-silica gel was found in both curing conditions. However, the cracking in the alkali-silica gel and lack of mullite formations in the 48-hour cured samples differentiated it from the 24-hour cured samples. Furthermore, the fly ash grains appeared more distributed in the matrix of the 48-hour cured sample, which appeared fully reacted on the surface. These observations implied that the prolonged curing condition did not aid the mullite formations. Furthermore, the shorter curing condition promoted the fly ash agglomeration in the geopolymer matrix, in which the mullite structures were observed.

#### 10.4.2.3 Sample 3 (0.86% CNC)

Micro-cracks and lacking mullite structures were observed in the 48-hour cured samples. Although most fly ash particles reacted well, some unreacted grains were still visible at the 10-micron magnification. These unreacted fly ash particles were attributed to the lower sodium hydroxide concentration of 9.7 M used, compared to the higher activator concentrations used in the previous two samples (9.72 M and 11.12 M for samples 1 and 2, respectively).

#### 10.4.2.4 Sample 4 (1.28% CNC)

The 24-hour curing condition caused agglomerated fly ash particles compared to the 48-hour curing condition. Both curing conditions caused cracking of the alkali-silica reaction gel. The 48-hour curing condition showed a lack of mullite formation. The fly ash particles were well reacted under both curing conditions. The good reactivity was attributed to the most potent alkaline activator concentration of 12 M being used for these samples. It was hypothesized that the higher cellulose nanocrystal concentration caused the micro-cracking in the samples due to cellulose nanocrystal agglomerates at the start of the curing procedure.

#### 10.4.2.5 Sample 5 (1.56% CNC)

Fly ash agglomerates were present in geopolymer samples under both curing conditions. However, there were more agglomerates in the 24 hour cured samples. Micro-cracks were only observed in the vitreous alkali-silica reaction gel of the 24-hour cured sample at the 100-micron magnification. No mullite was formed in the 48-hour cured sample. The fly ash reaction extent was not as pronounced as the previous samples (4). This observation was attributed to the fact

that the activator concentration was lower than in the previous samples (9.4 M compared to 12 M). Hence, it was implied that the higher cellulose nanocrystal concentration only affected the 24-hour cured sample. Inadequate mixing and homogenization of the cellulose nanocrystal agglomerates in the geopolymer matrix resulted in cracking at the 24-hour curing condition. The absence of the cracking in the 48-hour cured samples was attributed to the greater efficacy of the geopolymer reaction under the lengthened reaction conditions. Ultrasonication is recommended to homogenize the CNC solution (Cao et al., 2016a; Cao et al., 2016b; Lee et al., 2019).

#### 10.4.2.6 Sample 6 (1.7% CNC)

Although micro-cracks were observed for both curing conditions, they were more pronounced in the 24-hour cured sample. Abrasion-like formations were found in the alkali-silica reaction vitreous region. This finding implied that the 48-hour curing condition was better under this set of CNC concentration and alkaline activator concentration conditions. The formation of mullite structures was absent for both curing conditions. However, the agglomeration of fly ash particles was evident for the 24-hour curing condition. The implication was that the lower curing time resulted in the inefficient reaction characterized by micro-cracking and agglomeration of fly ash particles. The fly ash grains were not as reacted as in previous samples, as indicated by the smooth surfaces observed at the 8-micron magnification. This phenomenon was attributed to the lower activator concentration used.

#### 10.4.2.7 Sample 7 (2% CNC)

This sample was significant, as the upper extreme of both variables (alkaline activator concentration and CNC concentration) was imposed. Under these conditions, micro-cracking and mullite formation was only found in the 24 hour cured samples. Fly ash agglomeration was observed under both curing conditions and was attributed to CNC agglomeration, as the highest concentration of CNC were used in this sample. The full reactive effect of the high activator concentration on the fly ash particles was observed at the 48-hour curing condition. This finding reinforced the previous observation that the 48-hour curing was more conducive to the geopolymerization reaction. Furthermore, almost no alkaline silica reaction gel phase was observed. Only one smooth surface was detected. However, the surface contained pores and surface scratches and was therefore not wholly smooth. This finding emphasized the reactive nature of the 12 M activator concentration.

### ***10.4.3 Elemental Composition and Si/Al Ratio***

#### **10.4.3.1 General Elemental Composition Trends**

Based on the elemental composition of the samples (**Figure 10.4**, **Figure 10.5** and **Figure 10.6**), there was a greater concentration of silicon than aluminium in the geopolymer samples compared to the fly ash parent material (**Figure 10.7** and **Figure 10.8**). This finding implied that in phase two of the geopolymerization process involving the condensation of the precursor silicon and aluminium ions into monomers (Abdullah et al., 2011), more aluminium ions were used than silicon ions.

Based on **Figure 10.4** and **Figure 10.5**, the elemental composition was similar for all samples under both the curing conditions. The average elemental composition of all the 24-hour cured samples was compared against those of the 48 hour cured samples in **Figure 10.6**. Again, no significant trend was observed to suggest that the curing condition affected the elemental composition of the samples, even though pronounced differences in the morphology were observed in the SEM micrograph comparisons.

**Figure 10.7** and **Figure 10.8** compared the elemental composition of the precursor fly ash material with the different geopolymers produced from the fly ash for the 24-hour and 48-hour curing conditions, respectively. It was noteworthy that under the 48-hour curing condition, there was a greater composition of silicon and aluminium elements in the fly ash compared to all the geopolymers produced from the fly ash. This finding indicated that the silicon and aluminium elements were actively consumed in the geopolymerization reaction. However, the same trend was not observed in the 24-hour cured samples. This observation implied that the shorter curing time was inadequate from the perspective of geopolymerization efficacy. In addition, there was a greater carbon content observed in the fly ash compared to the geopolymers produced from it. This finding was attributed to the consumption of the organic content contained in the ash due to the heat curing process.

#### **10.4.3.2 Silicon to Aluminium Ratio**

The typical silicon to aluminium ratio of the geopolymers produced ranged between 2 and 4 (samples 1, 2, 3, 5, 6, and 7) and 4 to 10 (sample 1 at 48-hour curing and sample 4 at 24-hour curing) (**Figure 10.9**). Per the research of Davidovits (1999), a wide range of applications exist for these geopolymers, including refractory composites and foundry equipment. Only sample 4

at 48-hour curing exhibited a silicon to aluminium ratio close to unity (1.15), implying that this was the only sample suited to produce bricks, ceramics, and fire protection materials (Davidovits, 1999).

The absence of a clearly defined trend initiated the need for a second-degree trendline for the 24 and 48-hour curing conditions. A perfect symmetric and inverse parabolic trendline was observed for the 24-hour curing conditions, with the turning point at sample 4. The turning point corresponded to the maximum silicon to aluminium ratio of 10. The silicon to aluminium ratios of samples 5, 6, and 7 nearly mirrored samples 1, 2, and 3 for the 24-hour curing conditions. Two implications were derived from this observation. Firstly, if the silicon to aluminium ratios of samples 1, 2, and 3 are desired, they can be achieved using lower concentrations of CNC. Secondly, the alkaline activator concentrations of the “mirror” samples were similar (9.72 M and 12 M for samples 1 and 7, 11.12 M and 8 M for samples 2 and 6 9.7 M and 9.4 M for samples 3 and 5). Considering that the alkaline activator concentration holds a more significant influence over the silicon to aluminium ratio, the second implication was deemed valid. It was noteworthy that higher CNC concentrations contained great moisture contents, which could have decreased the alkaline activator concentration. Thus, at higher CNC concentrations, the effect of the alkaline activator may have been minimized.

For the 48 hour cured samples, the opposite trend was observed: a positive parabolic trendline. The turning point of the parabola occurred between samples 4 and 5. Unlike the parabolic trendline observed for the 24-hour cured samples, the parabolic trendline observed for the 48-hour cured samples was asymmetrical. The samples towards the left of the turning point exhibited greater silicon to aluminium ratios to the samples towards the right of the turning point. Both parabolic trendlines were significant, as they can approximate the silicon to aluminium ratio based on the alkaline activator concentration and the cellulose nanocrystal concentration of the samples.

#### ***10.4.4 Fracture Analyses***

The fracture analyses differed from the SEM micrographs of the crushed samples, as the fracture surfaces were visible. Although the CNC particles were too small to be viewed in the fracture micrographs, the effects of the curing condition and CNC concentration could be considered.

For sample 1, the geopolymerization reaction was visible from the degraded surfaces of the fly ash particles (Table 10.3). The same observation was made for the 2% CNC concentration sample (2). Overall, not many visible differences were detected between samples 1 and 2. This finding implied that the effect of the sodium hydroxide activator played a more significant role in the geopolymerization reaction than the CNC concentration. The same trend was observed with the 48 hour cured samples (3 and 4).

A defined lack of glassy, vitreous regions was observed in all samples. Previously, it was found that these vitreous regions are reaction products of the geopolymerization reaction (Davidovits, 1999). Considering that the samples were fractured in the middle, it was likely that the geopolymerization reaction was more prominent at the surface of the samples that were directly exposed to the heat during the respective curing processes.

Overall, large fly ash particles of varying reactivity were embedded in a sea of smaller particles. It was notable that the 2% CNC concentration samples (2 and 4) exhibited a lower void space compared to the 0% CNC concentration samples (1 and 3). Considering that the void space is linked to the porosity of the sample, this qualitative finding implied that the porosity of the sample decreased with CNC dosage. This result was confirmed and supported by the porosity analyses shown in the X-ray CT scanning results (Table 10.4). In addition, no mullite formations were shown in any of the fracture analysis micrographs.

#### ***10.4.5 X-ray CT Slice Imaging***

The X-ray CT slice images are shown in Table 10.4. By visual observation, there were more void spaces in the CNC-dosed geopolymer cured for 24 hours (sample 2) with respect to the baseline (sample 1, containing 0% CNC). The same trend was observed in the 48 hour cured samples. As confirmed by the internal porosity images, the larger void spaces in the CNC-dosed samples (2 and 4) with respect to the respective baseline samples (1 and 3) was attributed to the fact that the cellulose nanocrystal agglomerates shrink after exposure to the curing process, thus creating the void spaces within the sample matrix. Considering that these void spaces weaken the structural integrity of the sample, they must be avoided by preventing cellulose nanocrystal agglomerates. This recommendation can be achieved in two ways. Firstly, the novel ultrasonication methods recommended by Cao et al. (2016a), Cao et al. (2016b), and Lee et al. (2019) can be used to achieve a greater degree of homogeneity in the cellulose nanocrystal

aqueous solutions. Secondly, the respective cellulose nanocrystal aqueous solutions can be added to the geopolymer pastes, which can then be homogenized using the novel ultrasonication methods recommended by Cao et al. (2016a) Cao et al. (2016b) and Lee et al. (2019). From a practical perspective, the former method was recommended.

The 48-hour curing procedure caused internal cracks in the baseline samples as observed in the CT slice images of sample 3 compared to sample 1. The cracks were attributed to the rapid removal of moisture when the samples were de-moulded and rotated after the initial 24-hour curing period. Although longer curing periods cause greater strength development (Roopchund, 2016), the 48-hour curing procedure must be adjusted to minimize the possibility of cracking. As such, the adjusted curing procedure is recommended in **Table 10.6**.

**Table 10.6. Adjusted extended curing procedure to minimize sample cracking.**

Curing step	Description
1	Insert the samples into the oven.
2	Cure the samples at 40°C for an initial period of 2 hours.
3	Cure the samples at 60°C for 24 hours.
4	De-mould and rotate the samples.
5	Cure the de-moulded samples at 40°C for an initial period of 2 hours.
6	Cure the de-moulded samples at 60°C for 24 hours.

Step 5 is a transition step to ensure the gradual evaporation of moisture from the sample. The effect of the extended curing time was observed to minimize the void spaces within the baseline samples, as evidenced by the visual comparison of samples 1 and 3. A similar result was observed in the study of Bernardes et al. (2015), in which a reduced porosity was observed in the interior. However, the porosity reduction was not as pronounced near the surface of the samples. According to du Plessis and Boshoff (2019), this highlighted the need for a good selection of regions of interest for the porosity analysis and demonstrated the additional three-dimensional information obtained by X-ray CT scanning.



Although the random distribution of the cellulose nanocrystal agglomerates was expected to strengthen the internal matrix, this was not the case due to the formation of the void spaces. However, following the homogenization recommendations in the previous section, the CNC can be evenly and uniformly distributed within the sample matrix, thus fortifying the matrix. Despite this setback, it was noteworthy that the effect of the CNC was found to substantially prevent cracking of the samples under the extended curing condition.

#### ***10.4.6 Internal Porosity***

The porosity appeared uniform for each sample from every position (top, bottom, left, right, front and back). However, upon closer observation (Table 10.5), several trends were observed.

Sample 1 contained larger void spaces within the diameter range spanning 0.4 to 1.2 mm than sample 2, in which smaller void spaces, approximately 0.2 mm in diameter, were observed with clear patches of larger diameter spaces (approximately 2 mm in diameter).

When comparing the effect of the curing procedures on the baseline samples (sample 1 and 3), the void space range for the 24-hour curing procedure spanned 0.4 to 0.6 mm in diameter, while the void space for the 48-hour curing procedure was approximately 0.2 mm in diameter. This finding implied that the extended curing duration resulted in a decreased void space. This finding also implied a lower porosity, corresponding to a lower bulk density, and ultimately a greater degree of compressive strength (Roopchund, 2016).

When comparing samples 3 and 4, randomly arranged patches of 2 mm diameter void spaces were found in sample 4, thus reaffirming that the cellulose nanocrystal agglomerates occupied the observed void spaces before curing.

## 10.5 Conclusions

The effect of CNC on the geopolymer microstructure was less pronounced than the sodium hydroxide alkaline activator concentration. Considering that CNC affects the microstructure on a nanoscale, it was impossible to observe the direct effects of the CNC in the geopolymer matrix. Instead, the indirect effects of the CNC on the respective geopolymer matrices were observed.

Due to the CNC heterogeneity before being introduced into the geopolymer mixtures, at high CNC concentrations, the conglomeration of CNC caused the agglomeration of fly ash particles in the geopolymer matrix. This finding was noteworthy, as tightly packed fly ash particles lead to increased geopolymer density, resulting in increased compressive strength.

The longer curing time of 48 hours improved the geopolymer reaction, as evidenced by the fewer unreacted fly ash particles and pronounced lack of mullite formations in the respective geopolymer matrices. Considering that mullite is primarily formed from aluminium and silicon elements, it is undesirable as these elements could otherwise be used in the geopolymerization reaction by condensing into monomers to create polymeric structures in the matrix.

Based on the morphological observations, three parameters were identified for optimal geopolymer reaction: low to medium CNC concentration, high sodium hydroxide concentration, and longer curing time. However, the curing temperature and exposure to rapid thermal changes must be monitored to prevent the surface cracking of samples. Notably, the optimal production parameters were identified, as it indicated that the geopolymer matrix could be manipulated to yield desirable outcomes. This finding held tremendous implications for the future of geopolymer optimization, development, and distribution on an industrial scale.

Based on the study outcomes, it was recommended that fracture analyses be undertaken to determine the way the CNC interacts with the geopolymer matrix. In addition, Si/Al ratios could be manipulated by adding sodium silicate to target specific geopolymer applications outlined by Davidovits (2002).

The microstructure study aided in understanding the interactions between the geopolymer components at the microscale level. Thus, the aims of the study were met. Having such detailed knowledge of the interactions can facilitate the tailoring of geopolymer matrices to target specific applications. The geopolymer microstructure can be correlated to the mechanical results (density, compressive strength, and electrical resistivity) to create a database to facilitate the tailoring of

geopolymers for specific applications, thus improving the technical and commercial viability of geopolymers as green alternatives to Portland cement.

Although the actual CNC particles were too small (on the nanoscale) to be detected in the SEM analyses and X-ray CT slice images, the effects of the CNC on the geopolymer matrices were qualitatively ascertained. Overall, the CNC decreased the sample porosity. This finding was notable, as it implied that fewer void spaces were present when the samples were reinforced with CNC. The decreased porosity was linked to improved compressive strength and mechanical properties (Roopchund, 2016). Hence, CNC can successfully be applied to improve the mechanical properties of fly ash-based geopolymer materials.

The effects of the two curing conditions were not apparent from either analysis. The effect of the sodium hydroxide alkaline activator was deemed more significant on the extent of the geopolymerization reaction than the CNC addition parameter. These results confirmed the mechanical property findings reported in Chapter 8, and the thermal findings reported in Chapter 9. Overall, CNC holds remarkable potential for the improvement of novel green construction materials. Hence, CNC can be applied in the development and optimization of any novel green construction material as per the empirical development framework outlined in Chapter 8.

## CHAPTER 11: CONCLUSIONS

### 11.1 Summary of Findings

#### *11.1.1 Part A*

Chapter 2 identified the main CNC production process trends and steps based on a review of the global trends in commercial CNC production: feedstock pre-treatment, chemical treatment, separation, and purification. No single pre-treatment and purification method was standard. However, the two most common chemical treatments were acid hydrolysis and catalytic oxidation, and the two most common separation methods were gravity settling and centrifugation. These findings validated the process sequence proposed in the CNC process design Chapters (4 to 6). In Chapter 3, optimization strategies were proposed for the laboratory (APS + AH) CNC production process before up-scaling in the subsequent design Chapters (4 to 6). In addition, a baseline risk assessment was proposed to mitigate the safety concerns for the up-scaled process designs.

The Concept design of Chapter 4 revealed notable differences in the operation modes for the 1, 10, and 1000 kg/day CNC production scales. The 1 kg/day capacity is similar to the current laboratory-scale production. However, the transition from 10 kg/day to 1000 kg/day production involved automation using control interlocks and signals to ensure accurate timing, reagent dosing, and reaction conditions. The Concept design was expanded in the Basic design (Chapter 5), in which mass balances calculated the equipment sizes required in the up-scaled production capacities. Expanding on the process automation in the Concept design, the control strategies for each production process phase were outlined with respect to the control components and sequence of operation. The detailed design in Chapter 6 entailed the process piping design and commercial equipment selection, thus concluding the process design procedure.

Additionally, a process water treatment plant for the industrial CNC production process was designed using WAVE software (Appendix D). The software simulated the behaviour of the water treatment plant and enabled process optimization. This design marked the end of Part A of the study.

### ***11.1.2 Part B***

In Chapter 7, novel curing procedures, fiber reinforcement, and CNC additions were identified as parameters that could be manipulated to improve the commercial viability of novel green construction materials as alternatives to environmentally degrading OPC. The effects of these three potential improvement parameters were quantified based on the relevant literature studies using meta-analyses.

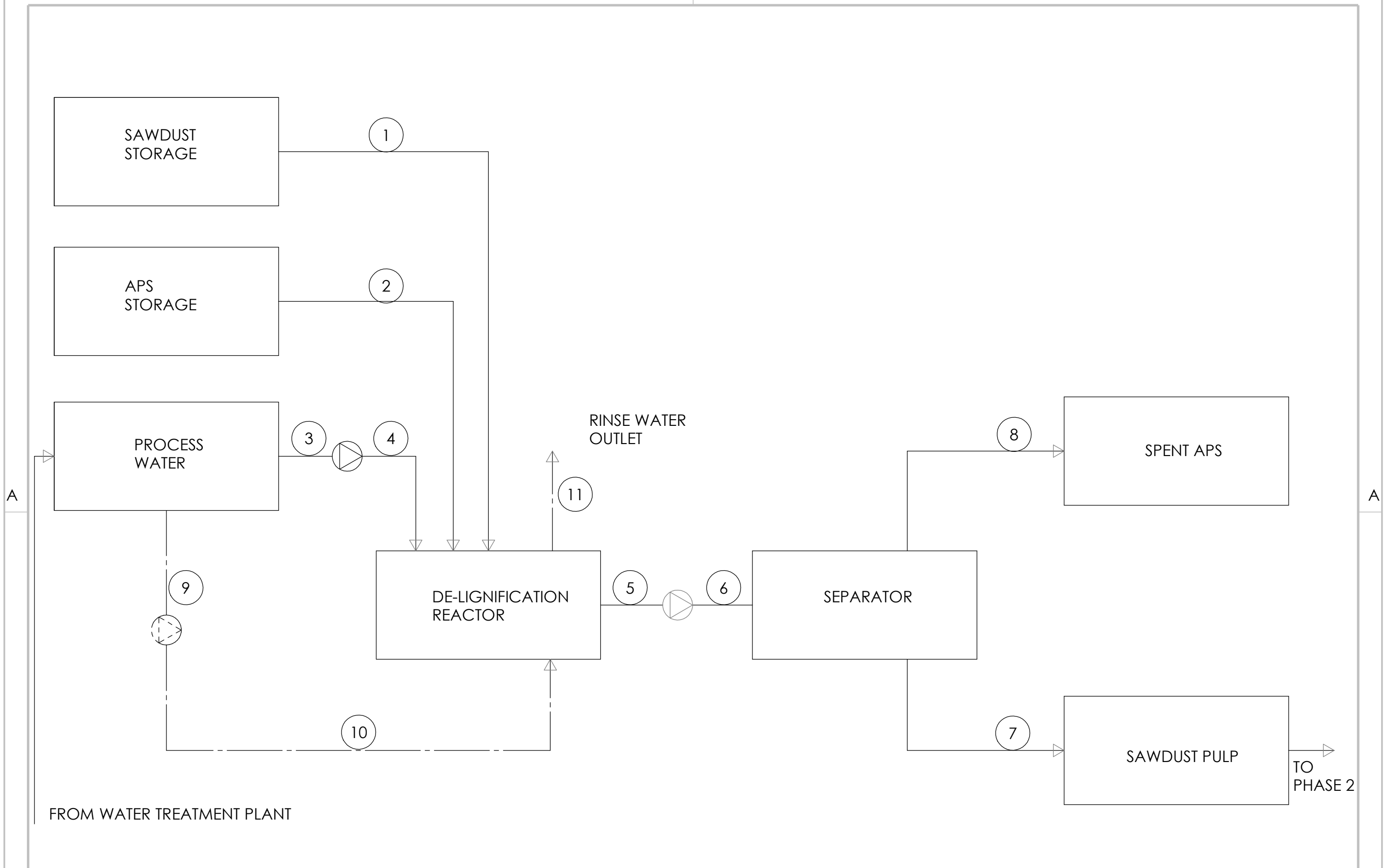
The meta-analysis proved that CNC as a reinforcing bio-additive (among others) exhibited a positive impact on conventional construction materials' compressive and flexural strength. This finding implied that further investigations of the impacts of CNC on fly ash-based geopolymer construction materials would be beneficial.

The empirical development framework reported in Chapter 8 was used to develop CNC-reinforced novel green geopolymer construction materials with significant statistical accuracy. Lower CNC concentrations (less than 0.5%) yielded higher strength geopolymers and corrosion resistance, while higher CNC concentrations prevented the cracking of geopolymers in unstable curing environments. The statistical methods enabled the custom development of specific mechanical properties in the geopolymers required by the application. In Chapter 9, thermal profiles of the geopolymers were undertaken by the simultaneous TGA-DSC methodology. The 1.7% CNC dosage was most effective in resisting sample mass loss at ascending temperature exposure. Hence, a relatively small quantity of CNC was required to improve the thermal stability of the geopolymers under elevated temperature exposure. The geopolymers exhibited endothermic behaviour, hence the potential for application in thermal resistance applications. The 48-hour curing procedure proved optimal for the development of thermal properties.

In Chapter 10, the effect of CNC on the geopolymer microstructure was less pronounced than the effect of the alkaline activator. High CNC concentrations caused the agglomeration of fly ash particles in the geopolymer matrix. The longer curing time of 48 hours improved the geopolymerization reaction, as evidenced by the fewer unreacted fly ash particles and pronounced lack of mullite formations in the respective geopolymer matrices. Based on the morphological observations, three parameters were identified for optimal geopolymer reaction: low to medium CNC concentration, high sodium hydroxide concentration, and longer curing time. Furthermore, the effects of the CNC on the geopolymer matrices were qualitatively ascertained through SEM fracture micrographs and X-ray CT slice images. CNC additions decreased the sample porosity,

## **APPENDIX A: PROCESS FLOW DIAGRAMS**

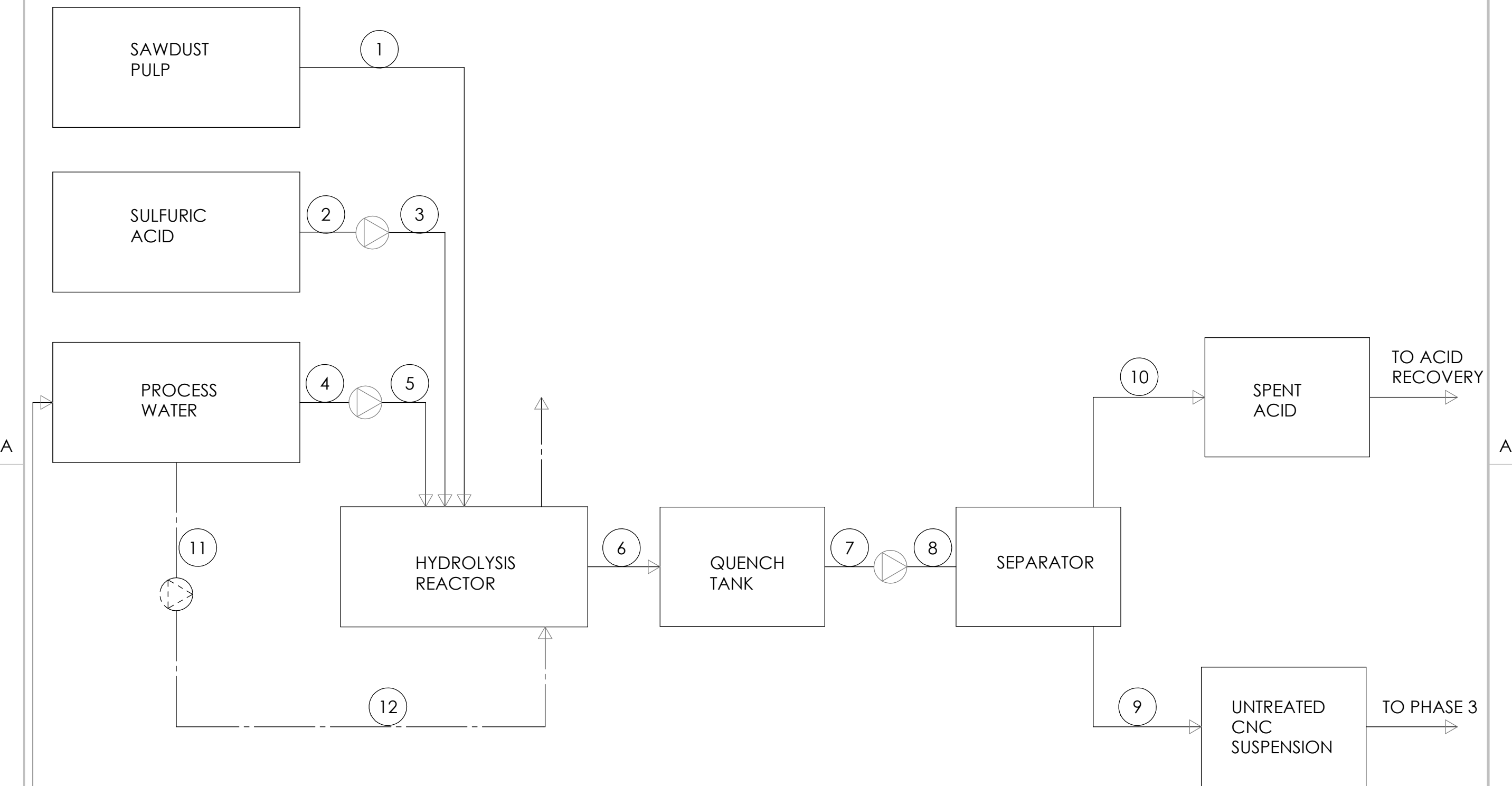
According to International Atomic Energy Agency (1990) the process flow diagrams (PFDs) are further developed versions of the BFDs. All the plant equipment were included and represented by standard symbols. In accordance with the International Atomic Energy Agency (1990), each phase of the CNC production process (sawdust de-lignification, acid hydrolysis, final product treatment, acid recycle and water treatment) was allocated individual PFDs. The PFDs provide accurate process information at a glance, by allocating reference labels to each unit operation and stream.



Stream	1	2	3	4	5	6	7	8	9	10	11
Description	Sawdust	APS	Process water suction	Process water discharge	Reactor product	Separator inlet	Sawdust pulp	Spent APS	Rinse water suction	Rinse water discharge	Rinse water outlet
Temperature (°C)	25	25	20	20	65	60	50	50	20	20	30
Pressure (barg)	1.01	1.01	1.46	1.60	1.23	1.60	1.01	1.01	1.46	1.60	1.25
Flowrate (m³/d)	> 4.8	> 4.8	2.74	2.74	4.28	4.28	3.85	0.43	2.74	2.74	2.74



DRAWING NO.	DESCRIPTION	NOTES	REVISIONS			DRAWN: K. BARNARD	DATE: 07 JULY 2020	SIGN:	CLIENT: UKZN-CSIR BIOREFINERY INDUSTRY DEVELOPMENT FACILITY  PLANT: CNC PRODUCTION
BIDF-CNC-01	PROCESS FLOW DIAGRAM CNC PRODUCTION PROCESS: PHASE 1 OF 3	SAWDUST DELIGNIFICATION	REV	BY	DATE	CHECKED: R. ROOPCHUND	DATE: 07 JULY 2020	SIGN:	



FROM WATER TREATMENT PLANT

Stream	1	2	3	4	5	6	7	8	9	10	11	12	13
Description	Sawdust pulp	Sulfuric acid suction	Sulfuric acid discharge	Process water suction	Process water discharge	Hydrolysis product outlet	Quenched product outlet	Separator suction	Separator discharge	Spent sulfuric acid	Rinse water suction	Rinse water discharge	Rinse water outlet
Temperature (°C)	10	22	22	20	42	40	22	22	22	22	20	20	30
Pressure (bar)	1.01	1.24	3.25	1.46	1.60	1.46	3.50	1.46	1.25	1.25	1.46	1.60	1.25
Flowrate (m <sup>3</sup> /d)	> 4.8	2.74	2.74	2.74	2.74	6.16	2.74	2.74	2.47	0.27	2.74	2.74	2.74



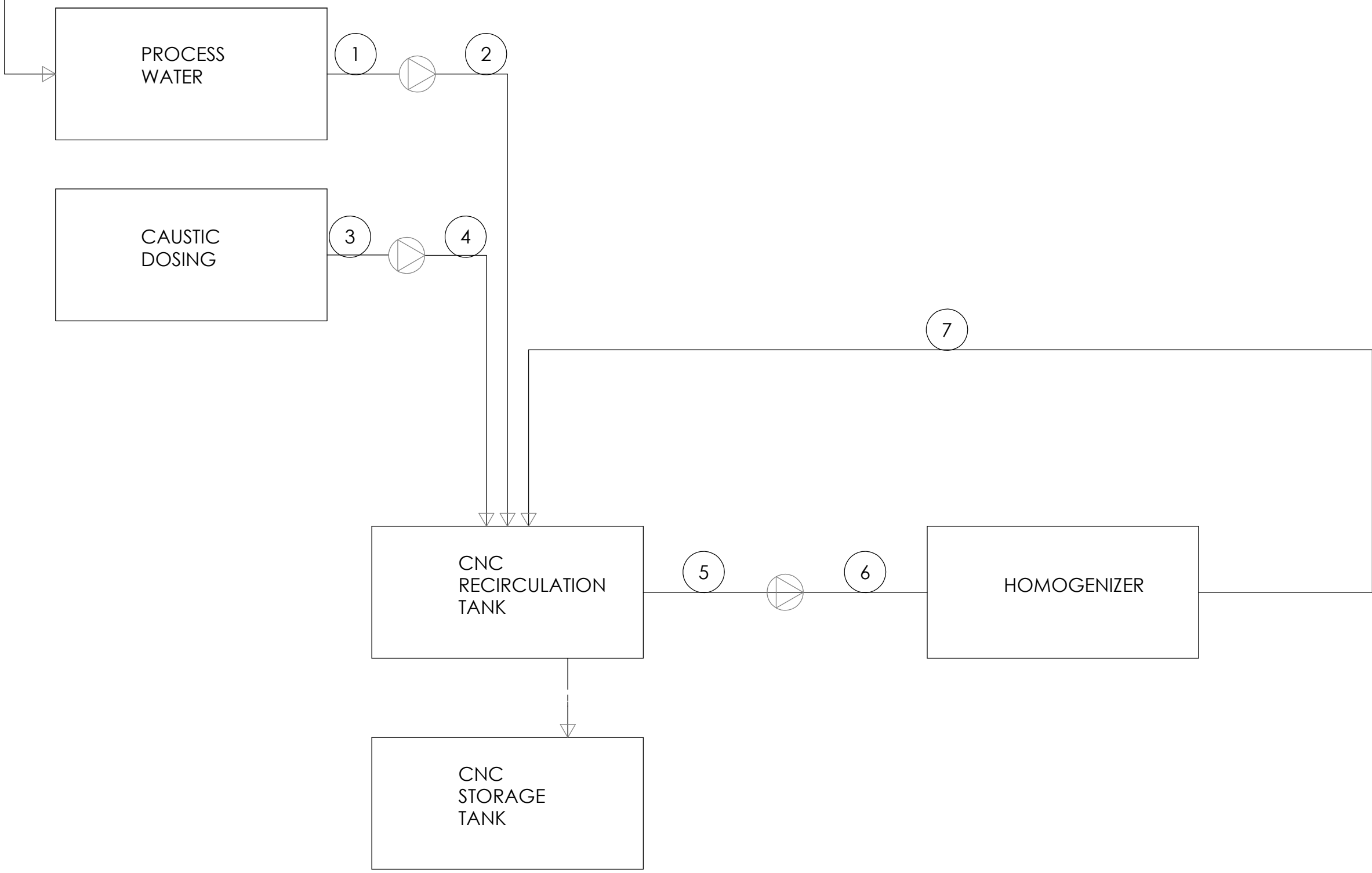
DRAWING NO.	DESCRIPTION	NOTES	REVISIONS			DRAWN: K. BARNARD	DATE: 07 JULY 2020	SIGN:	CLIENT: UKZN-CSIR BIOREFINERY INDUSTRY DEVELOPMENT FACILITY  PLANT: CNC PRODUCTION
BIDF-CNC-02	PROCESS FLOW DIAGRAM CNC PRODUCTION PROCESS: PHASE 2 OF 3	ACID HYDROLYSIS OF SAWDUST PULP	REV	BY	DATE	CHECKED: R. ROOPCHUND	DATE: 07 JULY 2020	SIGN:	





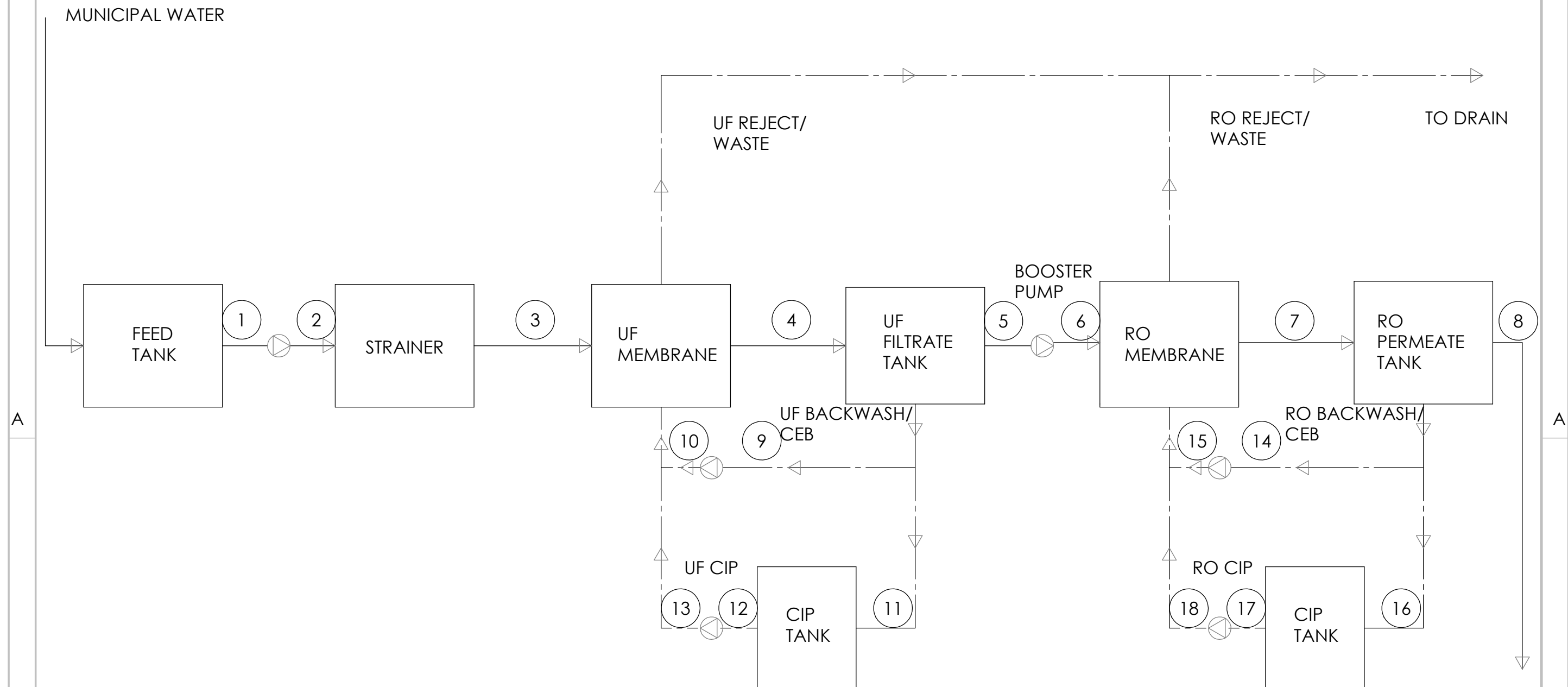
A

A

FROM WATER TREATMENT PLANT



		Stream	1	2	3	4	5	6	7			
		Description	Process water suction	Process water discharge	Caustic dosing suction	Caustic dosing discharge	Recirculation tank suction	Recirculation tank discharge	Recirculation loop			
		Temperature (°C)	20	20	20	20	21	25	26			
		Pressure (bar)	1.46	1.60	1.17	< 4.00	1.17	1.60	1.25			
		Flowrate (m <sup>3</sup> /d)	2.74	2.74	0.46	0.46	1.03	1.03	1.03			
DRAWING NO.	DESCRIPTION	NOTES	REVISIONS			DRAWN: K. BARNARD		DATE: 07 JULY 2020	SIGN:	<div><div>UNIVERSITY OF KWAZULU-NATAL INYUVESI YAKWAZULU-NATALI</div><div>CSIR our future through science</div></div>		
BIDF-CNC-03	PROCESS FLOW DIAGRAM CNC PRODUCTION PROCESS: PHASE 3 OF 3	CNC NEUTRALIZATION AND HOMOGENIZATION	REV	BY	DATE	CHECKED: R. ROOPCHUND		DATE: 07 JULY 2020	SIGN:			
										CLIENT: UKZN-CSIR BIOREFINERY INDUSTRY DEVELOPMENT FACILITY		
										PLANT: CNC PRODUCTION		



TO CNC PRODUCTION  
PROCESS

- PHASE 1 OF 3
- PHASE 2 OF 3
- PHASE 3 OF 3

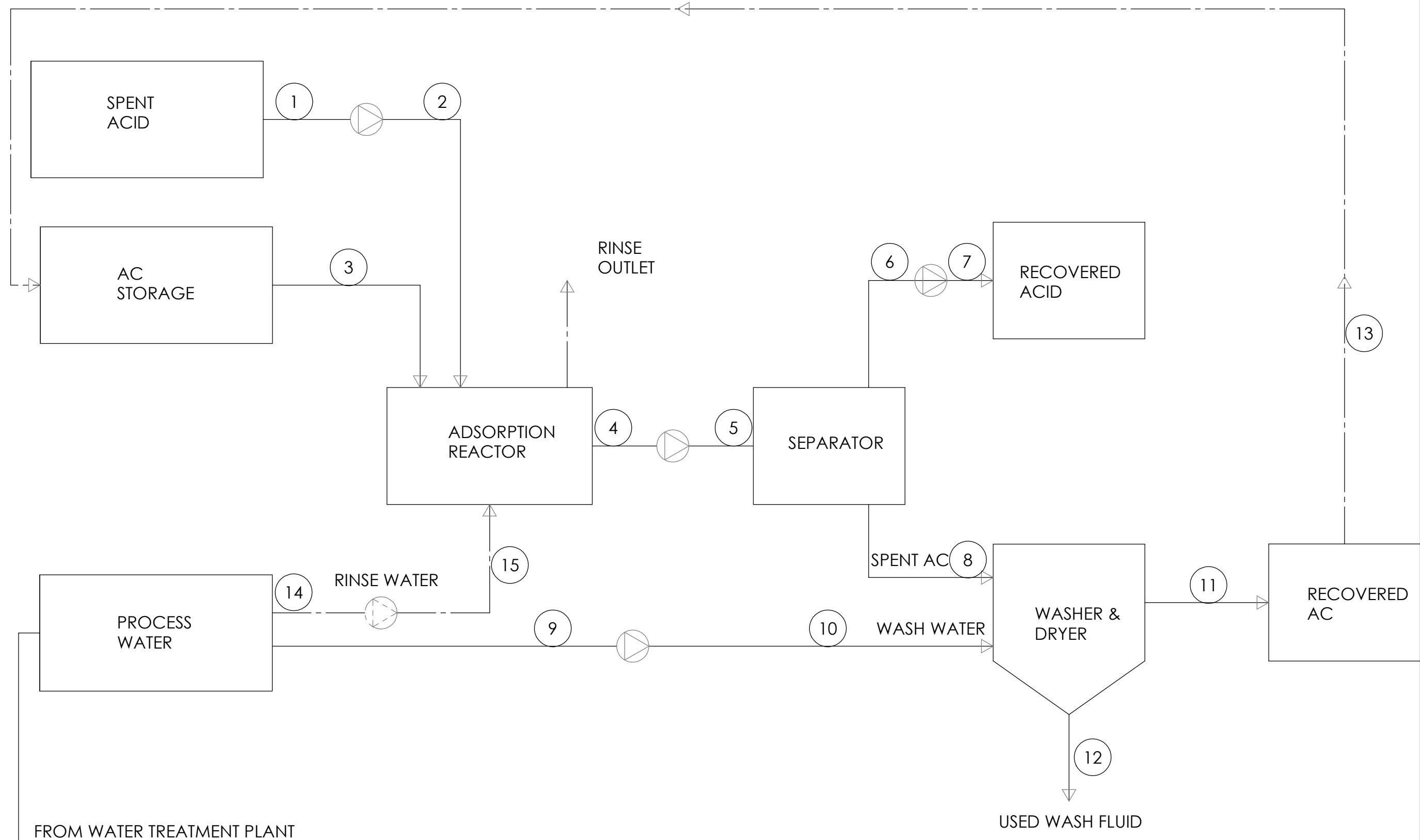
Stream	1	2	3	4	5	6	7	8	9	10	11	12	13	14	15	16	17	18
Description	Source water suction	Source water discharge	UF inlet	UF perm	RO booster pump suction	RO booster pump discharge	RO perm	RO supply	UF BW supply	UF BW/CEB discharge	UF CIP supply	UF CIP suction	UF CIP discharge	RO BW/CEB suction	RO BW/CEB discharge	RO CIP supply	RO CIP suction	RO CIP discharge
Temp (°C)	22	22	20	20	20	20	20	20	20	20	20	35	33	20	20	20	35	33
Pressure (bar)	1.46	1.8	1.8	0.5	0.5	5.2	4.6	1.46	0.16	2.5/1.13	0.16	0.03	2.5	0.16	2.5/1.13	0.16	0.03	2.5
Flowrate (m <sup>3</sup> /d)	102.2	102.2	101.7	100	100	100	75	75	79.2/47.5	79.2/47.5	23.3	24	24	79.2/47.5	79.2/47.5	23.3	24	24



DRAWING NO.	DESCRIPTION	NOTES	REVISIONS			DRAWN: K. BARNARD	DATE: 07 JULY 2020	SIGN:	CLIENT: UKZN-CSIR BIOREFINERY INDUSTRY DEVELOPMENT FACILITY
BIDF-WTP-01	PROCESS FLOW DIAGRAM WATER TREATMENT PROCESS	PRODUCTION OF PROCESS WATER	REV	BY	DATE	CHECKED: R. ROOPCHUND	DATE: 07 JULY 2020	SIGN:	PLANT: CNC PRODUCTION

A

A



Stream	1	2	3	4	5	6	7	8	9	10	11	12	13	14	15
Description	Spent acid suction	Spent acid discharge	AC inlet	Adsorption slurry suction	Adsorption slurry discharge	Recovered acid suction	Recovered acid discharge	Spent AC inlet	Wash water suction	Wash water discharge	Recovered AC	Used wash water	AC return	Rinse water suction	Rinse water discharge
Temperature (°C)	22	22	25	100	100	85	85	25	20	20	25	60	25	20	20
Pressure (bar)	1.01	< 5.2	1.01	1.01	1.60	1.00	< 5.2	1.01	1.46	1.60	1.01	1.25	1.01	1.46	1.60
Flowrate (m <sup>3</sup> /d)	2.74	2.74	> 4.8	6.16	6.16	2.74	2.74	> 4.8	2.74	2.74	> 4.8	> 2.74	> 4.8	2.74	2.74

DRAWING NO.	DESCRIPTION	NOTES	REVISIONS			DRAWN: K. BARNARD	DATE: 07 JULY 2020	SIGN:	CLIENT: UKZN-CSIR BIOREFINERY INDUSTRY DEVELOPMENT FACILITY  PLANT: CNC PRODUCTION
BIDF-ARP-01	PROCESS FLOW DIAGRAM ACID RECOVERY PROCESS	RECOVERY OF ACID FROM CNC PRODUCTION PROCESS PHASE 2 OF 3	REV	BY	DATE	CHECKED: R. ROOPCHUND	DATE: 07 JULY 2020	SIGN:	



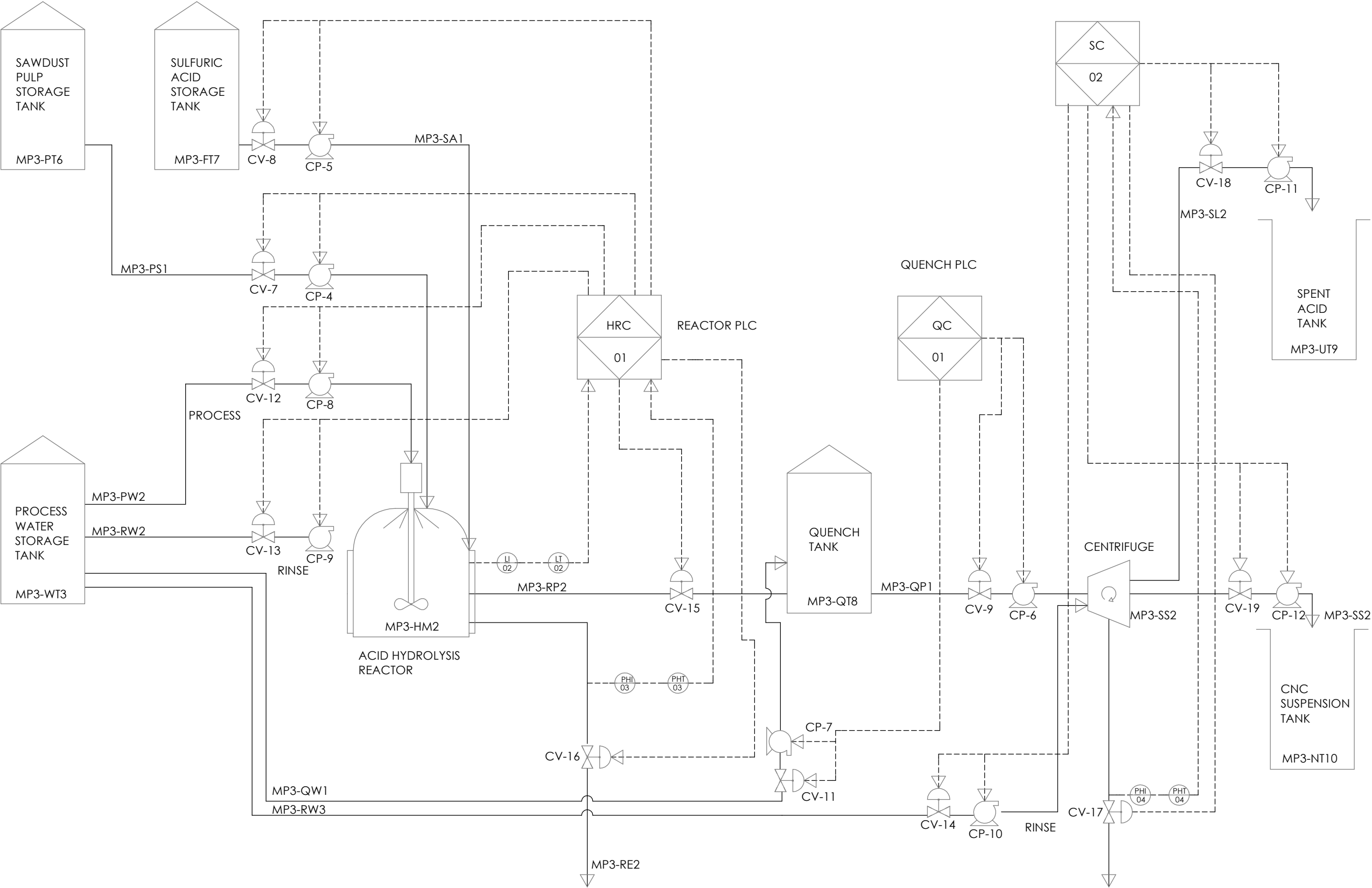
## **APPENDIX B: PIPING AND INSTRUMENTATION DIAGRAMS**



According to International Atomic Energy Agency (1990) the piping and instrumentation diagrams (P&IDs) are further developed versions of the PFDs. In accordance with the International Atomic Energy Agency (1990), each phase of the CNC production process (sawdust de-lignification, acid hydrolysis, final product treatment, acid recycle and water treatment) was allocated individual P&IDs based on their respective control and instrumentation strategies.



A

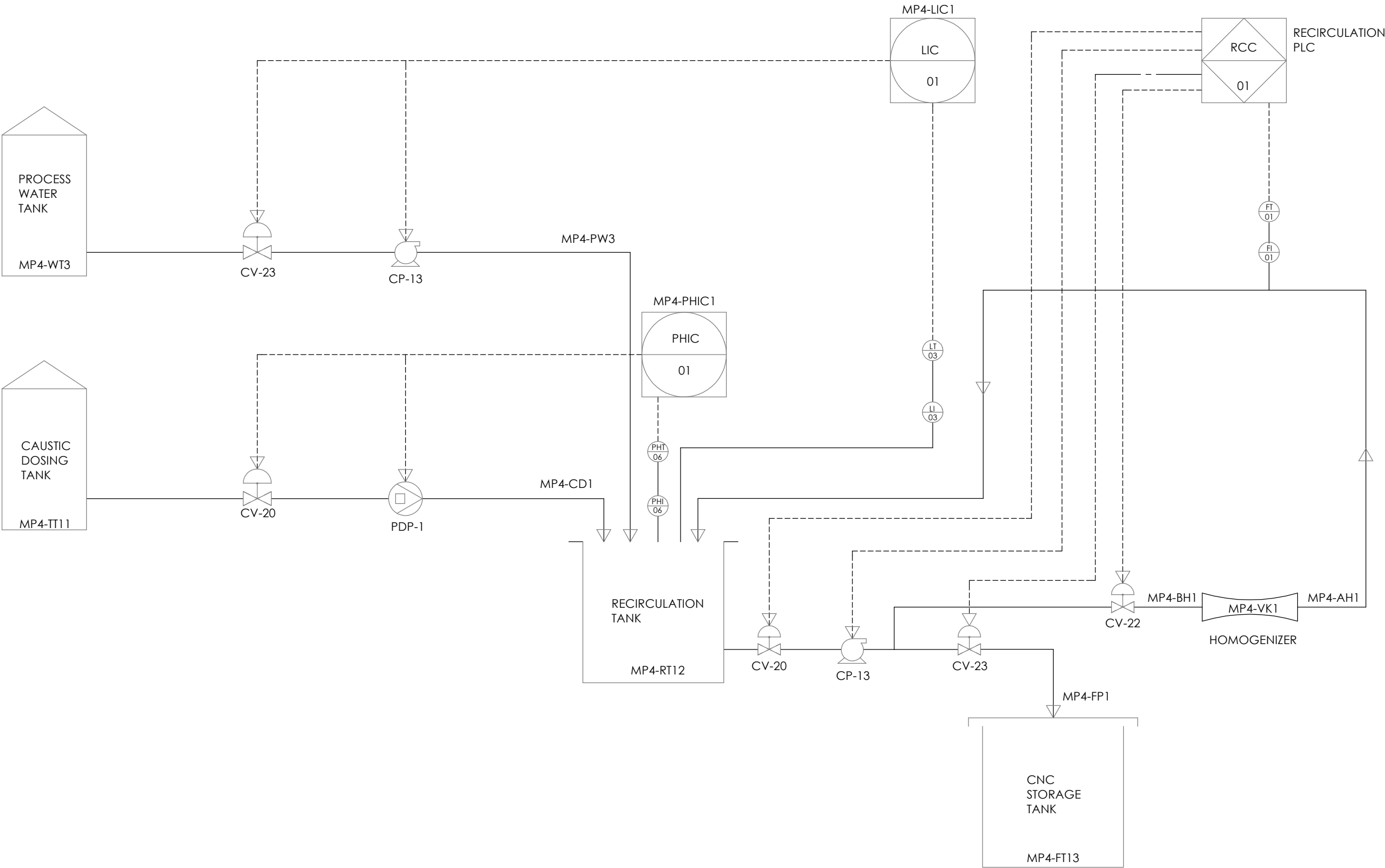
A




DRAWING NO.	DESCRIPTION	NOTES	REVISIONS			DRAWN:	DATE:	SIGN:	 UNIVERSITY OF KWAZULU-NATAL INYUVESI YAKWAZULU-NATALI	 CSIR our future through science	CLIENT: UKZN-CSIR BIOREFINERY INDUSTRY DEVELOPMENT FACILITY  PLANT: CNC PRODUCTION
BIDF-CNC-02CI	PIPING AND INSTRUMENTATION DIAGRAM CNC PRODUCTION PROCESS: PHASE 2 OF 3	ACID HYDROLYSIS OF SAWDUST PULP	REV	BY	DATE	CHECKED:	DATE:	SIGN:			
						R. ROOPCHUND	21 JULY 2020				

A


A



DRAWING NO.	DESCRIPTION	NOTES	REVISIONS			DRAWN: K. BARNARD	DATE: 21 JULY 2020	SIGN: KB
			REV	BY	DATE			
BIDF-CNC-03CI	PIPING AND INSTRUMENTATION DIAGRAM CNC PRODUCTION PROCESS: PHASE 3 OF 3	CNC NEUTRALIZATION AND HOMOGENIZATION				CHECKED: R. ROOPCHUND	DATE: 21 JULY 2020	SIGN:



UNIVERSITY OF  
KWAZULU-NATAL  
INYUVESI  
YAKWAZULU-NATALI

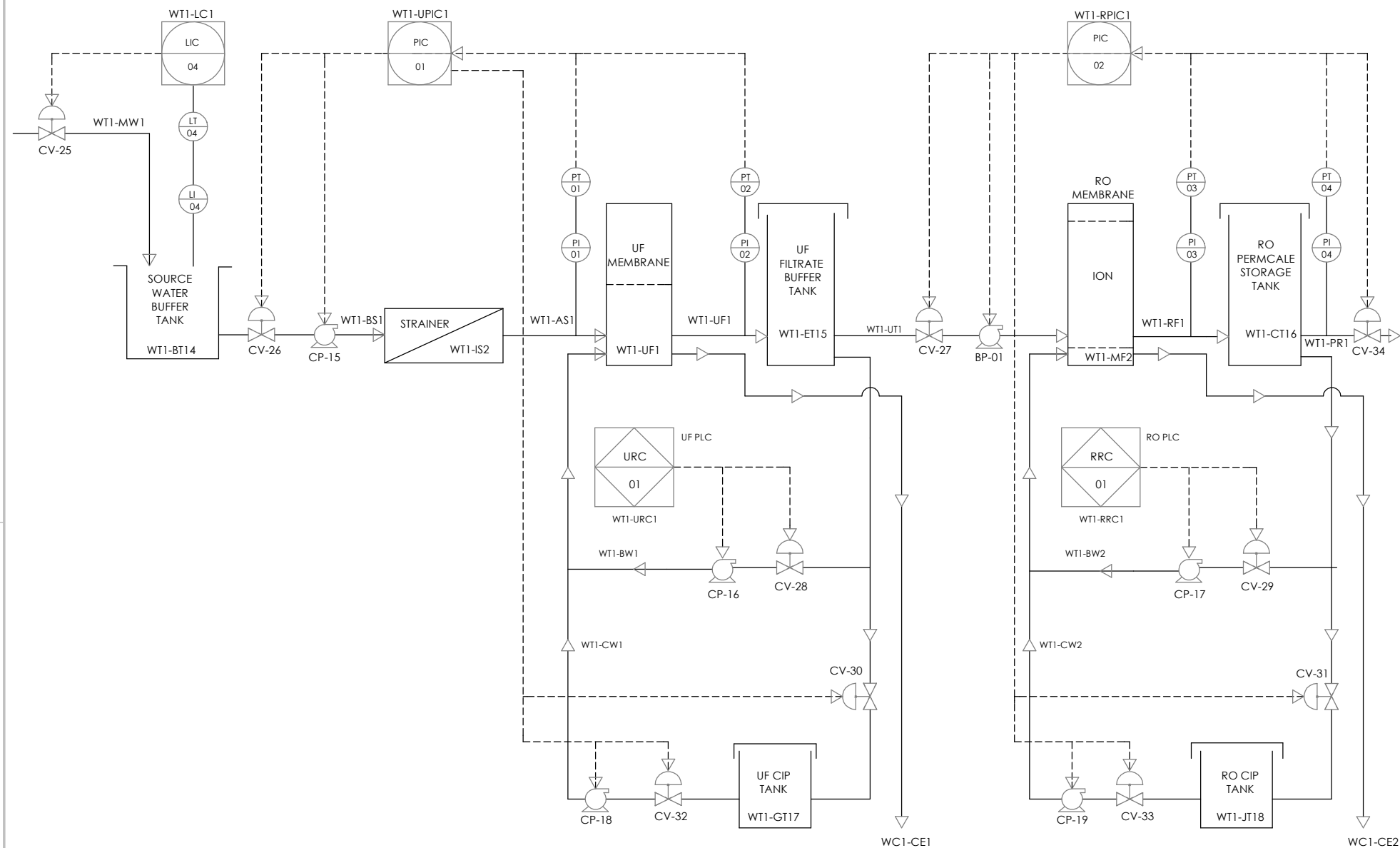




CSIR  
our future through science

CLIENT: UKZN-CSIR BIOREFINERY  
INDUSTRY DEVELOPMENT FACILITY  
  
PLANT: CNC PRODUCTION

A

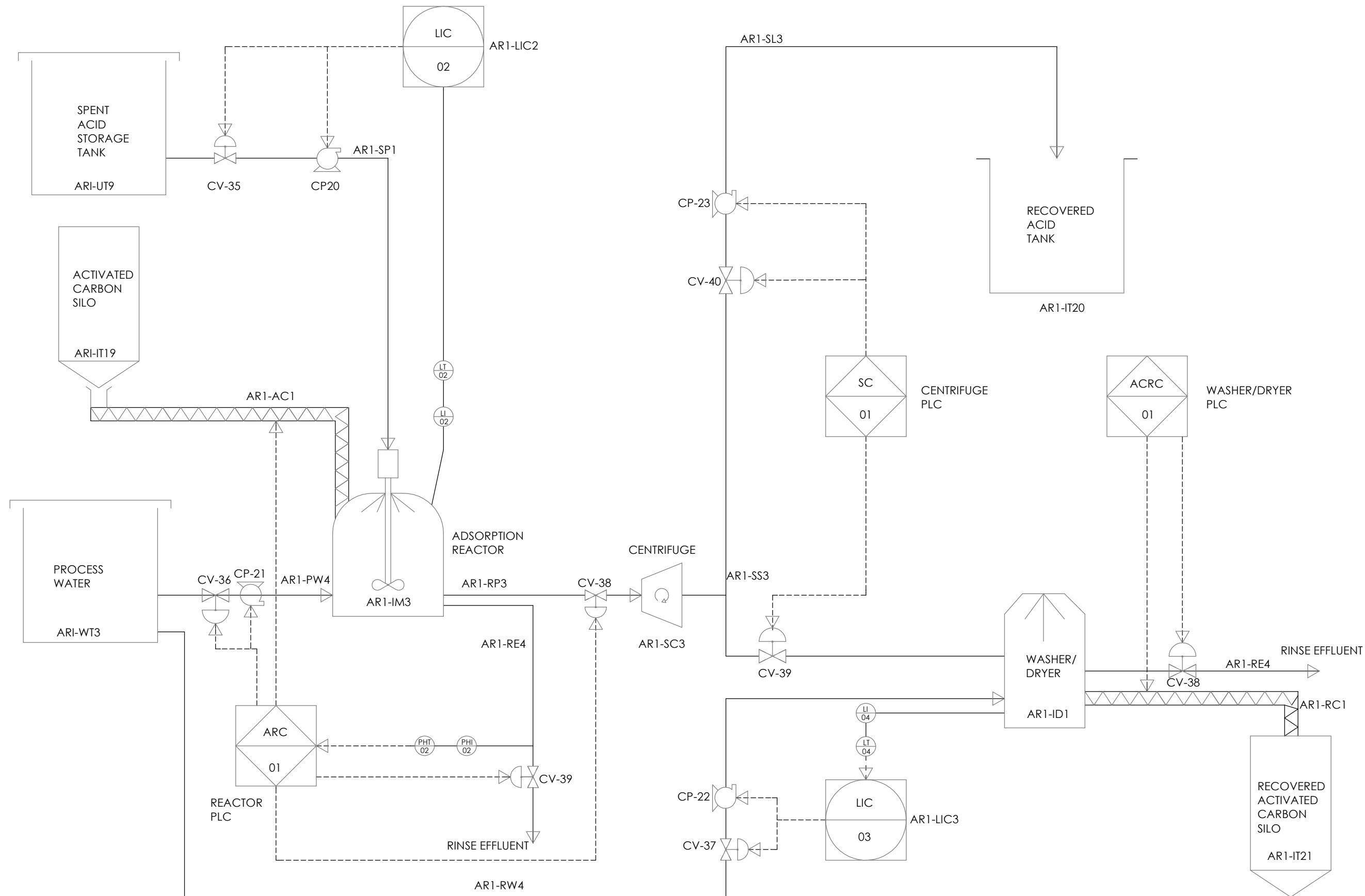
A





DRAWING NO.	DESCRIPTION	NOTES	REVISIONS			DRAWN: K. BARNARD	DATE: 21 JULY 2020	SIGN: KB			CLIENT: UKZN-CSIR BIOREFINERY INDUSTRY DEVELOPMENT FACILITY
			REV	BY	DATE						
BIDF-WTP-01CI	PIPING AND INSTRUMENTATION DIAGRAM WATER TREATMENT PROCESS	PRODUCTION OF PROCESS WATER				CHECKED: R. ROOPCHUND	DATE: 21 JULY 2020	SIGN:			PLANT: WATER TREATMENT



A



A

DRAWING NO.	DESCRIPTION	NOTES	REVISIONS			DRAWN:	DATE:	SIGN:	 	CLIENT: UKZN-CSIR BIOREFINERY INDUSTRY DEVELOPMENT FACILITY
BIDF-ARP-01CI	PIPING AND INSTRUMENTATION DIAGRAM ACID RECOVERY PROCESS	RECOVERY OF ACID FROM CNC PRODUCTION PROCESS PHASE 2 OF 3	REV	BY	DATE	K. BARNARD	21 JULY 2020	KB		
						CHECKED: R. ROOPCHUND	DATE: 21 JULY 2020	SIGN:		PLANT: ACID RECOVERY

## **APPENDIX C: ORIGINAL EQUIPMENT MANUFACTURER CATALOGUES**

## **APPENDIX D: DESIGN OF A WATER TREATMENT PLANT USING WAVE SOFTWARE**

### **D.1 Introduction**

Commercialization of laboratory-scale technologies is commonly implemented after pilot plant trials. The use of pilot plants is expensive and time-consuming. An alternative is to use software design tools. This Chapter entailed the design of a process water plant to produce de-mineralized water for the commercial-scale CNC production process. The design was accomplished using WAVE (Water Application Value Engine), a water treatment plant design tool. It was hypothesized that WAVE could be used to design the plant wherein UF (ultrafiltration) and RO (reverse osmosis) technologies were applied. WAVE was used to undertake the detailed design for the full-scale water treatment plant. Hence such simulation tools can replace pilot plants in optimizing industrial processes. The design was optimized by proposing mitigation factors to the reported design warnings.

The proper treatment of water to be used in a chemical process is critical for attaining a high-quality product and preventing the corrosion of process equipment (Liu et al., 2019b). De-mineralized water can be easily procured in laboratory-scale processes to enable the production of high-quality products with minimal impurities. However, in industrial production processes, water treatment processes must be designed and implemented to achieve this. The commercial-scale CNC production process requires a steady supply of de-mineralized water, which necessitated the design of a suitable water treatment plant for the treatment of municipal water. Traditional water treatment process designs are usually performed using rigorous and time-consuming programming methods (Niemi and Palosaari, 1994; Cardona et al., 2005). The input requirements, simulation methodology and results obtained from the software were critically analyzed and discussed in relation to literature reports.

The objective of this study was to create an awareness among Engineers and Academics regarding the use of WAVE as a potential water treatment plant design tool. Insights into the efficacy of the software may assist designing and optimizing water treatment plants to meet industrial requirements for process water. It was hypothesized that WAVE is an effective tool for designing a water treatment plant from technical and economic perspectives to produce

process water for chemical processes.

## **D.2 Materials and Methods**

WAVE, a freely available software developed by DuPont Water Solutions, was used to design the water treatment plant. WAVE has extensive applications in the water treatment industry, as it is the first software that can model multiple water treatment technologies on one simulation platform. The WAVE software was found to conform to all the requirements for model selection outlined in Chapter 3 (Considerations for model selection). For this design, WAVE enabled the modelling of UF and RO. The steps applied in the methodology are outlined.

### ***D.2.1 Preliminary Step***

The design was initiated by acquiring municipal water quality data. The plant location was envisioned to be Gauteng. Two of Gauteng's Municipal water sources were sourced and averaged for the input analysis (as input water to be treated to process water quality). The water analysis reports for the Johannesburg Metro and Ekurhuleni municipalities were obtained from the Rand Water's Water Quality Information Management Department for the latest available reporting timeframe (2016). The averaged source water data is shown in Table D.1 below.

**Table D.1 Gauteng Municipal Water Quality Data**

Parameters	Municipalities		Average
	Ekurhuleni	Johannesburg Metro	
Turbidity (NTU)	0.28	0.28	0.28
Total suspended solids (mg/L)	-	-	5.00
Silt density index	-	-	0.17
Total organic carbon (mg/L)	3.95	3.86	3.91
pH	8.01	8.06	8.04
Cations (mg/L)			
Ammonium	0.24	0.27	0.26
Potassium	2.86	2.78	2.82
Sodium	10.23	10.52	10.37
Magnesium	7.33	7.31	7.32
Calcium	18.45	17.89	18.17
Strontium	-	-	7.00
Barium	-	-	2.00
Anions (mg/L)			
Carbonate	74.51	70.17	72.34
Bicarbonate	-	-	248
Nitrate	0.13	0.13	0.13
Chloride	10.42	10.90	10.66
Fluoride	0.16	0.17	0.17
Sulfate	13.61	13.79	13.70

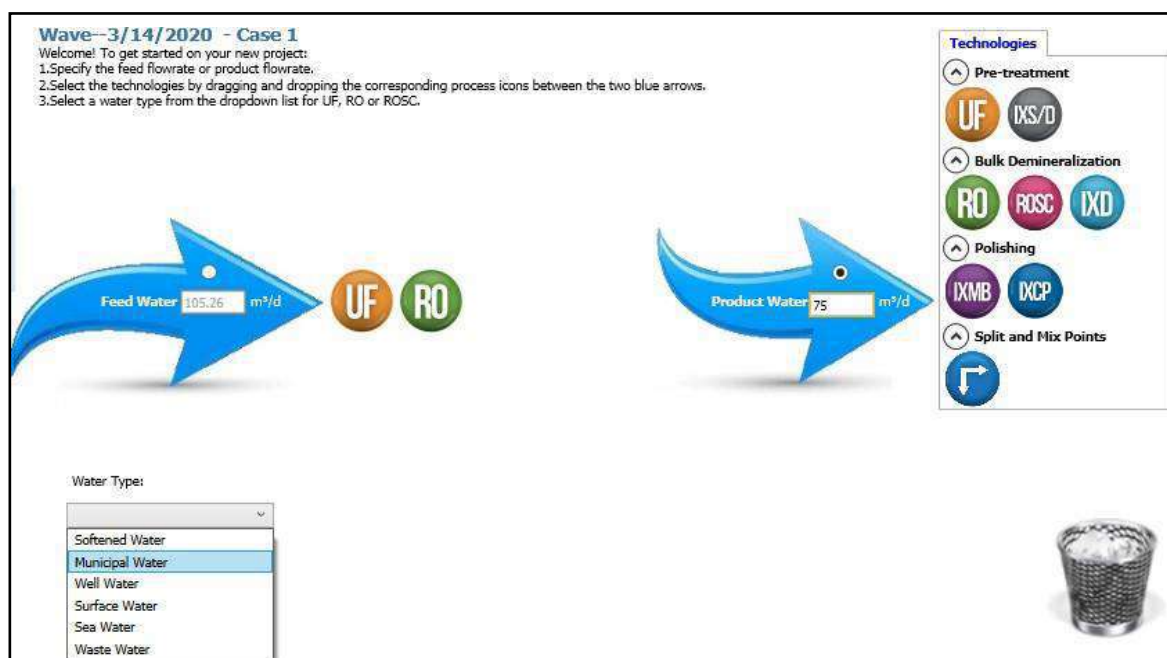
***D.2.2 Water Treatment Plant Simulations***

The first design step entailed configuring the water treatment process flowsheet. The configuration required specifying the sequence of unit operations for the water treatment process. Considering that municipal water has a relatively lower turbidity than traditional raw

water sources (such as river or rainwater) no pre-filtration step was deemed necessary.

#### D.2.2.1 UF Design

The UF unit was the first process operation specified. The RO operation was specified as the second stage in the water treatment process. Usually, a final polishing stage after the RO stage is used to remove any remaining ions contained in the RO permeate. However, no polishing unit operations were required in this design for two reasons. Firstly, the use of the polishing stage substantially increases the capital and operational costs of the water treatment plant. Secondly, with adequate maintenance and operation of the UF and RO units, the product water can conform to the quality standard of process water without the need for a polishing step. Once the plant configuration was specified, the water type was selected as “Municipal Water” and the required product water was specified at 75 m<sup>3</sup>/day. This specification was slightly greater than the actual requirement. Figure D.1 depicts the first stage of the water treatment plant design.



**Figure D.1. Stage 1 of the WAVE design simulation**

The next stage entailed specifying the municipal water quality. This step required the input of the source water data (Table D.1). The expected temperature limits were specified from 10 °C (minimum) to 40 °C (maximum), with a design temperature of 20 °C. Various components

comprising the water composition are functions of temperature. Hence, these specifications were required to enable the software to perform the computations accurately. This stage of the design is depicted in Figure D.2.

**Stream Definition**

Stream 1 100.00 %

Add Stream

**Feed Water - Stream 1**

Feed Parameters

Water Type: Municipal Water

Suggested Sub-type: NTU  $\geq$  2, TSS  $\geq$  5

\* Suggestion based on user Turbidity and TSS input. The selected Water Sub-type determines the Design Guideline to be used.

Water Sub-type: NTU  $\geq$  2, TSS  $\geq$  5

Solid Content

Turbidity: 0.28 NTU

Total Suspended Solids (TSS): 5.00 mg/L

SDI<sub>15</sub>: 0.17

Organic Content

Organics (TOC): 3.91 mg/L

Temperature

10.0 °C 20.0 °C 40.0 °C

Minimum Design Maximum

pH @20.0°C: 8.04 pH @25.0°C: 5.94

Additional Feed Water Information

**Cations**

Symbol	mg/L	ppm CaCO <sub>3</sub>	meq/L
NH <sub>4</sub>	0.257	0.713	0.014
K	2.822	3.612	0.072
Na	10.374	22.582	0.451
Mg	7.321	30.148	0.602
Ca	18.168	45.371	0.907
Sr	7.000	7.996	0.160
Ba	2.000	1.458	0.029
<b>Total Cations:</b>	<b>47.942</b>		<b>2.236</b>

**Anions**

Symbol	mg/L	ppm CaCO <sub>3</sub>	meq/L
CO <sub>3</sub>	72.340	120.653	2.411
HCO <sub>3</sub>	248.000	203.399	4.064
NO <sub>3</sub>	0.131	0.105	0.002
Cl	10.661	15.049	0.301
F	0.166	0.437	0.009
SO <sub>4</sub>	13.699	14.273	0.285
<b>Total Anions:</b>	<b>344.997</b>		<b>7.072</b>

**Neutrals**

Symbol	mg/L
SiO <sub>2</sub>	7
B	0.000
CO <sub>2</sub>	3.295
<b>Total Neutrals:</b>	<b>3.295</b>

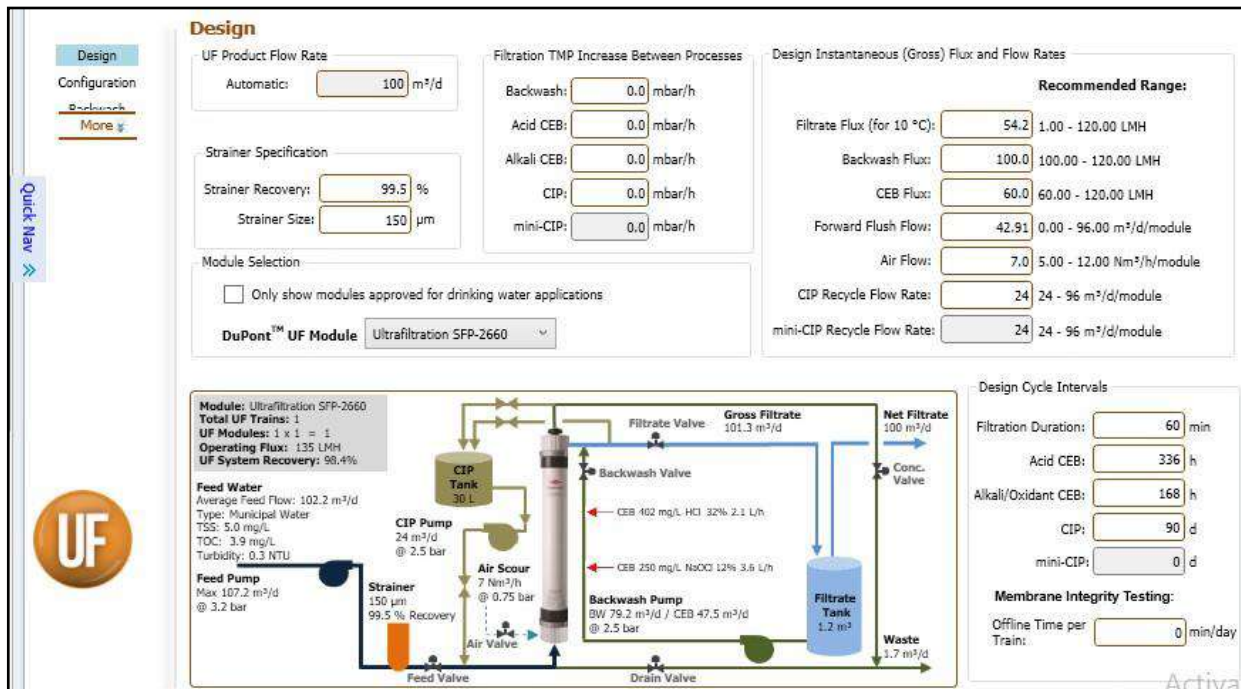
Total Dissolved Solids : 392.943 mg/L

Charge Balance: -4.837966 meq/L

Estimated Conductivity: 476.82  $\mu$ S/cm

**Figure D.2 Stage 2 of the WAVE design simulation**

Before proceeding to the next stage of the design, the WAVE performed an automatic ion balance. This was expected as the input values used were unbalanced averages and estimates in cases where data was not reported by Rand Water. In Figure D.2, the charge balance is shown as a substantial negative value. However, after the automatic balance, the charge balance was close to neutral (zero). Thereafter, WAVE automatically specified the layout and configuration of the UF stage based on the specified feed water data. Information such as the UF product flow rate, strainer specifications, module selection, feed pumps, chemical dosing and design cycle intervals were outputs of the software (Figure D.3).



**Figure D.3. Specification of the Ultrafiltration stage**

A summary report of the UF design was then made available by WAVE (Figure D.3). It was noteworthy that the software provided specifications of the backwash, chemically enhanced backwash and clean-in-place systems other than just the forward process. This is because the operational efficiency of the UF unit decreases with time as suspended solids accumulate on the membrane surface. The backwash system periodically passes a predetermined volume of water through the membrane in the opposite direction to the forward operation. This is done to dislodge the accumulated suspended solids from the membrane surface. After periodic intervals, the backwash process loses its potency. Hence, periodic chemically enhanced backwash operations are scheduled to maintain the efficiency of the UF membranes. In addition, periodic clean-in-place operations are performed on a greater interval than the chemically enhanced backwash operations. The clean-in-place is more rigorous than the chemically enhanced backwash operations to further ensure that the UF membranes are able to maintain their efficiency.

#### D.2.2.2 RO Design

One RO stage was selected to minimize the overall footprint and capital expense of the plant. WAVE recommended the RO element type, which was then specified. Based on this and the



results of the UF stage, the RO design was performed by the software. The RO design stage is depicted in Figure D.4.

**Reverse Osmosis Pass Configuration**

Configuration for Pass 1

Number of Stages: ☒ 1 ☐ 2 ☐ 3 ☐ 4 ☐ 5

Flow Factor:

Temperature: Design  °C

Pass Permeate Back Pressure:  bar

**Flows**

Feed Flow:  m³/d

Recovery:  %

Permeate Flow:  m³/d

Flux:  LMH

Conc. Recycle Flow:  m³/d

Bypass Flow:  m³/d

**System Configuration**

Feed → [RO Unit] → Concentrate (red line) and Permeate (blue line)

**Stages**

Stage 1	
# PV per stage	1
# Els per PV	6
Element Type	SEAMAX-440
Specs	
Total Els per Stage	6
Pre-stage ΔP (bar)	0.31
Stage Back Press (bar)	0.00
Boost Press (bar)	N/A
Feed Press (bar)	0
% Conc to Feed	0.00

**Figure D.4. Reverse Osmosis (RO) Design Stage**

### D.3 Literature Review

Much research has been performed on membrane technologies for water treatment such as UF (ultrafiltration) and RO (reverse osmosis) over the last two decades. Although these technologies were initially deemed impractical from an economic perspective, it is worth following the trajectory from pilot plant trials to industrialization in this theory section.

Rautenbach et al. (1996) used UF technology as a treatment option for municipal wastewater. Precipitation was used as a pretreatment step to UF. The system was tested on a pilot-scale using sand-filtered effluent of a municipal wastewater treatment plant. To further trial membrane technology, Rautenbach et al. (1996) used a combination of RO, nano-filtration and crystallization to treat dumpsite leachate. A 97% permeate recovery rate was attained. This demonstrated the viability of membrane technology in municipal and industrial water treatment applications. The latter study demonstrated a relatively low power consumption of 8.3 kWh/m<sup>3</sup> permeate, which was deemed considerably feasible in relation to the alternative technology of

evaporation. It is notable that Rautenbach et al. (1996) deemed the presented examples of municipal and industrial water treatment as illustrations of the impact of membrane processes on “modern wastewater treatment”. It was also indicated that UF and RO technologies were undergoing rapid development in specific energy reduction, investment costs reduction, improved recoveries, and the development of zero discharge processes (Rautenbach et al., 1996). Each of these focus areas have been addressed in subsequent studies (Clever et al., 2000; Knops et al., 2007; Lorain et al., 2007; Loganathan et al., 2015; Ho et al., 2015; Sun et al., 2015).

Sievers et al. (2017) denounced the feasibility of standard water treatment solutions. Instead, a combination of customized process technology was recommended to meet the demands of water treatment (Sievers et al., 2017). Hence, an increase in use of water treatment design software is expected to enable customized solutions within short timeframes. This statement agreed with the use of WAVE for the design of the water treatment plant for this current study. In addition, Sievers et al. (2017) presented a vision for year 2030, incorporating the (mega) trends and the research and development targets, challenges and resulting fields of action. The 2013 vision is a highly forward-thinking approach which could significantly help overcome technology challenges and their shortcomings. The most critical research and development target that Sievers et al. (2017) defined to enable the 2030 vision was continuous optimization of production systems to progressively reduce water demand and pollution loads. In light of this finding, it must be noted that the use of current water treatment design software is two-fold. Firstly, it enables the design of new plants. Secondly, it enables the optimization of existing plants to enable improved performance. It should be noted that WAVE is able to achieve both uses.

With respect to the membrane water treatment process, UF technology is often perceived as a pretreatment stage to the RO stage. This perception has been proved factual in various pilot plant studies (Clever et al., 2000; Knops et al., 2007; Lorain et al., 2007; Loganathan et al., 2015; Ho et al., 2015; Sun et al., 2015).

Rosberg (1997) researched UF technology as a cost-saving pretreatment technique for RO and

nano-filtration. At that time, UF was considered as a new and emerging technology which was not cost effective (Rosberg, 1997). Sand-filtration was more widely used as a pretreatment option. Subsequent research made it apparent that the exorbitant capital and operational costs of UF technology significantly decreased to the point that it is currently the preferred pretreatment option for RO technology (Lorain et al., 2007; Sun et al., 2015). Rosberg (1997) outlined the most common problems in RO systems as: precipitation or scaling, adsorption of organic fouling, deposition of colloidal dust, and biofouling. Rosberg (1997) claimed that the correct pretreatment for an RO system is a critical factor in the overall effectiveness of the water treatment plant. In this regard, it is noteworthy that Rosberg (1997) deemed UF as the “perfect pretreatment for RO”.

Rosberg (1997) perceived UF as a “reliable technology” as it can remove suspended solids, colloidal matter, viruses, and bacteria. Hence, Rosberg (1997) deemed the technology suitable for pretreating surface water for RO, recycling of backwash from sand filters and recycling of industrial and municipal water. The municipal water that is treated to process water for the chemical process in the study has better quality than surface water which the author proposed the UF to be used for. This validated the use of UF in the water treatment plant designed in this research article.

Clever et al. (2000) researched process water production from river water using pre-filtration, UF and RO on a pilot scale. The water treatment plant researched by Clever et al. (2000) resembled the water treatment plant designed in this research article except that the feed source was municipal water, rather than river water as investigated by Clever et al. (2000). The pre-filtration system removed suspended matter in the river water to prevent clogging of UF membranes. Clever et al. (2000) considered UF as a “new technology” to the industrial water treatment sector. This indicated that in the three-year period between the two studies by Rosberg (1997) and Clever et al. (2000), UF gained momentum and exhibited industrial implementation. The results indicated reliable plant operation with high availability. The system effectively removed suspended particles and microbes from river water, yielding high quality permeate (less than 0.05 NTU). Based on these results, an industrial plant was built to produce of 36 m<sup>3</sup>/h RO permeate for a major steel company. It was envisioned that the

operational expertise gained from the pilot plant would be transferred to the industrial plant.

With the onset of the fourth industrial revolution, pilot plants are no longer the only means of gaining operational and maintenance expertise on a proposed plant design. Currently, software simulations are able to accurately model and predict the actions of a proposed design. Such tools provide a “virtual reality” of a plant without having to physically build it. Optimizations can be easily implemented on the virtual plant to ensure that the best possible design will be implemented in reality. Such is the case with WAVE.

Over time, Knops et al. (2007) validated the UF-RO configuration for seawater water treatment from an economic perspective. They concluded that the higher operating cost of ultrafiltration compared to conventional pretreatment was an obstacle in using ultrafiltration membranes for seawater water treatment. As part of the study, Knops et al. (2007) proposed a new UF membrane to achieve a 2-7% decrease in operating costs. Knops et al. (2007) used typical operating conditions to quantify parameters for an industrial water treatment system. The parameters included UF membrane investment amortization; UF operating costs; operating cost reduction of the water treatment plant; and increased output of the water treatment plant due to greater operational capability and shorter construction time. These parameters provided a detailed economic breakdown of the proposed system. It is noteworthy that WAVE can automatically provide a cost analysis of the proposed design. This enables the cost analysis to be monitored. If the cost exceeds the budgeted amount, the design can be revised until the system is deemed affordable.

Similar to the evaluation of UF for the pretreatment of seawater for RO water treatment in the study by Knops et al. (2007), Lorain et al. (2007) ascertained the technical pretreatment benefits of UF membranes for RO in seawater water treatment. RO manufacturers recommend that the silt density index should not exceed 3 to avoid the rapid fouling of the RO membranes, which increases the plant downtime due to maintenance demands (Lorain et al., 2007). Lorain et al. (2007) performed studies on a pilot unit coupling two different pre-treatments (sand filtration and UF) and a standard RO membrane element. The seawater silt density index was between 6.1 and 6.4. Lorain et al. (2007) compared the effect of the two pre-treatments. The

results indicated that the silt density index after the UF modules was 1.2–2 while it was 5.8–5.9 with sand filtration. A 28% RO permeability reduction was measured over 30 days with sand filtration. The estimated frequency of RO chemical cleaning was between 12 and 18 days. With the UF pre-treatment, the RO permeability was unchanged over 20 days without chemical cleaning. These results experimentally validated the use of UF as an effective pretreatment means for RO.

Loganathan et al. (2015) investigated the UF-RO configuration for the treatment of basal aquifer water to reuse it in the production of synthetic oil. The investigation was significant in that it aimed to achieve zero-liquid discharge by designing a pilot plant comprised of the following process units: chemical oxidation, polymeric UF, RO and evaporation-crystallization technologies. The evaporation-crystallization unit evaporated water from the RO reject stream, consequently resulting in crystallization of the salts. Laboratory and pilot-scale tests on the RO reject indicated that feed softening was required to avoid scaling in the evaporator due to the high amounts of calcium, magnesium, and bicarbonate in the water to be processed. Overall, the findings of Loganathan et al. (2015) demonstrated that the zero-liquid discharge approach was effective in both producing freshwater and minimizing brine discharges. Considering the environmental benefits of zero-liquid discharge, it is recommended that crystallization be applied to the design of new and existing water treatment plants. In terms of water treatment plant design using WAVE, this must be done as a post-simulation step, as WAVE does not enable this option within the simulation.

“Hybrid” systems refer to the use of coagulants and flocculants to aid the pretreatment stage of the water treatment process. The work of Ho et al. (2015) and Sun et al. (2015) demonstrated a common enabler of the hybrid water treatment system. Ho et al. (2015) investigated the use of inline coagulation-UF as the pre-treatment of RO brine treatment and recovery on a pilot plant scale. This work is notable because most pretreatment measures entail the use of a strainer followed by the UF. Coagulants are typically used in water treatment to aid the “grouping or clumping together” of dissolved organic matter. This aids the separation efficiency of the dissolved organic matter from the water being treated. In the research of Ho et al. (2015), polyaluminium chloride, aluminium chlorohydrate and ferric chloride were used as coagulants.

The results indicated that ferric chloride achieved the optimal dissolved organic carbon removal (up to 60%). In addition, ferric chloride yielded the highest phosphate (99%) and silica removals (14%) at its optimum dosage and pH. Similarly, Sun et al. (2015) investigated the combined effect of various pretreatment systems on pilot-scale seawater water treatment. The pretreatment systems studied included ferric chloride flocculation, dual-stage sand filtration and UF. The membrane specific flux was used to evaluate the performance of the UF. Sun et al. (2015) found that the combination of UF with ferric chloride flocculation pretreatment reduced the specific flux during a chemically enhanced backwash period. Furthermore, they found that ferric chloride flocculation/dual-stage sand filtration/UF effectively stabilized the specific flux during a chemically enhanced backwash period compared to ferric chloride flocculation/UF alone. Although this hybrid technology has clear advantages, it was not required in the water treatment plant designed in the current study. It is noteworthy that WAVE does not currently offer the capability to implement hybrid technologies, such as coagulation within the current simulation regime.

After reviewing various water treatment pilot plant configurations by Clever et al., (2000), Knops et al., (2007), Lorain et al. (2007), Loganathan et al. (2015), Ho et al., (2015) and Sun et al., (2015), it is worth considering the simulations-based research in water treatment plant design and optimization. In this current fourth industrial revolution, it is expected that software simulations will advance to the point that they can provide a virtual reality of processes. This would eliminate the need to build pilot plants to perform industrial trial runs. In this phase of the review, simulation- based research was critiqued in relation to the WAVE software used in the water treatment plant design in this research article.

Niemi and Palosaari (1994) developed a flowsheet simulation of UF and RO processes. It is noteworthy that while much research was being undertaken on water treatment pilot plant studies, they were among the first researchers to undertake simulation efforts in this domain. As part of their studies, they developed a membrane separation model for reverse osmosis and ultrafiltration processes. The model could calculate the membrane area of a process, whilst the stream matrix of the process was determined by the UNICORN simulation program. The membrane separation model could also calculate the permeate flux and solute rejection in small

increments of the membrane tube. Niemi and Palosaari (1994) fitted polynomial equations to the experimental data or used mass transfer models to calculate the permeate flux and rejection. Experimental data were partially required to determine the parameters of the mass transfer model equations by parameter fitting. The membrane separation model was tested by simulating the reverse osmosis of aqueous ethanol and acetic acid solutions and ultrafiltration of aqueous sodium carboxymethylcellulose and poly (vinylpyrrolidone) solutions. Multistage recycle separation processes with four or five recycle stages were used as test processes, from which reliable results were found. Although the flowsheet simulation approach used in the study was effective in the past, technology has advanced to the point that parameter fitting tools and mass transfer equations are built into current software packages to enable efficient process simulations. In addition, the software tool used by Niemi and Palosaari (1994) required a comprehensive set of input data, which is not required by currently available simulation tools. WAVE offers both advantages.

Resonating with various studies in which UF was used as a pretreatment stage to RO (Lorain et al., 2007; Sun et al., 2015) Cardona et al. (2005) perceived the UF-RO configuration as an optimization technique. The UF unit was coupled with a two-stage RO system for seawater water treatment. The study by Cardona et al. (2005) was simulation-based, unlike previous studies in which pilot plants were used (Clever et al., 2000; Knops et al., 2007; Lorain et al., 2007; Loganathan et al., 2015; Ho et al., 2015; Sun et al., 2015). The water treatment plant was simulated in Excel using Visual Basic macros. This simulation method reported by Cardona et al. (2005) differed from that of WAVE used in the current study. Firstly, WAVE enabled the ability to preset stage and pass numbers for both UF and RO systems. Secondly, the pretreatment step in the work of Cardona et al. (2005) was specified on a separate platform to the main simulation. This differed functionally from WAVE, which automatically incorporated the pretreatment step in the design configuration.

Cardona et al. (2005) considered UF as a “low energy consumption process”- a sharp contrast to the expensive description of UF technology in the earlier research of Rosberg (1997). This demonstrates the manner in which the perception of membrane technologies in water treatment has become favourable with over time.

The scaling of RO membranes is a universal concern that was investigated by Karabelas et al. (2020). According to this study, the water treatment industry is challenged by the inadequacy and inaccuracy of available methods to assess feed-water scaling propensity, selection and optimization of scaling control schemes, and monitoring of membrane scale-formation during plant operation. Hence, Karabelas et al. (2020) outlined the mechanisms involved in scaling within RO membrane modules, monitoring and mitigation procedures. In their study, Karabelas et al. (2020) indicated that the rate of scale-mass deposition per unit membrane-surface-area was the most appropriate parameter for modeling and quantifying incipient scaling. Based on this finding, they recommended the development of a comprehensive predictive tool to be used in the early stage of RO-plant design and optimization, when efforts should be considered to control scaling. Furthermore, they suggested combining the results from well-designed small-scale membrane- scaling tests with theoretically-sound modeling of water treatment module performance. In this regard, it is noteworthy that WAVE is able to issue design warnings with respect to the scaling of RO membranes. In line with the suggestions made by Karabelas et al. (2020), WAVE enables the input parameters to be manipulated until optimal results are obtained with respect to optimal operation of the water treatment plant being designed.

#### **D.4 Results**

The complete set of simulation results from the WAVE software can be found after the Conclusions of this Appendix. The most pertinent results are outlined below.

##### ***D.4.1 UF Results***

The UF Results are shown in Figure D.5, Table D.2 and Table D.3.



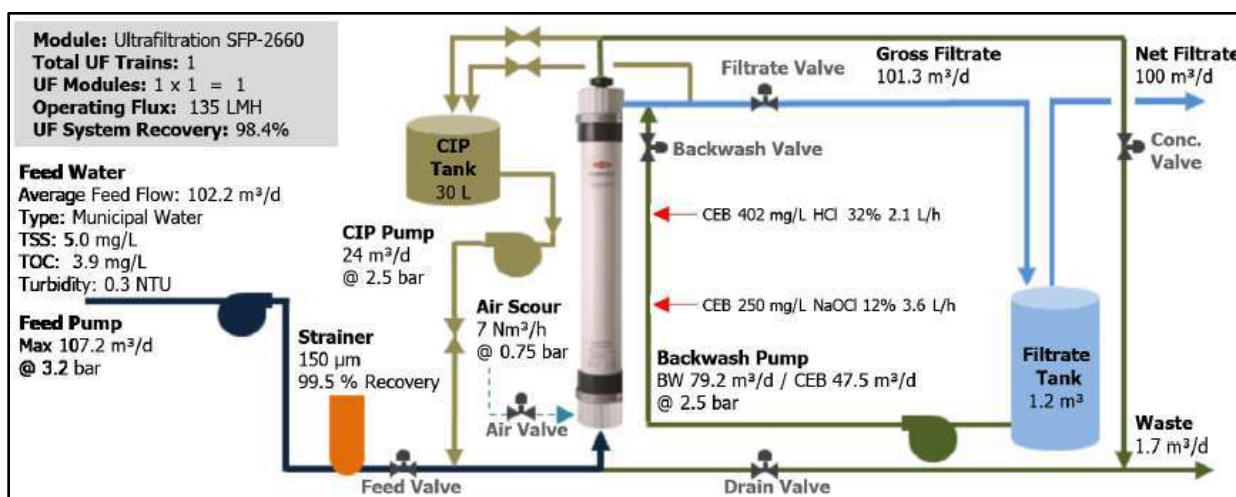


Figure D.5. Summary of the UF Design

Table D.2. UF Feed and Permeate Streams Comparison

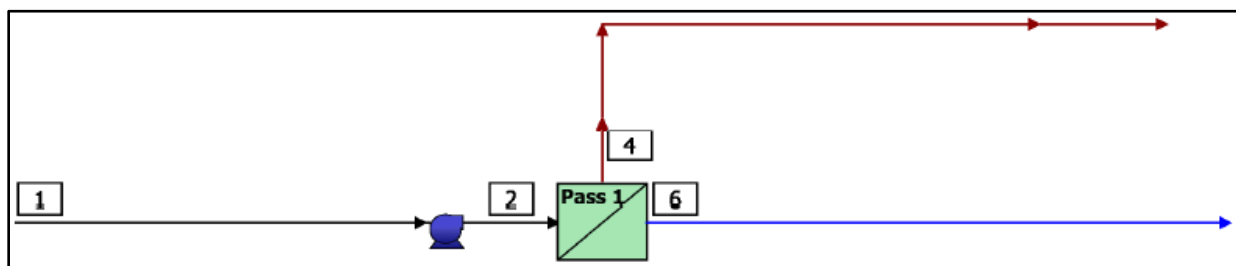
Parameter	Feed	Permeate
Temperature (°C)	20.0	20.0
Turbidity (NTU)	0.3	≤ 0.1
Total suspended solids (mg/L)	5.0	0.0
Total organic carbon (mg/L)	3.9	3.5
Silt density index	0.2	≤ 2.5
Total dissolved solids (mg/L)	449	449
pH	8.1	8.1

Table D.3. UF Module Details

Parameter	Details
Name	Ultrafiltration SFP-2660
Membrane area (m²)	33
Length (m)	1.863
Diameter (m)	0.165
Weight (empty) (kg)	25
Weight (water-filled) (kg)	41
Water volume (L)	16

### D.4.2 RO Results

The RO Results are shown in Figure D.6, Table D.4 and Table D.5 below.



**Figure D.6. RO Flow Diagram**

**Table D.4. RO Stream Information**

Stream	Description	Flow (m <sup>3</sup> /day)	Total dissolved solids (mg/L)	Pressure (bar)
1	Raw feed to RO system	100.0	444.2	0.0
2	Net feed to Pass 1	100.0	444.3	5.2
4	Total concentrate from Pass 1	25.0	1,755	4.6
6	Net product from RO system	75.0	3.05	0.0

**Table D.5. RO Ion Removal**

Ion	Chemical formula	Feed	Permeate	% Removal
Ammonium	NH <sub>4</sub> <sup>+</sup>	0.63	0.02	96.83
Potassium	K <sup>+</sup>	6.93	0.10	98.56
Sodium	Na <sup>+</sup>	25.46	0.33	98.70
Magnesium	Mg <sub>2</sub> <sup>+</sup>	17.97	0.08	99.55
Calcium	Ca <sub>2</sub> <sup>+</sup>	44.59	0.19	99.57
Strontium	Sr <sub>2</sub> <sup>+</sup>	17.18	0.07	99.59
Barium	Ba <sub>2</sub> <sup>+</sup>	4.91	0.02	99.59

Carbonate	CO <sub>3</sub> <sup>2-</sup>	3.22	0.00	100.00
Bicarbonate	HCO <sub>3</sub> <sup>-</sup>	313.3	2.16	99.31
Nitrate	NO <sub>3</sub> <sup>-</sup>	0.05	0.01	80.00
Chloride	Cl <sup>-</sup>	4.34	0.05	98.85
Fluoride	F <sup>-</sup>	0.07	0.00	100.00
Sulfate	SO <sub>4</sub> <sup>2-</sup>	5.58	0.01	99.82
Total dissolved solids	-	444.2	3.05	98.56

**Table D.6. UF and RO Cost Comparison**

Parameter	Daily cost (\$)		Specific (per m <sup>3</sup> )	
	UF	RO	UF	RO
Service water				
• Feed water	0.23	3.50	-	-
• Wastewater disposal	1.50	17.26	-	-
Electricity cost	0.86	1.6	-	-
Specific energy	-	-	0.10 kWh	0.24 kWh
Chemicals				
• Citric acid	0.01	-	-	-
• Sodium hypochlorite	0.01	-	-	-
Feed pump	-	1.63	-	-
Utility and chemical cost	2.26	22.4	-	-
Specific water cost	-	-	\$ 0.023	\$ 0.298

## **D.5 Discussions**

### **D.5.1 UF Design**

Although no pre-filtration stage was selected in the flowsheet configuration, WAVE suggested a 150  $\mu\text{m}$  strainer to filter out approximately 0.5  $\text{m}^3/\text{day}$  of large, suspended solids that would otherwise clog the UF membranes. In Figure D.3, the UF detailed design report provided an overview of the forward and reverse modes of operation (backwash, chemically enhanced backwash and clean-in-place). The process flow diagram for the UF operation also included the recommended strainer. The other key UF parameters included the pump hydraulics and electrical costs, membrane pressure ratings and storage tank dimensions. It is noteworthy that each of these specifications is vital in practically implementing the design during the execution phase.

The UF feed and permeate results in Figure D.3 indicated that the total suspended solids of the UF permeate stream was reduced to zero. This was logical, as the purpose of the UF was to remove the suspended solids contained in the source water. The reduced total suspended solids also decreased the turbidity by two thirds. The total organic carbon was also slightly reduced. It was significant that the UF operation had no effect on the total dissolved solids of the source water, as the total dissolved solids reduction was anticipated to take place by the subsequent RO operation. Based on the specified municipal water source, WAVE specified the UF module details as outlined in Table D.3. The indicated module dimensions and expected mass was of practical significance for on-site implementation. Two UF design warnings were issued. The warnings indicated that the filtration flux and trans-membrane pressure values marginally exceeded the design limits. This result was not a cause for concern as the feed flowrate and backwash frequency can be adjusted to counteract the warnings.

Other indications on the design report included the UF operations of filtration mode and backwash cycles. In addition, the pump and valve conditions were indicated as a function of the UF operation steps (including the backwash, chemically enhanced backwash and clean-in-place stages). The availability of the UF operational information is beneficial for control and instrumentation engineering, where a detailed knowledge of the interrelations between pump

and valve functioning for each operational step is required. The UF design report was concluded with the utility and chemical costs (service water, electricity and dosing chemicals) as indicated in Table D.2, the dosing chemicals are required to maintain the pH of the water within acceptable limits to prevent membrane scaling. The utility and chemical costs were relatively low at \$ 2.26 per day, corresponding to a specific water cost of \$ 0.023 per cubic meter of water produced.

#### ***D.5.2 RO Design***

Unlike the integrated process flow diagram presented for the UF system in Figure D.3, no detailed report was specified for the RO system. Instead, WAVE output a block flow diagram as shown in Figure D.4. The corresponding stream information was specified in Table D.4. It was significant that the total dissolved solids were reduced from 443.2 mg/L to 3.05 mg/L in the RO permeate stream (98.56% reduction). This is a substantial total dissolved solids reduction which would enable the RO permeate to function as deionized water for chemical process. Hence, this result substantiated the one pass configuration that was specified in the inputs.

Regarding the RO system specifications, WAVE recommended that only one RO train be used. Generally, the number of trains and passes varies according to the contamination degree of the source water with respect to the solutes to be removed. It was expected that the municipal water source would contain less solutes than others, such as seawater (Cardona et al., 2005; Knops et al., 2007; Lorain et al., 2007; Sun et al., 2015). Hence the one train, one pass RO system specified by WAVE was deemed realistic. The implementation of a standby RO train would double the capital cost. Hence, no standby train was recommended. From a technical perspective, the no-standby recommendation was justified as the proposed “duty” RO system was equipped with integrated regeneration capabilities, such as periodic backwashes, chemically enhanced backwashes, clean-in-place and (optional) chemical dosing for anti-scaling and anti-fouling.

The overall system recovery was specified at 75%. This recovery is adequate to meet the deionized water supply required by the Biorefinery production process. Two types of RO

design warnings were issued: the concentrate flow rate fell below the minimum limits and the element recovery exceeded the maximum limits. As with the UF design, these warnings indicated that the system was not projected to fully perform in accordance with the simulated design. Both warnings directly deal with the issue of flowrate or UF product throughput through the RO membranes. Hence, it is recommended that a holding tank be used to store the UF permeate (product water) prior to the RO section. This will ensure that the RO booster pumps have an adequate supply of water to pump through the RO membranes. Consequently, this will enable the RO system to meet the minimum concentrate flow rate and element recovery limits.

In addition to the above warnings, the RO design report indicated solubility warnings related to potential scaling of the RO membranes by the dissolved solids. To counteract these warnings, WAVE recommended the use of anti-scalants that can be dosed into the water supply to the RO membranes. It is recommended that the anti-scalants be dosed directly into the holding tank to counteract the former design warnings. It is significant that the design warning enables the implementation of mitigation factors prior to plant implementation. This is a form of predictive maintenance.

The solute (ion) concentrations of the feed and permeate streams are indicated in Table D.5. The percentage reduction effected by the RO operation is indicated in the last column. As expected, the RO operation resulted in a substantial reduction in solutes (exceeding 97%). The removal of the ions was linked to the 98.56% total dissolved solids reduction.

The UF and RO costs were compared in Table D.6. The RO utility and chemical costs amounted to \$ 22.4 per day. This cost is approximately tenfold the corresponding UF utility and chemical costs and is attributed to the greater power requirements to achieve the substantial differential pressure across the RO membranes to remove the dissolved solids from the water. Consequently, the specific cost was \$ 0.298 per cubic meter of RO water produced. In addition, the wastewater disposal cost was significantly greater than that for the UF system. This is because the salt reject stream must be treated before being released to the environment. For this purpose, crystallization may be used (Loganathan et al., 2015).

Two shortfalls of WAVE were perceived. Firstly, hybrid pretreatment methods (Ho et al., 2015; Sun et al., 2015) are not currently integrated into the water treatment simulations. Hence, these methods must be simulated separately from the main water treatment design. Secondly, WAVE lacks the capability for crystallization process modelling to treat the salt reject streams. Again, if crystallization is required, separate simulations will be required outside WAVE. Despite these shortfalls, WAVE provided a comprehensive detailed design of the water treatment process required to produce deionized water for the Biorefinery production process. The design was performed without any major cost requirement (efficiently). Hence, the hypothesis of this research article was deemed true. The simulations can be performed with very few input requirements unlike previous simulation models (Niemi and Palosaari, 1994; Cardona et al., 2005).

The practical implications of this research article were twofold. Firstly, WAVE can be used by Engineers and Academics to efficiently and effectively design new water treatment systems. Estimate source water quality results can be used if the actual source water analyses are not available. Secondly, Engineers can use WAVE to optimize existing water treatment plants by identifying design warnings and subsequently implementing mitigation measures.

## **D.6 Conclusions**

The use of water treatment plant simulations on current and developing design software tools such as WAVE implies that water treatment pilot plant trials are no longer required prior to industrial implementation. This has time and money-saving implications for Academics and Engineers. Each WAVE simulation can present a customized water treatment solution, which addresses the concern that standard water treatment solutions are not feasible. The use of WAVE also enables the 2030 vision of Sievers et al (2017) regarding the “continuous optimization of production systems”. WAVE is capable of predicting design warnings and recommending corresponding mitigation measures. Hence, it is able to address the RO challenges outlined by previous studies. The hypothesis that WAVE can be used to design the water treatment plant to produce process water for a novel South African Biorefinery production process was proved.